Synthesis, Characterization and Amphiphilic Self-Assembly of Inorganic Nanoparticles Functionalized with Polymer Brushes of Variable Composition and Chain Length

by

Brian Coleman
B.Sc., McMaster University, 2012

A Thesis Submitted in Partial Fulfillment
of the Requirements for the Degree of

MASTER OF SCIENCE

in the Department of Chemistry

Synthesis, Characterization and Amphiphilic Self-Assembly of Inorganic Nanoparticles Functionalized with Polymer Brushes of Variable Composition and Chain Length

by

Brian Coleman
B.Sc., McMaster University, 2012

Supervisory Committee

Dr. Matthew Moffitt, Supervisor

(Department of Chemistry)

Dr. Irina Paci, Departmental Member

(Department of Chemistry)

Supervisory Committee

Dr. Matthew Moffitt, Supervisor

Department of Chemistry

Dr. Irina Paci, Departmental Member

Department of Chemistry

ABSTRACT

The synthesis, characterization and amphiphilic self-assembly of polymer brush functionalized nanoparticles (PBNPs) using a block copolymer template is described herein. To study the effect of polymer brush composition on self-assembly, four samples were created using a mixture of PS-*b*-PAA (polystyrene-*block*-polyacrylic acid) and PMMA-*b*-PAA (poly(methyl methacrylate)-*block*-polyacrylic acid) diblock copolymers to create PBNPs with a CdS quantum dot (QD) core and different ratios of PS and PMMA in the coronal brush. Static light scattering showed that despite differences in brush composition, the PBNPs formed nanoparticles of similar aggregation number and chain density but showed evidence of asymmetric structure in a common solvent for both blocks at higher PS contents. After subsequent hydrolysis of the hydrophobic PMMA to hydrophilic poly(methacrylic acid) (PMAA), these amphiphilic particles were then self-assembled in THF/H_2O solution in which it was determined that increasing the hydrophobic content of the brush composition, the initial nanoparticle concentration (c_0) or the added salt content (R_{NaCl}), would cause the assembly of low curvature assemblies. Compilation of this data allowed for the construction of phase diagrams for PBNP systems based on brush composition and c_0 at different salt contents. Lastly, PS-*b*-PAA-*b*-PMMA triblock copolymers with variable PMMA chain length were assembled into PBNPs around a CdS QD core using a

block copolymer template approach. Light scattering showed these particles also had similar aggregation number and chain density despite the difference in PMMA chain length. After hydrolysis of PMMA to PMAA these particles were then self-assembled in THF/H_2O mixtures to determine the role of PMAA block length on the produced morphological structures. The resulting assemblies suggest that chain length played a minimal role in their self-assembly

TABLE OF CONTENTS

List of Tables

List of Figures

LIST OF ABBREVIATIONS

CdS – cadmium sulfide

cmc – critical micelle concentration

cwc – critical water concentration

DLS – dynamic light scattering

EDC - *N*-ethyl-*N*'-(3-dimethylaminopropyl)carbodiimide methiodide

GPC – gel permeation chromatography

LSFCM – laser scanning fluorescence confocal microscopy

NMR – nuclear magnetic resonance

NOESY – nuclear Overhauser effect spectroscopy

NP – nanoparticle

PAA – polyacrylic acid

PBNP – polymer brush functionalized nanoparticle

PMAA – poly(methacrylic acid)

PMMA - poly(methyl methacrylate)

PS – polystyrene

PtBA – poly(*tert*-butylacrylate)

QD – quantum dot

SLS – static light scattering

TEM – transmission electron microscopy

Acknowledgements

For Leah

Chapter 1

General Introduction

1.1 General Introduction

The ever-growing needs of the modern world requires the creation of new classes of materials to drive innovation and scientific research beyond the current limits of human ingenuity. One avenue of particular interest is that of colloidal inorganic nanoparticles, whose capabilities and functionalities have intrigued the scientific community and opened up promising new lines of investigation and inquiry. Specifically, metallic and semiconducting nanoparticles with their alluring size-tunable properties (e.g. photoluminescence, non-linear optics and surface plasmonic resonances), have found their place in fields as varied as fluorescent bio-imaging[1-3], sensors[4-7], heavy metal detection in water[8], photonics[9-12] and drug delivery agents[13-15]. But for all of their promise, the controlled assembly of these nanoparticles has proven difficult in their naked, non-functionalized form. In order to control the assembly of inorganic nanoparticles into films and colloids, researchers either follow a lithographic (top-down) approach or a self-assembly (bottom-up) based methodology. Top down lithographic approaches such as photolithography[16-19], colloidal lithography[20,21] and electron lithography[22-25] have proven capable of assembling quantum dots, but are less economically viable and don't allow for the organization of nanoparticles in colloidal structures. The bottom up approach of self-assembly has seen an increased focus, including the co-assembly of inorganic nanoparticles with block copolymers in solution.[26-30] The addition of a coronal brush of polymers to the inorganic nanoparticles gives far superior solubility and dispersability in the solution phase, leading to greater control over the assembly, deposition and application of these materials.

This thesis consists of three main components. In Chapter 2, a novel approach for the self-assembly of cadmium sulfide (CdS) nanoparticles functionalized with a pair of diblock copolymers will be presented. This innovative approach uses a blend of diblock copolymers to

create a mixed polymer-brush functionalized nanoparticle (PBNP). While previous approaches attempt to functionalize to[31] or from[32] a previously synthesized inorganic nanoparticle, or grow in-situ from a triblock copolymer template[33], this diblock copolymer template approach uses materials that allows for the creation of PBNPs with readily variable brush composition, allowing for the role of brush composition in self-assembly to be explored.

Chapter 3 of this thesis highlights the self-assembly of a series of blends of these mixed brush functionalized nanoparticles in a tetrahydrofuran (THF) / H_2O solution. Of particular note are the differences in hierarchical assemblies created by altering the ratio of polystyrene (PS) and poly(methacrylic acid) (PMAA) found in the polymer brush coating.

Chapter 4 will investigate the effect of PMAA chain length on the self-assembly of polymer brush-functionalized nanoparticles. To this end, a pair of triblock copolymer templated mixed polymer brush nanoparticles were produced and the different hierarchical assemblies created by altering the number of monomer units found in the PMAA coronal chains were investigated.

This remainder of Chapter 1 will be divided as follows. The first section consists of a discussion of types of polymers and important properties. This will be followed by a description of diblock and triblock copolymer micellization in selective solvents, as well as amphiphilic block copolymers in aqueous solvents. An introduction to quantum dots and the quantum confinement effect will follow. The next component will describe synthetic approaches to the creation of PBNPs, followed shortly by an examination of different types of mixed brush block copolymer functionalized nanoparticles and their hierarchical assemblies. The penultimate section will consist of background information of the major characterization techniques used to examine these materials. Finally, specific goals of this thesis will be defined.

1.2 Polymers and Block Copolymers

1.2.1 Polymers

A *polymer* is a large molecule consisting of a repeating series of smaller molecules (*monomers*) linked together.[34] The monomers are then known as *repeat units* once polymerization has occurred and the number of times that repeat unit is found is known as the *degree of polymerization*.

If there is only one monomer unit that repeats in the polymer chain, it is known as a *homopolymer*. If there are several different repeat units found throughout the polymer, this is known as a *copolymer.* There are several types of copolymers based on how the repeat units are ordered within the polymer. Such varieties of copolymer include: *random copolymers, block copolymers, alternating copolymers* and *graft copolymers* (Figure 1.1).

AAAAAAAAAAAAAAAABBBBBBBBBBBBB	Block Copolymer
ABABABABAAABABBBABBAABABABAABA	Random Copolymer
ABABABABABABABABABABABABABABAB	Alternating Copolymer
AAAAAAAAAAAAAAAAAAAAAAAAAAAAA B B B B	Graft Copolymer

Figure 1.1. Varieties of possible copolymers formed using A and B repeat units

A block copolymer is a polymer in which multiple chains of a single repeat unit are covalently linked to each other. If there are two chains linked together, the polymer is a *diblock*

copolymer. If there are three chains linked together, whether it be in an ABA, BAB or ABC orientation (where all three blocks are different), this is known as a *triblock copolymer*. A random copolymer consists of two or more repeat units distributed randomly throughout the chain. An alternating copolymer consists of two repeat units attached in an interchanging fashion. A graft copolymer consists of one block of repeat units attached onto the backbone of another block.

1.2.2 Molecular Weight Distribution

Polymers are dissimilar from small molecules in that a sample of multiple polymer chains will have a distribution of molecular weights. This is attributed to the random nature of the polymerization reaction itself, as all chains do not grow at exactly the same rate.[35] The size of the polymer is characterized by its average molar mass, which is based on the molar mass of an individual repeat unit and the number of times it repeats (degree of polymerization).

Due to the distribution of molecular weights found in each sample of polymer chains, there are two different averages that are generally reported for a given polymer. The number average molecular weight, M_n, is based on the number of polymer chains with a given molecular weight found in the sample.[34] It is defined by the following equation:

$$M_n = \frac{\Sigma N_i M_i}{\Sigma N_i} \qquad \text{(Equation 1.1)}$$

where N_i is the number of molecular species i of molecular weight M_i. This value is often determined from techniques that measure molecular weight based on the colligative properties of polymer solutions, as they are dependent on the number of polymer chains present.

The second molecular weight average that is often reported is the weight-average molecular weight, M_w.[34] This value is usually measured by techniques that are more sensitive to the size of the polymers in a given sample. This means that larger polymer chains are weighted much more than smaller chains in the final average molecular weight. M_w is defined by equation (1.2).

$$M_w = \frac{\Sigma W_i M_i}{\Sigma W_i} = \frac{\Sigma N_i M_i^2}{\Sigma N_i M_i} \qquad \text{(Equation 1.2)}$$

W_i is the weight of all the molecules of species i with molar mass M_i. Using these two average molecular weight values, one can determine the width of the molecular weight distribution, or *polydispersity index (P.I.).* The polydispersity index can be determined by the use of equation (1.3):

$$P.I. = \frac{M_w}{M_n} \qquad \text{(Equation 1.3)}$$

A polydispersity index of 1 denotes a sample that is *monodisperse*, in which all of the polymer chains all the same length. Most polymers will have a *P.I.* value >1 due to the distribution of polymer chains lengths.

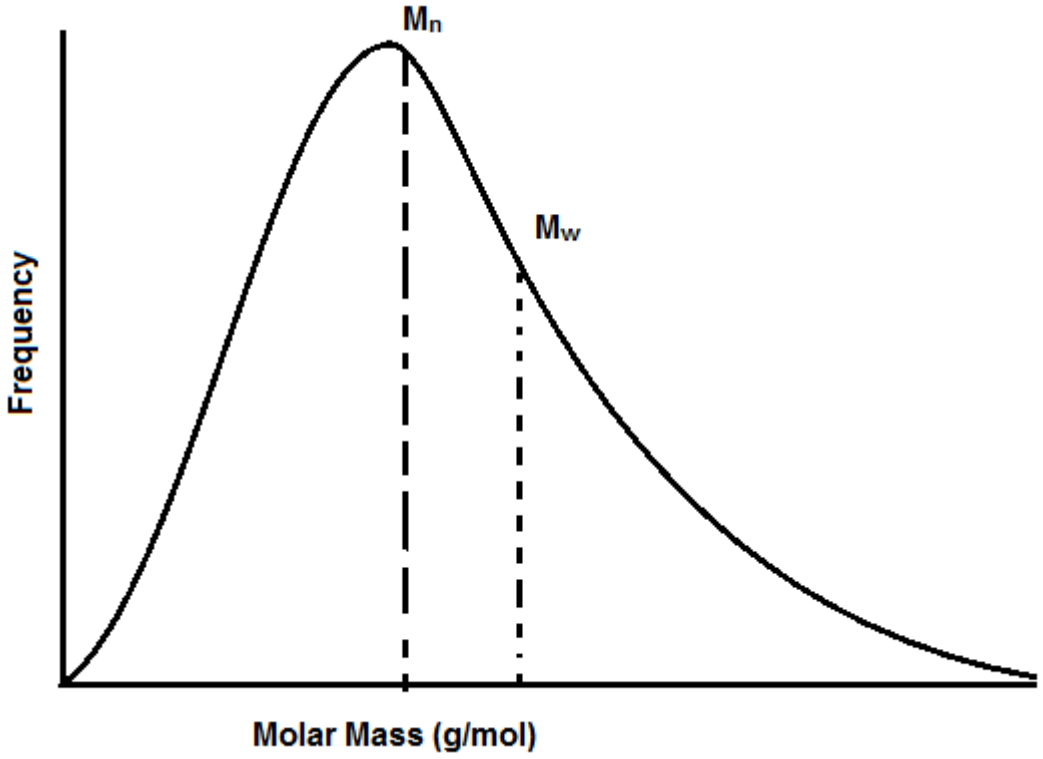

Figure 1.2. Depiction of the positions of M_n and M_w based on the molar mass distribution of a theoretical polymer.[36]

1.3 Micellization of Diblock and Triblock Copolymers in Selective Solvents

1.3.1 Formation of Block Copolymer Micelles

The dissolution of diblock copolymers in a solvent that is a *good* solvent for one block segment and a *poor* solvent for the other block will often lead to the aggregation of single chains into micelles. The insoluble blocks collapse in the solvent to form a central core while the soluble block will become swollen with the solvent, forming the corona of the micelle. This micellization only occurs once the concentration of polymer chains reaches the *critical micelle concentration (*cmc*).*[35] Micelles are placed in two general categories. *Reverse micelles*, where the

hydrophobic block forms the corona and the hydrophilic block forms the core. These tend to form in organic solvents. If aqueous solvents are used, the micelles are known as *regular micelles* and the hydrophilic block instead forms the corona and the hydrophobic block is found in the core. The micelles can be further categorized as "star-like" if the block that forms the corona is long as that which forms the core, or "crew-cut" if the opposite case is true.[37]

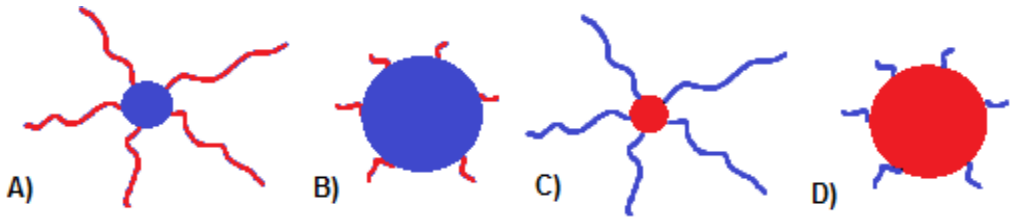

Figure 1.3. Schematic depicting A) regular star-like B) regular crew-cut C) reverse star-like and D) reverse crew-cut. A and B would form in aqueous solvents while C and D would be formed in organic. Red indicates hydrophobic blocks while blue indicates hydrophilic blocks.

1.3.2 Thermodynamics of Block Copolymer Micellization

In order for micellization to occur, the overall Gibbs free energy of the solution, ΔG, must be negative for the micellization process to be spontaneous.[38] ΔG can be defined in terms of enthalpy (ΔH) and entropy (ΔS) and their relationship is defined by equation 1.4:

$$\Delta G = \Delta H - T\Delta S \qquad \text{(Equation 1.4)}$$

T in this case is the temperature. The micellization of block copolymers arises from a series of enthalpic and entropic driving forces created by the interaction of the polymer chains with the solvent environment. In organic solvents, there is an overall decrease in entropy brought about by the localization of the polymer blocks at the corona/core interfacial region as well as the chain stretching during the packing of the core and coronal blocks in the micelle. Both of these

factors lead to a loss of conformational entropy and hence a more negative entropy term. This is counter balanced by a decrease in enthalpy that results from the interchange energy that is produced when the core forming block moves from a region of unfavourable polymer/solvent interactions to a more favourable area of polymer/polymer interactions in the core of the micelle. This interchange enthalpy is the main driving force for micellization in organic solvents.[39,40]

When these block copolymers are placed in an aqueous solvents, there are a different combination of factors in play. While there is an entropic penalty associated with the formation of micelles, this is counteracted by the *hydrophobic effect*. The hydrophobic effect refers to the increase in entropy of the water as micelle structures form, excluding the water molecules from the hydrophobic block on the micelle corona. This overall increase in entropy caused by the hydrophobic effect is much stronger than the entropic penalty of the block copolymer assembly, leading to the formation of micelles above the cmc.[41,42]

1.3.3 Micellization of Ionic Diblock Copolymers in Organic Solvents

An ionic block copolymer is one in which one of the blocks on the block copolymer contains charged repeat units.[42] The large electronic difference between the charged ionic blocks and the hydrophobic coronal blocks provides the necessary driving force for phase separation between these two blocks, leading to micellization.[43] In the present work, a cadmium acrylate base will be used to deprotonate poly(acrylic acid), creating a charged acrylate block that will have a very unfavourable interaction with the apolar organic solvent (benzene). The polyacrylate block will form the core of the micelles and while the hydrophobic polystyrene or poly(methylmethacrylate) block will disperse favourably in the solvent to form the corona of the micelle. This has been represented in Figure 1.4:

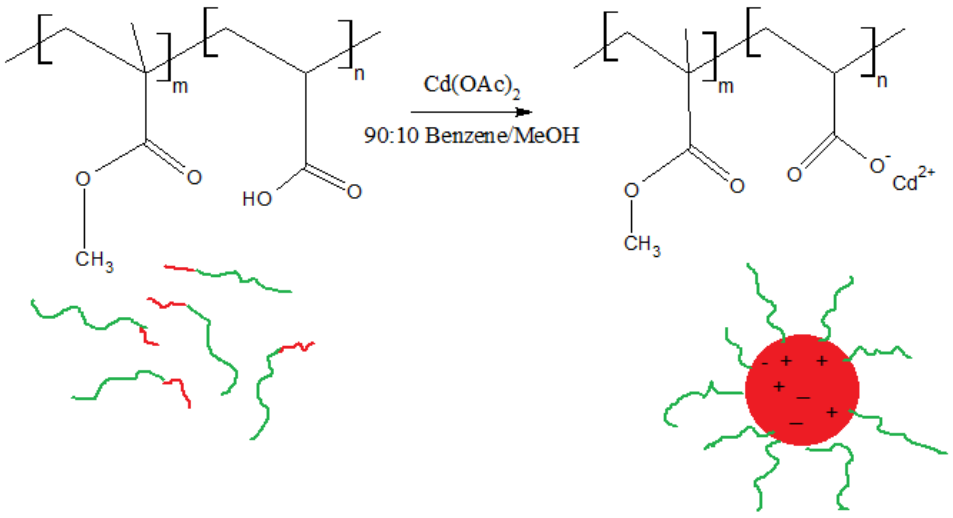

Figure 1.4. Formation of block ionomer micelles by deprotonation of poly(acrylic acid) chains in organic solvent. The polymer structure before and after deprotonation are displayed with their corresponding configurations at each step of the synthesis.

1.4 Inorganic Nanoparticles and Quantum Dots

Inorganic metallic or semiconducting nanoparticles are used in a broad array of applications due to their ability to display useful properties attributed to their small size compared to their bulk counterparts. A nanoparticle is usually found to be between 1-10 nm in length, larger than single molecules but smaller than bulk solids.[44] The size-dependent properties of nanoparticles arise from increased surface-to-volume ratio as well as changes in electronic structure compared to bulk solids.[43] For example, comparing the melting points of bulk CdS with a sample of CdS in the nanoparticle regime, bulk CdS has a melting point of ~1600 °C while a nanoparticle of CdS that is 2.5 nm will have a much lower melting point around ~400 °C[45]. This large disparity in melting point is a direct result of the increased surface energy brought on by the larger surface area of the nanoparticle.

Quantum dots are a specific type of inorganic nanoparticle consisting of semiconducting material whose optical and electronic properties are strongly-dependent on the size of the particle.[150] The molecular orbitals in bulk semiconductors are so numerous and closely-spaced in energy that they can be viewed as continuous bands. The valence band consists of the lower energy orbitals which are generally filled with available electrons first. The conduction band consists of the higher energy orbitals which are either partially filled with electrons or are empty. When a photon of light excites the semiconductor with sufficient energy, electrons are excited from the valence band to the conduction band. The valence band will now have a positively charged hole where the electron once was while the negatively charged electron is now located in the conduction band. The pairing of the hole with the electron is known as an *exciton,* which has a size characterized by the Bohr exciton radius.

When the size of the particle becomes comparable to the size of the exciton Bohr radius, the properties of the material change due to the *quantum confinement effect*. As the particles get smaller, the number of available states at a given energy level that electrons are allowed to occupy decreases. This is also known as the density of states, found in units of *N*/eV, where *N* is the number of states.[151] Figure 1.5 shows how the decreased density of states creates larger transitions between energy levels, requiring more energy for each transition.[152]

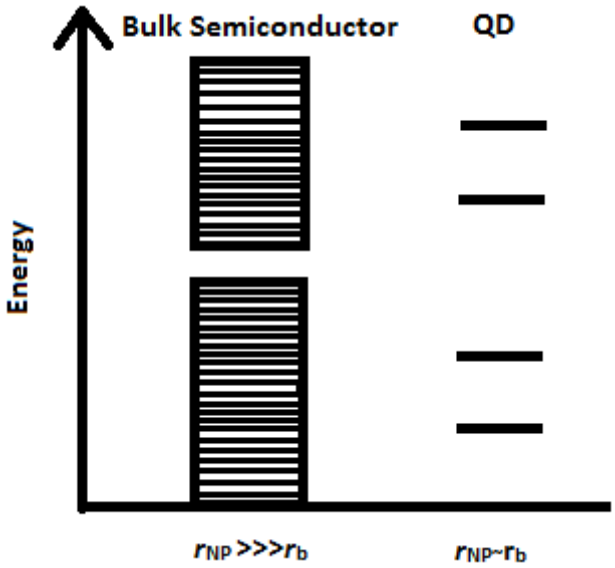

Figure 1.5. Schematic depicting of the change in the density of states once the size of the particle (r_{NP}) approaches the exciton Bohr radius (r_b)

Quantum dots have been described using the particle-in-a-box model by Brus[46], in which the particle is represented by the electron and the box takes on the spherical shape of the nanoparticle. In the model, the electron is confined by an infinitely high surface energy on the nanoparticle itself. Under these conditions, the exciton energy of the semiconducting nanoparticles was determined to be:

$$E^* = E_g + \frac{\hbar^2 \pi^2}{2R^2}\left[\frac{1}{m_e} + \frac{1}{m_h}\right] - \frac{1.8e^2}{\epsilon R} + \cdots \qquad \text{(Equation 1.5)}$$

where E^* is the energy of the exciton, E_g is the energy of the band gap, R is the radius of the particle, m_e and m_h are the masses of the electrons and holes in the lattice, e is the charge of an electron and ϵ is the permittivity. The positive confinement term (second from the right) is inversely proportional to the square of the radius of the particle, meaning that as the size of the particle decreases, the energy of the exciton increases exponentially. The negative term (first from the right) is the bound exciton energy term. It arises from the Coulombic attraction between

the electron and the hole that comprise the exciton. As the positive confinement term scales more strongly with size than the electrostatic term, the net result is that as the size decreases the positive term dominates and the energy increases. [46] The absorption spectra of CdS nanoparticles of differing sizes dispersed in aqueous solution can be found in Figure 1.6:

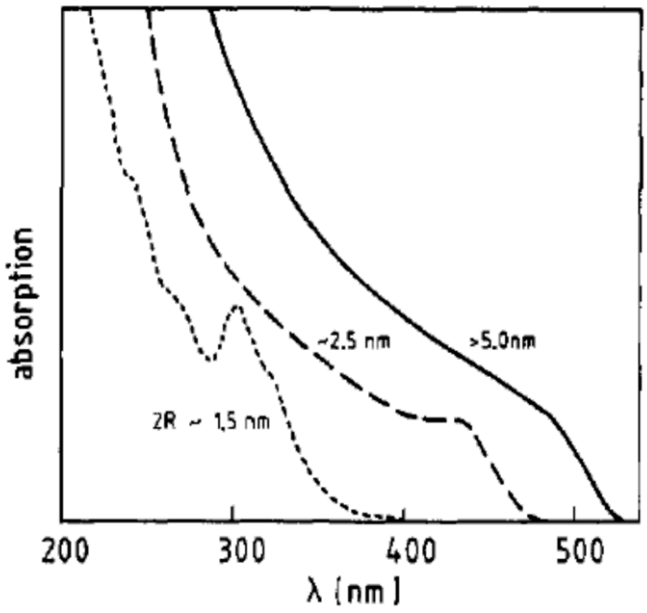

Figure 1.6. UV-Vis absorption spectra of CdS QDs of different mean sizes in aqueous solution[43]

NPs that were greater than 5 nm absorbed wavelengths of light smaller than 515 nm. As the size of the particles decrease, the absorption threshold shifts to higher energy wavelengths that correspond to shorter wavelengths (blue shift). This demonstrates how the quantum confinement effect (and subsequent absorbance) is dominated by the size of the nanoparticle in question.

Quantum dots have found uses in many applications. Quantum dots of TiO_2 has been used in dye-sensitive solar cells as a charge carrier transporter to accept electrons from the sensitizer dyes into their conduction band, promoting the flow of electrons in the cell (Figure 1.7).[153] Quantum dots are used because varying the size of the nanoparticle allows for greater tunability of the band gap compared to bulk materials. This allows one a greater variety of options for the other components in the solar cell that can be paired with a specific size of QD.

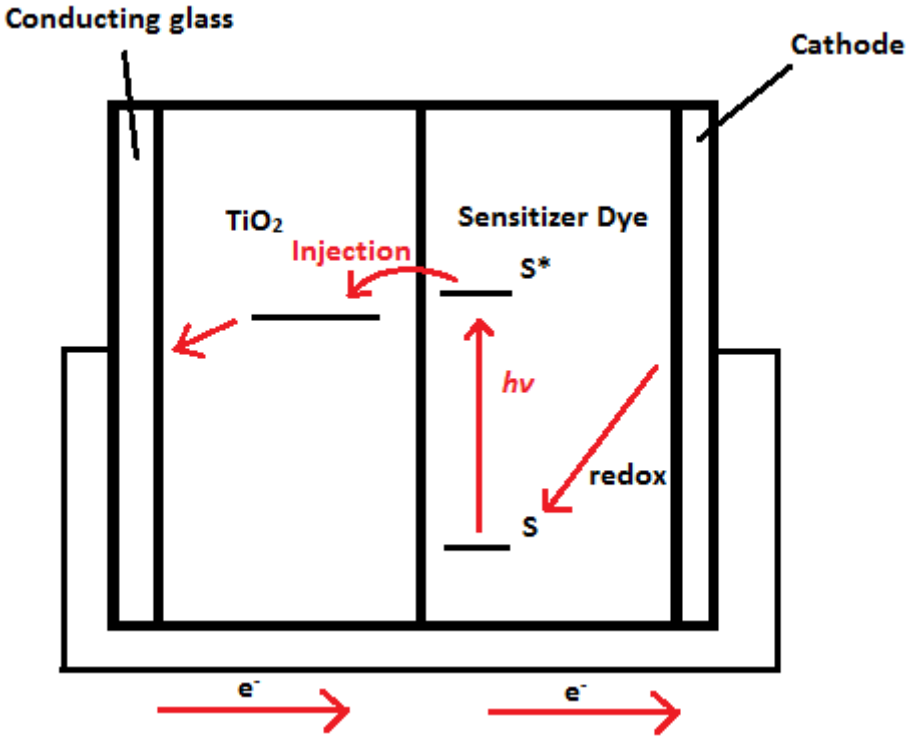

Figure 1.7. Schematic depicting the flow of electrons through a dye-sensitized solar cell using a TiO_2 nanocrystal.

QDs have also been used commercially by companies such as Sigma-Aldrich (Qdot®)[154] and Nanoshel Pvt Ltd (InP/ZnS QDs (surface modified))[154], as well as many researchers in the scientific community for the labelling of biological samples.[156-159] The size-dependent optical properties of the QDs have also allowed for new avenues of research to solve our most pressing issues. In the field of quantum computing, quantum dots are used to confine electrons of a selected spin within energy wells. A gate between these electrons is controlled by a current. When the gates are open, the wavelengths of the electrons are allowed to overlap and interfere. The pairing of up and down spins in a series of combinations allows for more information to be stored and processed than the current binary system.[160-162] QDs are also finding uses in the field of display materials. New classes of QDs such as inorganic halide perovskite quantum dots are showing strong photoluminescence across the entire visible as a result of the quantum confinement effect, a feat not seen for previous cadmium chalcogenide species due to limitations in processing. These new class of QDs are far more robust than previous materials while producing similar quantum yields, removing one more barrier towards active use in modern electronic displays[163-165] As can be seen, QDs are continuing to be used for new approaches and applications in the modern world.

1.5 Synthesis of Polymer/Nanoparticle Composite Micelles

Initial approaches for the brush functionalization of inorganic NPs involved the use of either a graft-to or a graft-from methodology. A graft-to approach involves the use of preformed polymer chains with functionalized terminal groups that undergo a ligand exchange with groups located on the inorganic NP (see Figure 1.6.A).[27]

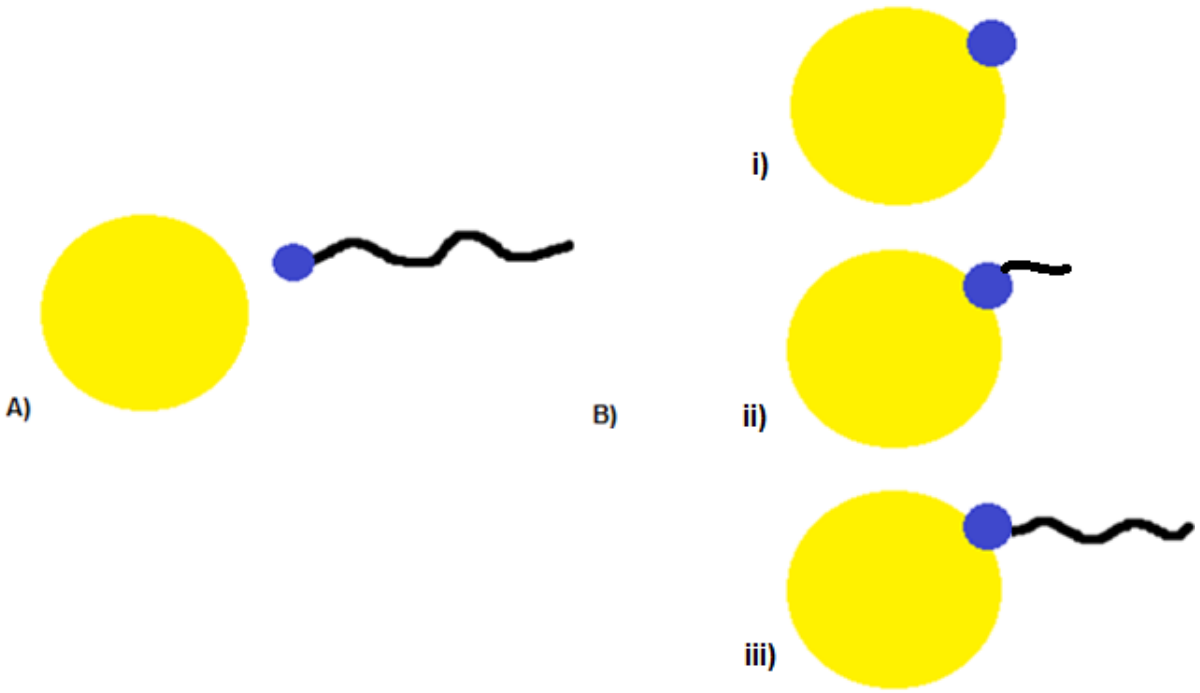

Figure 1.8. Schematic presenting A) graft-to approach and B) graft-from approach depicting the i) anchor ligands found on the NP ii) initiation of polymer growth initiation site iii) and continued growth of the polymer chain

Emrick *et al.* used this technique to displace pyridine ligands on the surface of CdSe/ZnS core-shell QDs with thiol-terminated PEO.[31] A similar procedure was carried out by Lennox *et al.* to attach thiol terminated PS and PEO chains to Au NPs during their growth stage.[47,48] In each case, both polymers and nanoparticles were performed before attaching them through ligand exchange.

A graft-from approach involves the growth of polymers from initiation sites located on the NP (Figure 1.6.B). Emrick's group has grown PS and PS-*b*-PMMA on CdSe QDs using a nitroxide mediated living radical polymerization.[32] Work by Fukuda *et al.* created a PMMA brush on Au nanoparticles using surface-initiated living radical polymerization via a copper

complex.[49] Nitroxide-mediated radical polymerization was also used by Takahara *et al* to control the growth of PS and poly(3-vinylpyridine) (P3VP) on the surface of Fe_3O_4.[50] The graft-to approach had proven useful in creating PBNPs and allows for tunability of the length of polymer chains as they grow on the NP.

A different approach to the creation of PBNPs is to use a block copolymer micelle template. This methodology uses block copolymers to create reverse micelles in a polar solvent and metal ions complex with the core forming region as NP building blocks. The nanoparticles are then precipitated within the cores and become covalently attached to the polymer brushes of the micelle. This technique has been used by Moller *et al.* to precipitate Au NPs with a PS polymer brush coating from within PS-*b*-P2VP[51,52] and PS-*b*-PEO micelles.[53] Eisenberg[54] and Moffitt[55] used a PS-*b*-PAA dibock copolymer template to synthesize PS brush functionalized CdS NPs. This approach has also been performed to create PS/PMMA mixed polymer brush covalently attached to a CdS QD using a PS-*b*-PAA-*b*-PMMA triblock copolymer template.[33] This technique will be further explored in this work for both a PS-*b*-PAA-*b*-PMMA triblock copolymer template and a mixed PS-*b*-PAA/PMMA-*b*-PAA diblock copolymer template.

1.6 Varieties of Mixed Brush Block Copolymer Nanoparticles

Multiple varieties of PBNPs have been identified by Moffitt[27] based on the number of brush components, the arrangement of the brush components on the core NP surface and the degree of anisotropy found in the NP at rest or when induced by external stimuli, such as solvent. The three classes are labelled as type I, type II and type III PBNPs.

A type I PBNP is characterized by having an isotropic, single-component brush. A schematic depicting this can be found in Figure 1.9 A). Due to the repulsive nature of the polymer chains, self-assembly of these nanoparticles often leads to two-dimensional arrays, as seen in Figure 1.6 b). Au NPs covalently linked to PS chains using a PS-*b*-PEO template as synthesized by Moller *et al* (an example of a type I PBNP) shows a periodic array of NP cores evenly spaced apart based on repulsive effects between PS chains in the corona.[52] The ability to create periodicity has shown promise in creating sensors and photonic devices.[56]

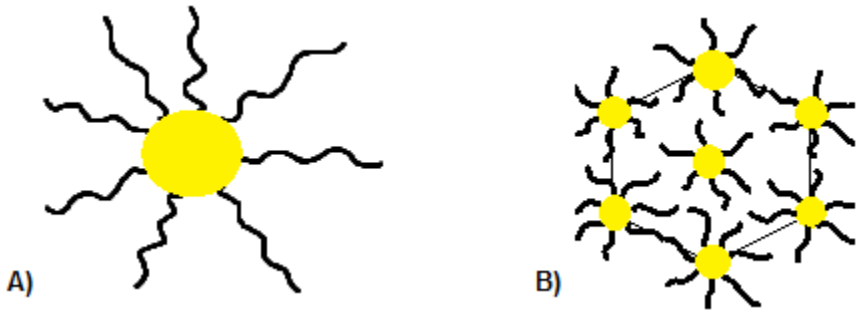

Figure 1.9. Schematic depicting A) a type I PBNP and B) the repulsive interactions caused by polymer brushes, creating nanoparticle arrays.

In comparison, a type II PBNP is defined as having anisotropic patterning that arises from either single or multicomponent particles. The polymer brush pattern is imprinted directly onto the NP surface, creating either a patchy or Janus distribution (Figure 1.10). A Janus distribution is one in which the polymer brushes phase separate around the NP core, forming singular regions containing a single polymer. A patchy distribution is one in which polymer brushes of the type form multiple clusters throughout the brush layer.

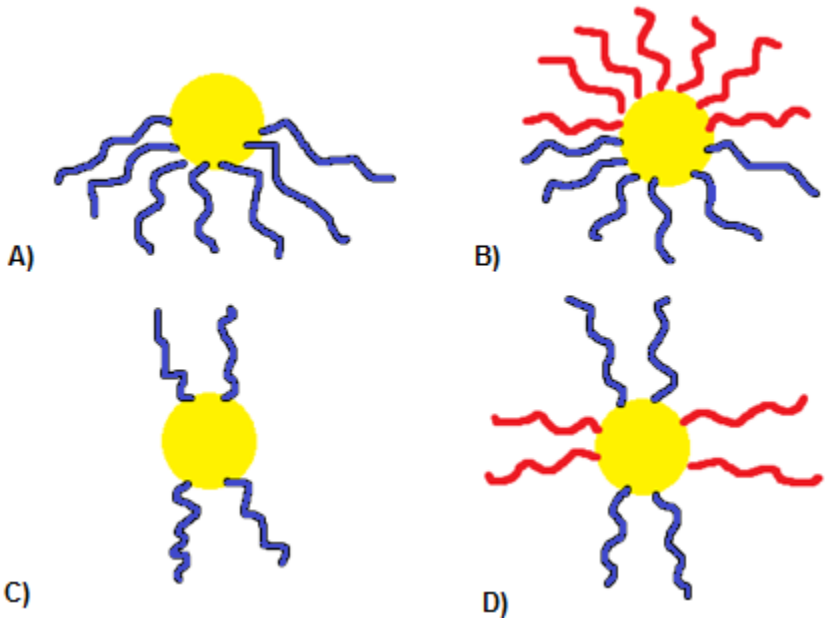

Figure 1.10 Schematic representing type II PBNPs with single component (A,B) and multicomponent (C,D) anistropic brushes. They are represented as having either Janus (A,C) and patchy (B,D) polymer chain distributions.

While type I PBNPs self-assemble into periodic arrays due to polymer repulsion, type II PBNPs are surface patterned so that they are inherently phase separated. As the two polymer chains are incompatible, they will phase separate around the NP in the core. As a result, the NPs will form the interface between the polymer layers. Kumacheva *et al.* created so called "pom-pom" building blocks made of Au nanorods with cetyl trimethylammonium bromide (CTAB) ligands located on the ends of the rods. She was able to use the CTAB regions to graft together multiple Au nanorods due to the anisotropic nature of the ligands on the NPs.[57] Chen *et al.* used a hydrophilic and hydrophobic ligand on the surface of a Au NP to selectively bind PS-*b*-PAA to one side of the Au and a nonpolymeric hydrophilic ligand to the other. This created a Janus like distribution, with the Au NP forming the interface between each brush.[59] These materials exist because of how the polymer interacts and separates around the NP.

Type III PBNPs differ from the previous two cases in that they are contextually anisotropic.[59-61] The polymers are not attached to the core NP in a pattern beforehand, but are induced to form anisotropic distributions due to chemical incompatibility with solvent. As the cores are relatively small compared to length of the polymer chains, any changes in the solvent will allow the polymer chains to wrap around the core in order to find their lowest energy conformation. A schematic of these particles before and after stimulation can be found in Figure 1.11.

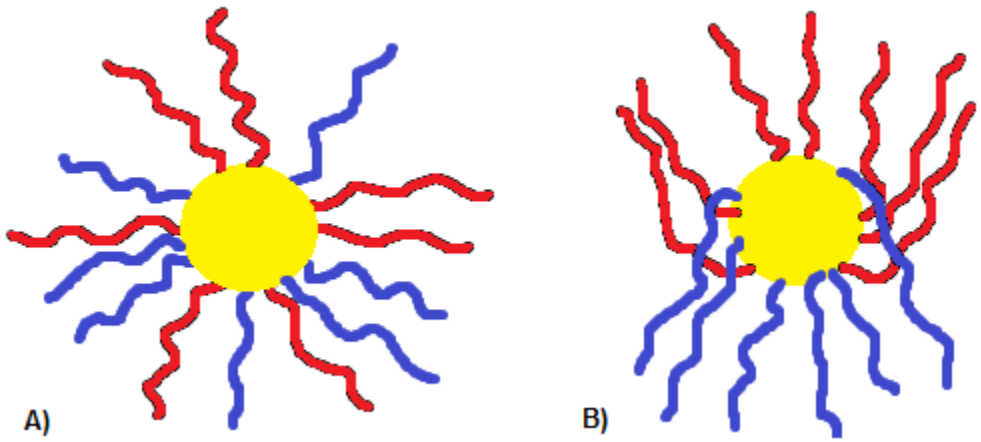

Figure 1.11. Schematic depicting A) before generation of anisotropy and B) after generation of anisotropy.

Type III PBNPs have been prepared by Song *et al*, using a mixed graft-to/graft-from method for attaching PEO chains and growing PMMA chains to Au NPs.[62] The chains wrapped around the core when dispersed in water, creating a patchy topology. Moffitt *et al* created mixed brush micelles from a PS-*b*-PAA-*b*-PMMA triblock copolymer template covalently attached to a CdS core.[63] The random distribution of chains rearranged to form a Janus morphology once placed in H_2O, creating a CdS QD interface in the resulting macromolecular morphologies. Each of these methods create particles in which anisotropy must be induced.

1.7 Major Characterization Techniques

A series of techniques were employed to characterize the synthesized PBNPs at different stages throughout this work. Gel permeation chromatography (GPC) , dynamic and static light scattering (DLS and SLS) and transmission electron microscopy (TEM) were used to determine the sizes and structural integrity of the particles at many stages of the synthetic process. TEM and laser scanning confocal fluorescence microscopy (LSCFM) were used to characterize the self-assembled morphologies in Chapters 3 and 4. This section will give a brief introduction for each of these techniques.

1.7.1 Gel Permeation Chromatography (GPC)

GPC is a form of chromatography in which the separation column is packed with a mechanically stable, highly cross-linked gel. This gels consists of a distribution of pore sizes that will impede the flow of particles through the column. Specimens with smaller hydrodynamic radii in the eluent solution will become trapped in the pores, increasing their retention times as larger radii particles continue along the column.[35] While many GPC systems perform calibrations based upon the creation of a calibration curve comparing elution times determined for standards of known molecular weight, calibration of the Viscotek Model 302 liquid chromatography system uses the intensity of the elution peak for a known standard based on the low angle light scattering detector and applies an algorithm that calibrates voltage outputs and offset volumes in the machine.[64]

1.7.2 Static and Dynamic Light Scattering (SLS and DLS)

Static light scattering is employed to find the M_w, R_g *and* A_2 of a given NP sample. It measures the time-average scattered light intensity from polymer or micelle solutions at multiple concentrations (c) and angles (θ). Zimm plot analysis allows the determination of the weight-average molecular weight (M_w), radius of gyration (R_g), and the second virial coefficient (A_2) according to the Zimm equation (equation 1.6)[35]:

$$\frac{K_c}{R_\theta} = \frac{1}{M_w P(\theta)} + 2A_2 c \qquad \text{(Equation 1.6)}$$

Where R_θ is the Rayleigh Ratio which can be derived from $R_\theta = i_\theta r^2 / I_0$, where I_0 is the intensity of incident light, i_θ is the scattered light intensity per unit volume at angle θ, and distance r from the sample to the observer. $P(\theta)$ is an angle-dependent term called the form factor, which describes attenuation in the scattering light intensity due to interparticle interference and is dependent on particle size and shape.

$$P(\theta) = [1 + \frac{16\pi^2 r_g^2}{3\lambda^2} \sin\frac{\theta}{2}^2] \qquad \text{(Equation 1.7)}$$

K is the composite of optical and fundamental constants of which the differential refractive index, dn/dc, is included (equation 1.8):

$$K = \frac{2\pi^2 n_0^2 (\frac{dn}{dc})^2}{\lambda_0^4 N_A} \qquad \text{(Equation 1.8)}$$

Where N_A is Avogadro's number, n_0 is the refractive index of the solvent and λ is the wavelength of the incident light.

r_g describes the average distance from the center of gravity to the chain ends of a polymer in solution. A_2 is a thermodynamic quantity that attractive and repulsive forces in between polymers or particles in solution. It is dependent on solvent and temperature.

Dynamic light scattering is used to determine the hydrodynamic radii, r_h, of a polymer or micelle sample.[33] DLS experiments measure the normalized time correlation function of an electric field using a cumulant expansion for pointlike, isotropic particles with a distribution of particle sizes:

$$|g(\tau)| = \exp[-\Gamma\tau + \left(\frac{\mu_2}{2!}\right)\tau^2 + \cdots] \qquad \text{(Equation 1.9)}$$

where Γ is the intensity-weighted mean relaxation rate (first moment), μ_2,is the second moment, and τ is the delay time. When Γ is determined at various scattering angles, it can be related to the effective translational diffusion coeffeicient D_T through equation 1.10:

$$\Gamma = D_T q^2 \qquad \text{(Equation 1.10)}$$

where q is the scattering vector which can be determined from equation 1.11:

$$q = \frac{4\pi n}{\lambda}\sin\frac{\theta}{2} \qquad \text{(Equation 1.11)}$$

where n is the refractive index of the scattering liquid, λ is the wavelength of incident light and θ is the scattering angle. In order to account for interparticle interactions in solution, D_T is expressed as a function of concentration:

$$D_T = D_o(1 + k_d c) \qquad \text{(Equation 1.12)}$$

in which the single-particle diffusion coefficient, D_o is obtained by extrapolation to zero concentration. The hydrodynamic radius, r_h, can be calculated from D_o values using the Stokes-Einstein equation (equation 1.13):

$$R_h = \frac{kT}{6\pi D_o} \qquad \text{(Equation 1.13)}$$

where k is the Boltzmann constant, T is the temperature, and η is the solvent viscosity. The result of r_g/r_h[65] can give information about the shape of the particle in solution. $r_g/r_h \sim 0.775$ indicates the presence of hard spheres, 1.1 agrees with star-like structures and 1.5 is the theoretical value for rod-like polymer chains.[66,67]

1.7.3 Transmission Electron Microscopy (TEM)

TEM is a technique used to view NPs on the nanoscale through the use of an electron beam instead of a typical light source. Electrons are used and give much higher resolution as the wavelength of an electron is orders of magnitude smaller than that of visible light. An electron gun sits atop a vertical column and directs a beam of electrons through a series of lenses to focus the beam. The electrons in the beam will either scatter upon contact with the specimen or remain unhindered on its path to the objective aperture and onto a fluorescent screen. The image that is produced will present dark and light regions, the darkest of which show where more scattering has occurred (usually at electron dense regions of the material). Lighter regions represent either a lack of specimen or a regions of low electron density in the specimen, allowing the electrons to pass through with limited scattering.[68]

1.7.4 Laser Scanning Confocal Fluorescence Microscopy (LSCFM)

LSCFM is a fluorescence imaging technique in which fluorescent emissions from QDs or organic dyes provide contrast between fluorescent and non-fluorescent regions of the microscopes optical regime on the micron scale. A laser provides excitation light at a given wavelength that is expanded by a lens and reflected off a dichroic mirror onto the sample. As the sample becomes excited, the emitted light is focused back through the lens and dichroic mirror and then through a focusing lens and pinhole aperture to the photomultiplier detector. The computer then compiles an image by scanning through *x*- and *y*-directions.[70]

LSCFM has a distinct advantage over ordinary epifluoresnce microscopy in that there is an adjustable pinhole in the photomultiplier detector that allows for optical sections to be measured at various depths along the *z*-direction throughout the sample. Therefore, 3-D images can be attained by compiling snapshots of each optical section using computer software imaging.

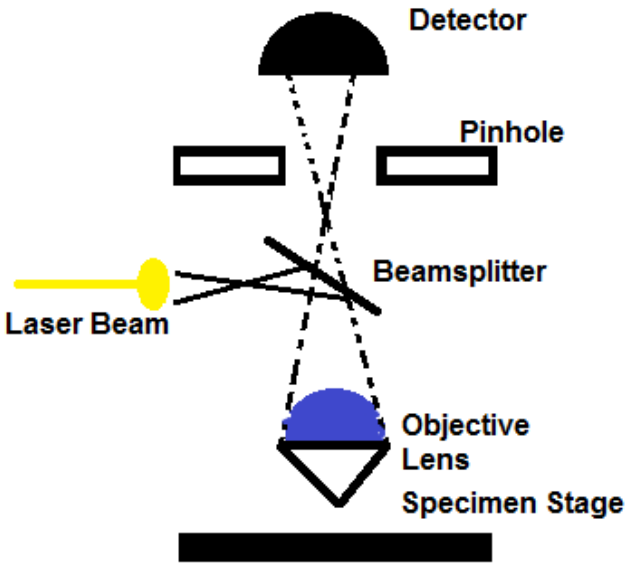

Figure 1.12 Schematic representation of laser scanning confocal fluorescence microscopy (LSCFM).[70]

1.8 Content of this Thesis

This thesis will consist of three main parts: 1) the synthesis and characterization of PS/PMAA-(CdS) NPs from mixed diblock copolymer templated brush approach 2) the self-assembly of the PS/PMAA-(CdS) in aqueous solutions to probe the effects of brush composition on the created morphologies and 3) the synthesis, characterization and self-assembly of PS/$PMAA_{(x)}$-(CdS) NPs created from a triblock copolymer templated approach to determine the effect that varying the length of the PMAA block will have on self-assembly. The content of each chapter will be described below.

Chapter 2 describes the synthesis and characterization of PS/PMAA-(CdS) NPs created from a mixed PS-*b*-PAA/PMMA-*b*-PAA reverse micelle template in which CdS QDs were precipitated in the core. Four different weight fractions of PS/PMMA were created: f_{PS} = 0.5, 0.7, 0.8 and 0.9. GPC and dispersability tests were used to determine the stability of the particles in various solvent. SLS and DLS were used to measure the aggregation number and size of the mixed brush particles in solution. UV-Vis spectroscopy and TEM were used to probe the size and optical properties of the CdS QD core while 2D ^{1}H NOESY NMR was used to determine the chain distribution around the core. These particles represent a new diblock copolymer mixed brush templated approach to making PBNPs.

Chapter 3 outlines the self-assembly of the NPs synthesized in Chapter 2 in aqueous solvent. The effect of changing brush composition was probed, as well the effect of initial nanoparticle composition and the effect of salt addition to the solutions before assembly. The produced morphologies were visualized using TEM and LSCFM and their characteristic sizes were measured by TEM and DLS. Based on the trends that appear in this data, a series of phase

diagrams will be developed, creating an invaluable tool for further experimentation in the field of polymer brush functionalized nanoparticles.

The final chapter outlines the synthesis and characterization of PS/$PMAA_{(x)}$-(CdS) NPs designed from a PS-*b*-PAA-*b*-PMMA triblock copolymer template in which CdS QDs precipitated within the NPs after micellization. The two triblock copolymers have identical PS and PAA blocks lengths but different PMMA block lengths (x = 154 and x = 54) in order to determine the effect that changing the soluble block length will have on self-assembly of these NPs once PMMA has been hydrolyzed to PMAA. These particles will be extensively characterized to test for NP stability, brush distribution, QD stability and NP size information in various solvents. Self-assembly experiments in aqueous solvent will be performed in which differences in PMAA block length, initial nanoparticle concentration and salt content will be probed in order to determine their effect on the morphological aggregates formed.

Chapter 2

Synthesis and Characterization of Polystyrene/Poly(meth acrylic acid) Mixed Brush-Functionalized Inorganic Nanoparticles of Variable Brush Composition

2.1 Introduction

In recent years, there has been an increased amount of interest in the potential applications for inorganic nanoparticles (NPs), including quantum dots (QDs), but there currently exist limitations on the ability of these particles to organize and self-assemble into organized arrays and structures. For example, Gopalakrishnan *et al.*[1] attempted to use CdSe as a bio-imaging agent for the examination of cellular processes. Poor dispersability and biocompatibility of CdSe in the human body meant that the NPs would have to be modified before entering the bloodstream. Once a phospholipid coating was applied to the NPs, the nanoparticles became dispersible and were able to be used in the human body. This same problem can be found in fields as varied as photonics[71,72], drug delivery[73,74], sensors[4,6,8,] and biolabelling[1,75], where the inability of NPs to self-assemble into more ordered and deliberate structures and morphologies has been a major stumbling block. Therefore, it has become necessary to develop methods that allow us to control assembly into larger structures on a functional length scale. Recently, polymer functionalization of NP surfaces has been used as a method of incorporating colloidal NPs into polymer nanocomposites, as well as imbuing their own mechanical, optical and electronic properties onto the nanocomposite.[76] Methods of polymer functionalization of NPs include the growth of polymers on the surface of an NP (grafting-from approach),[31,50,77] attaching polymers to binding sites already located on the NP (grafting-to approach)[32,78] or growth of NPs from within block copolymer micelles.[54,55,79]

Initial work on polymer-brush functionalized inorganic NPs was performed with only a single type of polymer chain within the brush.[80-82] While this type of polymer brush provides dispersability in organic solvents and polymer materials, structural complexity arising from self-assembly of these particles is limited since particle-particle interactions are isotropic. The

polymer brushes can either assemble into ordered arrays of NPs separated by the extended polymer chains if the interparticle interactions are repulsive (good solvent environments), or into disordered aggregates of NPs if the interparticle interactions are attractive (poor solvent environments). For example, Spatz et al. created ordered arrays of PS-coated Au NPs by treating PS-P2VP with $HAuCl_4$ in toluene to induce micellization. The Au^{3+} ions were then reduced to form Au particles in the core of the micelle. Repulsive interactions between the extended PS chains created an ordered array of the Au NPs in a film.[52]

In order to increase the structural complexity arising from self-assembly, anisotropic interparticle interactions have been introduced by synthesizing mixed polymer brushes consisting of two different polymer chain types.[60,82] By adopting a mixed brush of polymers instead (so-called "smart" NPs), each component in the mixed brush will respond differently to specific solvent environments due to the amphiphilicity of the particles, leading to anisotropic interactions with each. For example, Song *et al.* created Au NPs coated with a mixed polymer brush consisting of both a hydrophobic (poly(methyl methacrylate)) and hydrophilic (polyethylene glycol) polymer. These particles then self-assembled into the vesicles when the solvent environment was changed from chloroform to water, as a result of microphase separation of the two polymer brushes around the Au NP.[62]

A more recent approach to creating mixed polymer brush NPs involves the self-assembly of triblock copolymers. This method was initially used to create polymer micelles with mixed coronal layers,[83,84] but was later adapted to produce composite nanoparticles with inorganic NP cores surrounded by a mixed brush layer.[33,85] The constituent triblock copolymers consist of two different end blocks that are soluble in the solvent medium and a central core-forming block that is insoluble. For example, in our group, Guo *et al.* used a polystyrene-*block*-poly(acrylic acid)-

block-poly(methyl methacrylate) (PS-*b*-PAA-*b*-PMMA) triblock copolymer to produce cadmium sulfide (CdS) QDs surrounded by a mixed brush of PS and PMMA chains.[33] Guo later assembled these particles in THF/H_2O mixtures to produce a wide variety of morphologies, including eccentric worm-like structures (Figure 2.1).[63]

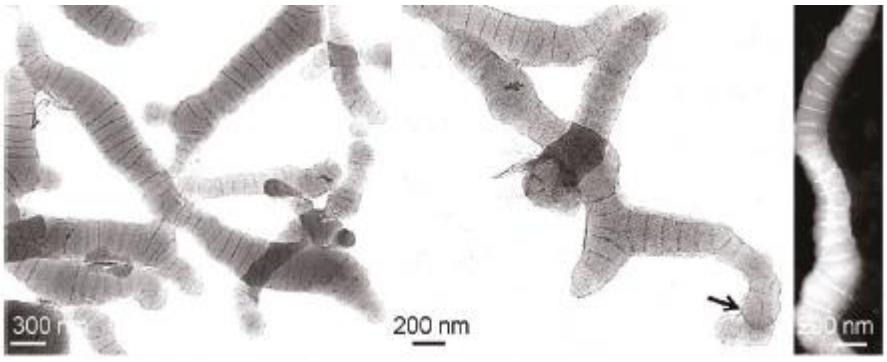

Figure 2.1. Worm-like structures produced from the self-assembly of Guo's SM-NPs in THF/H_2O.[63]

The present work focuses on the blending of two diblock copolymers instead of a single triblock copolymer to create a semiconductor quantum dot with a mixed brush polymer layer. The use of triblock copolymers gives a 50 / 50 composition of each chain due to their linked nature. Block copolymer literature has shown that changes in ratio of hydrophilic and hydrophobic components strongly influence the morphologies arising from self-assembly;[86,87,88,89,90] however, the effect of brush composition on the self-assembly of amphiphilic nanoparticles has not yet been systematically studied. By using a pair of block copolymers, the brush composition can be changed with ease by varying the ratio of the two blend components. This chapter will describe the synthesis and characterization of the resulting NPs and the subsequent chapter described their self-assembly in different solvent environments.

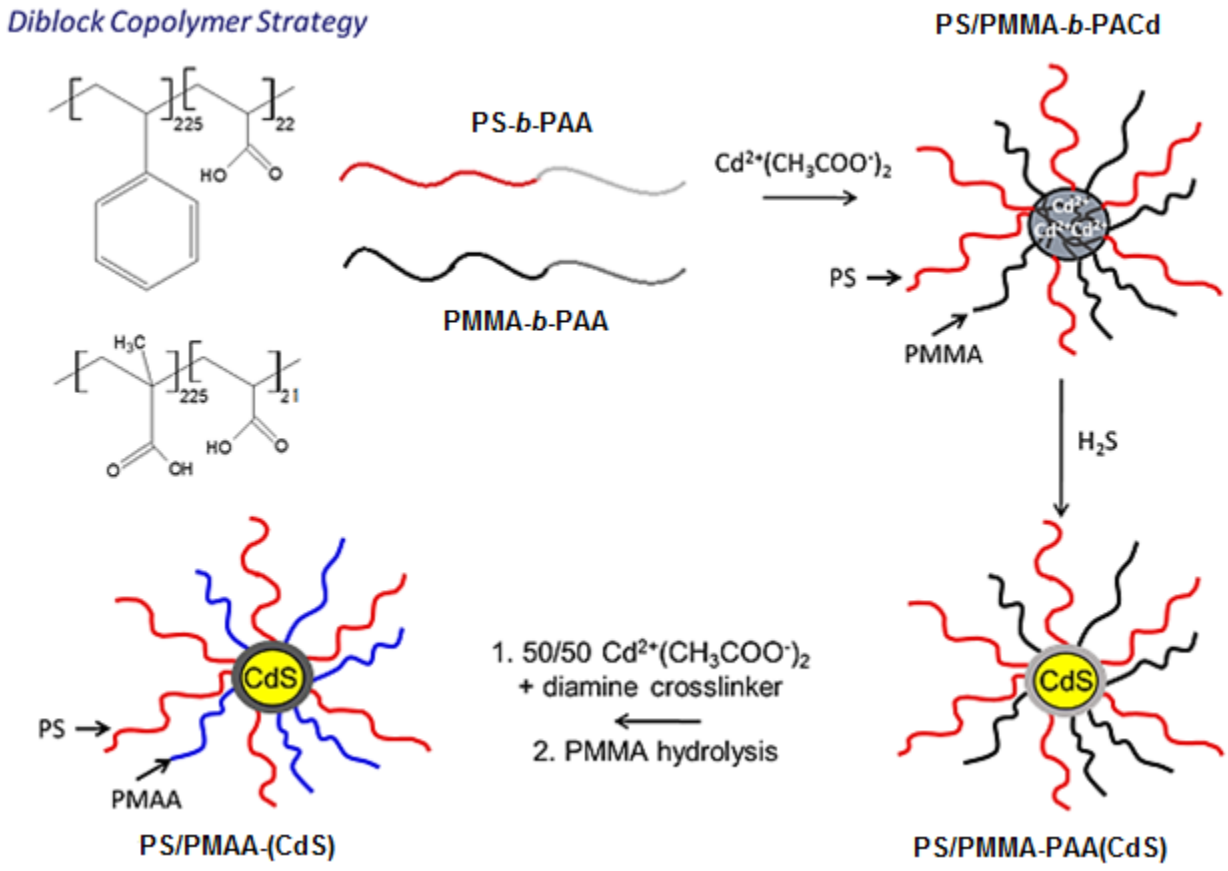

Figure 2.2. Schematic depicting the multistep process for the synthesis of PS/PMAA-(CdS) NPs

2.2 Experimental

2.2.1 Hydrolysis of Polystyrene-block-poly(tert-butyl acrylate) (PS-b-PtBA) and Selective Hydrolysis Poly(methyl methacrylate)-block-(tert-butyl acrylate) (PMMA-b-PtBA) Diblock Copolymers

For this study, starting materials were either purchased in the *tert*-butyl acrylate form from Polymer Source Inc. The purchased samples will be referred to as follows: PS(225)-*b*-

PtBA(22) and PMMA(225)-*b*-PtBA(21), respectively, where the numbers in brackets indicate the number-average degrees of polymerization for each block. As described below, each of these two copolymers were hydrolyzed to the poly(acrylic acid) (PAA) form before continuing on to create mixed brush micelles of differing blend compositions of PS-*b*-PAA to PMMA-*b*-PAA.

PS-*b*-P*t*BA was hydrolyzed to PS-*b*-PAA and PMMA-*b*-PtBA was hydrolyzed to PMMA-*b*-PAA using the following method. The *tert*-butyl acrylate form of each copolymer was dried overnight at 70 °C under vacuum. It was then dissolved in toluene to make a 2 wt % solution. The clear, colourless solution was stirred overnight until all polymer was dissolved. The solution was then refluxed at 115 °C overnight with *para*-toluene sulfonic acid (5 mol % relative to the *tert*-butyl acrylate content). The dark brown, opaque solution was then concentrated to half of its initial volume via rotary evaporation and precipitated into isopropanol cooled by an ice/water bath to 0 °C. The fluffy white powder was then recovered by vacuum filtration, washed further with 3 x 5 mL cold isopropanol and dried in a vacuum oven at 70 °C for two days.

2.2.2 Preparation of Amphiphilic CdS Quantum Dots with Polystyrene/Poly (methacrylic acid) (PS/PMAA) Mixed Brushes of Varying Composition

2.2.2.1 Preparation of Polystyrene-*block*-poly(cadmium acrylate) / Poly(methyl methacrylate)-*block*-poly(cadmium acrylate) Mixed Reverse Micelles (PS/PMMA-*b*-PACd)

PS(225)-*b*-PAA(22) was dissolved in a 90/10 (v/v) benzene/methanol solution to make 2 wt % solution and stirred overnight to equilibrate. In a separate flask, PMMA(225)-*b*-PAA(21) was dissolved in a 90/10 (v/v) benzene/methanol solution to make 2 % w/w solution and stirred overnight to equilibriate. Several ratios of PS/PMMA were targeted, and are labelled in terms of

their weight fractions of polystyrene (f_{PS}): f_{PS} = 0.5, 0.7, 0.8 and 0.9. Initial experiments suggested that extra PMMA-*b*-PAA diblock copolymer should be added as the PMMA-*b*-PAA sample in use had a large component that would not micellize (33%). Therefore, the two stock solutions of PS(225)-*b*-PAA(22) and PMMA(225)-*b*-PAA(21) were blended gravimetrically and the blend ratios were made in which the PMMA-*b*-PAA fraction was 33% higher than the targeted ratio with the expectation that the extra chains would be fractionated out later. The actual blend ratios before mixellization were f_{PS} = 0.40, 0.61, 0.72 and 0.86. These were allowed to stir for two hours. To each of the four solutions 3 moles of $Cd(Ac)_2$ were added per mol of acrylic acid repeat unit in a continuous stream under constant stirring. This was allowed to stir overnight. Each solution was freeze-dried to remove the solvent, producing a fluffy white powder. This sample was dried overnight in a vacuum oven at 70 ^{o}C. The resulting sample was then washed multiple times with methanol and the filtrate was tested with aqueous Na_2S solution. The sample was washed until three consecutive tests of the filtrate resulted in no yellow colour in the solution. Once completed, the micellized PS/PMMA copolymer blends were dried again overnight at 70 $^{\circ}$C under active vacuum.

In order to remove unmicellized polymer chains, fractionation of the micellized PS/PMMA copolymer blend was required. The micellized PS/PMMA samples were dispersed in THF (5 % w/w). The dispersion was then stirred at a constant rate while deionized water was added dropwise to the cloud point (i.e. until the dispersion remained turbid for several minutes after the addition of the last drop). The solution was left overnight, producing two layers. The top layer consisted of the lighter single chains while the bottom layer contains the heavier reverse micelles. The top layer was decanted. Deionized water was then added to the bottom layer to precipitate the samples, allowing them to be filtered. The filtrate was dried for overnight at 70 $^{\circ}$C.

The next day a portion was dissolved in THF and GPC analysis was performed to determine the fraction of single chains that remained. This process was repeated until the GPC showed less than ~10 wt % of single chains relative to the micelle fraction. The dried fractionated samples were designated PS/PMMA-*b*-PACd.

2.2.2.2 Preparation of CdS Quantum Dots in Reverse Micelle Cores

The fractionated PS/PMMA-*b*-PACd samples were placed in an atmosphere of 100% humidity in a humidity chamber at 70 °C for one week (see Figure 2.3). After this treatment, the samples were placed under an atmosphere of "wet" H_2S. The H_2S was bubbled into a sample chamber containing PS/PMMA-*b*-PACd for 10 hours, followed by 1 h of nitrogen to purge the lines of H_2S. During exposure to H_2S, the white PS/PMMA-*b*-PACd slowly turned yellow. The yellow powder was then placed inside a vacuum oven under active vacuum and room temperature overnight to remove any excess H_2S gas. These samples were designated PS/PMMA-*b*-PAA(CdS).

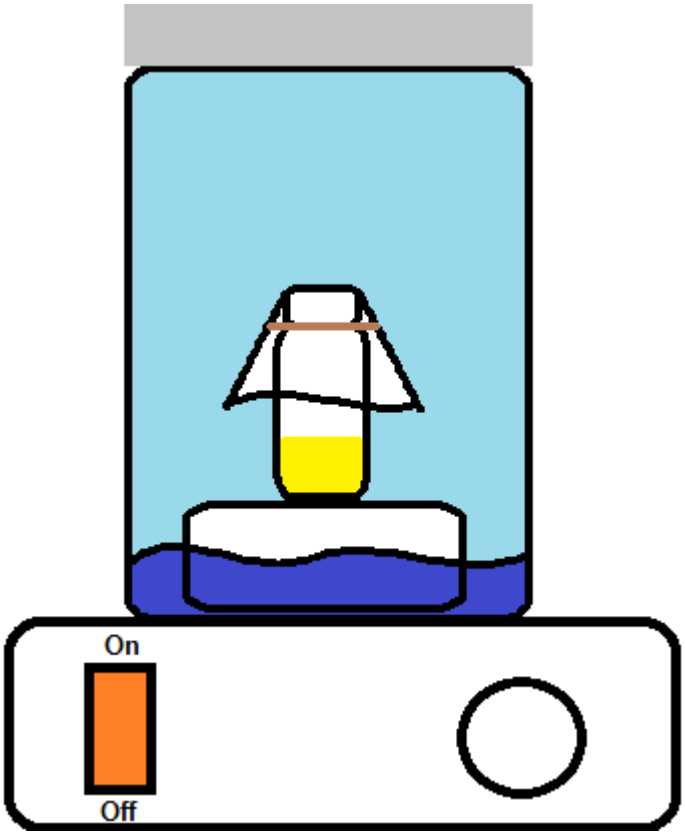

Figure 2.3. Schematic depicting the humidity chamber setup. The sample is placed inside a large jar on a platform. The sample is in a vial that is covered with a piece of lens paper held on with an elastic. The bottom of the jar contains water which is heated to 60 ºC. The humidity that forms is held in by an aluminum foil cap.

2.2.2.3 Core Cross-linking Reverse Micelles Containing CdS Quantum Dots

To stabilize the PS/PMMA-*b*-PAA(CdS) NPs, crosslinking of PAA chains in the micelle core was carried out. The yellow powder was first ground into a fine powder and then dispersed in THF to 2 wt %. Immediately upon dispersion, 0.5 equivalents of $Cd(Ac)_2$ in methanol (0.5 mol $Cd(Ac)_2$ per 1 mol of acrylic acid repeat units) were added in one quick addition and the solution was allowed to stir overnight. The next day, a 1.0 wt % solution of *N*-ethyl-*N*'-(3-dimethylaminopropyl)-carbodiimide methiodide (EDC) activator in water (0.5 molar equivalents

EDC per mol acrylic acid repeat units) was added and allowed to stir for 2 hours. This was followed by the addition of a 1.0 wt % solution of 2,2'-(ethylenedioxy)bis(ethylamine) (EDDA) in water (0.25 mol per mol of acrylic acid repeat units) in one portion and was then left to stir overnight. The sample was concentrated further and precipitated into cold methanol. The resulting pale yellow solid was then filtered and dried under vacuum for 2 days at 70 °C. These samples were designated PS/PMMA$_{XL}$(CdS).

2.2.2.4 Hydrolysis of PMMA Brush Chains to PMAA

Finally, the PMMA chains in each of the PS/PMMA-PAA$_{XL}$ (CdS) samples were hydrolyzed to PMAA to produce amphiphilic NPs of variable hydrophobic/hydrophilic brush composition. First, PS/PMMA-PAA$_{XL}$ (CdS) was dispersed to 10 wt % in 1,4-dioxane with KOH (2 mol KOH per mol methyl methacrylate repeat units) and 18-crown-6 (0.2 mol 18-crown-6 per mol of methyl methacrylate repeat units). This dispersion was placed under argon in a sealed high-pressure Schlenk tube and the reaction was heated to 110 °C for 4 days. After 4 days, the dispersion was concentrated further and precipitated into a cold 0.2 M acetic acid solution. This was then filtered under vacuum and placed under active vacuum in a vacuum oven for 3 days at 70 °C. The resulting amphiphilic NPs were designated PS/PMAA$_{XL}$(CdS); however, since these are the final building blocks for self-assembly experiments described in the next chapter, we use the short-hand designation PS/PMAA-CdS, $f_{PS} = x$ in Chapter 3 when referring to these samples, where x denotes the actual mass fraction of hydrophobic PS blocks relative to the total mass of brush chains (f_{PS} = 0.5, 0.7, 0.8, 0.9).

2.2.6 Gel Permeation Chromatography (GPC)

All GPC measurements were carried out on a Viscotek Model 302 liquid chromatography system. It was furnished with refractive index (RI), low-angle light scattering (LALS, $\theta = 7^{o}$) and right-angle light scattering (RALS, $\theta = 90^{o}$) detectors. The eluent for this system was THF run at a flow rate of 1 mL/min and the column temperature was set at 35 °C. Samples were dispersed in HPLC grade THF to concentrations of ~1 mol/L and filtered through poly(tetrafluoroethylene) (PTFE) filters with a nominal pore size of 0.45 μm before injection into the column. The data was collected on a Dell Dimension 2300 computer using GPC software from Viscotek. Three columns (purchased from Tosoh Biosciences LLC) were connected in series: one TSKgel G3000Hhr columns, one TSKgel GM-HHR-M and then a second TSKgel G3000Hhr. The packing material of these columns is styrene-divinyl benzene.

2.2.7 Nuclear Magnetic Resonance (NMR)

^{1}H NMR spectra of diblock copolymers and subsequent micellization products were recorded using a Bruker AC 300 MHz spectrometer. 2D ^{1}H nuclear Overhaueser effect spectroscopy (NOESY) experiments of the PS/PMMA-PAA$_{XL}$ (CdS) products were performed on a Bruker Avance 500 MHz spectrometer at 27 °C. For the 2D NOESY spectra, 320 experiments of 2k data points were recorded. 24 scans were used for each increment using standard Bruker software. A mixing time of 500 ms was used for best results.

2.2.8 UV-Vis Absorption Measurements

Absorption spectra were recorded on a Perkin Elmer UV-Vis-NIR with a three detector module. It consists of a photomultiplier tube (PMT) for the UV-Vis range, an indium gallium

arsenide (InGaAs) detector and a lead sulfide (PbS) detector for the near infra-red (NIR) range. Samples were dispersed to ~1 mg/mL in spectroscopic grade tetrahydrofuran, toluene, acetone and chloroform. A background of pure solvent was recorded for each individual solvent to subtract from the ensuing measurement.

2.2.9 Transmission Electron Microscopy (TEM)

Microscopy was performed on a JEOL JEM-1400 TEM operating at a voltage of 80 kV with a Gatan Orius SC1000 camera. PS/PMMA-CdS_{XL} samples for transmission electron microscopy were prepared by dispersing the NPs in benzene at 1 wt %. 2 drops of this solution were applied to a copper grid (300 mesh) coated with a carbon film coating. The solution was allowed to settle on the grid for 15 seconds before excess solvent was dabbed off with a kimwipe. The grids were allowed to dry for 2 hours before images were taken. Hydrolyzed PS/PMAA-CdS_{XL} samples were prepared by dispersing the NPs in THF at 1 wt %. Application and drying of these samples follows the previous procedure for the PS/PMMA-PAA_{XL} (CdS) samples. Particle size measurements and statistical analysis were performed on the ImageJ software from Softonic. Three images were taken from three different randomly selected locations on each grid from which a minimum of 200 total particles were measured to determine average sizes.

2.2.10 Dynamic Light Scattering (DLS)

DLS measurements were carried out on a Brookhaven Instruments photon correlator spectrometer equipped with a BI-200SM goniometer, a BI-900AT digital autocorrelator, and a

Melles Griot He-Ne Laser (632.8 nm) with a maximum power output of 75 mW. In order to remove dust from scintillation vials, rigorous cleaning was applied before adding sample.

The scintillation vials were first washed with 5 mL of 95 % ethanol filtered through two poly(tetrafluoroethylene) (PTFE) filters with a 0.20 μm nominal pore size connected in series. The vials were then capped and vortexed for 30 seconds. The solvent was removed and the process was repeated 10 more times. Upon completion, the vials were covered with a piece of lens paper held on with an elastic band and placed upside down in an oven at 80°C for 2 days to remove solvent.

Stock solutions of PS/PMMA$_{XL}$(CdS) NPs were dispersed separately in THF, toluene and acetone at concentrations of ~5 mg/mL. These solutions were filtered through two PTFE filters with a 0.45 μm nominal pore size connected in series. Any required dilutions were performed by adding known quantities of appropriate filtered solvent (solvent was filtered through two PTFE filters with a 0.20 μm nominal pore size connected in series). Unless otherwise stated, DLS measurements were conducted at a scattering angle of 90°. For each experiment, 3 repeat measurements of the autocorrelation function were obtained. All measurements were performed at 23 °C.

2.2.11 Static Light Scattering (SLS)

SLS measurements were carried out on a Brookhaven Instruments photon correlator spectrometer equipped with a BI-200SM goniometer and a Melles Griot He-Ne Laser (632.8 nm) with a maximum power output of 75 mW. In order to remove dust from scintillation vials, rigourous cleaning was applied before adding sample. The method of cleaning scintillation vials was identical to that applied above for DLS measurements.

Stock solutions of PS/PMMA-(CdS) NPs were prepared separately in THF, toluene and acetone at a concentration of ~5 mg/mL. These solutions were filtered through two PTFE filters with a 0.45 μm nominal pore size connected in series. Three solutions for triplicate measurements were made from the same stock solution and diluted to ~1 mg/mL. Measurements of scattered light intensity were performed at 12 different scattering angles from 30°- 120° and at five different dispersion concentrations (in the range of ~0.05 - ~1 mg/mL) obtained by successive gravimetric dilution with filtered solvent (solvent was filtered through two PTFE filters with a 0.20 μm nominal pore size connected in series). In this manner, triplicate Zimm plots for each sample-solvent pair were obtained. All measurements were carried out at 23 °C.

Values of d*n*/d*c* for each sample-solvent pair analyzed by light scattering were required in order to extract molecular weight information from Zimm plot data. These measurements were carried out on a Brookhaven Instruments BI-DNDC differential refractometer. Stock solutions of PS/PMMA-(CdS) NPs were dispersed separately in THF, toluene and acetone at a concentration of ~5 mg/mL. A series of five solutions was prepared in a concentration range of ~1 - ~5 mg/mL with ~1 mg/mL increments between concentrations. All dilutions were performed by adding known quantities of appropriate filtered solvent (solvent was filtered through two PTFE filters with a 0.20 μm nominal pore size connected in series). Determinations of d*n*/d*c* were performed in triplicate. All d*n*/d*c* measurements were carried out at 23 °C.

2.2.12. Fourier Transform Infrared (FTIR) Spectroscopy

IR Spectroscopy measurements were carried out on a Thermo Nicolet IR 200 Spectrometer. Sample dispersions of ~1 mg /mL of carbon tetrachloride were prepared and

allowed to stir overnight. The solutions were placed on a NaCl plate and allowed to dry to create a thin polymer film.

2.2.13. Powder X-Ray Diffraction (XRD)

Step-scan x-ray diffraction data was obtained on a Rigaku Miniflex diffractometer with variable divergence slit, 4.2° scattering slit and 0.3 mm receiving slit. Diffraction matters from polymer brush-coated QDs were obtained by casting ~5 mg of sample from a 1 mg/mL THF solution onto a zero-background holder. Measurements were made by scanning over a 2θ range 10-100° with Cr radiation (30 kv, 15 mA) (wavelength is 0.228 nm). The scanning step size was 2°/min.

2.3 Results and Discussion

2.3.1.1 Hydrolysis of Polystyrene-block-poly(tert-butyl acrylate) (PS-b-PtBA) to Polystyrene-block-poly(acrylic acid) (PS-b-PAA)

Diblock copolymers in the *tert*-butyl acrylate forms from Polymer Source were hydrolyzed into the acrylic acid form. The PS-*b*-PAA reaction was confirmed a success based on FTIR. The spectrum following hydrolysis (Figure 2.4) shows that the strong broad peak at 1729 cm^{-1} that is due to the C=O stretch of the ester has been replaced by a broad peak at 1711 cm^{-1} which corresponds to the carboxylic acid of the PAA unit. Another peak of interest is that of the C-O stretch of the ester at 1150 cm^{-1} which is completely absent upon completion of the reaction.

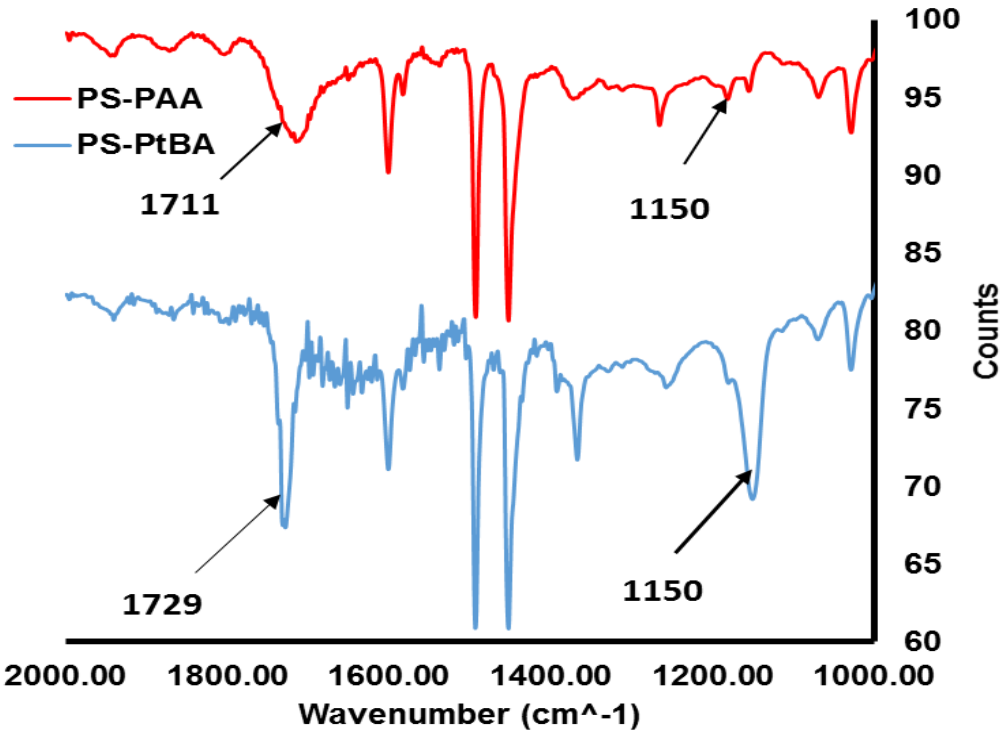

Figure 2.4. IR spectrum comparing PS-*b*-PtBA and PS-*b*-PAA

After performing a similar hydrolysis reaction on the PMMA-*b*-PtBA diblock copolymer, ^{1}H NMR was used to determine the success of the reaction (Figure 2.5). NMR was used instead of FTIR due to the overlap of the PMMA carboxylate group with the P*t*BA carboxylate group in the latter spectrum. The *tert*-butyl protons of the ester found at 1.43 ppm in the PMMA-*b*-P*t*BA starting material disappear once the hydrolysis is complete. The methyl ester associated with PMMA remains untouched during this hydrolysis, as the integration of the peak at 3.6 ppm (peak a) remains unchanged (integration of 3.00 before and after hydrolysis).

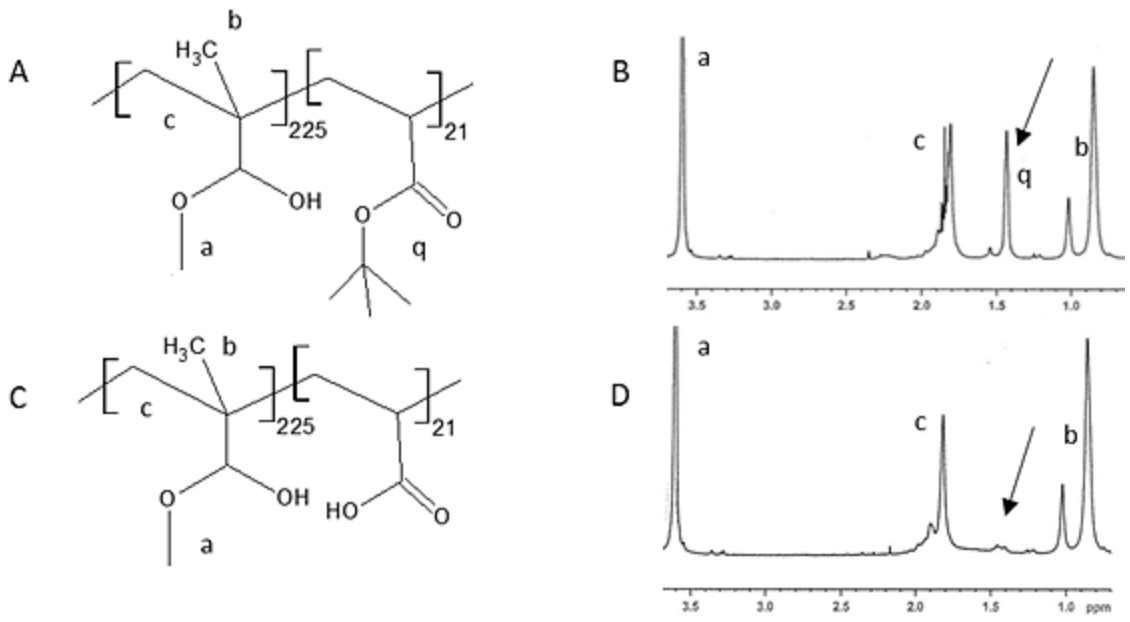

Figure 2.5. NMR Peak labelling for A) PMMA-*b*-PtBA and C) PMMA-*b*-PAA. ^{1}H NMR spectrum of comparing B) PMMA-*b*-PtBA and D) PMMA-*b*-PAA.

2.3.2.1 Micellization and Fractionation of Polystyrene-block-poly(cadmium acrylate) / Poly(methyl methacrylate)-block-poly(cadmium acrylate) Blends

Four compositions of mixed reverse micelles were targeted: f_{PS} = 0.5, 0.7, 0.8, 0.9. Upon addition of $Cd(Ac)_2$ to the diblock copolymer blend solutions, each solution became turbid indicating increased Rayleigh scattering from the newly formed micelles. The benzene was removed by freeze-drying in order to create dry, white powder. Based on preliminary experiments, it was expected that not all of the polymer chains would micellize; since the extra polymer will interfere with subsequent self-assembly steps, it therefore had to be removed. Using the technique of fractionation allowed for the removal of single chain impurities. The amount of free polymer can be monitored using GPC. For each diblock copolymer blend composition

before fractionation, two main peaks are found in the gel permeation chromatograph, as seen in Figure 2.6:

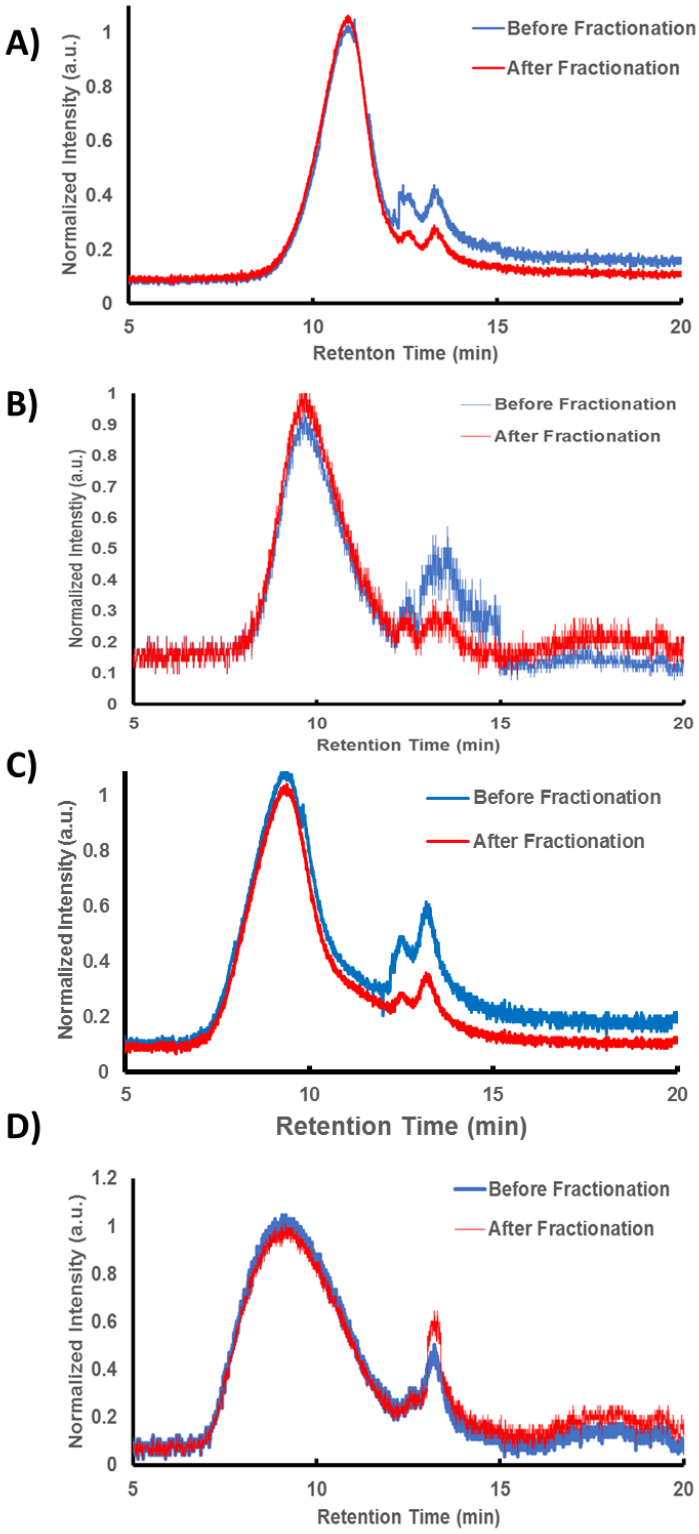

Figure 2.6. Gel permeation chromatographs (refractive index detector) of f_{PS} = A) 0.5 B) 0.7 C) 0.8 and D) 0.9 for PS/PMMA-PACd NP before (blue curve) and after (red curves) fractionation.

Before fractionation (blue curve), the broad peak at ~11 minutes is due to micelles while the narrow peak at ~14 minutes is due to unmicellized chains. To determine the relative weight fractions of these two populations, the peaks were integrated using the OmniSEC 3.0 software provided by Viscotek. Before fractionation, the micelles were found to be ~80 wt % of the sample compared to ~20 wt % single chains. After fractionation (red curve), the fraction of single chains has decreased and integration reveals its contribution to be $\leq$ 10 wt %. Each of the four blends were similarly fractionated such that the single chain fraction was $\leq$ 10 wt % following fractionation in all cases (Table 2.1).

Table 2.1. Calculated Micelle to Single Chain Weight Fractions after Fractionation

f_{PS}	Micelle Weight Fraction	Free Polymer Weight Fraction
0.5	0.91	0.09
0.7	0.92	0.08
0.8	0.90	0.10
0.9	0.90	0.10

2.3.3 Characterization of Polystyrene-block-poly(cadmium acrylate) / Poly(methyl methacrylate)-block-poly(cadmium acrylate) Mixed Reverse Micelles, PS/PMMA-b-PACd

Once the four blends were micellized and fractionated it was important to determine the actual polymer composition of the resulting nanoparticles, since fractionation and the resulting loss of single chains can give rise to a change in the composition if the amount of PS and PMMA

copolymer in the single chains was not equal. Nuclear magnetic resonance spectroscopy (NMR) was employed for this task. Figure 2.7 displays an NMR spectrum of blend after micellization.

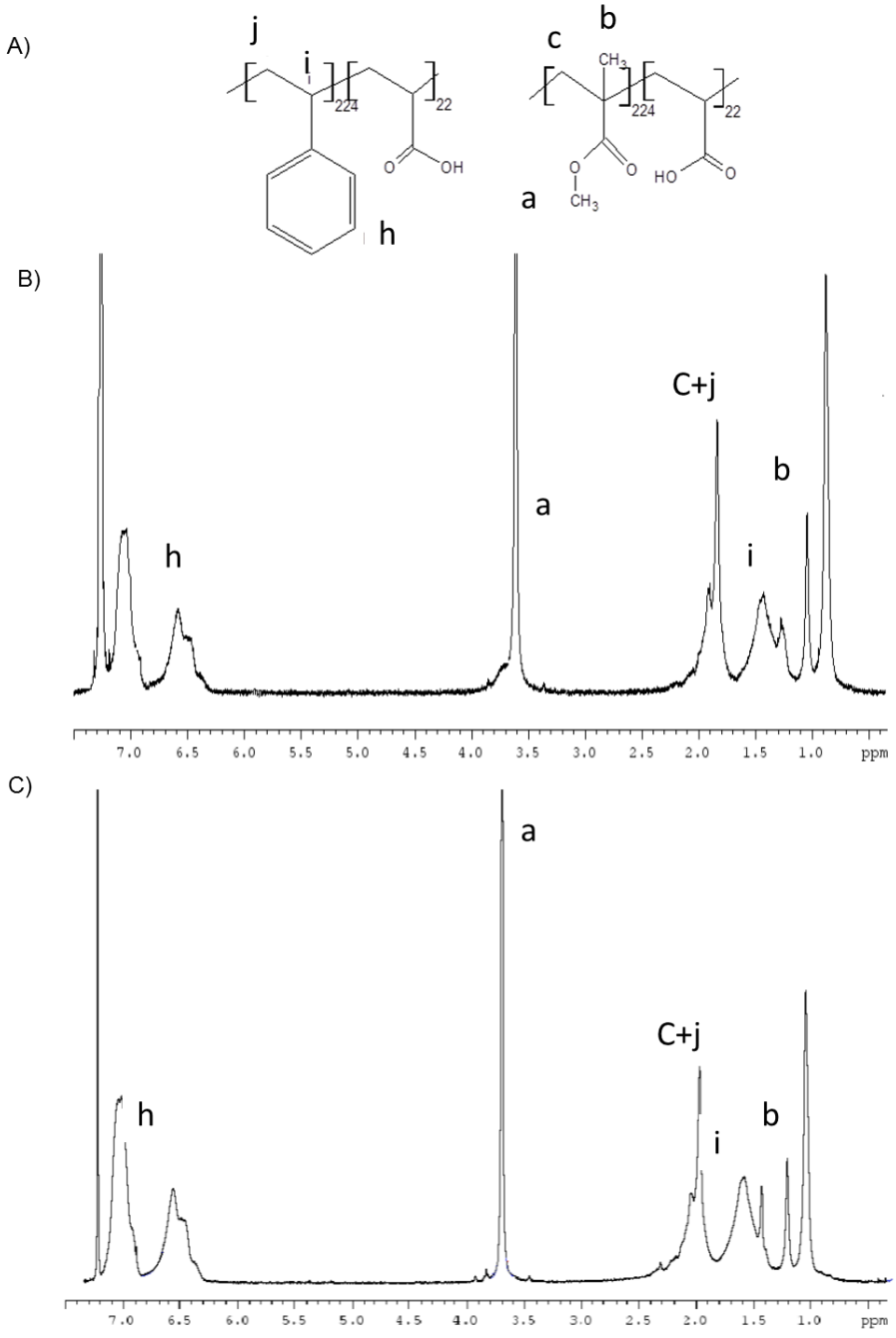

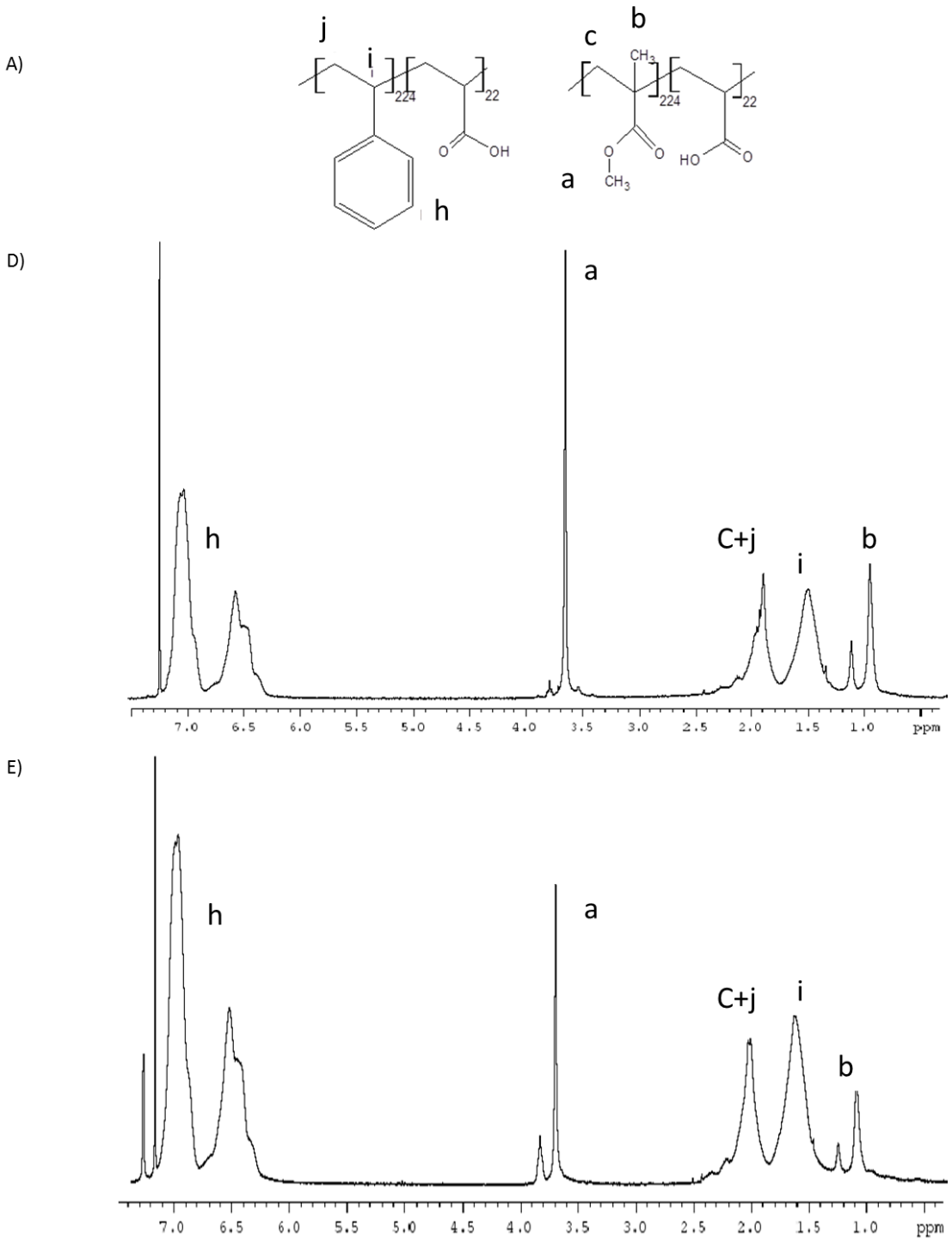

Figure 2.7. A) ^{1}H NMR peak labelling for PS-*b*-PAA and PMMA-*b*-PAA. ^{1}H NMR spectra of f_{PS} = B) 0.5 C) 0.7 D) 0.8 and E) 0.9 PS/PMAA-*b*-PACd blend micelles after fractionation are shown.

By comparing the peak integrations of the aromatic protons (6.2-7.2 ppm) of PS and the methyl ester protons (3.61 ppm) of the PMMA, the composition of each blend can be determined. As an example, a f_{PS} = 0.5 blend of the two polymers would have an expected integration of 5 aromatic protons for every 3 methyl ester protons. On the other hand, asymmetric blends would be weighted to reflect the higher proportion of PS in the sample. A sample calculation for the f_{PS} = 0.8 blend is shown in Equation 2.1.

$$\frac{NMR\ styrene\ peak\ integration}{NMR\ methoxy\ peak\ integration} * \frac{3\ methoxy\ protons}{5\ styrene\ protons} = \frac{moles\ styrene}{moles\ methyl\ methacrylate}$$

$$\frac{5}{.9} * \frac{3}{5} = \frac{15}{4.5} = 3.33333 = \frac{moles\ styrene}{moles\ methyl\ methacrylate} \qquad \text{(Equation 2.1)}$$

$$\frac{molar\ mass\ styrene}{molar\ mass\ methyl\ methacrylate} * \frac{moles\ styrene}{moles\ methyl\ methacrylate}$$

$$= \frac{mass\ styrene}{mass\ methyl\ methacrylate}$$

$$\frac{104.5\ \text{g/mol}}{100.121\ \text{g/mol}} * 3.33333 = 3.47912 = \frac{mass\ styrene}{masss\ methyl\ methacrylate}$$

$$= \frac{mass\ styrene}{mass\ styrene + \frac{mass\ styrene}{3.47912}} = \ f_{PS}$$

$$f_{PS} = \frac{1}{1 + 1/3.47912} = \frac{1}{1 + 0.28743} = 0.78$$

The actual blend composition of each diblock copolymer blend series can be found in Table 2.2, the results of which show agreement with each of the targeted compositions f_{PS} = 0.5, 0.7, 0.8 and 0.9.

Table 2.2. Final Blend Compositions of each PS/PMMA-*b*-PACd Blend after Fractionations by Comparison of ^{1}H NMR signals of the PS Aromatic Region and the PMMA Methoxy Region

f_{PS}	NMR PS (aromatic) : PMMA (methyl) Proton Ratios	Actual Blend Composition
0.5	5 : 3.5	0.47
0.7	5 : 1.4	0.69
0.8	5 : .9	0.78
0.9	5 : .31	0.91

The dispersability of these NPs of different brush compositions in solvents of widely varying polarity proved their mixed brush structure. Figure 2.8 displays each blend composition dispersed in tetrahydrofuran, toluene, chloroform and acetone. Each of tetrahydrofuran, toluene and chloroform are good solvents for both PS and PMMA, allowing easy dispersion of the NPs and yielding clear colloidal dispersions. Acetone is a poor solvent for PS but a good solvent for PMMA. If multiple NP populations existed made up of only one copolymer or the other, one would expect to precipitation of the PS-*b*-PACd NPs. A clear dispersion, such as produced by the f_{PS} = 0.5 and 0.7 blends in all four solvents, indicates that a mixed polymer brush has been created. In the case of the f_{PS} = 0.8 blend, the acetone dispersion is rather turbid, but no precipitate forms. The lack of precipitation suggests a mixed brush corona, while the turbidity likely arises from the fact that the fraction of PS in the NP is large compared to the PMMA leading to some agglomeration of NPs but without macroscopic precipitation. The PS chains will collapse in a poor solvent like acetone, while the PMMA chains will remain expanded enough to

maintain dispersion. This effect is more pronounced in the f_{PS} = 0.9 blend in acetone, as solid precipitate is visible. In this case, it is likely that the polystyrene fraction was much too large for it to remain dispersed leading to precipitation.

Based on the data obtained from the GPC, ^{1}H NMR and the dispersability tests, we concluded that a series of PS/PMMA-*b*-PACd mixed reverse micelles with different brush compositions had been synthesized.

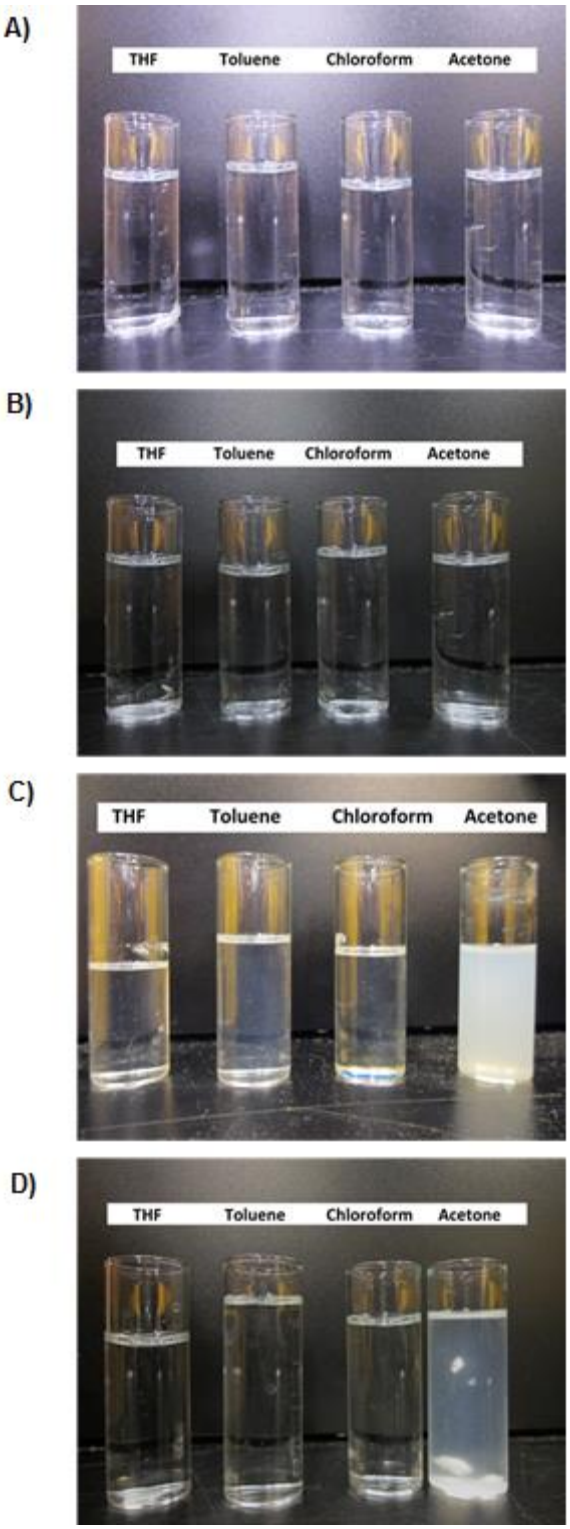

Figure 2.8. Images of f_{PS} = A) 0.5 B) 0.7 C) 0.8 and D) 0.9 PS/PMMA-*b*-PACd diblock micelles dispersed in THF, toluene, chloroform and acetone.

2.3.4 Characterization of Crosslinked PS/PMMA Mixed Brush Coated CdS QDs Before Hydrolysis of PMMA Chains, PS/PMMA$_{XL}$(CdS)

2.3.4.1 Gel Permeation Chromatography and Dispersability Tests

By precipitating the CdS quantum dots in the core of the NPs, a side effect is a decrease in the thermodynamic stability of the core; as the acrylic acid repeat units become reprotonated, treatment with H_2S eliminates the driving force for micellization making the micelles unstable. However, subsequent cross-linking the core provides stability and prevents NPs dissociation during subsequent synthesis steps. Although due to low stability in THF uncrosslinked PS/PMMA-*b*-PAA(CdS) could not be evaluated by GPC, Figure 2.9 compares GPC chromatograms of the cadmium acrylates mixed micelles (PS/PMMA-*b*-PACd) and the corresponding crosslinked CdS QDs with mixed brush layers, PS/PMMA$_{XL}$(CdS), for the four different blend compositions.

In each case, the PS/PMMA$_{XL}$(CdS) form appears as a narrower peak at higher retention times than the PS/PMMA-*b*-PACd form. The change in retention time points to a decrease in hydrodynamic size and a narrowing of the hydrodynamic size distribution. It is hypothesized that crosslinking of the cores makes the cores more compact through contraction. This in turn pulls the attached coronal polymer brushes inwards, decreasing the overall size of the NPs. Another important observation is that the combination of CdS QD formation and subsequent core crosslinking has not increased the single chain content of the resulting NPs. Therefore it has been concluded that the reverse micelles have remained intact throughout the formation of CdS QDs and the subsequent crosslinking of the PAA polymer chain found in the core of the NPs found in the PAA.

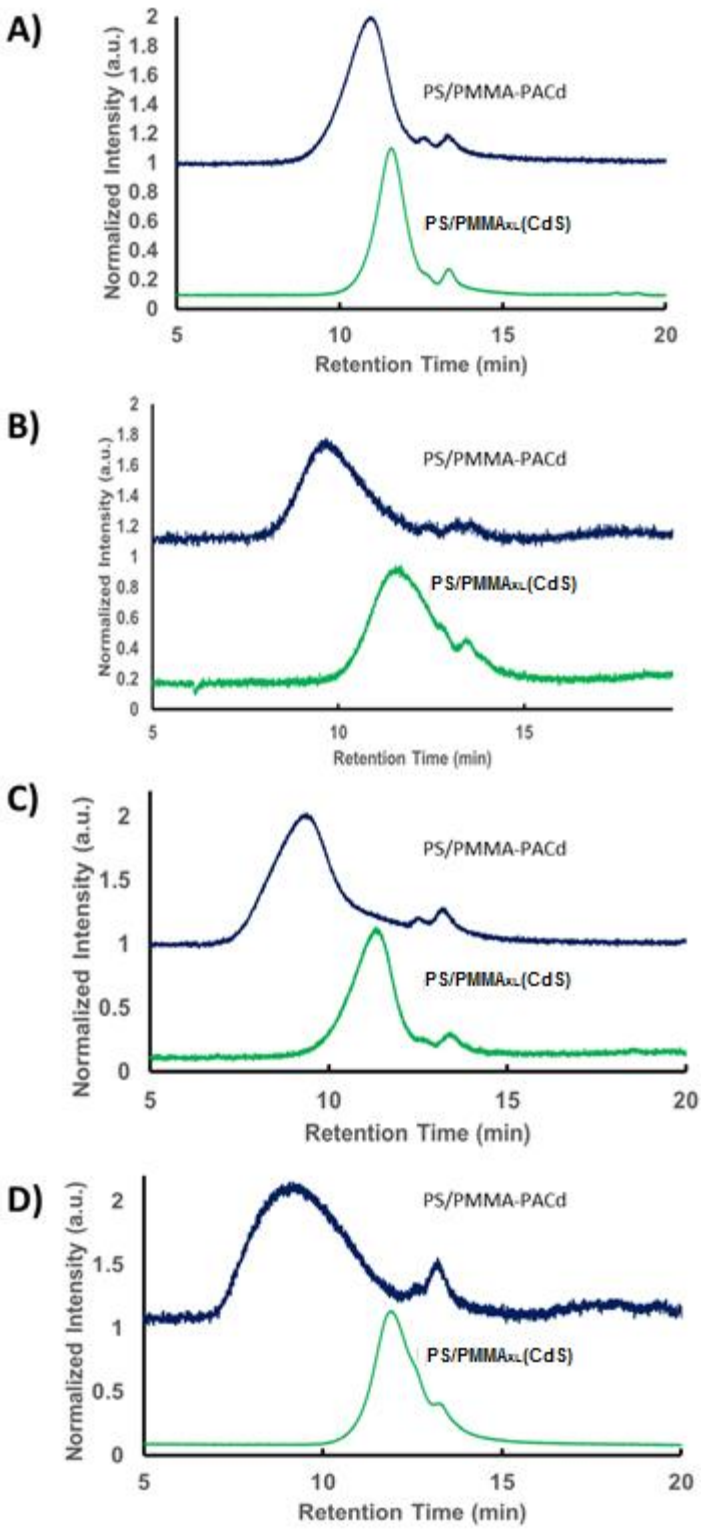

Figure 2.9. GPC (refractive index response detector) comparison of f_{PS} = A) 0.5 B) 0.7 C) 0.8 and D) 0.9 PS/PMMA$_{XL}$(CdS) NPs

The four PS/PMMA$_{XL}$(CdS) NPs with different brush compositions were also dispersed in a series of solvents of different polarities to test whether the mixed brush of the original reverse micelles was retained. Figure 2.10 shows that each PS/PMMA$_{XL}$(CdS) composition dispersed in chloroform, tetrahydrofuran, toluene and acetone without precipitation, supporting the mixed brush structure of the NPs. For the two brush compositions with the highest PS content, f_{PS} = 0.8 and 0.9, significant turbidity (without precipitation) is noted in acetone (Figure 2.10, C and D), suggesting that the lower content of soluble PMMA chains in these NPs cannot preclude some aggregation of NPs in this solvent.

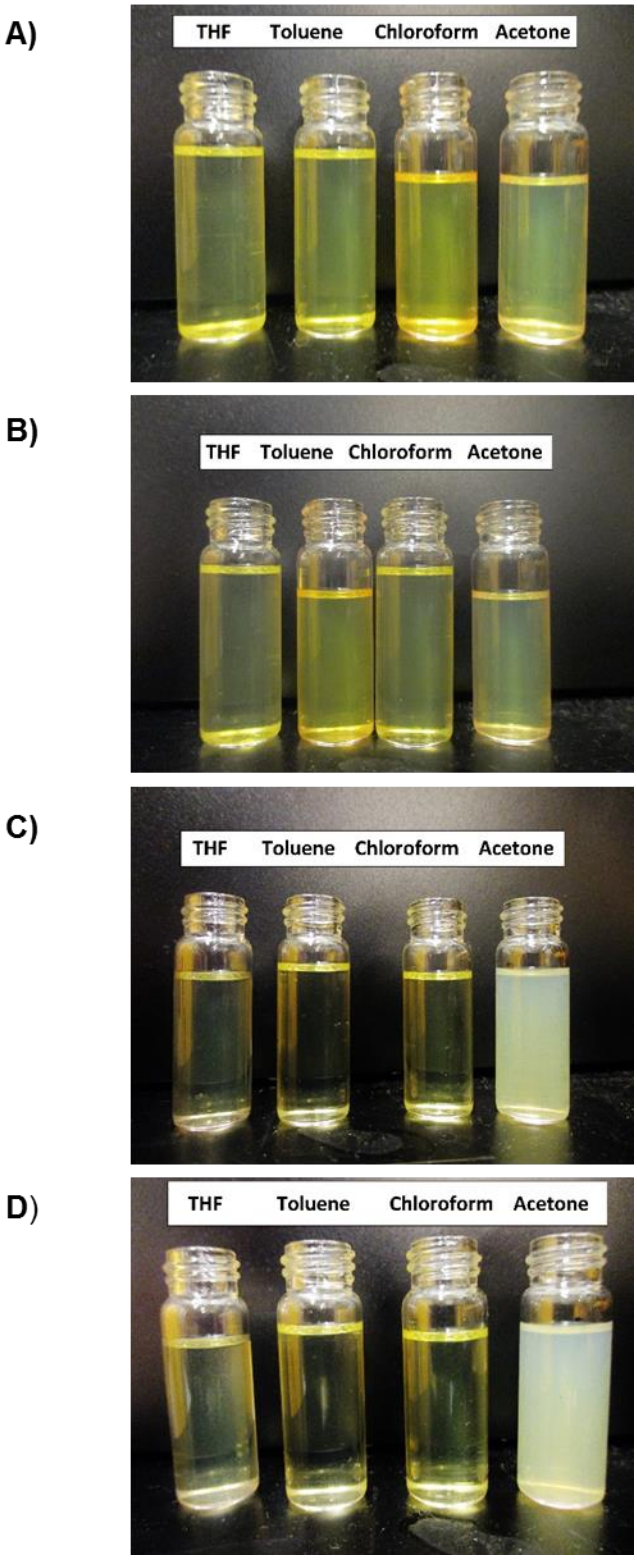

Figure 2.10. Images of f_{PS} = A) 0.5 B) 0.7 C) 0.8 and D) 0.9 PS/$PMMA_{XL}$(CdS) NPs dispersed in THF, toluene, chloroform and acetone.

2.3.4.2 UV-Visible Spectroscopy and Transmission Electron Microscopy

The optical properties of the CdS QDs cores were probed by UV-Vis spectroscopy. The resulting spectra provide information on QD size via the quantum confinement effect. Figure 2.11 shows normalized UV-Vis absorbance spectra for the four PS/PMMA$_{XL}$(CdS) NPs, each in a series of solvents (THF, Toluene and Chloroform) of differing dielectric constants. For all brush compositions, when the three solvent spectra are normalized there is a near overlap of the three curves. This indicates that the QD is well protected in the NP core and does not undergo growth within any of the various solvents. Each of the NP samples exhibit a single exciton peak or shoulder. Using the absorbance threshold of the THF solution curves (Figure 2.12 inset) for each NP brush composition, QD sizes were determined using Equation 2.2.

$$2r_{CdS} = \frac{1}{(0.1338 - 0.0002345 * \lambda_{thresh})} \qquad \text{(Equation 2.2)}$$

This formula was derived by Moffitt[91] by fitting data published previously by Henglein.[44] For all brush compositions, QD diameters determined from UV-vis were in the range of 4.3-4.9 nm.

Table 2.3. Summary of Optical Characteristics and Quantum Dot Core Size by UV-Vis Spectroscopy

f_{PS}	λ_{ex} (nm)	λ_{thresh} (nm)	d_{CdS} (nm)
0.5	455	479	4.7
0.7	461	484	4.9
0.8	453	485	4.9
0.9	448	471	4.3

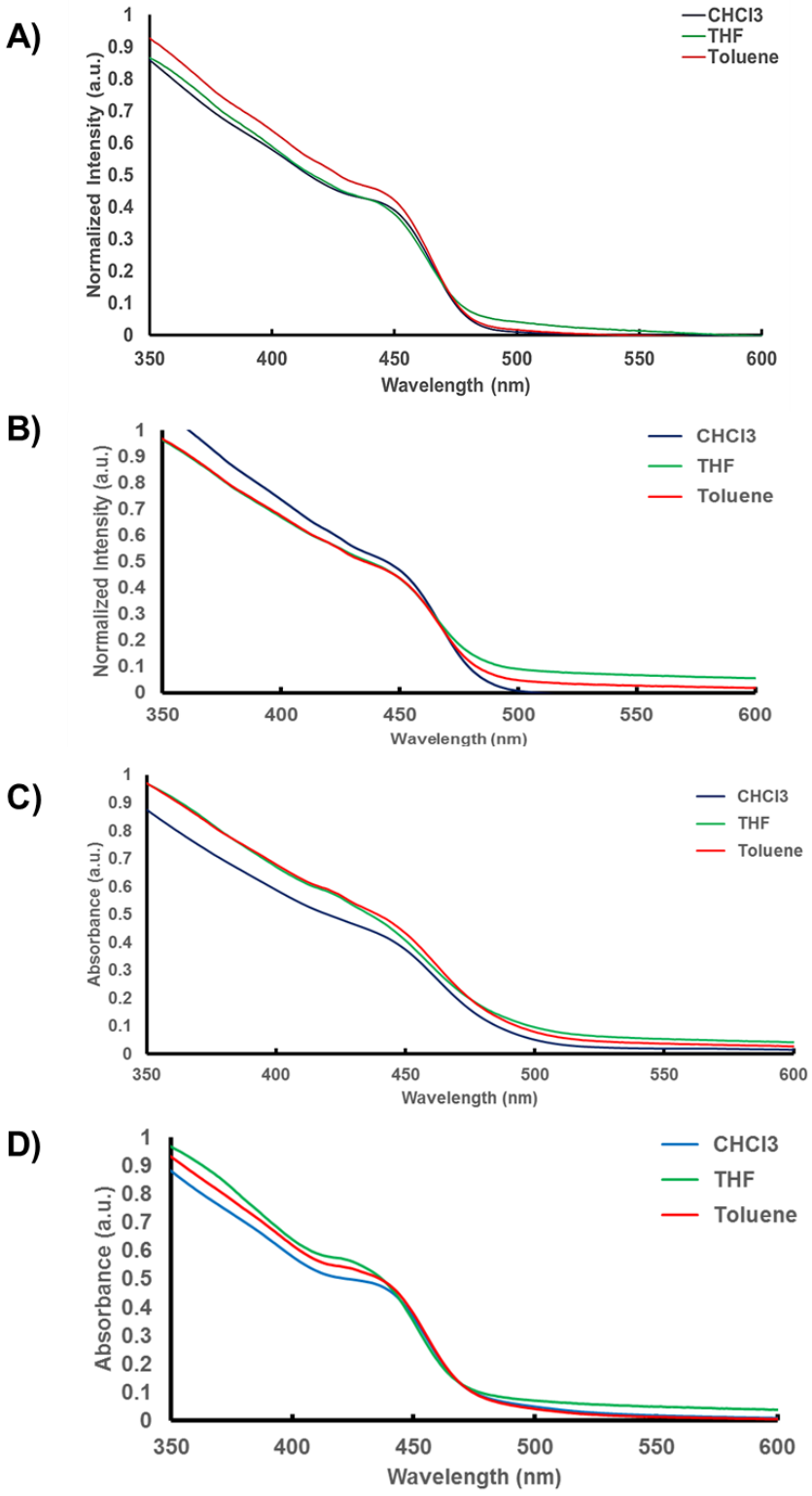

Figure 2.11. UV-Visible spectra of f_{PS} = A) 0.5 B) 0.7 C) 0.8 and D) 0.9 PS/PMMA$_{XL}$(CdS) NPs in THF, toluene and $CHCl_3$.

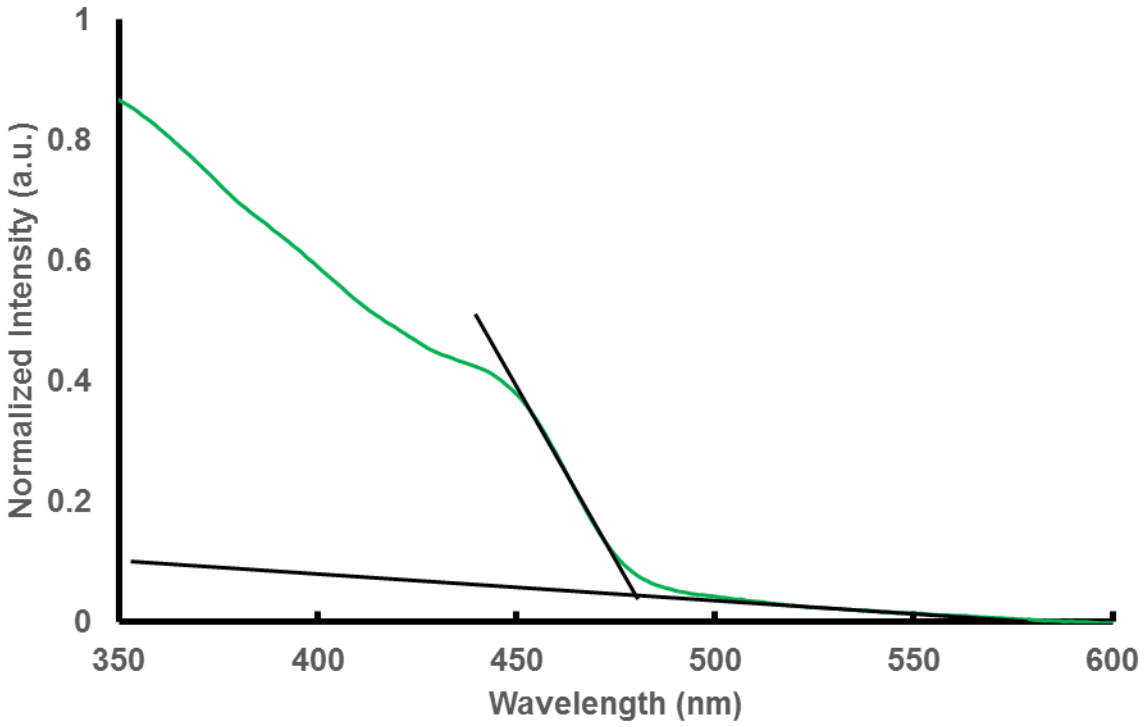

Figure 2.12. UV-Visible spectra of f_{PS} = 0.5 PS/PMMA$_{XL}$(CdS) NPs in THF showing the threshold determination from the extrapolation of the steepest part of the curve and the extrapolation of the baseline. The extrapolation for the remaining blend ratios can be found in Appendix C.

More detailed information on QD sizes and size distributions was obtained using transmission electron microscopy (TEM). Figure 2.13 shows a representative TEM image of each of the NP compositions. The electron-dense CdS QDs appear as dark spots underneath the microscope. The quantum dots were well dispersed across the grid, with only limited clustering of the particles appearing, suggesting that the various brush compositions provided good solution dispersion in the casting solvent (benzene). Size histograms from sizing of ~200 QDs on multiple images from several locations throughout the grid is shown in Figure 2.12. The average QD sizes with standard deviations are also shown in the figure. QD diameters from TEM (in the range of 6.1-6.4 nm for all NP compositions) were found to be slightly higher than predicted by UV-Vis, likely due to aggregation that occurs during drying in the TEM. These aggregates were likely not present in the solution state during UV-vis measurements.

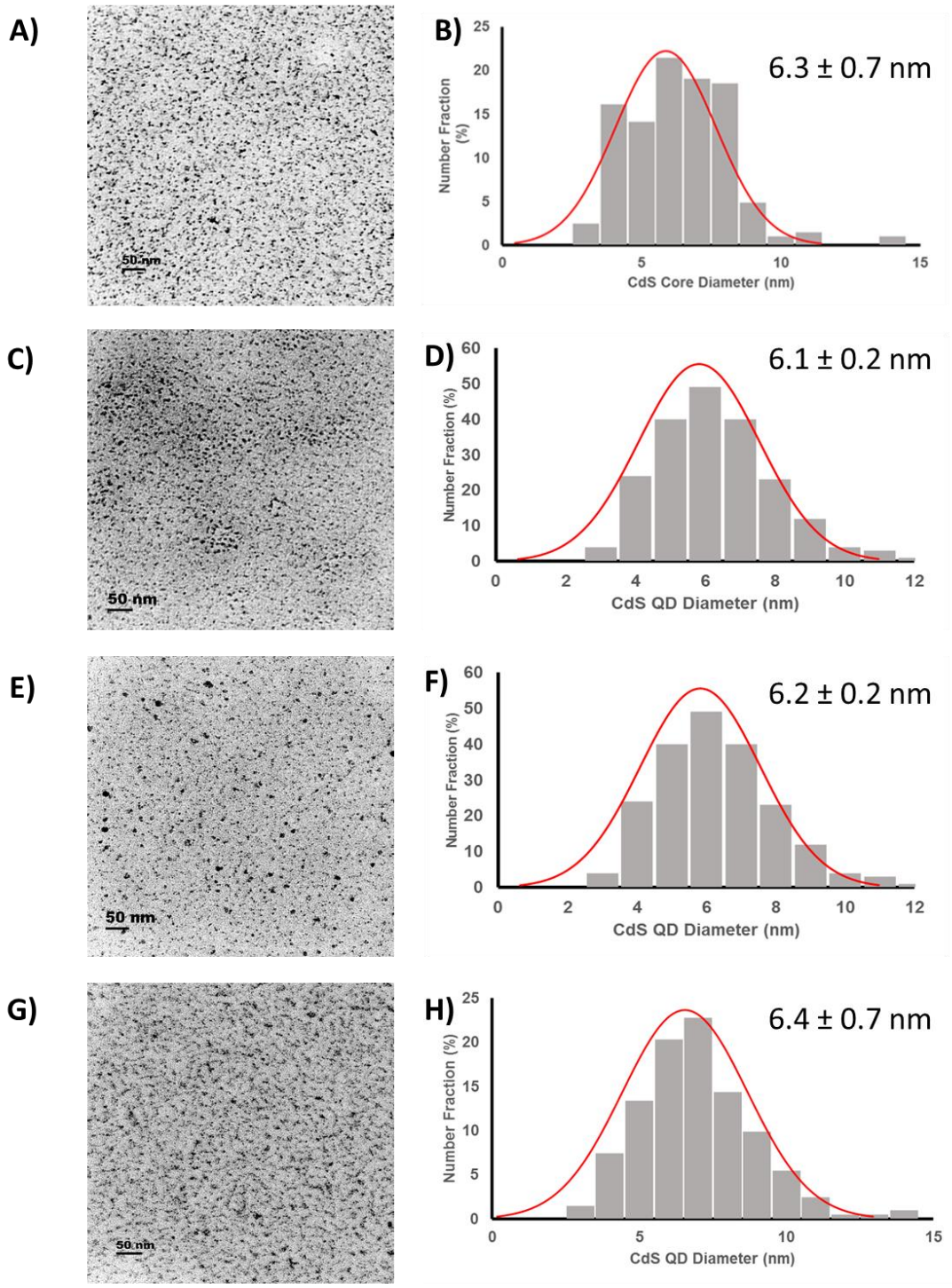

Figure 2.13. TEM image and associated CdS QD size distribution analysis of A,B) f_{PS} = 0.5 C,D) f_{PS} = 0.7 E,F) f_{PS} = 0.8 and G,H) 0.9 PS/PMMA$_{XL}$(CdS) deposited cast from a 1 mg/mL benzene solution dispersed onto a carbon coated copper TEM grid. CdS QD size distribution determined from ~200 QD particles.

2.3.4.3 Static and Dynamic Light Scattering

The use of static light scattering (SLS) and Zimm plot analysis allows for the determination of several important variables of the PS/PMMA$_{XL}$(CdS) NPs, including the weight-average molecular weight, M_W, and the root-mean-square *z*-average radius of gyration, R_g. These values can be determined from the Zimm equation (Equation 2.3):

$$\frac{K_c}{R_\theta} = (\frac{1}{M_w} + 2A_2c)[1 + \frac{16\pi^2 r_g^2}{3\lambda^2}\sin\frac{\theta}{2}^2] \qquad \text{(Equation 2.3)}$$

SLS measurements were taken for each NP sample and Zimm plots were created for analysis of these values. The plots can be found in Figure 2.14.

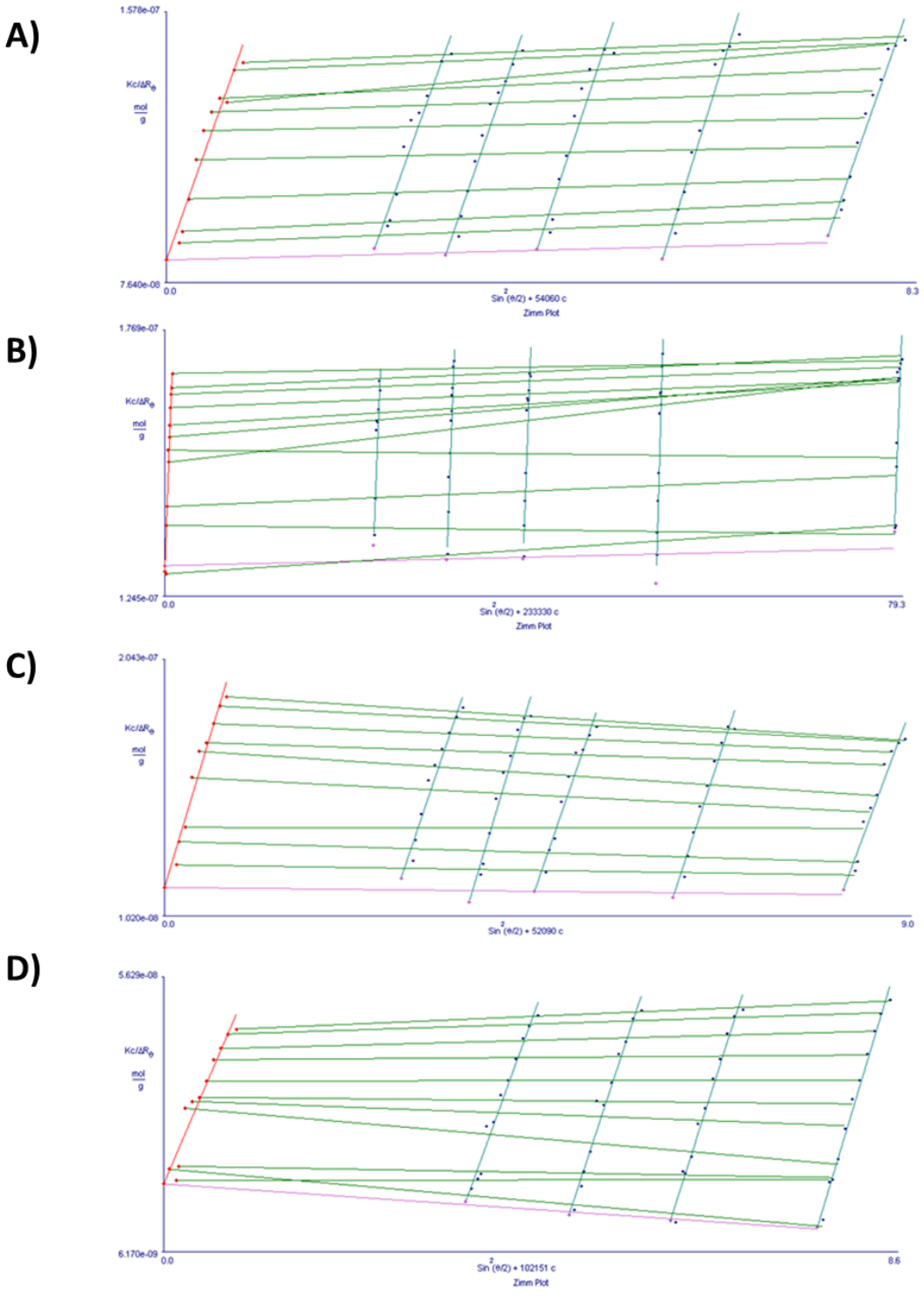

Figure 2.14. Representative Zimm plot for of light scattering data (SLS) for the f_{PS} = A) 0.5 B) 0.7 C) 0.8 and D) 0.9 PS/PMMA$_{XL}$(CdS) NPs in THF. The measured angles were from 30° to 145° in increments and the solution concentrations were from .1 mg/mL to .01 mg/mL

In order to determine the M_w from SLS measurements, the d*n*/d*c* of the material needed to be measured. These terms are related through the K_c value (Equation 2.4):

$$K = \frac{2\pi^2 n_0^2 (\frac{dn}{dc})^2}{\lambda_0^4 N_A} \qquad \text{(Equation 2.4)}$$

Where N_A is Avogadro's number and λ is the wavelength of the incident light. For each blend, three repeat measurements were taken in THF and the results are found in Table 2.4.

Table 2.4. Expected and Measured d*n*/d*c* Values for each PS/PMMA$_{XL}$(CdS) NP Blend in THF

f_{PS}	Expected d*n*/d*c*	Measured d*n*/d*c*
0.5	0.129	.138 ± .007
0.7	0.152	.154 ± .001
0.8	0.161	.165 ± .002
0.9	0.175	.170 ± .004

The expected d*n*/d*c* values were determined by a weighted average of the d*n*/d*c* of PS and PMMA as determined by Equation 2.5:

$$dn/dc_{\ f_{PS}} = (dn/dc_{PS} * f_{PS}) + (dn/dc_{PMMA} * (1 - f_{PS}) \qquad \text{(Equation 2.5)}$$

Where f_{PS} is the polystyrene fraction in the blend. The values measured show a strong correlation to the theoretical values. Small deviations from the theoretical value are expected due to the small d*n*/d*c* contribution from the CdS and PAA in the NP core.

Once the d*n*/d*c* was determined, SLS measurements and Zimm plot analysis of each PS/PMMA$_{XL}$(CdS) NP could be carried out. From these plots, the weight-average molecular

weights (M_w) and the root-mean-square z-average radius of gyration (R_g) of each NP THF could be determined and are listed in Table 2.5.

Table 2.5. Summary of the PS/PMMA$_{XL}$(CdS) Results from Static and Dynamic Light Scattering in THF

f_{PS}	M_w (x10^6 g/mol)	Z	V_{core}	ρ_{chains} (chains/nm^2)	r_g (nm)	r_h (nm)	r_g/r_h	t_b (nm)	Extension (%)
0.5	3.00 ± 0.03	104 ± 1	299	0.48	52 ± 1	47.7 ± 0.6	1.09	43.6	77.5
0.7	2.5 ± 0.1	86 ± 9	264	0.43	33 ± 2	22.1 ± 0.8	1.49	18.1	32.2
0.8	3.28 ± 0.06	112 ± 2	325	0.49	37 ± 1	26.1 ± 0.4	1.42	21.8	38.8
0.9	2.8 ± 0.8	95 ± 9	265	0.48	130 ± 4	27.1 ± 0.2	4.79	23.1	41.1

Aggregation numbers (Z) were calculated by dividing the M_w values by a weighted-average molecular weight of the two constituent unimers ($M_{n,PS\text{-}b\text{-}PAA}$ = 25,098 g/mol and $M_{n,PMMA\text{-}b\text{-}PAA}$ = 24,040 g/mol) plus one CdS unit per carboxylate group (22 × 144.47 g/mol = 3178 g/mol) and one additional Cd^{2+} ion for every two carboxylate groups (11 ×112.411 g/mol = 1237 g/mol), according to the sample calculation for the f_{PS} = 0.5 in Equation 2.6:

$$Z = \frac{M_W}{(f_{PS}*25098)+((1-f_{PS})*24040)+4415} \qquad \text{(Equation 2.6)}$$

$$= \frac{3.00e^6}{(0.47*25098)+((1-0.47)*24040)+4415} = 104$$

Aggregation numbers are all within 20% of a mean aggregation number of ~120, showing that despite the different relative amounts of PS and PMMA in the coronal chains, the similar core-forming PAA blocks for the two copolymers led to similar micelle aggregation

numbers for the various blends. This is reasonable, since for block copolymer reverse micelles it has been shown that aggregation numbers are more strongly affected by the length and nature of the core-forming blocks than by the length and nature of the coronal blocks.[37]

The chain surface densities of the mixed brushes could be determined from these aggregation numbers and from the surface area of the PACd encapsulated CdS NP. The PS/PMMA polymer brush is grafted to a hybrid core consisting of a central QD and a surface layer of collapsed PACd chains; we estimate a total core diameter ($2r_c$) based on QDs size from TEM surrounded by Z chains with 22 PACd repeat units each in the melt state.[149] This is determined by Equation 2.7 in which a sample calculation for f_{PS} = 0.5 is performed. The resulting values these are reported in Table 2.5.

$$\frac{Z * 22 * (M_{PAA} + M_{Cd}/2)}{N_A} = mass\ of\ PACd\ layer$$

$$\frac{104\ \text{chains}\ *\ 22 * (72\ + 56)}{6.023x10^{23}} = 4.865 \times 10^{-19}\text{g} = mass\ of\ PACd\ layer$$

$$\frac{mass\ of\ PACd\ layer}{density\ of\ PACd\ layer} = volume\ of\ PACd\ layer \qquad \text{(Equation 2.7)}$$

$$\frac{4.865 \times 10^{-19} g}{2\frac{g}{cm^3}} = 2.43 \times 10^{-19} cm^3 = 243\ nm^3 = volume\ of\ PACd\ layer$$

$$V_{CdS} = \frac{4}{3}\pi r_{CdS}^3 = 54.3\ nm^3$$

$$V_c = V_{CdS} + volume\ of\ PACd\ layer = 297\ nm^3$$

$$r_c = \sqrt[3]{\frac{3V_c}{4\pi}} = 4.14\ nm$$

As the cores appear to have a roughly spherical shape, their surface area was determined using Equation 2.9, with a sample equation performed for f_{PS} = 0.5:

$$A = 4\pi r_c^2 \qquad \text{(Equation 2.9)}$$

$$A = 4\pi(4.14)^2 = 215\ nm^2$$

By using aggregation numbers from SLS (Table 2.5), the ratio of chains/nm^2 can be determined by Equation 2.10., which also shows a sample calculation for f_{PS} = 0.50.

$$\rho_{chains} = \frac{Z}{A} \qquad \rho_{chains} = \frac{104\ chains}{215\ nm^2} = 0.48\ \frac{chains}{nm^2} \qquad \text{(Equation 2.10)}$$

For the four blends, the average chain density and associated standard deviation are 0.47 ± 0.2 chains / nm^2. Thus despite their variable composition the density of the different mixed brushes are very similar.

Radii of gyration, r_g, of the various NPs in THF can be determined from Zimm plot analysis. r_g values refer to the root-mean-square distance of scattering centers from the center of mass of the particle. These values are determined from the Zimm equation by extrapolating θ on the Zimm plot to 0. The f_{PS} = 0.7 and 0.8 blends were quite similar with values of 33 ± 2 and 37 ± 1 nm respectively. The f_{PS} = 0.5 blend was a bit higher at 52 ± 1 nm and the f_{PS} = 0.9 blend was almost double at 130 ± 4 nm. The f_{PS} = 0.7 and 0.8 values are consistent with previous PBNPs, but the R_g of f_{PS} = 0.9 and 0.5 were quite dissimilar from the others.[33]

Hydrodynamic radii values, r_h, were measured using dynamic light scattering (DLS). r_h is a term that measures the apparent size of particles in a solvent environment, taking the full extension of the polymer chain into account. r_h values (found in Table 2.5) show similar sizes for the f_{PS} = 0.7, 0.8 and 0.9 NPs and the f_{PS} = 0.5 NPs are almost twice the size. The r_h values of the

f_{PS} = 0.5, 0.7 and 0.8 blends appear to be similar to the r_g values previously obtained from the Zimm plot analysis and produce r_g / r_h numbers between 1-1.5. The r_h of the f_{PS} = 0.9 blend is significantly lower than that of the r_g, giving an r_g / r_h of 4.79 that is much larger than the other three blends. The f_{PS} = 0.9 blend is the most asymmetric (Figure 2.15), with most of it consisting of PS and only 10 % represented by PMMA. The d*n*/dc of PS and PMMA in THF different from each other: PS in THF is 0.185 and PMMA in THF is 0.08[92]. As d*n*/d*c* term is proportional to the r_g in the Zimm equation, these values have a direct influence on r_g. It is hypothesized that the polymers in the corona are phase separating into Janus or patchy particles, producing a scattering of the particle that is no longer spherical. The distribution of scattering centers goes form being isotropic (spherically symmetric) to anisotropic as the composition of the brush becomes highly asymmetric.

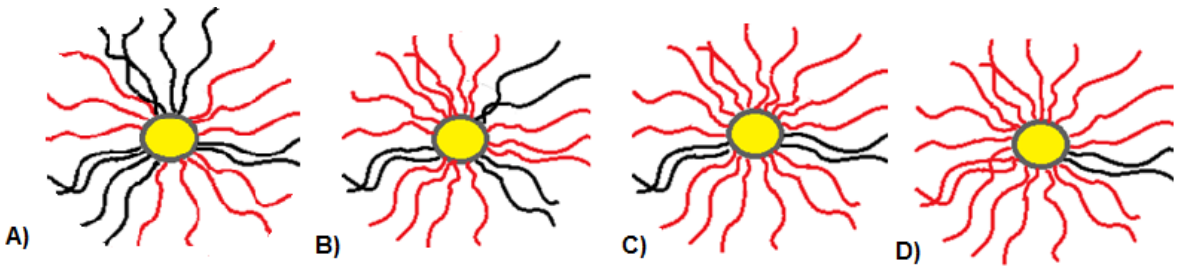

Figure 2.15. Schematic depicting the change in brush symmetry as f_{PS} is increased from A) 0.5 B) 0.7 C) 0.8 and D) 0.9.

While the values of r_h reported in Table 2.5 are average values from a fit of the distribution of exponentials to a Gaussian function, CONTIN analysis provides more detailed information of the shape of the distribution of hydrodynamic particle diameters in solution for each blend performed at 90 ^{o} at low solution concentrations show a single population of particles (Figure 2.16).

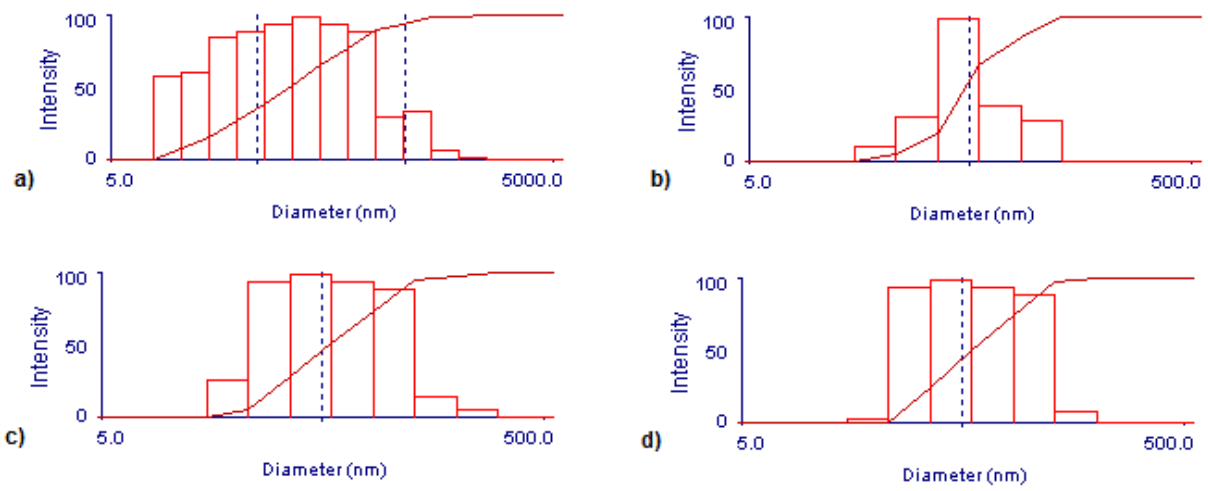

Figure 2.16. Hydrodynamic particle size distribution from CONTIN analysis of dynamic light scattering of f_{PS} = A) 0.5 B) 0.7 C) 0.8 and D) 0.9 PS/PMMA$_{XL}$(CdS) blends in THF. These results were obtained at a 90 ^{o} scattering angle and concentration of ~0.1 mg/mL

r_h can also be used to determine the thickness of the polymer brush, t_b, in solution (Figure 2.17).

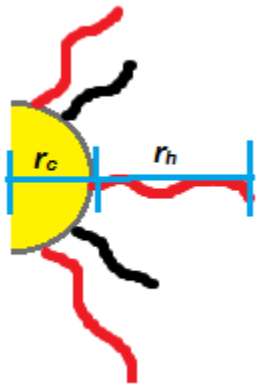

Figure 2.17. Schematic showing how brush thickness, t_b, is determined from r_c and r_h.

By taking the difference between the r_h and the r_c (the radius of the core based on TEM measurements and the added PAA core shell), the brush thickness can be found (Table 2.5).

While the f_{PS} = 0.7, 0.8 and 0.9 blends all displayed a brush thickness from 16-21 nm, the f_{PS} = 0.5 blend showed a brush thickness of almost double (41.6 nm). As THF is a good solvent for both PS and PMMA (Flory-Huggins interaction parameter $\chi_{PS\text{-}THF}$ = 0.474 and $\chi_{PMMA\text{-}THF}$ = 0.442)[33], both polymers are expected to be extended in the corona in THF (although the PMMA should have slightly more extension due to its higher χ parameter). As PMMA has the higher χ and both PMMA and PS have the same number of repeat units, PMMA will be further extended than the PS chains. Therefore, it should constitute the longest component of the polymer brush, the percentage extension of PMMA chains in THF compared to the fully-stretched (all-trans) conformation can be calculated using equation 2.9:

$$\text{Chain extension (\%)} = 100 \times (t_b/[aN]) \qquad \text{(Equation 2.9)}$$

Where a is the length of one repeat unit at full extension (a = 0.25 nm) and N is the number of PMMA repeat units in the polymer chain (N = 225). The chain extension of the f_{PS} = 0.7, 0.8 and 0.9 blends were comparable in that they rested within a range of ~ 29-37 %, but the f_{PS} = 0.5 showed 73.6 % extension. It is believed that the coronal brush orientation around the quantum dot core and the ratio of r_g / r_h can explain this greater extension. The ratio of r_g / r_h is indicative of the shape of a particle in solution. A value of 0.77 corresponds to a perfect sphere, a value of 1.1 would be a spherical starlike micelle and larger values would start to depict particles with high aspect ratios (such as cylindrical shapes). As the r_g / r_h of this NP sample appears to show a spherical shape, it is hypothesized that the packing density is not uniform over the whole brush. There are local regions that have denser packing compared to others, despite the fact that the average packing density is the same. Further experimentation is required to explore this phenomenon. Based on the r_g / r_h values, it is believed that the f_{PS} = 0.9 particles take on an asymmetric brush distribution, but it is difficult to draw conclusions about the other NPs.

2.3.4.4 NOESY NMR Investigation of Mixed Brush Structure

Along with aggregation numbers and chain densities from static light scattering, it is important to determine the more detailed structure of the mixed brush, namely how the PS and PMMA chains are distributed throughout the brush. Three main distributions have been identified: Janus,[93-95] patchy[96,97] and random distributions[33] (Figure 2.18)

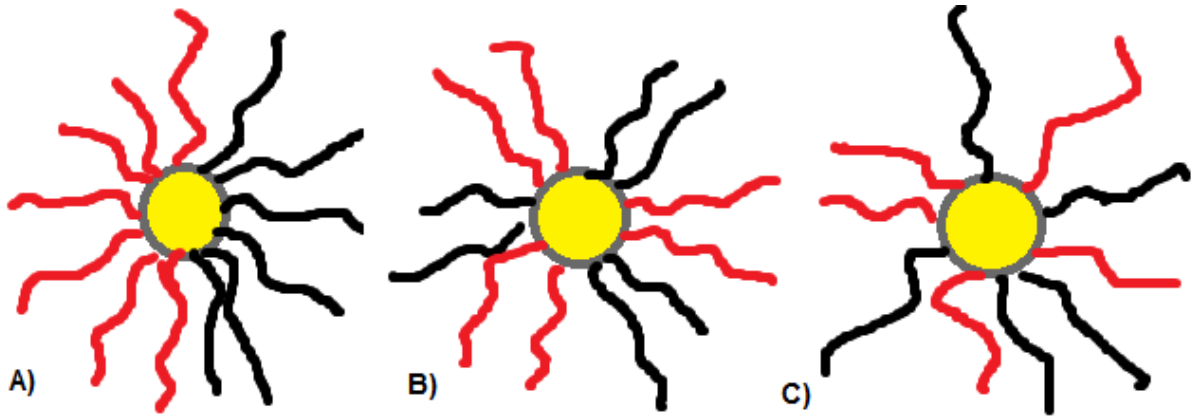

Figure 2.18. Schematic depicting a A) Janus, B) Patchy and C) Random distribution of chains.

These distributions are based on how the polymer brushes are distributed around the core NP. Janus sees a complete phase separation of each polymer brush, creating anisotropic regions that have a single composition. Patchy particles separate into multiple anisotropic regions of hydrophobicity or hydrophilicity. Random distributions are isotropic, showing no phase separation or directionality. Work by Glotzer *et al*[98-100] has shown that the distribution of chains around the NP core can play an important role in the self-assembly of these particles, so it is important to probe how the chains are distributed.

Previous work from out group by Guo *et al.*[33] found that when a triblock copolymer with terminal PS and PMMA blocks was self-assembled to form a mixed brush, 2D ^{1}H NOESY NMR

experiments suggested that the PS and PMMA chains were distributed statistically (random brush) over the surface of the QD-containing cores. As 2D ^{1}H NOESY NMR investigates through space interactions between protons close together, this technique can be used to probe PS and PMMA interactions at or near the CdS core in the PS/PMMA$_{XL}$(CdS)NPs. Based on the strength of any NOE signal between styrene and methoxy peaks, the mixed brush particles may be classified as Janus brushes (no signal), patchy brushes (limited signal) or random brushes (stronger signal).

Peak labels for the two main polymer chains can be found in Figure 2.19 A). The ^{1}H 2D NOESY NMR spectra for each PS/PMMA$_{XL}$(CdS)NP sample (Figure 2.19 B-E) and a 50/50 blend of PS-*b*-PAA/PMMA-*b*-PAA in $CDCl_3$ that is used as a control (Figure 2.19 F) can be found below.

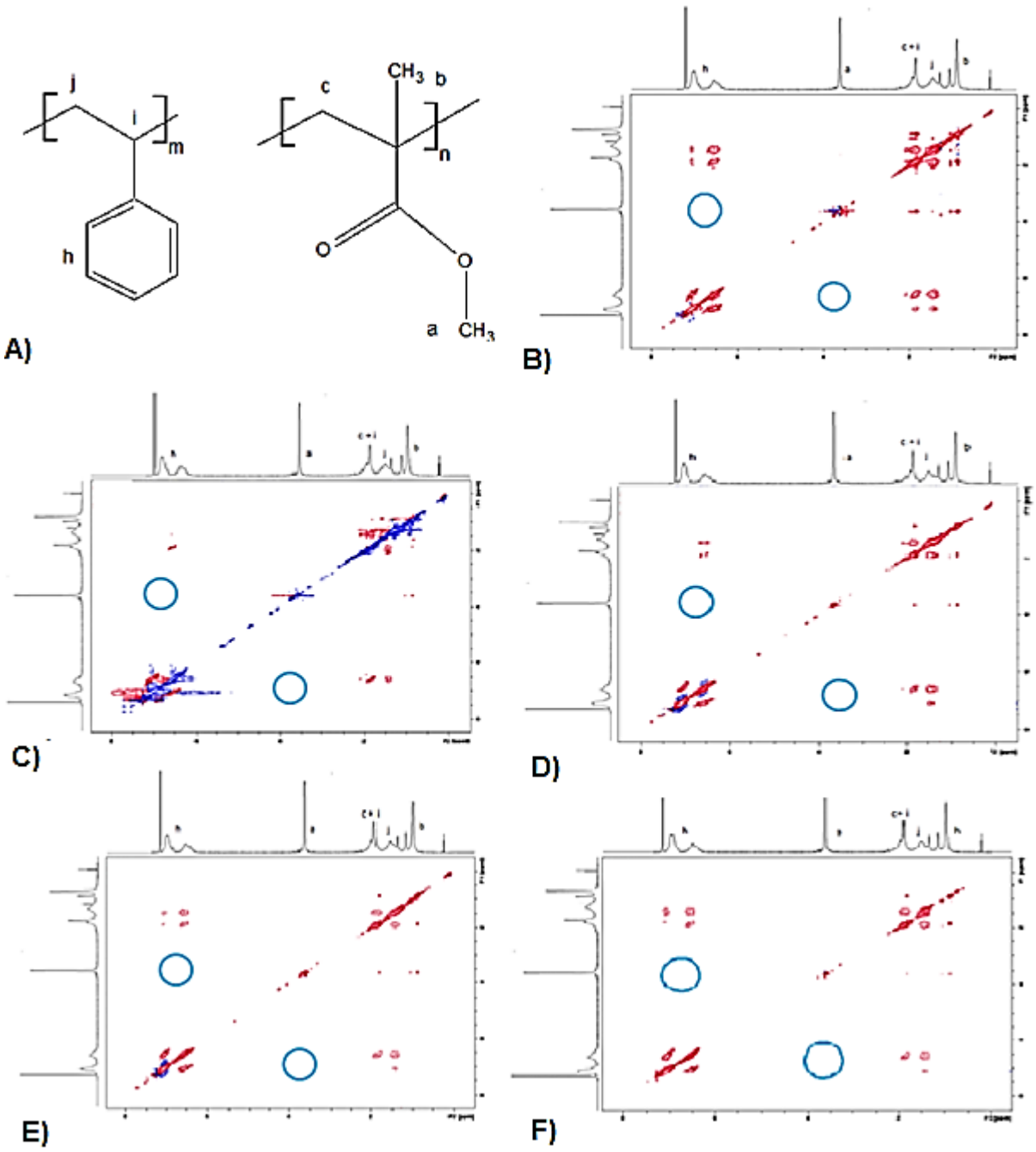

Figure 2.19. A) NMR Peak labelling for PS-*b*-PAA and PMMA-*b*-PAA. 2D ^{1}H NMR NOESY spectra of f_{PS} = B) 0.5 PS/PMMA$_{XL}$ (CdS) NPs C) 0.7 D) 0.8 E) 0.9 and F) PS-PAA/PMMA-PAA unmicellized reference in $CDCl_3$. Light blue circles in each spectra show the region where a cross-coupling signal is expected between the aromatic region of PS and the methacrylate region of PMMA. These signals were not present.

In the case of all four blends, no cross-coupling signals were detected between the aromatic region of the PS chains and the methacrylate region of the PMMA chains (similar to that of the reference in 2.19.F). This lack of signal would suggest the chain distribution of mixed brushes is patchy or Janus. This is in contrast with the triblock copolymer-based samples produced by Guo[33] which were found to have a random distribution. A likely reason for this lies in the use of two diblock copolymers that consisted of much shorter diblock. The use of two shorter diblock copolymers would allow for greater mobility during micellization due to less steric crowding from each brush. Longer polymer blocks would be limited in the free volume available during micellization, as their increased bulk would increase interactions. The particles would be unable to find locations of lowest energy (separating out hydrophobic and hydrophilic blocks), leading to a random distribution. The shorter diblock copolymers also have the advantage of not being tethered together, increasing their ability to form anisotropic regions around the core. Therefore, the bulk of the polymer plays a large role in controlling the polymer brush distribution during micellization.

2.3.4 Hydrolysis of PMMA Brush Chains to PMAA: Converting PS/PMMA$_{XL}$(CdS) to PS/PMAA-(CdS)

Once the structural characterization of PS/PMMA$_{XL}$(CdS) NPs was complete as described above, the polar but hydrophobic PMMA chains in the mixed brushes were hydrolyzed to hydrophilic PMAA using KOH and 18-crown-6 in refluxing dioxane under a N_2 atmosphere over 4 days. The ^{1}H NMR spectra and peak assignments comparing the unhydrolyzed and hydrolyzed forms of each NP can be found in Figure 2.20. The disappearance of the methoxy peak of PMMA at 3.60 ppm signifies the hydrolysis is complete and PMAA has been

synthesized in the mixed brush layer, making the resulting PS/PMAA$_{XL}$(CdS) NPs amphiphilic due to their mixed brushes of hydrophobic PS and hydrophilic PMAA chains.

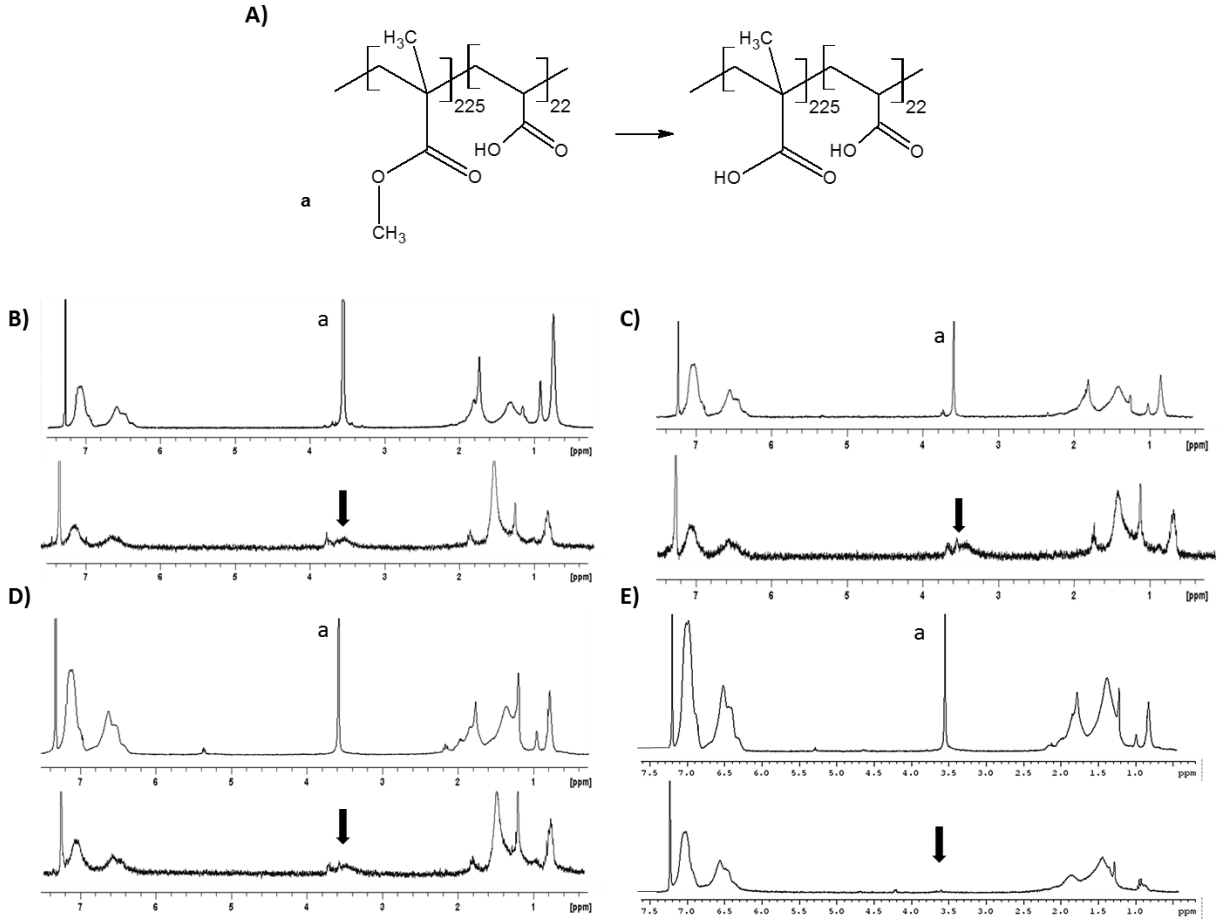

Figure 2.20. [1] H NMR peak assignments of A) PMMA-*b*-PAA and PMAA-*b*-PAA. [1]H NMR spectra of f_{PS} = B) 0.5 C) 0.7 D) 0.8 and E) 0.9 before and after hydrolysis of PS/PMMA$_{XL}$(CdS)

As the conditions for the hydrolysis are quite robust, it was necessary to determine the structural integrity of the NPs by GPC after hydrolysis. Figure 2.21 shows a comparison of GPC data for each of the f_{PS} = 0.5, 0.7, 0.8 and 0.9 PS/PMMA$_{XL}$(CdS) NPs (before hydrolysis) with the corresponding PS/PMAA-(CdS) NPs (after hydrolysis). Comparison of GPC traces reveals that before hydrolysis there are three visible peaks. One large one at 11.3 min (representing the

nanoparticle hydrolysis results in the main NP peak broadening and shifting to lower retention times (larger hydrodynamic size in THF) in all but the f_{PS} = 0.8 case (Figure 2.10c) where the NP peak shifts to slightly higher retention time after hydrolysis. Most importantly, the relative fraction of single chains represented by the single chain peak at higher elution volumes has not increased significantly, indicating that the NPs held their structural integrity during the crosslinking step. More specifically, peak integration of GPC traces reveals the percentage of single chains in all of the PS/$PMAA_{XL}$(CdS) NP samples to be in the range of 7 – 12 wt % (peak deconvolution of f_{PS} = 0.8 can be found in Appendix B).

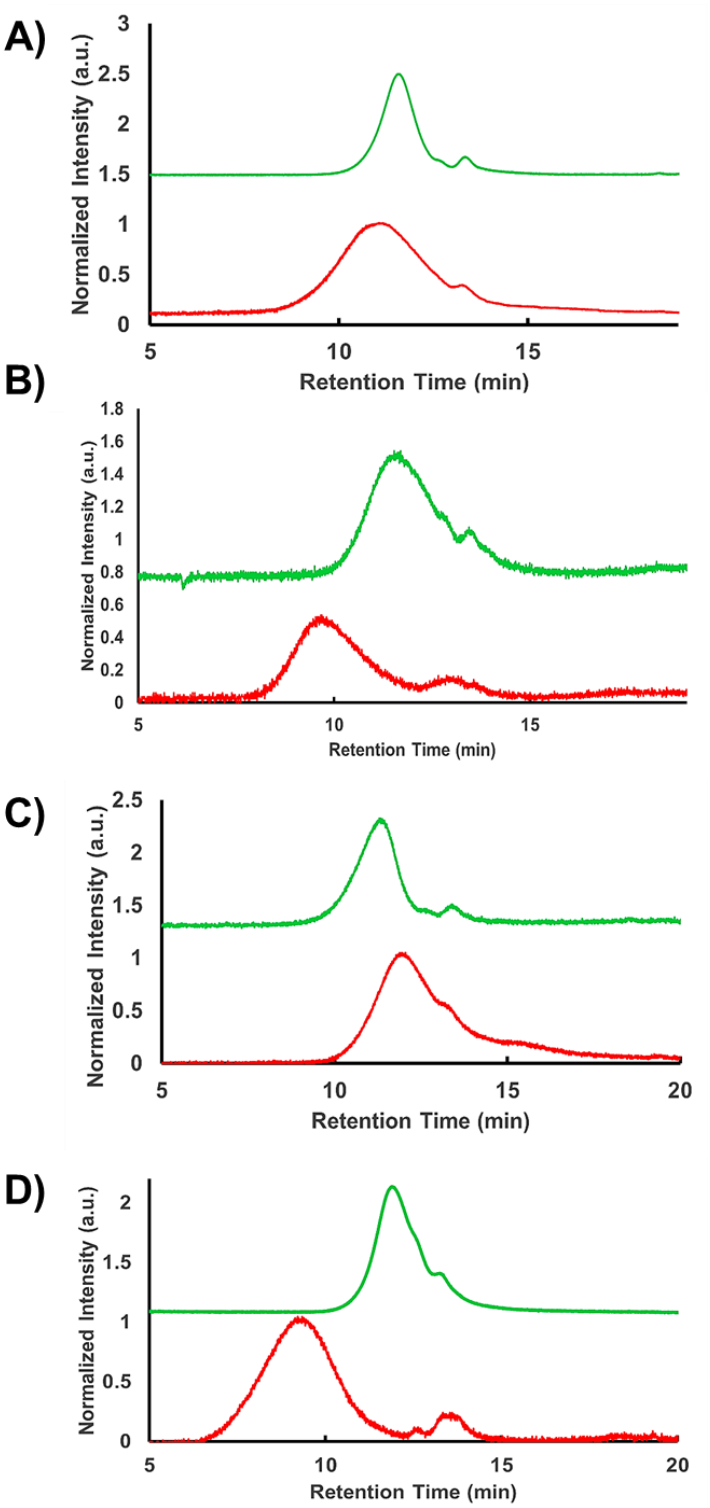

Figure 2.21. GPC (refractive index detector response) comparison of f_{PS} = A) 0.5 B) 0.7 C) 0.8 and D) 0.9 PS/PMMA$_{XL}$ (CdS) NP and the hydrolyzed PS/PMAA$_{XL}$ (CdS) NP. All GPC chromatograms were run using THF as the eluent solvent.

2.3.5 Characterization of Crosslinked PS/PMAA Mixed Brush Coated CdS QDs After Hydrolysis of PMAA Chains, PS/PMAA$_{XL}$(CdS)

2.3.5.1 Dynamic Light Scattering (DLS)

Due to the transformation of PMMA to PMAA, the coronal brush now takes on a hydrophilic component, changing how the particle interacts with organic solvents. DLS measurements were taken of each NP and are presented in Table 2.6:

Table 2.6. DLS Cumulant Analysis Measurements of r_h for each PS/PMAA-(CdS) NPs in THF at a 90° Angle.

f_{PS}	r_h – PMMA (nm)	r_h – PMAA (nm)
0.5	47.7 ± 0.6	350 ± 20
0.7	22.1 ± 0.8	109 ± 2
0.8	26.1 ± 0.4	92 ± 1
0.9	27.1 ± 0.2	78 ± 2

Upon hydrolysis of PMMA, the r_h of each NP greatly increased compared to the pre-hydrolysis form. Such a large increase in size would suggest some aggregation is occurring in THF. The aggregation seems to be more predominant at lower f_{PS} (f_{PS} = 0.5), while increasing f_{PS} seems to limit aggregation (f_{PS} = 0.9). At lower f_{PS}, more chains are being changed from hydrophobic to hydrophilic, which will lead to more aggregation in polar organic solvent as chains collapse. At higher f_{PS}, the PS in the polymer brush is extended into the solvent, repelling other NPs through steric interactions. As the f_{PS} decreases, fewer PS brushes are available in the

corona to repel other NPs. Meanwhile, the partially charged, hydrophilic PMAA chains will likely have collapsed around the CdS core in organic solvent, excluding less free volume in solution and allowing other NPs to come into closer proximity. As they become closer, charge interactions between the CdS cores and the charged PMAA (even in their collapsed state) allow for aggregation of NPs.[63] The limitation of repulsive steric interactions and the charge interactions allow for aggregation at lower f_{PS}, creating larger r_h.

The retention time presented by GPC is based on the hydrodynamic diameter of the particle as it moves through the column. In the case of f_{PS} = 0.5, 0.7 and 0.9, the size of the NP peak increases compared to its non-hydrolyzed form (Figure 2.21). The f_{PS} = 0.8 form is the only exception to this trend, as the size of the particle appears to shrink. While hydrodynamic size is but one variable that determines how long the particle is retained in the column, no other evidence has been found to suggest there are other factors at play. It is possible that the distribution of chains around the f_{PS} = 0.8 NPs differs from the others, causing it to have a longer retention time. The r_g / r_h of this sample did show a decrease compared to the f_{PS} = 0.7 NPs, possibly suggesting a more symmetric brush distribution than f_{PS} = 0.7, but this would not explain the overall longer retention time compared to the other three samples. This result requires further experimentation and thought at this time.

CONTIN analysis was also performed on each NP sample, as seen in Figure 2.22. Each NP solution showed a single distribution of particles, suggesting that these r_h values were not arising from a mixed population of large and small particles.

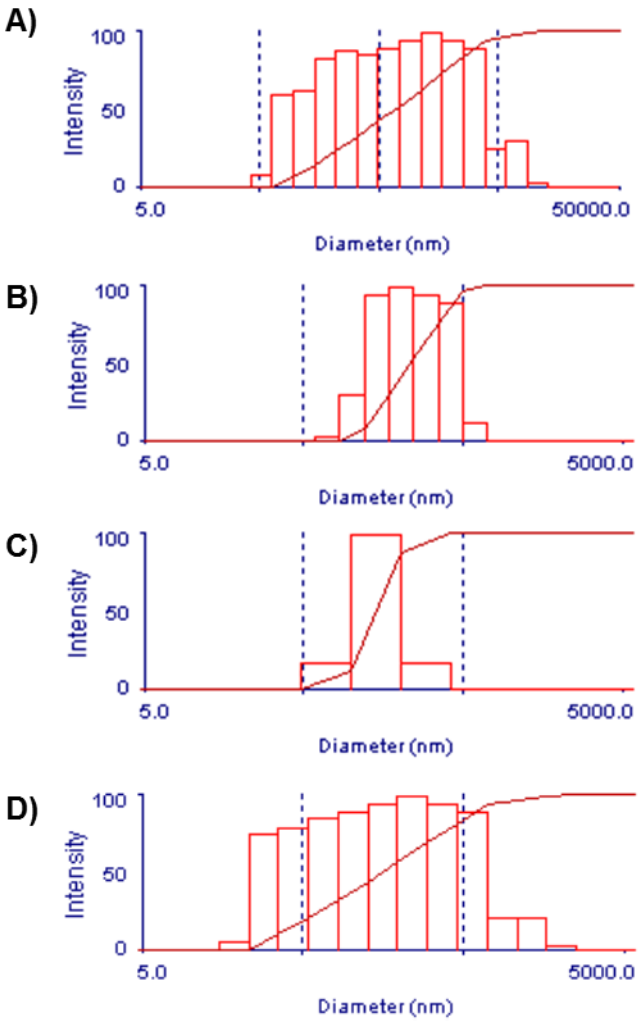

Figure 2.22. CONTIN analysis of f_{PS} = A) 0.5 B) 0.7 C) 0.8 and D) 0.9 PS/PMAA-(CdS) NPs. All measurements were determined in THF at an angle of 90°.

2.3.5.2 Transmission Electron Microscopy (TEM)

As one of the main goals of the creation of these NPs is to later self-assemble them by water addition to THF dispersions, it is important to note if the particles self-assemble before addition of water in THF. While aggregation can occur during the drying stage, this does not necessarily indicate aggregation in the solution phase. As disassembly is uncommon during the drying step, good dispersion on the grid likely indicates good dispersion in the solution phase. TEM was used to view the individual quantum dots found in each PS/PMAA-(CdS) NP. The high electron density associated with the CdS core allows them to be easily visible under TEM as black spots, as seen in Figure 2.23. These samples were cast from a benzene solution as casting from THF resulted in significant drying artifacts on the TEM grid.

In each image, the black dots represent the CdS cores of the NP. In the case of f_{PS} = 0.5, 0.7 and 0.9 there is good dispersion between particles. In the case of the f_{PS} = 0.8 blend, some clustering of the particles can be seen. Despite this, individual QDs are still visible. Size distribution analysis of the QD diameter shows singular distributions for each blend. The average QD diameter of the each of these particles can be found in Table 2.7.

Table 2.7. QD Core Sizes of PS/PMAA-(CdS) NPs as Determined from TEM

f_{PS}	QD Diameter (nm)
0.5	6.9 ± 0.8
0.7	6.3 ± 0.5
0.8	6.2 ± 0.4
0.9	6.1 ± 0.6

These core sizes are similar to QD sizes measured before hydrolysis with a slight increase in size for f_{PS} = 0.5, but it within standard deviation. Therefore, the QDs have neither grown nor dissociated during the hydrolysis step. This is likely due to the fact that the CdS core is encapsulated by the PAA polymer layer, protecting it from solvent effects and heat.

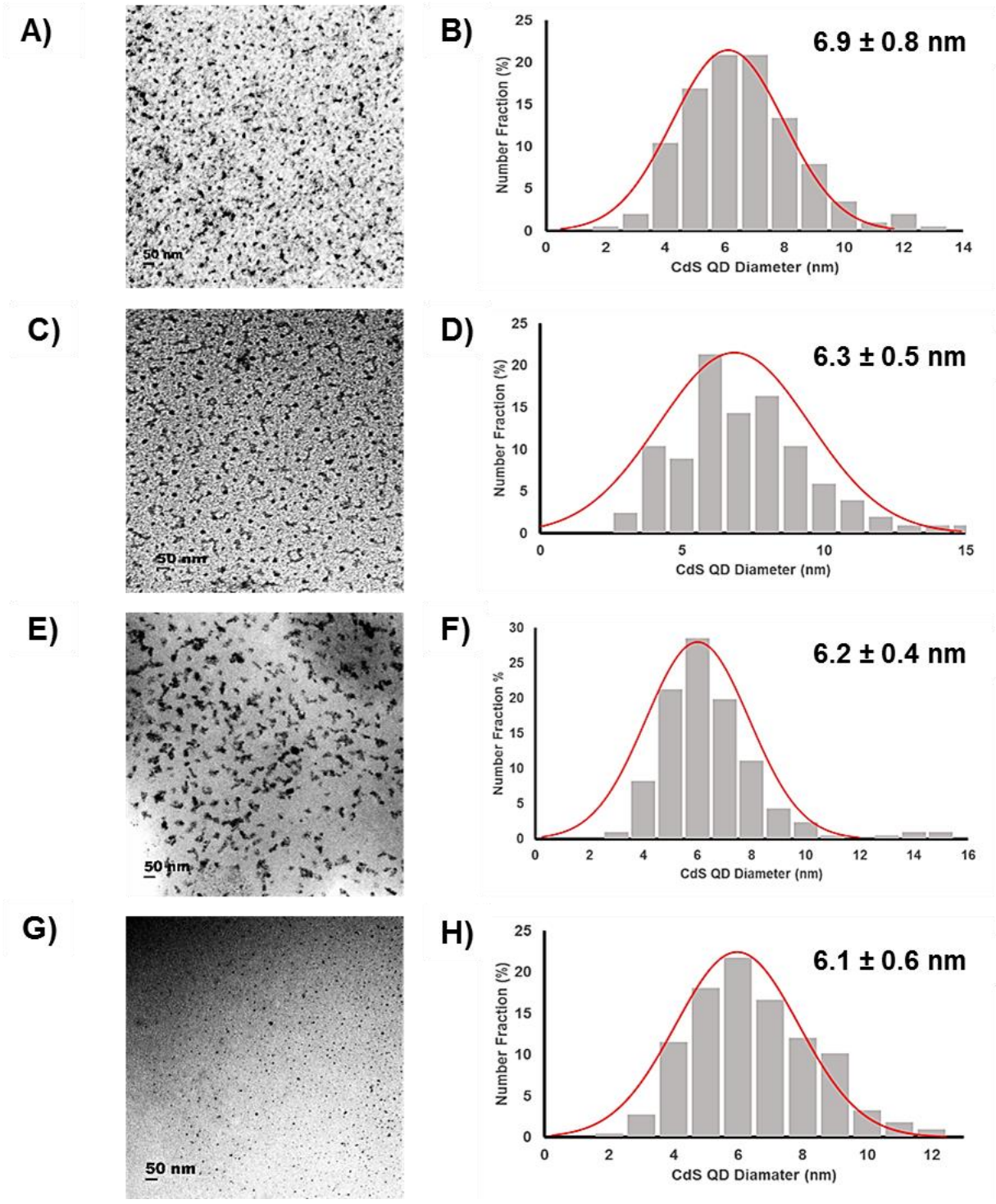

Figure 2.23. TEM images and CdS QD size distribution of f_{PS} = A,B) 0.5 C,D) 0.7 E,F) 0.8 and G,H) 0.9 PS/PMAA-(CdS) NPs cast from a 1 mg/mL benzene solution

2.3.5.3 Powder X-Ray Diffraction (XRD)

As the CdS QDs in the NP cores should be crystalline, we finally used powder XRD to characterize the ionic lattice structure of CdS in the core. The powder x-ray diffractograms of each PS/PMAA-(CdS) blends can be found in Figure 2.24. These diffraction patterns match that of cubic CdS as found in the JCPDS database.[63] The one exception is the peak that is found at 2θ ~30 °. The *d* spacing of this peak (determined using Bragg's Law) is 0.56 nm. It was determined using light scattering that the chain density of each particle is ~1 chain/nm^2, corresponding to an interchain distance of ~1 nm. Therefore this scattering peak may arise from mean distance between PS and PMAA polymer chains at the surface of the CdS core, as proposed earlier in the work of Guo *et al.*[33] By looking at the brush composition dependence of the diffractograms for the first time, this work further supports the assignment of the 2θ ~30° peak to interchain scattering at the QD surface: we note that the intensity of the peak relative to the CdS reflections increases with the PS content, consistent with the fact that PS is a more electron dense polymer than PMMA and will therefore scatter x-rays more strongly.

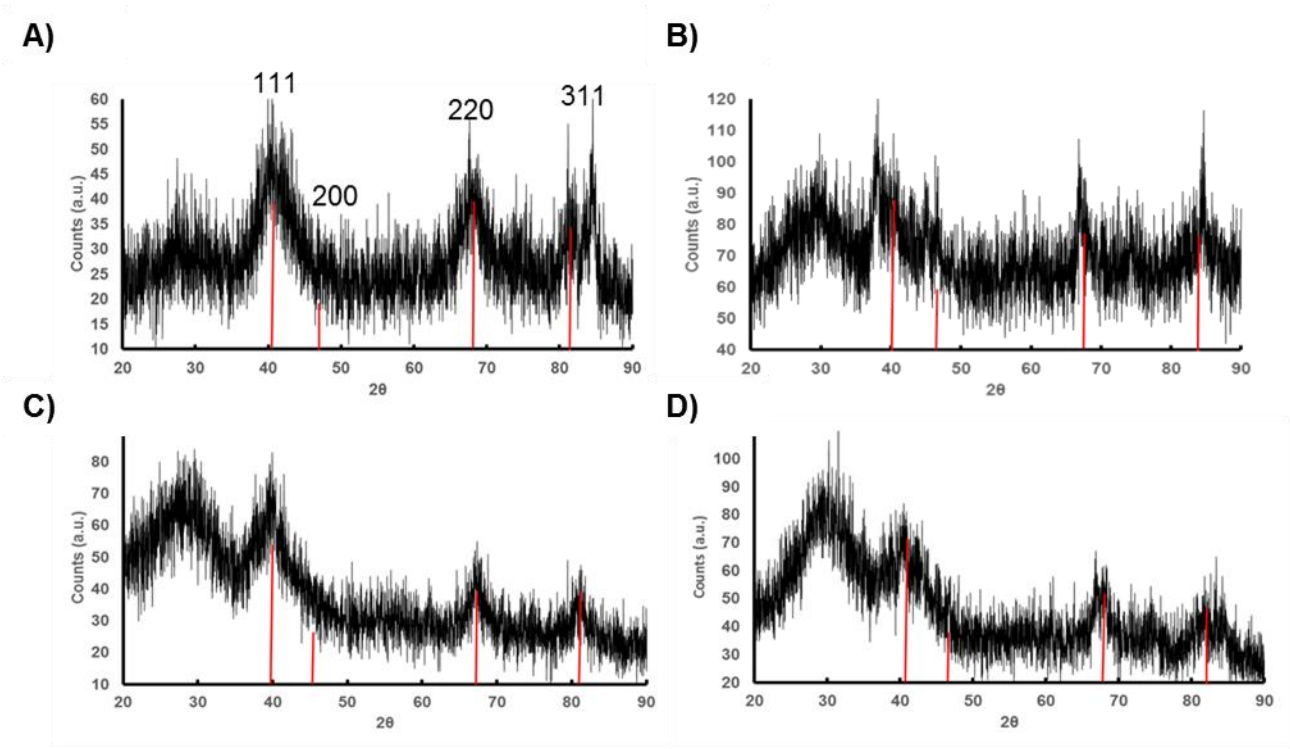

Figure 2.24. Powder x-ray diffractograms from f_{PS} = A) 0.5 B) 0.7 C) 0.8 and D) 0.9 PS/PMAA-(CdS) NPs with red lines indicating the location of the four main peaks associated with cubic CdS

2.4 Conclusions

It has been shown that PS/PMAA$_{XL}$ (CdS) NPs were synthesized and characterized in four blend compositions of increasing PS content by using a novel diblock copolymer blending approach. GPC and ^{1}H NMR evidence suggests that NPs with a brush composition of f_{PS} = 0.5, 0.7, 0.8 and 0.9 were synthesized. UV-Vis spectroscopy demonstrates that the CdS QDs have a strong exciton shoulder and that the fluorescent nature fot he CdS QDs remains after micellization and crosslinking. 2D NOESY NMR indicates the mixed polymer brush takes on a patchy or Janus conformation around a central CdS QD core. Light scattering shows evidence that of the four f_{PS} compositions have similar aggregation numbers and brush densities despite

the changes in the brush composition, but different conformational structure (the r_g of f_{PS} = 0.5) and asymmetry of the particles (different shape ratio, (r_g/r_h) of the f_{PS}. The PMMA chains were hydrolyzed to PMAA in order to change them from hydrophobic to hydrophilic without causing dissociation of the NP or the QD core. This approach opens up new avenues to creating functionalized NPs beyond graft-to and graft-from approaches. The creation of this mixed brush presents an opportunity to test the effect of brush composition on the self-assembly of these inorganic NPs from THF and water, as will be discussed in Chapter 3.

Chapter 3

Amphiphilic Self-Assembly of Polystyrene/Poly(methacrylic acid) Mixed Brush-Functionalized Inorganic Nanoparticles of Variable Brush Composition

3.1 Introduction

The applications that can arise from the self-assembly of quantum dots (QDs) and inorganic nanoparticles (NPs) into hierarchical colloidal assemblies can be found in research fields as varied as bio imaging[1-3,75], drug delivery[73,74,100,102,103] , sensors[4,6,8,104] , and optics.[105-108] In order to take advantage of these applications, materials scientists have recently sought to tune the morphologies and regulate the internal organization of nanoparticle assemblies.[16,24,109-113] Many approaches to this challenge use polymers as a matrix or scaffold for nanoparticle assembly. For example, nanoparticle assemblies have been produced from NP "bricks" and polymer "mortar".[114,115] Srivastava *et al*. used a poly(amidoamine) dendrimer to fix the interparticle spacing between Au NPs functionalized with a surface monolayer of carboxylic acid.[116] Another approach involves the use of electrostatic interactions to decorate polymer spheres with NPs using layer-by-layer assembly.[117,118] For example, Wang *et* al. prepared a layer-by-layer assembly of CdTe NP-labelled PS beads held together by electrostatic attractive interactions between negatively-charged carboxyl groups on the surface of the CdTe NPs and positively-charged NH_3^+ groups of poly (allylamine hydrochloride).[119] A third method has been to use block copolymer colloidal assemblies to give structure and organization to NPs.[120-122] For example, Moffitt *et al.* synthesized CdS NPs that were grown within block ionomer reverse micelles before being further assembled into large compound micelles in aqueous solution.[123] As promising as these results are, the number of tunable morphologies by such methods has been limited and control over the organization of QDs and inorganic NPs is still greatly restricted.

In order to introduce greater control and structural complexity to NP self-assembly in a colloidal media, scientists have looked to the self-assembly of amphiphilic block copolymers in aqueous media for inspiration. A high degree of morphological variability has been shown by

such systems, producing a wide array of colloidal polymeric structures, including nanoscale spheres, cylinders, vesicles among others.[124-127] The amphiphilic character of diblock copolymers consisting of spatially-separated hydrophobic and hydrophilic blocks is analogous to the well-studied amphiphilicity of small-molecule surfactants and phospholipids in water, in which molecular assembly is driven by microphase separation of hydrophobic segments into nanoscale domains surrounded by covalently-connected hydrophilic segments.[26,128,129] For example, Zhang *et al.* produced morphological aggregates ranging from spheres to cylinders to vesicles *via* self-assembly of polystyrene-*block*-poly(acrylic acid) (PS-*b*-PAA) block copolymers in DMF/H_2O mixtures; morphologies were varied by adding different quantities of salt to the solution prior to assembly.[130]

With such rich self-assembly behaviour of block copolymer amphiphiles as an example, a new strategy has been explored in recent years to imitate block copolymer systems through the creation NP/polymer colloidal hybrids with amphiphilic character.[26,54,124,131,132,] Amphiphilic particles can be produced by decorating nanoparticle surfaces with spatially-separated regions of hydrophobic and hydrophilic domains.[33,60] For example, Zubarev *et al.* functionalized gold NPs with a mixture of hydrophobic (polybutadiene) and hydrophilic (poly(ethylene oxide)) polymer chains by connecting to surface anchors that are linked electrostatically by thiol-Au interactions.[133] In another study, a V-shaped molecule of PS and PEO poly(ethylene oxide)) bridged together by a carboxylic acid functionalized bridging unit was attached to the surface of Au NPs through a condensation reaction with a surface ligands already attached to the Au NPs. When placed in an aqueous environment, this led to their amphiphilicity-driven self-assembly based on the hydrophobic effect as the hydrophobic and hydrophilic arms phase separated.[60]

More recently, our group has applied reverse micelles of polystyrene-*block*-polyacrylic

acid-*block*-poly(methyl methacrylate) (PS-*b*-PAA-*b*-PMMA) triblock copolymers as a colloidal template to form CdS NPs surrounded by a mixed brush of PS and PMMA chains that show structural environmental response to different solvent environments.[33] When the PMMA chains were then hydrolyzed to poly(methacrylic acid) (PMAA) chains, amphiphilic NPs were produced which self-assembled in aqueous solvent mixtures to form spheres, vesicles and unusual worm-like morphologies.[63] This triblock methodology allows only for mixed brushes with equal parts hydrophilic and hydrophobic polymer chains, and is not amenable to convenient variations in the composition of the mixed brush.

In Chapter 2 of this work, the synthesis and extensive characterization of amphiphilic CdS NPs surface-functionalized with mixed polymer brushes of variable composition (f_{PS} = 0.5, 0.7, 0.8 and 0.9) was described. The NPs were produced from colloidal templates of mixed reverse micelles formed from various coassembled blends of PS-*b*-PAA and poly(methyl methacrylate)-*block*-poly(acrylic acid) (PMMA-*b*-PAA), followed by core-crosslinking and hydrolysis of the PMMA brush chains to PMAA. In this chapter, we explore the amphiphilic self-assembly of these various NPs with different PS/PMAA brush compositions in mixed solvents of THF/water and characterize the resulting hierarchical colloidal assemblies. In addition to brush composition, we also look at the effect of initial NP concentration and salt addition on the resulting self-assemblies. Finally, we compile the extensive morphology data from multiple experiments into phase diagrams describing the rich and tunable morphological behaviour of this system.

3.2 Experimental

3.2.1 Self-Assembly of PS/PMAA-CdS NPs in Mixtures of THF and Water

The NP/polymer assemblies described in this chapter were produced using the following method. PS/PMAA-CdS NPs of variable brush composition (described in Chapter 2, summarized in Table 3.1) were dispersed in 2 g of THF (99.9+% HPLC grade, Sigma Aldrich, [H_2O] < 0.02 %) to initial concentrations of c_o = 0.25, 0.5 or 0.75 wt % PS/PMAA-CdS. For some experiments, 3.0 M NaCl (EMD, reagent grade) solutions in deionized water were added prior to self-assembly such that the ratio of NaCl to methacrylic acid repeat units was R_{NaCl} = 1.5 or R_{NaCl} = 3.0 (the added water in the salt solutions was taken into account when determining the cwc). The dispersions were set to a constant, rapid stirring rate as deionized water was added dropwise at a rate of 10 µL / 10 s. The point at which the solution became turbid was noted, as this cloud point indicates the critical water concentration (cwc) for self-assembly. Water addition was continued up to 75 wt %, at which point the aggregates that formed were assumed to be kinetically frozen based on previous work in the literature.[63] For most experiments, the dispersion was then poured immediately into 10 mL of deionized water, followed by dialysis against 500 mL of deionized water for 5 days to remove THF (dialysis tubing made of pre-wetted regenerated cellulose with a 50000 molecular weight cutoff of 50000 was supplied by Spectrum Labs.) Water was changed every hour for the first 4 hours, then after four hours before changing it every twelve hours for the remaining period. For annealing experiments, after water had been added dropwise to 75 wt %, dispersions were allowed to stir for 2 weeks before being quenched in 10 mL of deionized water, followed by dialysis against deionized 500 mL water for 5 days to remove THF. All solutions were covered in aluminum foil to protect against decomposition from light sources. For all experiments water was changed every hour for the first

4 hours, then after four hours before changing it every twelve hours for the remaining period. The stir rate of the stir plate was held constant for all experiments. The temperature in the room during self-assembly was measured as 22 °C ± 1 °C. Upon completion of dialysis, all samples were stored in a dark drawer.

Table 3.1. Hydrodynamic Radius (r_h), Aggregation Number (Z) and Chain Density (ρ_{chains}) for each Brush Composition of PS/PMAA-CdS in THF

f_{PS}	**Actual PS weight fraction**	**Z**	ρ_{chains} **(chains/nm^2)**	r_h **(nm)**
0.5	0.47	104 ± 1	0.48	350 ± 20
0.7	0.69	86 ± 9	0.43	109 ± 2
0.8	0.78	112 ± 2	0.49	92 ± 1
0.9	0.91	95 ± 9	0.48	78 ± 2

3.2.2 Transmission Electron Microscopy

TEM imaging was performed on a JEOL JEM-1400 electron microscope operating at an electron accelerating voltage of 80 kV. Following dialysis, various PS/PMAA-CdS assemblies were deposited from post-dialysis dispersions without dilution onto a carbon-coated 300 mesh copper grid; after waiting 2 minutes a Kimwipe was used to remove excess solvent then the grids were allowed to dry overnight at room temperature. Particle sizing was performed on images taken from multiple regions of the TEM grid; a minimum of 100 particles were measured for analysis of each sample.

3.2.3 Dynamic Light Scattering

DLS measurements were carried out on a Brookhaven Instruments photon correlator spectrometer equipped with a BI-200SM goniometer, a BI-900AT digital autocorrelator, and a Melles Griot He-Ne Laser (632.8 nm) with a maximum power output of 75 mW. In order to remove dust from scintillation vials, rigorous cleaning was applied before adding sample.

The scintillation vials were first washed with 5 mL of 95 % ethanol filtered through two poly(tetrafluoroethylene) (PTFE) filters with a 0.20 μm nominal pore size connected in series. The vials were then capped and vortexed for 30 seconds. The solvent was removed and the process was repeated 10 more times. Upon completion, the vials were covered with a piece of lens paper held on with an elastic band and placed upside down in an oven at 80°C for 2 days to remove solvent.

Any required dilutions were performed by adding known quantities of appropriate filtered solvent (solvent was filtered through two PTFE filters with a 0.20 μm nominal pore size connected in series). Unless otherwise stated, DLS measurements were conducted at a scattering angle of 90°. For each experiment, 3 repeat measurements of the autocorrelation function were obtained. All measurements were performed at 23 °C.

3.2.4 Laser Scanning Confocal Fluorescence Microscopy

Laser scanning confocal fluorescence microscopy measurements were carried out on a Zeiss LSM 410 equipped with an Ar/Kr laser. All solution films were excited at 488 nm, using a bandpass 485 ± 20 nm line selection filter and a FT 510 dichroic beam splitter. A long-pass 515 nm emission filter was employed such that only light above 515 nm reached the PMT. A Zeiss Plane-Aprochromat 63 x oil-immersion objective was employed. A pinhole diameter of 1.31

Airy Units was used for all measurements, resulting in an optical section thickness of 0.75 μm FWHM. Slides were prepared by placing 1 mL of post dialysis NP solution onto a glass slide. A cover slip was placed over top and was taped down to prevent motion.

3.3 Results and Discussion

3.3.1 Overview of PS/PMAA-CdS Self-Assembled Morphologies

A series of different morphologies were revealed when various PS/PMMA-CdS NPs of different brush compositions (f_{PS}) were self-assembled under different initial NP concentrations (c_0) and with prior addition of different amounts of salt (R_{NaCl}). This section will give a general structural overview of each of the observed morphologies with representative TEM images of each morphology. Observed morphologies arising from amphiphilic self-assembly of NPs include spheres, cylinders, vesicles, compound vesicles and large compound supermicelles, each of which have analogues among morphologies formed from self-assembly of amphiphilic block copolymers.[43,130,134,135]

Identification of each structure from TEM was based on several pieces of information. First, the structure of the pre-assembled NPs allows us to recognize that the use of a hydrophilic and hydrophobic polymer anchored to a CdS NP should lead to phase separation of the polymer blocks. Therefore, the CdS NPs should form the interface between hydrophobic and hydrophilic regions. Hydrophobic PS will likely be found inside the superstructure, while hydrophilic PMAA will be found on the corona or in internal pockets, or lumens, where H_2O can be found.

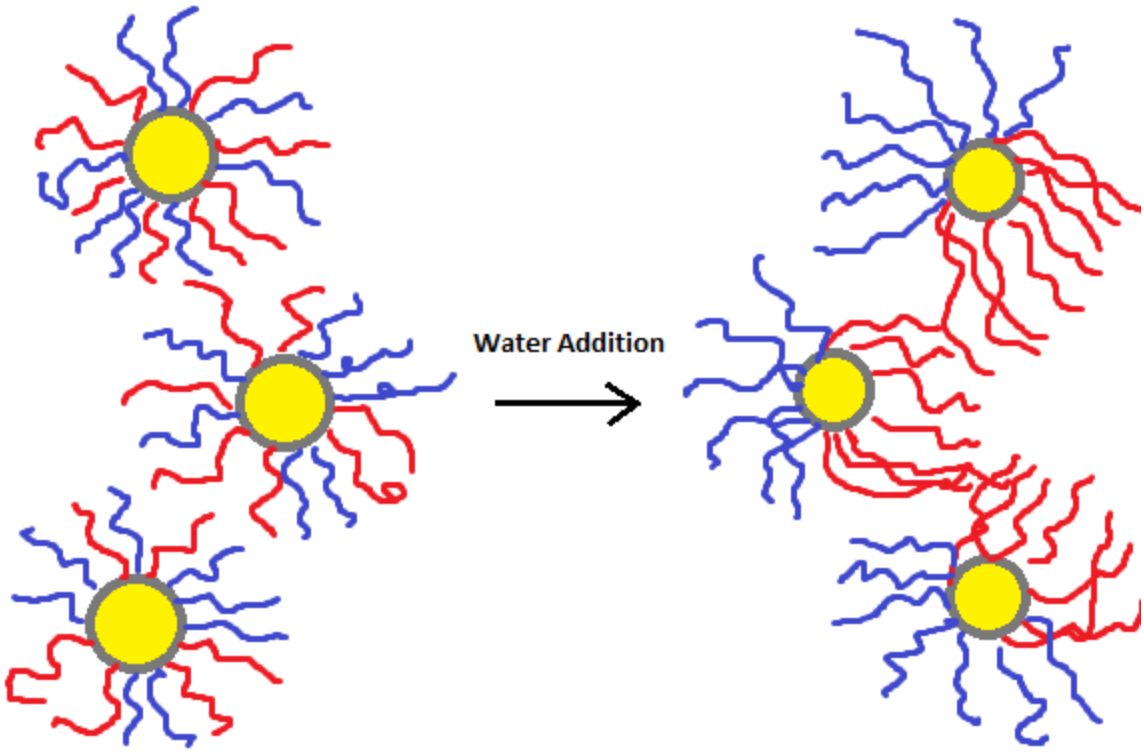

Figure 3.1. Schematic detailing the phase separation of PS and PMAA polymer chains when solution changes from THF to H_2O. The NPs form the interface between each region.

TEM imaging is a powerful tool for determining the structure of polymeric and polymer/nanoparticle composite colloids. TEM shows regions of high electron density as dark regions and low electron density as light regions. CdS is the most electron-rich component of the NPs and given their expected location at the interface between hydrophobic and hydrophilic regions create dark interfaces around the periphery and sometimes within the assemblies. PS is less electronic dense than CdS and condensed hydrophobic PS regions appear as either gray or black depending on the thickness of the PS region (and thus the pathlength of the electron beam). PMAA is much less electron dense than PS and presents as light regions.

3.3.1.1 Spheres

The assembly morphology with the highest internal curvature is the sphere (Figure 3.2). Spheres consist of a spherical filled core of PS chains protected from the aqueous environment by a coronal layer of PMAA chains. The CdS QDs must therefore assemble at the core surface that is found at the interface between the two polymer chains. Figure 3.2 A) shows a schematic of a sphere formed from self-assembled PS/PMMA-CdS while B) shows a representative TEM image of spheres. In most cases the dense packing of QDs appears as a dark contiguous ring around the PS cores in the two dimensional projection of these three dimensional structures; however, some individual QDs can also be identified from the images.

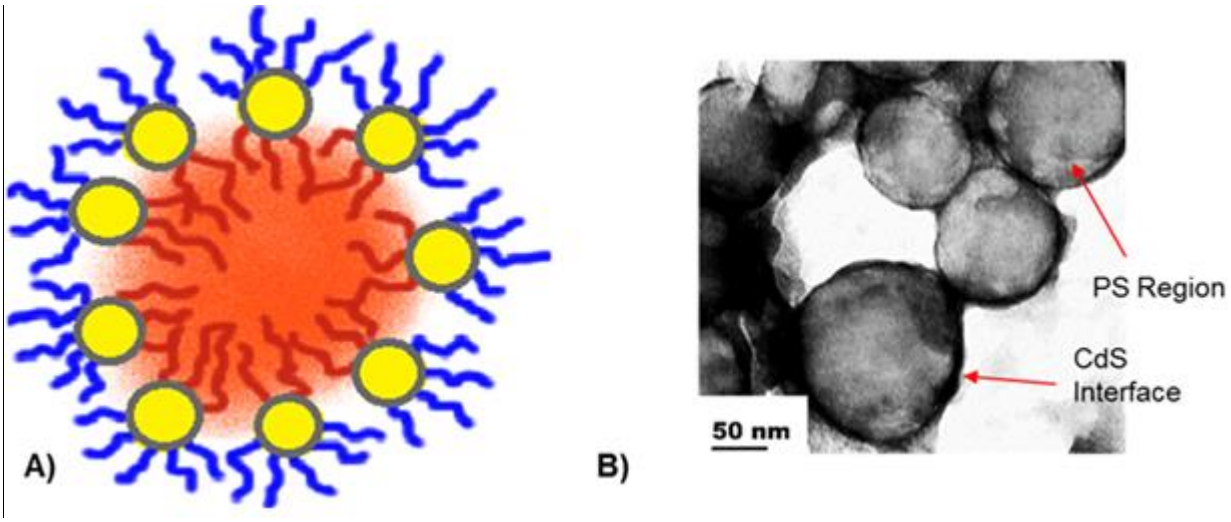

Figure 3.2. A) Schematic representing a spherical PS/PMAA-CdS assembly. B) Representative TEM image of spheres formed from the self-assembly of PS/PMAA-CdS (f_{PS} = 0.5) with c_0 = 0.25 wt % and R_{NaCl} = 0 (no salt added).

3.3.1.2 Cylinders

We also observed NP assemblies best described as cylinders, with large aspect ratios (> 2:1) (ratio between length and width). Cylinders have an intermediate internal curvature, lower than spheres but higher than vesicles. The inside NP cylinders consist of a filled cylindrical core of hydrophobic PS chains decorated on the outside by a coronal layer of hydrophilic PMAA chains. Again, CdS QDs are packed at the PS/PMMA interface over the surface of the cylindrical PS cores. The formation of a cylindrical shape decreases internal curvature relative to spheres, allowing a greater packing density of amphiphilic NPs. The structure of the cylinder morphology and a corresponding TEM image is described in Figure 3.3.

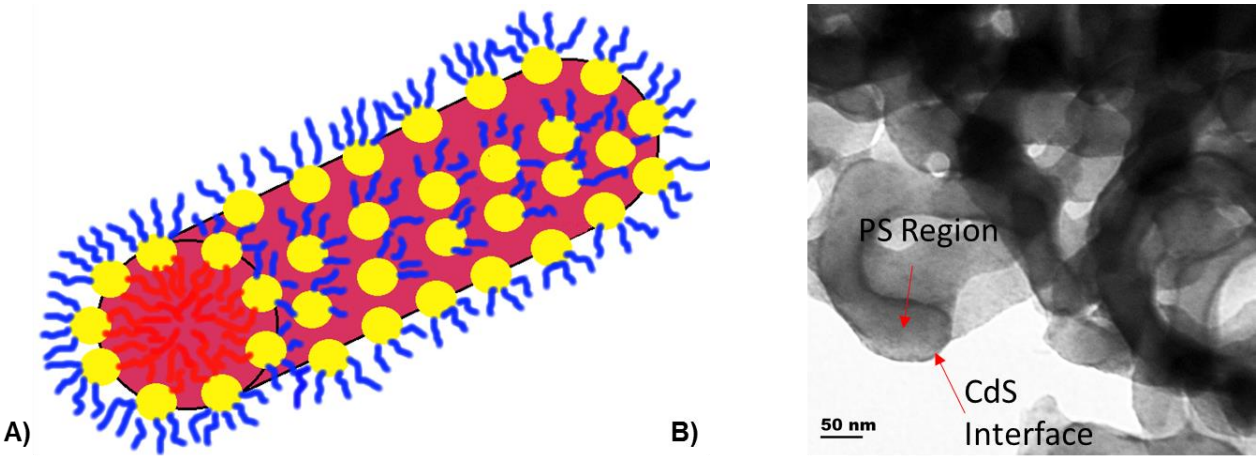

Figure 3.3. A) Schematic representing a cylindrical PS/PMAA-CdS assembly. B) Representative TEM image of cylinders formed from the self-assembly of PS/PMAA-CdS (f_{PS} = 0.5) with c_0 = 0.50 wt % and R_{NaCl} = 1.5.

3.3.1.3 Vesicles

We also observed vesicular NP assemblies, analogues of vesicles formed from self-assembly of block copolymers or phospholipids. Vesicles are spherical low-internal curvature bilayer structures consisting of inward-pointing PS chains making up the vesicle wall. The wall encapsulates a water-containing lumen with PMMA chains extending from both internal and external surfaces of the wall. CdS QDs are arranged in two concentric layers as they pack at each of the two PS/PMMA interfaces (internal and external). A vesicle has less internal curvature than both cylinders and spheres which further decreases the steric interactions between PS chains allowing denser packing of NPs. A schematic of a vesicle and a representative TEM image of vesicles can be found in Figure 3.4.

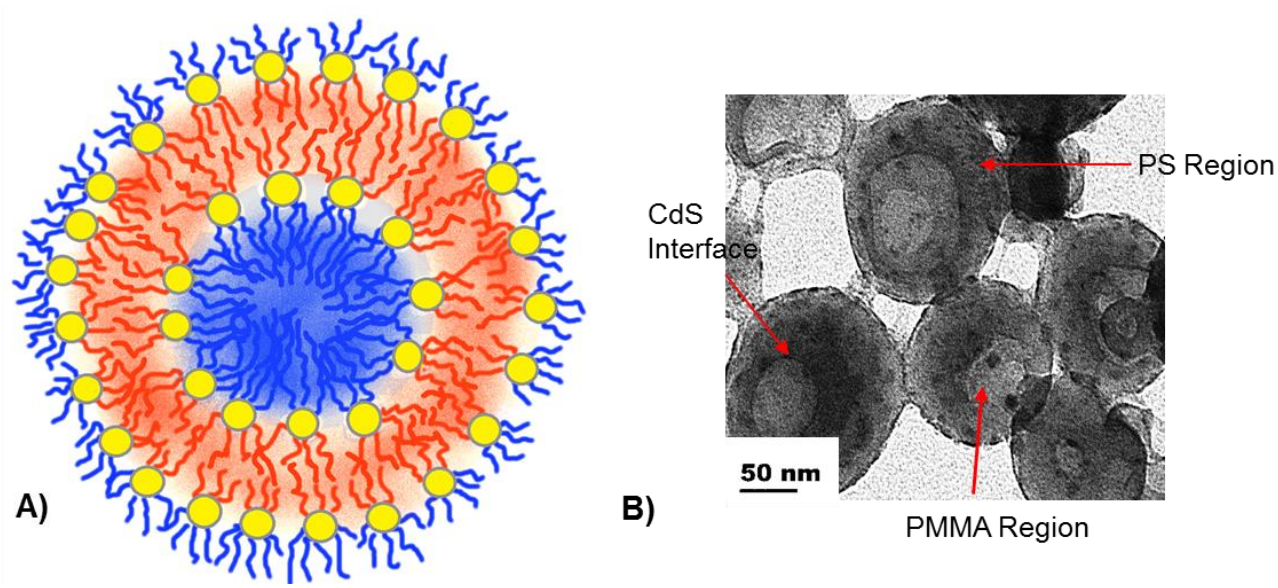

Figure 3.4. A) Schematic representing a PS/PMAA-(CdS) vesicle. B) Representative TEM image of vesicles formed from the self-assembly of PS/PMAA-(CdS) (f_{PS} = 0.8) with c_0 = 0.50 wt % and R_{NaCl} = 0 (no salt added).

3.3.1.4 Compound Vesicles

A compound vesicle is similar to a vesicle but with multiple smaller lumens within the assembly. The multiple lumens are surrounded by high-curvature convex surfaces which increase the free volume for PS chains and decrease their steric interactions relative to simple vesicles, at the cost of increasing the crowding of PMMA chains on the concave side of the interface. It has been suggested by Eisenberg[130] that compound vesicles of block copolymers are a kinetic structure as opposed to a thermodynamic structure. It is believed that they are formed from many vesicles that normally fuse together. But if the rate of collision between vesicles is faster than the rate of fusion, multiple lumen may be present. In this work, we suggest that compound vesicles of PS/PMAA-(CdS) are thermodynamically stable structures, as they are found in solution after annealing, but further experimentation is needed to fully deem whether they are a separate thermodynamically-driven morphology or a kinetic structure en route to vesicles. A schematic and representative TEM image of a large compound vesicle can be found in Figure 3.5.

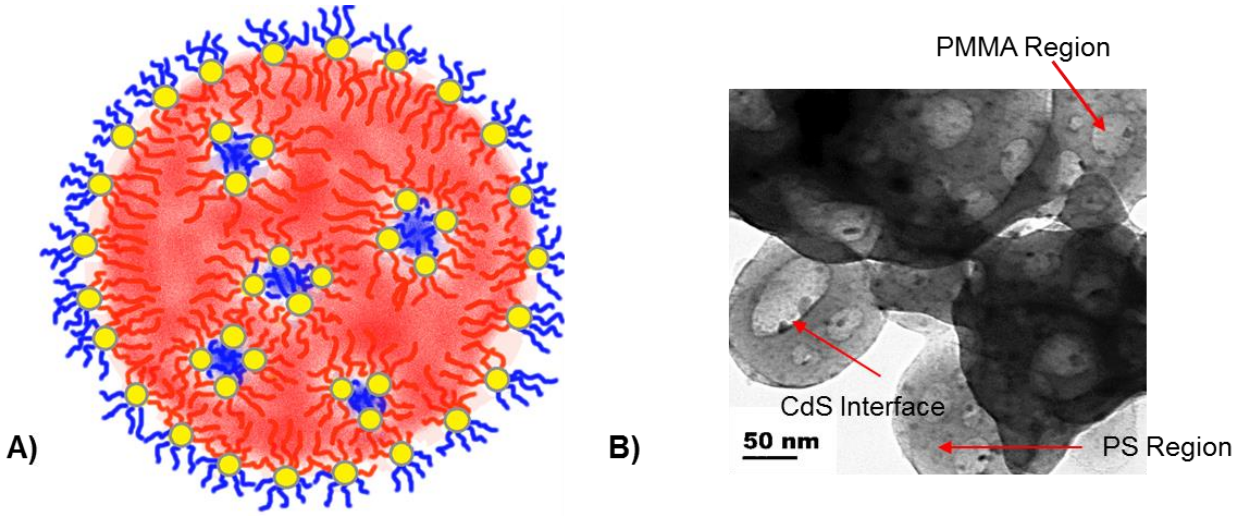

Figure 3.5. A) Schematic representing a PS/PMAA-(CdS) large compound vesicle. B) Representative TEM image of compound vesicles formed from the self-assembly of PS/PMAA-(CdS) (f_{PS} = 0.8) with c_0 = 0.75 wt % and R_{NaCl} = 0 (no salt added).

3.3.1.5 Large Compound Supermicelles

The final self-assembled morphology observed in our experiments is the large compound supermicelle, analogous to the large compound micelles (LCMs) of block copolymers described first by Eisenberg and coworkers[134]. As represented in the schematic, these particles are best described as roughly spherical aggregates of individual NPs each with collapsed PMAA chains and PS chains forming the hydrophobic matrix of the particle interior; the periphery of the aggregate is lined with a stabilizing layer of NPs with PS chains pointing inward and PMAA chains pointing outwards and providing colloidal stability. These aggregates represent the highest convex surface area for PS chains and thus the minimum steric crowding for PS chains of all the described morphologies in this section. A schematic and representative TEM image of a large compound supermicelle can be found in Figure 3.6.

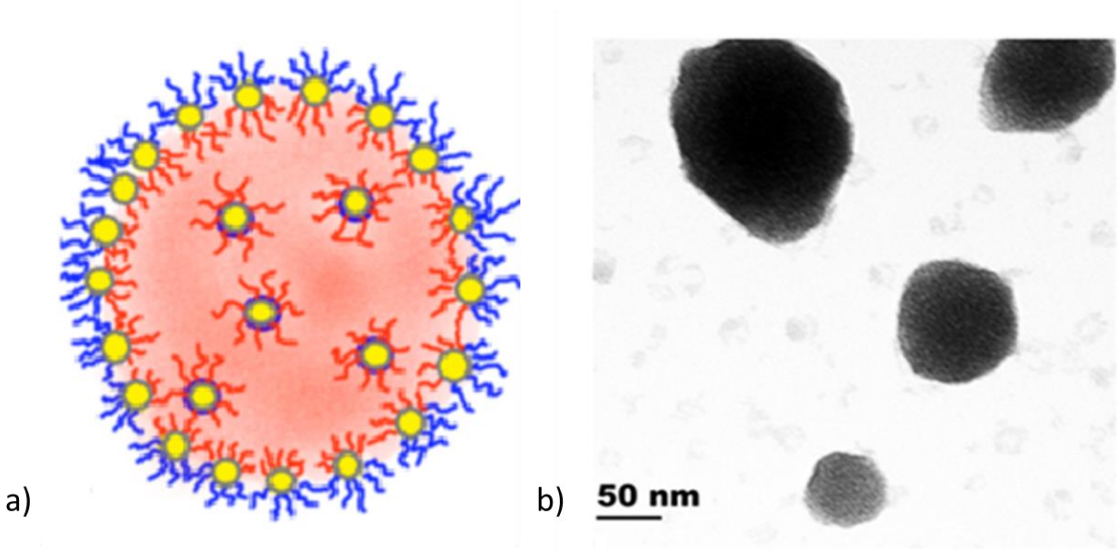

Figure 3.6. A) Schematic representing a PS/PMAA-(CdS) large compound supermicelle. B) Representative TEM image of large compound supermicelles formed from the self-assembly of PS/PMAA-(CdS) (f_{PS} = 0.9) with c_0 = 0.50 wt % and R_{NaCl} = 1.5.

In summary, an important driving force for morphological change is the relaxation of steric crowding of PS chains through changes in interfacial curvature. This depends on the curvature of the interface from which the PS chains radiate (concave or convex, and magnitude of curvature). Thus, for the assemblies described so far, the morphologies can be ranked in order of decreasing steric crowding of PS chains:

Spheres (*high concave curvature*) > Cylinders (*intermediate concave curvature*) > Vesicles (*low concave curvature*) > Compound Vesicles (*intermediate convex curvature*) > Large Compound Supermicelles (*high convex curvature*)

3.3.1.5 Unimicellar Dots

Under some conditions, discussed below, NP self-assembly does not occur above the critical water content. Instead, the PS chains on individual amphiphilic NPs collapse to form a condensed core with a single CdS QD at its center. These hydrophobic spherical unimicellar cores are then stabilized in water by the remaining hydrophilic PMAA chains extending into the aqueous environment. A schematic and representative TEM image of a unimicellar dots are shown in Figure 3.7.

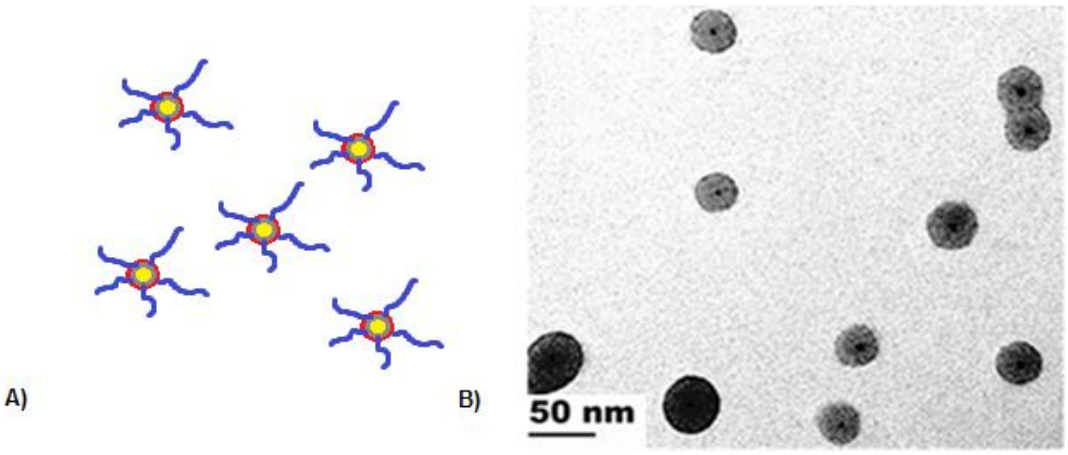

Figure 3.7. A) Schematic representing a PS/PMAA-(CdS) unimicellar dot. B) Representative TEM image of unimicellar dots formed from PS/PMAA-(CdS) (f_{PS} = 0.9) with c_0 = 0.50 wt % and R_{NaCl} = 0 (no salt added).

3.3.2 Mixed Morphologies and Annealing Experiments

Most of the self-assembly experiments described below gave rise to a single or strongly dominant morphology. However, there were a few exceptions in which multiple morphologies were present. For example, when f_{PS} = 0.8, c_0 = 0.50 wt % and R_{NaCl} = 0, all three morphologies of spheres, vesicles, and compound vesicles were found when the dispersion was quenched into excess water immediately upon reaching a water concentration of 75 wt % by dropwise addition (Figure 3.8 A).

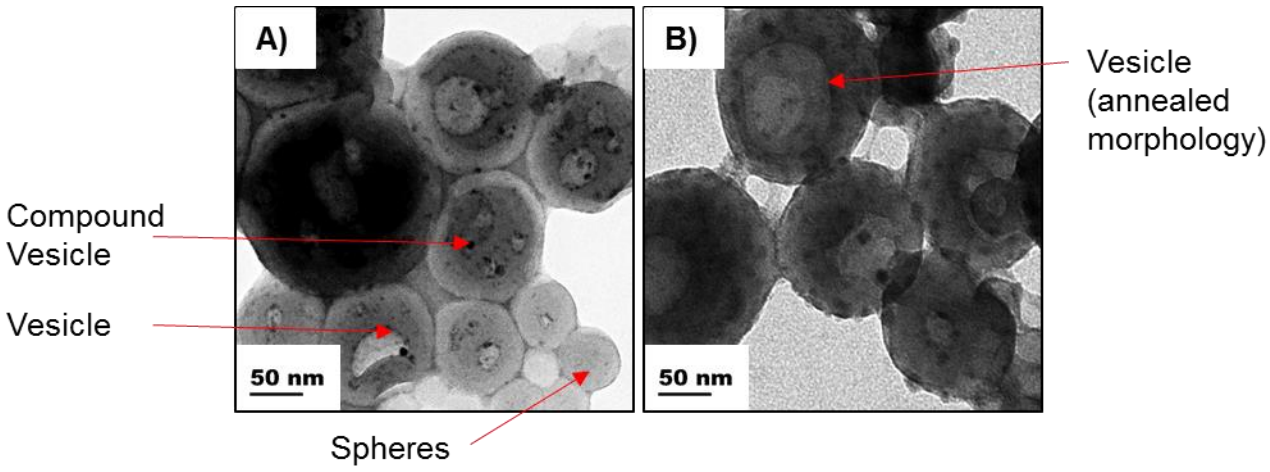

Figure 3.8. Schematic depicting the morphologies assembled at f_{PS} = 0.8, c_0 = 0.50, R_{NaCl} = 0.0 A) with immediate quenching and B) with two week annealing period before quenching.

There are two possible explanations for this. The first is that these conditions represent a triple point arising from the intersection of phase boundaries between all three morphologies. The second more likely possibility is that during the self-assembly process several morphologies became kinetically frozen before reaching equilibrium. Therefore to determine the true equilibrium morphology in such cases, NPs were self-assembled under identical conditions except the quenching step was delayed for two weeks in order to allow the structures to reach equilibrium. For example, examination of the TEM results from the f_{PS} = 0.8, c_0 = 0.50 wt % and R_{NaCl} = 0 self-assembly experiment after two weeks annealing showed that two of the three morphologies in the original mixture had given way to a population of pure vesicles (Figure 3.8B) indicating that vesicles are the equilibrium morphology under these conditions. Other cases showing the effect of annealing on mixtures of morphologies are also shown in Figure 3.9. In the cases represented in Figure 3.9, the morphology obtained after two weeks annealing is the one presented when discussing the various trends in the following sections and in subsequent phase diagrams.

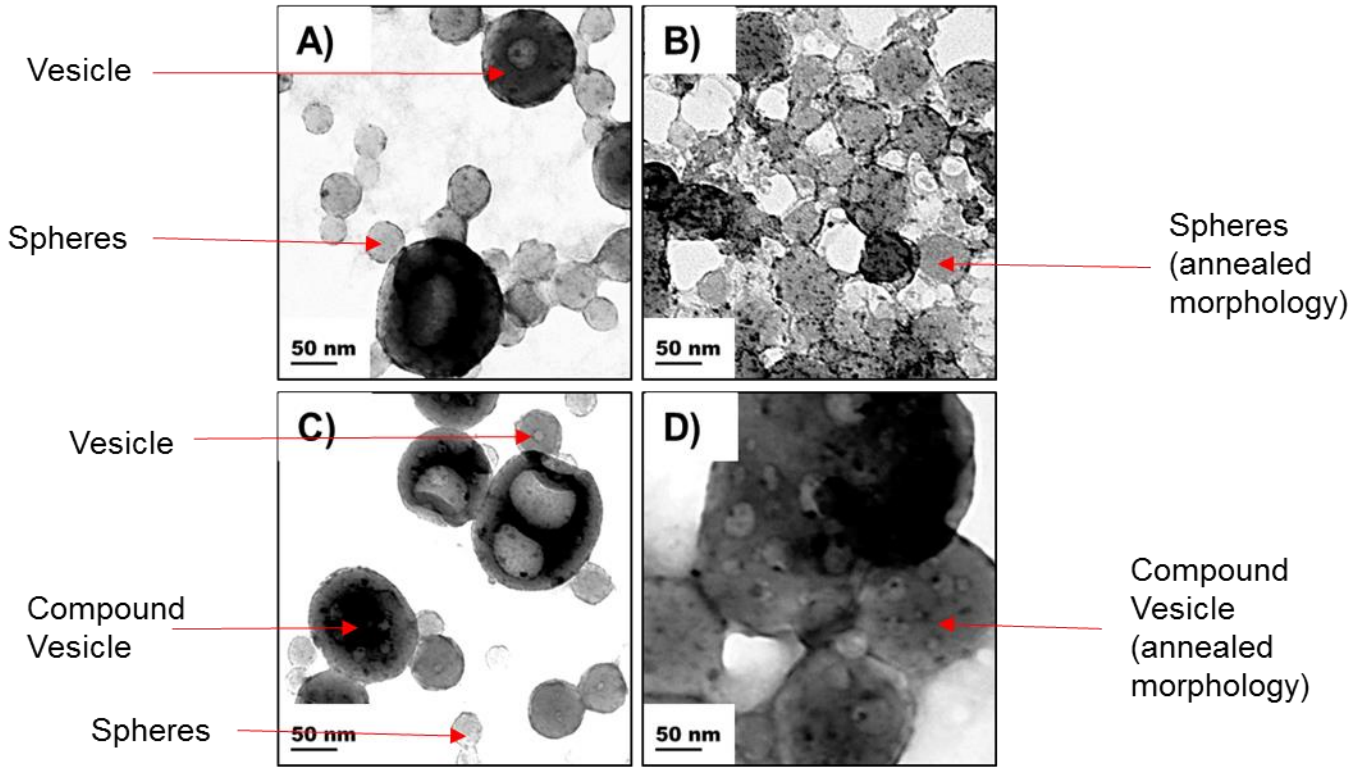

Figure 3.9. TEM images showing the morphologies found when f_{PS} = 0.5 was assembled with c_0 = 0.50, R_{NaCl} = 0.0 A) with immediate quench and B) with annealing. TEM images also show f_{PS} = 0.8, c_0 = 0.75, R_{NaCl} = 0.0 C) with immediate quench and D) with annealing.

3.3.3 Measurement of the Critical Water Concentration

During each self-assembly experiment, the critical water concentration (cwc) was determined visually when the clear solutions became turbid upon addition of water. These results can be found in Table 3.2. As each experiment was performed only once these are only roughly estimated values.

Table 3.2 Critical Water Concentrations (wt % water) Determined from the Addition of Water to a Solution of PS/PMAA-(CdS) in THF

R_{NaCl}	c_o	f_{PS} = 0.5	f_{PS} = 0.7	f_{PS} = 0.8	f_{PS} = 0.9
0.0	0.25	~11	~9	~14	~12
	0.50	~10	~8	~12	~10
	0.75	~7	~7	~11	~7
1.5	0.25	~11	~12	~11	~9
	0.50	~12	~12	~12	~11
3.0	0.25	~13	~9	~11	~9
	0.50	~13	~10	~12	~12

Perhaps surprisingly, the cwc values appear to show no clear trend with brush composition or salt addition. However, increasing c_0 appears to decrease the cwc when no salt is present, indicating a stronger driving force for self-assembly.

3.3.4 Effect of Brush Composition (f_{PS}) on Amphiphilic Self-Assembly of NPs

The ability to vary the brush composition on the surface of amphiphilic NPs allows us to explore the effect on self-assembly as NPs go from a symmetric composition (f_{PS} = 0.5) to being increasingly hydrophobic (f_{PS} = 0.7, 0.8 and 0.9). Figure 3.10 presents TEM images of the assemblies resulting from self-assembly of each NP brush composition when water is added to an NP dispersion with a constant initial concentration of c_0 = 0.50 wt %.

From the figure, we see that spheres are formed when the brush composition is symmetric (f_{PS} = 0.5, Figure 3.10A), whereas under the same self-assembly conditions a more hydrophobic brush forms vesicles (f_{PS} = 0.7, Figure 3.10B). Vesicles are also observed when the PS content of the brush increases further to f_{PS} = 0.8 (Figure 3.10C). Finally, at the highest PS content of the brush (f_{PS} = 0.9), unimicellar dots are formed (Figure 3.10D).

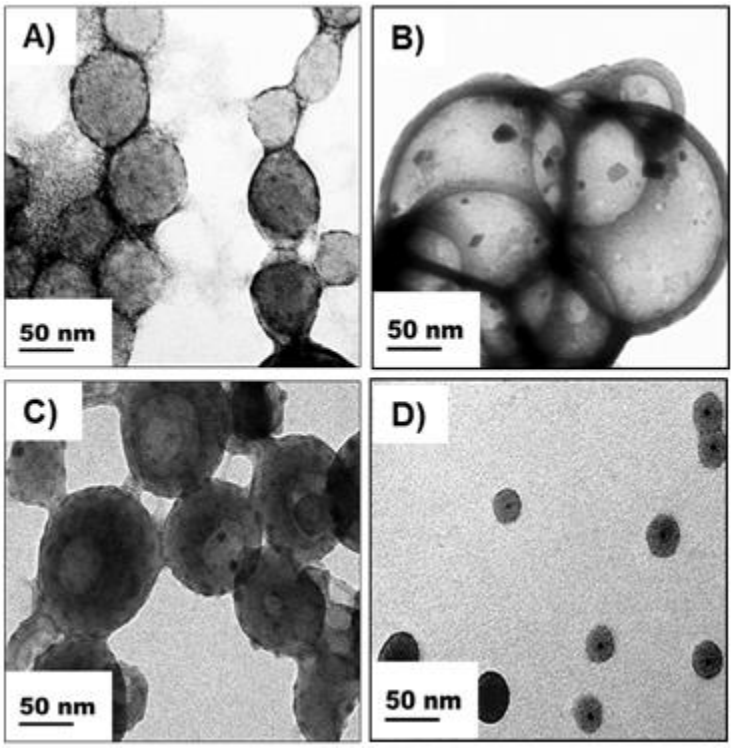

Figure 3.10. Representative TEM images of the assemblies formed from PS/PMAA-(CdS) f_{PS} = A) 0.5 B) 0.7 C) 0.8 and D) 0.9 with c_0 = 0.50 wt % and R_{NaCl} = 0 (no salt added).

As the PS content of the brush increases relative to the PMAA content, the general trend appears to be the transition from higher curvature assemblies (spheres) to lower curvature assemblies (vesicles). Interestingly, an identical trend has been found for amphiphilic block copolymers as the length of the hydrophilic block decreases relative to the length of the hydrophobic block. For example, Zhang *et al.* found that when the length of the PAA block decreased relative to the PS block, micellar aggregates of PS-*b*-PAA transitioned from spheres, to cylinders, to vesicles.[134] Similar to the block copolymer system, in the current case of amphiphilic NP self-assembly this trend can be understood by the increasing relative contribution of PS stretching to the free energy of the system as the PS composition increases; this effects a lowering of the internal curvature which decreases the steric crowding of PS chains

and lowers their stretching along with the associated entropic penalty. An exception to this trend appears to be the f_{PS} = 0.9 case, in which case an intraparticle conformational rearrangement leading to unimicellar dots appears to be thermodynamically favoured over interparticle self-assembly. The reason for unimicellar dot formation is not completely understood, although one possible explanation is that the small number of hydrophilic PMAA chains relative to hydrophobic PS chains in the f_{PS} = 0.9 brush would require an extremely dense packing of NPs at the interface upon self-assembly, which would lead to excessive repulsion between PMMA chains on neighboring NPs; instead, the PS chains on individual NPs collapse to minimize their exposure to water, allowing the few PMAA chains to surround and protect any exposed PS segments. We will see later that salt addition can induce self-assembly of the f_{PS} = 0.9 NPs, forming various morphologies through screening of electrostatic interactions, which is consistent with the above explanation for unimicellar dot formation in the absence of salt.

We note that a very similar general trend with respect to NP brush composition is found for self-assembly at a higher initial NP concentration of c_0 = 0.75 wt % (Figure 3.11). In this case, the NPs with the lowest PS content form vesicles (f_{PS} = 0.5, Figure 3.11A), whereas when the PS content increases to f_{PS} = 0.7 and 0.8, the formation of compound vesicles provides interfaces at which steric crowding of PS chains is relaxed relative to vesicles (Figure 3.11, B and C respectively). Finally, when the PS content increases to f_{PS} = 0.9, unimicellar dots are again formed instead of interparticle assemblies (Figure 3.11D), similar to the c_0 = 0.50 wt % case.

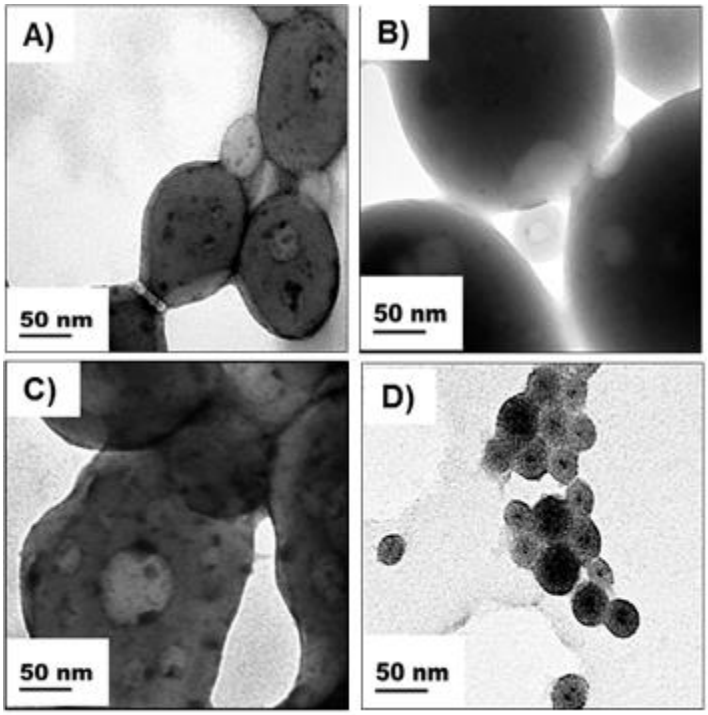

Figure 3.11. Representative TEM images of the assemblies formed from PS/PMAA-(CdS) f_{PS} = A) 0.5 B) 0.7 C) 0.8 and D) 0.9 with c_0 = 0.75 wt % and R_{NaCl} = 0 (no salt added).

The composition of the polymer brush plays a key role in determining the morphology that appears upon self-assembly. The dual hydrophilic/hydrophobic nature of the NP brush leads to intraparticle phase separation of the two polymer brushes as water is added (Janus particle conformation, Figure 3.13) followed by interparticle phase separation above the cwc (self-assembly), leading to PS and PMAA domains with QDs localized at the interface.

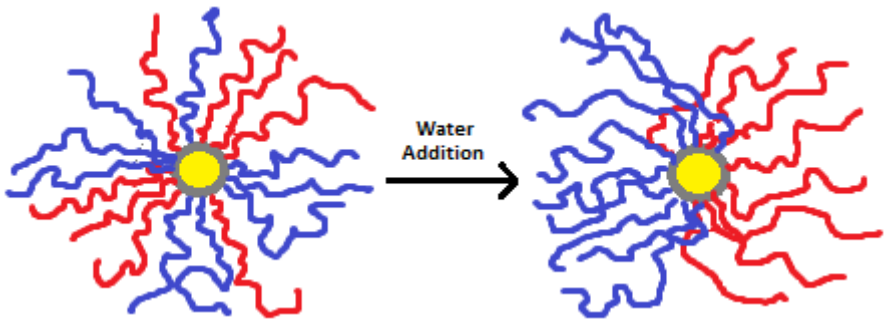

Figure 3.12. Depiction of intraparticle phase separation to form a Janus particle confirmation as water is added to dispersions of PS/PMAA-CdS in THF.

Changes in brush composition will affect the relative number of chains in the corona and in the core of any self-assembly product (spheres, cylinders, vesicles, etc.). NPs with a higher f_{PS} will have a greater amount of PS chains located inside the core, while less PMAA can be found on the corona to facilitate dispersability. Depending on the surface that these polymers are located, repulsive effects from chain stretching and surface crowding will affect the free energy of the particle. As shown in Figure 3.13, concave surfaces induce greater repulsive interactions between radiating chains (less free volume) while convex promote lower repulsive interactions (more free volume).

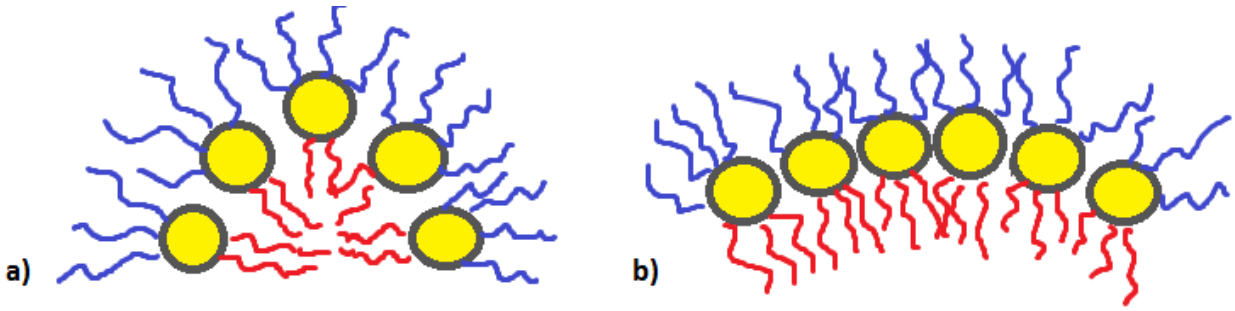

Figure 3.13. Comparison of chain interactions that occur at A) high curvature and B) low curvature

As the f_{PS} increases, the increased hydrophobicity of the NPs requires a denser packing of NPs at the interface, leading to increased stretching of PS chains. If the PS chains are located on a concave surface, steric interactions between polymer chains will require greater chain extension, incurring a larger entropic free energy penalty. In order to relax these steric interactions, a change to a lower curvature interface becomes favourable, allowing PS chains to become less extended without lowering the packing density of NPs. This explains changes in morphology from spheres to vesicles, for instance, as f_{PS} increases. Of course, any change in interfacial curvature that decreases repulsive interactions between PS chains will increase repulsive interactions between PMAA chains on the other side of the interface; therefore, a morphology change is only expected if the overall effect is a lowering of the free energy.

3.3.5 Effect of Initial PS/PMAA-(CdS) Concentration (c_0) on Amphiphilic Self-Assembly of NPs

While the composition of the polymer brush is one variable of interest for the self-assembly of these NPs, another easily controlled variable is the initial PS/PMAA-(CdS) concentration, c_0, before self-assembly. This is also a variable known to affect the morphologies arising from the self-assembly of block copolymers in solution,[43,123] and so it was of interest to

determine its effect on the amphiphilic self-assembly of our NPs. Three initial concentrations were selected for experimentation: c_0 = 0.25, 0.50 and 0.75 wt %. Except for the f_{PS} = 0.9 NPs, which formed unimicellar dots at all initial concentrations, each NP brush composition showed morphological differences as the initial concentration increased. To illustrate this point, we show morphologies formed from f_{PS} = 0.7 NPs for all three initial concentrations in Figure 3.14.

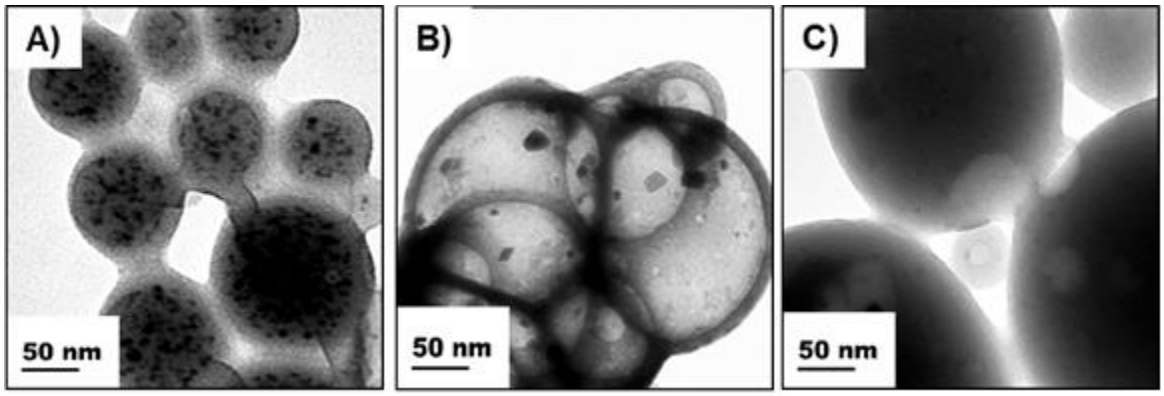

Figure 3.14. Representative TEM images of the assemblies formed from PS/PMAA-(CdS) f_{PS} = 0.7 with c_0 = A**)** 0.25 B) 0.50 C) 0.75 wt % and R_{NaCl} = 0 (no salt added).

As shown in Figure 3.14 A, spheres formed from f_{PS} = 0.7 NPs when the initial concentration was c_0 = 0.25 wt %. On the other hand, the same NPs formed vesicles from a higher initial concentration of c_0 = 0.50 wt % (Figure 3.14 B). Finally, at the highest investigated initial concentration of c_0 = 0.75 wt %, compound vesicles were formed (Figure 3.14 C). These data suggest a trend from a high-concave curvature interface for the PS chains (spheres), to a low-concave curvature interface (vesicles), to an intermediate-convex curvature interface (compound vesicles) as the initial concentration increases. This is explained by the increase in the thermodynamic driving force for self-assembly, obviated by the lower cwc values (Table 3.2), as the initial PS/PMAA-(CdS) concentration increases. Previous work has been done to

determine the effect of c_o on the self-assembly of diblock copolymer systems. Eisenberg *et al.* has shown that increasing c_o leads to an increase in aggregation number in NPs as described by Equation 3.1.[43]

$$N_{agg} = 2(\frac{c_o}{cwc})^{\frac{1}{2}} \qquad \text{(Equation 3.1)}$$

where N_{agg} is the aggregation number. Higher aggregation numbers and denser packing of NPs at the interface are the result of a strong self-assembly driving force. This in turn increases stretching of PS chains and an increased entropic penalty to the free energy. Thus, the described changes in morphology occur to allow steric crowding (and thus stretching) of PS chains to be reduced without lowering the packing density of NPs at the interface. Very similar trends have been previously shown for block copolymer self-assembly, underlining the similar driving and regulating forces for self-assembly in the current system.

3.3.6 Effect of Salt Addition on Amphiphilic Self-Assembly of NPs

The purpose of adding NaCl to the self-assembly solutions is to screen the negative charge that is generated upon water addition as PMAA deprotonates, and thus decrease the repulsive interactions between the chains. Self-assembly experiments were carried out at three different salt contents (including no salt): R_{NaCl} = 0, 1.5 and 3.0 (where R_{NaCl} refers to the molar ratio of NaCl to MAA repeat units). Morphologies arising from all self-assembly conditions in the presence of NaCl are described in connection with the phase diagrams presented in the next section. However, here we discuss the effect of salt addition by considering the morphologies formed by two different NP samples, f_{PS} = 0.7 and f_{PS} = 0.9, both at initial concentrations of c_0 = 0.25 wt %, for the three different cases of salt addition: R_{NaCl} = 0, 1.5 and 3.0.

We first consider the effect of salt addition on the self-assembly of f_{PS} = 0.7 NPs. When no salt is present during self-assembly (R_{NaCl} = 0, Figure 3.15A), spherical assemblies are formed. On the other hand, addition of salt at a ratio of R_{NaCl} = 1.5 gives rise to vesicles (Figure 3.15B); a higher concentration of salt, R_{NaCl} = 3.0, leads to the formation of compound vesicles (Figure 3.15C). This trend can be explained by Na^+ cations screening electrostatic repulsion between negatively-charged PMAA chains in solution. These repulsive interactions counteract the driving forces for self-assembly by limiting the packing density of NPs at the interface; when these repulsive contributions are screened by salt, the packing density thus increases, effecting curvature changes to minimize steric interactions between PS chains. The observed transition of PS chains from a high-concave curvature interface (spheres, Figure 3.15A) to a low-concave curvature interface (vesicles, Figure 3.15B) to an intermediate-convex curvature interface (compound vesicles, Figure 3.15C) is thus consistent with the increased screening effect of increased salt concentration. Interestingly, similar morphology transitions have been effected by salt addition to self-assembling PS-*b*-PAA block copolymers in aqueous media,[126] further suggesting that general self-assembly principles translate well between the macromolecular and the colloidal amphiphiles.

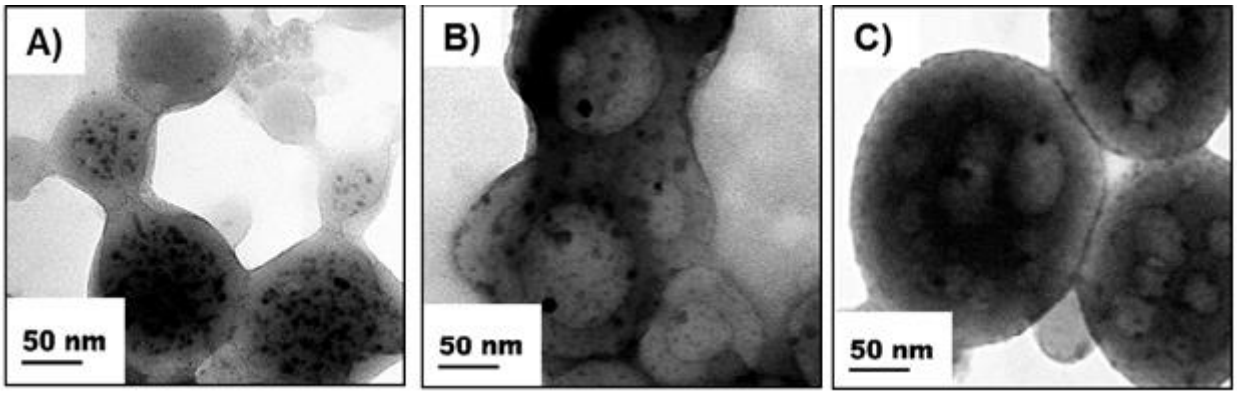

Figure 3.15. Representative TEM images of the assemblies formed from PS/PMAA-(CdS) f_{PS} = 0.7 with c_0 = 0.25 wt % and R_{NaCl} = A) 0.0 B) 1.5 C) 3.0

Similar effects of salt addition are found for the self-assembly of f_{PS} = 0.9 NPs, except, as discussed previously, in the absence of salt these colloids formed unimicellar dots rather than self-assembling into higher order colloidal objections (Figure 3.16 A). However, when salt is added to ratio of R_{NaCl} = 1.5, self-assembly does occur and gives rise to vesicles (Figure 3.16 B), with higher salt addition also forming vesicles (R_{NaCl} = 3.0, Figure 3.16 C). As discussed previously, this suggests that unimicellar dot formation from f_{PS} = 0.9 NPs occurs due to preclusion of self-assembly by repulsive interactions between PMAA chains; in this case, the introduction of screening by even a small concentration of Na^+ ions relaxes this thermodynamic constraint, allowing self-assembly into vesicles to occur.

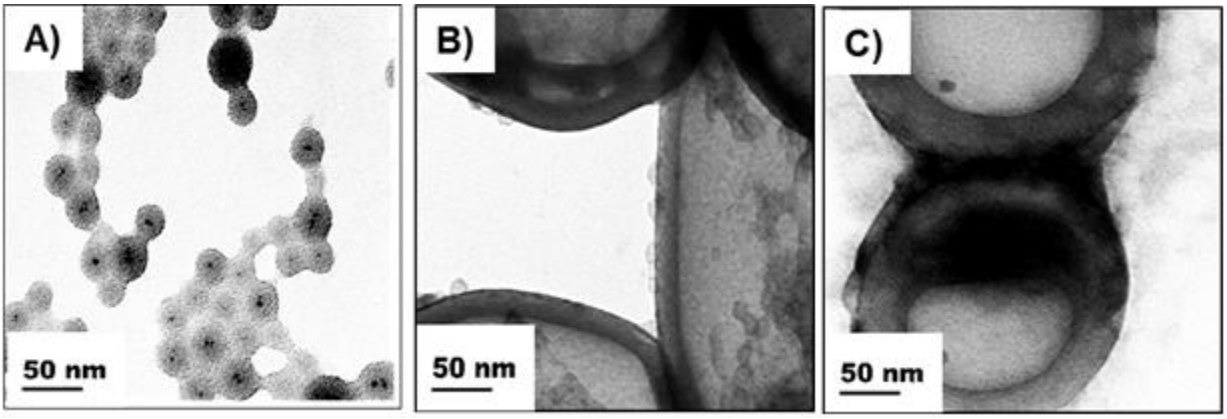

Figure 3.16. Representative TEM images of the assemblies formed from PS/PMAA-(CdS) f_{PS} = 0.9 with c_0 = 0.25 wt % and R_{NaCl} = A) 0.0 B) 1.5 C) 3.0

3.3.7 Phase Diagrams of PS/PMAA-(CdS) in THF/Water

The large number of variables for PS/PMAA-(CdS) self-assembly explored in this work allow rough phase diagrams to be mapped out, which effectively illustrate the range of morphological control in this system. While more data points are required to determine the exact location of phase boundaries, the phase boundaries represented in the various initial NP concentration (c_0) vs. PS brush fraction (f_{PS}) diagrams below represent good approximations from our current data set. We choose to represent salt dependence using separate c_0 - f_{PS} phase diagrams for each of the three different R_{NaCl} values (including no salt).

Figure 3.17 shows the resulting phase diagram and accompanying TEM data for PS/PMAA-(CdS) self-assembly in THF/water without added salt (R_{NaCl} = 0). In the presented phase diagram (Figure 3.17), the morphological trends with respect to brush composition f_{PS} and c_o can be visualized quite clearly. Spheres (red region) appear under low NP concentration and low PS content, vesicles (blue region) are found at more intermediate NP concentrations and PS

content and compound vesicles (purple region) appear at high NP concentration and PS content; however, when the brush composition is too rich in PS (f_{PS} = 0.9), the only morphology observed at all NP concentrations are unimicellular dots (yellow region). This unimicellar dot phase region reflects the previous observation that the extremely hydrophobic brush composition cannot sustain larger morphologies in an environment without NaCl addition.

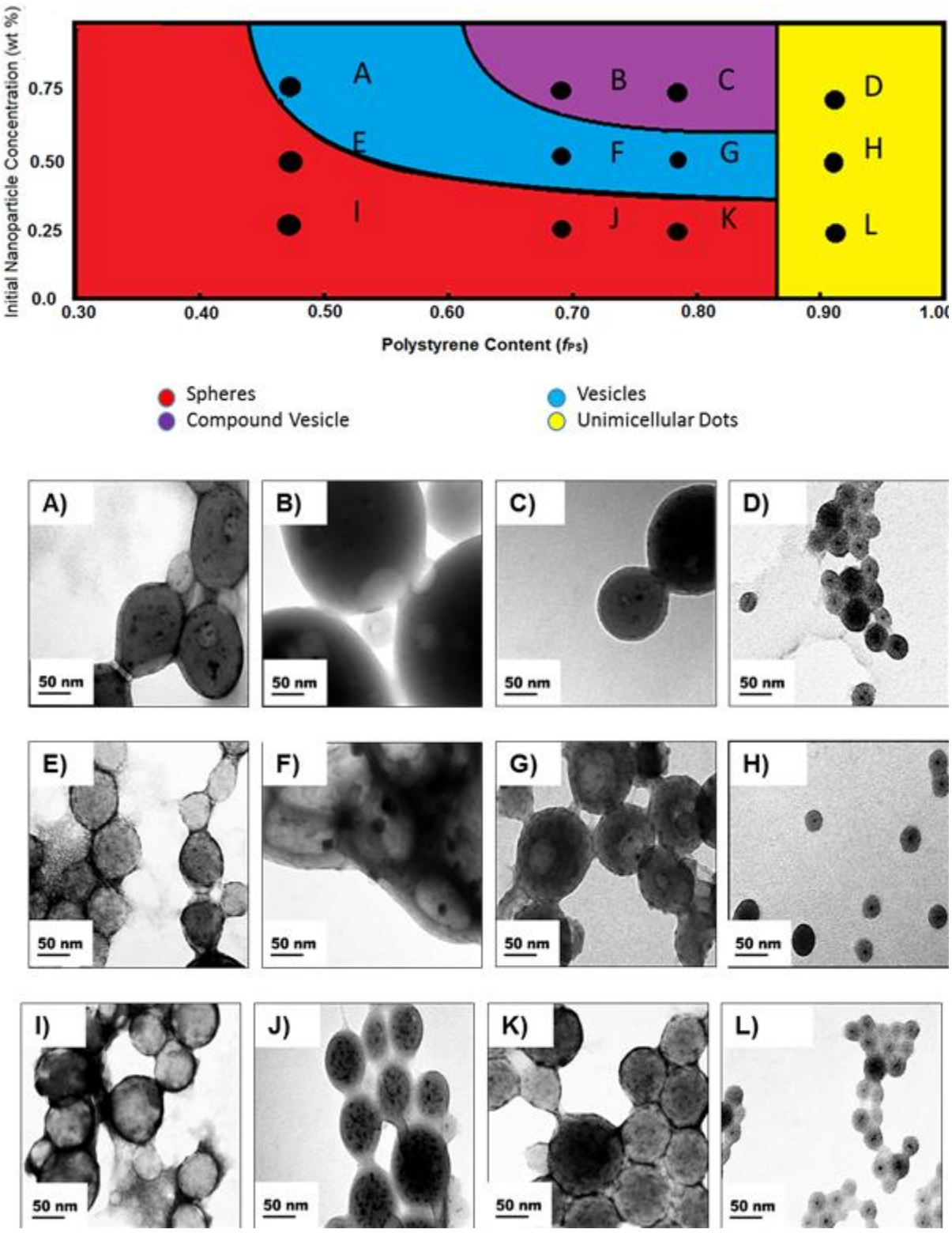

Figure 3.17 Phase diagram comparing brush composition with c_o when no salt is added. Each number is related to a representative TEM image found below.

As discussed in the previous section, the presence of salt during self-assembly has a profound effect on the resulting morphologies due to screening of repulsive interactions between PMAA chains. Figure 3.18 shows the resulting phase diagram and accompanying TEM data for PS/PMAA-(CdS) self-assembly in THF/water with added salt at a ratio of $R_{NaCl} = 1.5$. Compared to the $R_{NaCl} = 0$ phase diagram, the data points here are even more limited, as self-assembly experiments at the highest initial concentration have not yet been carried in the presence of salt. However, the phase diagram does illustrate that, like the $R_{NaCl} = 0$ case, the general trends of morphological curvature favouring decreased steric crowding of PS chains as both the initial concentration and PS content increase still hold. However, compared to the $R_{NaCl} = 0$ case, the presence of salt generally tends to change morphologies to lower the steric crowding of PS chains as repulsive interactions between PMAA chains are relaxed. For example, the region of spheres in the $R_{NaCl} = 1.5$ phase diagram has become smaller than in the $R_{NaCl} = 0$ phase diagram, restricted to only the lowest c_0 and f_{PS} values. Instead of spheres at $f_{PS} = 0.5$ and $c_0 = 0.50$ wt % (as in the $R_{NaCl} = 0$ case), lower-curvature cylinders are formed for $R_{NaCl} = 1.5$. In addition, in the $R_{NaCl} = 1.5$ phase diagram, the formation of vesicles and compound vesicles have both shifted to lower initial concentrations compared to the $R_{NaCl} = 0$ phase diagram. In the case low initial concentration ($c_0 = 0.25$ wt %), the vesicle region extends to the $f_{PS} = 0.9$ brush composition, where only unimicellar dots were formed in the absence of salt. In the case of intermediate concentration, the compound vesicles phase region gives way to the first appearance of large compound supermicelles as the brush composition increases from $f_{PS} = 0.8$ to $f_{PS} = 0.9$, a morphology that did not form in the absence of salt within the range of investigated c_0 and f_{PS} values.

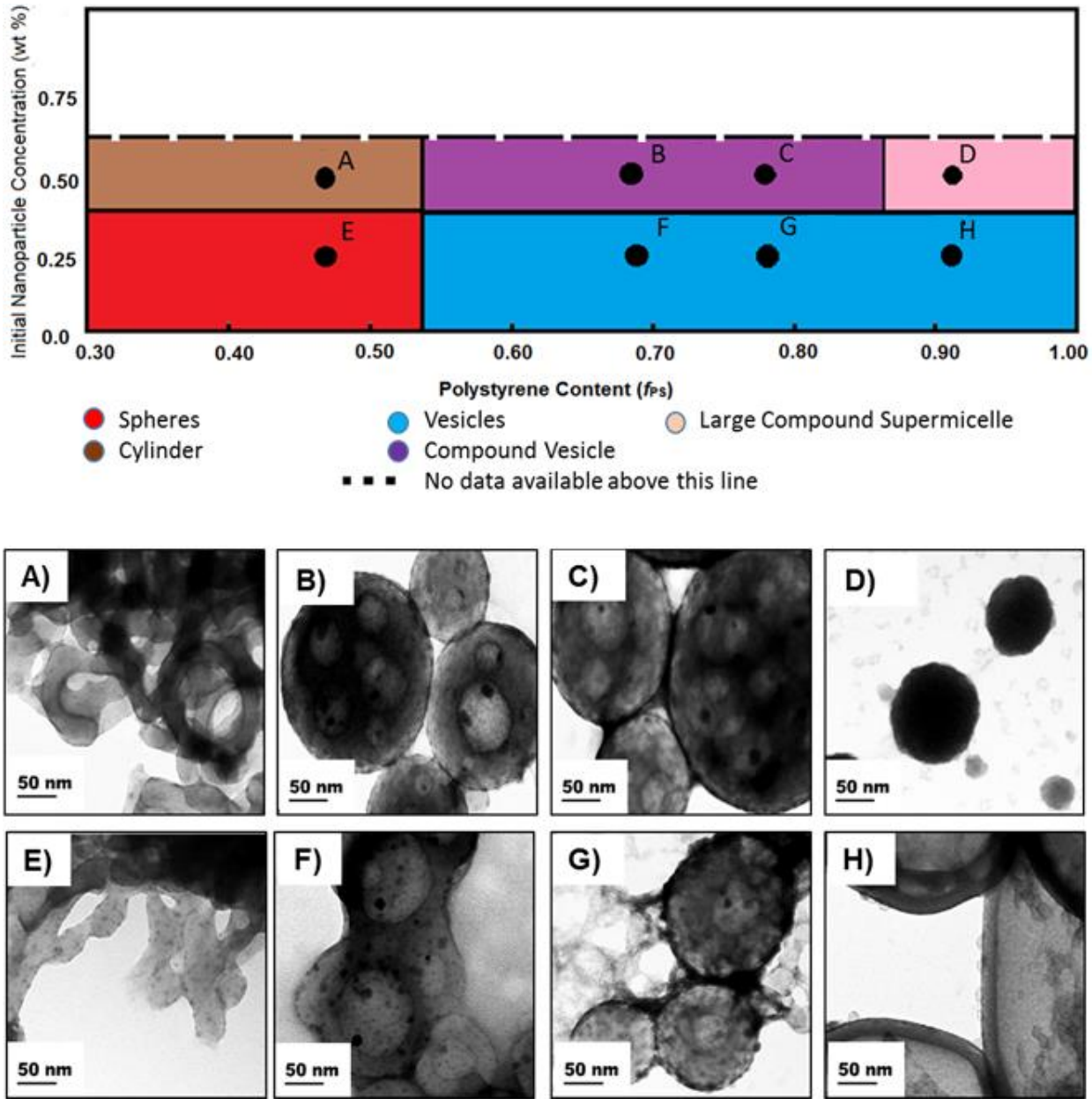

Figure 3.18 Phase diagram comparing brush composition with c_o when R_{NaCl} = 1.5. Each number is related to a representative TEM image found below. As only the 0.25 and 0.50 wt % experiments were performed, the white space above the dotted line is left for easier comparison with the R_{NaCl} = 0.0 case.

As the salt content is increased further to R_{NaCl} = 3.0, the resulting changes in the phase diagram are consistent with even stronger screening PMAA repulsion, shifting morphologies to even lower concave curvatures for PS chains. Figure 3.19 shows the resulting phase diagram and accompanying TEM data for PS/PMAA-(CdS) self-assembly in THF/water with added salt at a ratio of R_{NaCl} = 3.0. Here, the high curvature sphere region has disappeared entirely. When comparing this phase diagram with the previous R_{NaCl} = 0 and R_{NaCl} = 1.5 cases, the observed morphological trends appear to be more complex. Vesicles can be found at both high (f_{PS} = 0.90) and low (f_{PS} = 0.90) PS contents when the initial concentration is c_o = 0.25 wt %. Sandwiched between these points, compound vesicles can be found for f_{PS} = 0.7 and 0.8. When the initial concentration is increased to c_o = 0.50 wt%, the morphologies found in the R_{NaCl} = 3.0 phase diagram are generally the same as in the R_{NaCl} = 1.5 case with a few exceptions. While the f_{PS} = 0.50 sample at c_0 = 0.50 wt % and R_{NaCl} = 3.0 appears to have cylinder structures like the R_{NaCl} = 1.5 samples, the cylinders found at R_{NaCl} = 1.5 are much more defined. The cylinders present at R_{NaCl} = 3.0 present as more of a network of spheres and cylinders. It is believed this mixture is a kinetic mixture and annealing experiments will be performed in the hopes of identifying the free energy minimum under these conditions. Another exception is that for R_{NaCl} = 3.0, macroscopic precipitation occurred at c_o = 0.50 wt % and f_{PS} = 0.9, indicating that assemblies under these condition were not stable in the colloid state due to excessive screening and precipitated out of dispersion.

As stated, the number of data points used to construct these phase diagrams was limited to 7-12 points per diagram. While this means that those figures represent approximate identification of morphological phase regions, the trends in morphological change are quite evident and allow the phase diagrams to be a useful tool for choosing appropriate conditions to

selectively form a wide range of different morphologies from amphiphilic NPs. While phase diagrams have become more commonplace for block copolymer self-assembly in selective solvents,[136-140] and Nie *et al*[148] have presented a phase diagram for amphiphilic plasmonic micelle-like NPs showing the assemblies formed at different M_w and particle size, the present work is believed to represent the first empirical phase diagrams describing the self-assembly of amphiphilic NPs as a function of $f_{PS,}$ c_0 and R_{NaCl}.

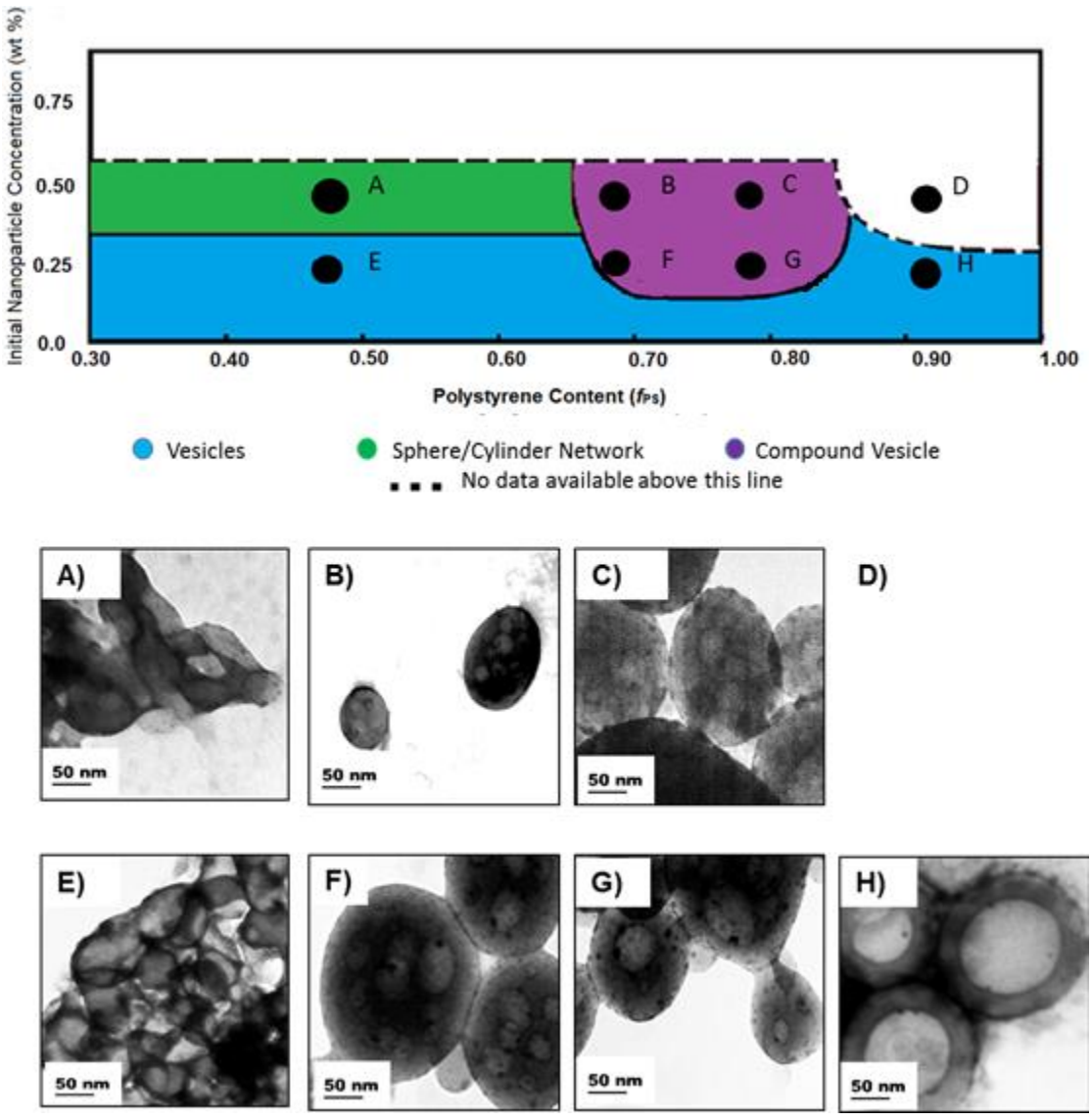

Figure 3.19. Phase diagram comparing brush composition with c_o when R_{NaCl} = 3.0. Each number is related to a representative TEM image found below. As only the 0.25 and 0.50 wt % experiments were performed, the white space above the dotted line is left for easier comparison with the R_{NaCl} = 0.0 case.

3.3.8 Measurement of the Characteristic Dimension of each Assembly by TEM

The characteristic dimension of each assembly was measured by TEM and presented in Table 3.3; this is the dimension defined by two PS chain lengths within the assembly and so can be used to determine the extent of PS stretching. For spheres, the diameter was measured; for cylinders, the width was measured; and for vesicles, the wall thickness was measured.

Table 3.3. Table Showing Measurements of the Characteristic Dimension of Each Assembly as measured by TEM

R_{NaCl}	c_0	f_{PS} = 0.5	f_{PS} = 0.7	f_{PS} = 0.8	f_{PS} = 0.9
0.0	0.25	98 ± 1[s]	84 ± 1[s]	97 ± 5[s]	37 ± 1[d]
	0.50	78 ± 1[s]	30 ± 4[v]	50 ± 14 [v]	44 ± 3[d]
	0.75	78 ± 5 [v]	--[e]	--[e]	41 ± 1[d]
1.5	0.25	70 ± 10[s]	74 ± 10 [v]	71 ± 12 [v]	30 ± 3 [v]
	0.50	40 ± 8[c]	--[e]	--[e]	--[f]
3.0	0.25	7 ± 1[v]	--[e]	--[e]	35 ± 2 [v]
	0.50	57 ± 4[c]	--[e]	--[e]	*

All measurements are presented are in nm. [s]sphere (diameters), [c]cylinder (width), [v]vesicle (wall thickness), [d]unimecellar dot (diameters). [e]compound vesicles and [f]large compound supermicelles lack a characteristic dimension *macroscopic precipitation occurred. Standard deviation of each measurement was determined from measurements of three different regions of the TEM grid; a minimum of 100 particles were measured for analysis of each sample.

A couple of trends appear. The unimicellar dots produced by the f_{PS} = 0.9 appear to have a consistent size at each initial nanoparticle concentration. This likely arises from each being

produced by a single dot instead of an aggregation of many particles. Vesicle wall thickness of each NP sample increased with increasing R_{NaCl}; the increased salt will minimize charge interactions between PMAA chains, allowing for these chains to pack more tightly on the external curvature of the bilayer. This allows more PS chains to pack inside the vesicle wall and become extended, increasing the size of the wall.

As the thickness of PS layer of the unimicellar dots can be clearly viewed, a calculation can be performed to determine the Z of these particles (Equation 3.2) and compare it with the Z = 95 determined for the PS/PMMA$_{XL}$(CdS) stage of the NP synthesis. A sample calculation for f_{PS} = 0.9, c_0 = 0.25 wt %, R_{NaCl} = 0.0 will be performed below (Equation 3.2) and the results will be found in Table 3.4.

$$V_{unimicellar} = \frac{4}{3}\pi r^3_{unimecllar}$$

$$V_{unimicellar} = \frac{4}{3} * \pi * 18.5nm^3 = 26521\ nm^3$$

$$V_{PS} = V_{unimicellar} - V_{core}$$

$$= 26521\ nm^3 - 265\ nm^3 = 26256\ nm^3$$

$$m_{PS} = V_{PS} * \rho_{PS} \qquad \text{(Equation 3.2)}$$

$$= 26256nm^3 * \frac{1cm^3}{1e^{21}nm^3} * \frac{1.01g}{1cm^3} = \frac{2.63e^{-17}g\ PS}{NP}$$

$$Z = \frac{m_{PS} * N_A}{\#\ of\ repeat\ units * M_{PS}}$$

$$= \frac{2.63e^{-17}PS-b-PAA}{NP} * \frac{1\ mol}{104.15\ g\ PS-b-PAA} * \frac{6.023e^{23}\ repeat\ units}{1\ mol} * \frac{1\ chains}{225\ repeat\ units}$$

= 676 chains/NP

Table 3.4. Aggregation Number Calculated from the Measurement of the TEM Particle Size for each Unimicellar Dot

$c_{0\ (wt\ \%)}$	$r_{unimicellar}$ (nm)	$V_{unimicellar}$ (nm^3)	V_{core} (nm^3)[a]	Z_{TEM}	Z_{LS}[b]
0.25	18.5	26521	265	676	95
0.50	22	44602	265	1140	95
0.75	20.5	36087	265	921	95

[a] and [b] are taken from Table 2.5

Each value is 7-12x greater than the aggregation number found earlier via static light scattering. As these are based on the volumes which are proportional to $V \sim r^3$, a 7-12x increase in Z_{TEM} arises from an approximate 1.8-2.3x increase in extension of each chain. Table 2.5 showed that the f_{PS} = 0.9 was only showed 41 % extension at the PS/$PMMA_{XL}$(CdS) stage, so a 1.8-2.3x increase in chain extension is possible. These results also show that the PS chains have not collapsed completely to the random coil dimension and remain in the bulk state, likely due to steric bulk impeding any further collapse. This calculation assumed that the ρ_{PS} was ~1.00 g/cm^3, but this may not be the case and that any decrease in density would lead to an increase in aggregation number. Another possibility is that these particles have also collected some of the 10 % of PS-*b*-PAA and PMAA-*b*-PAA single chains that were never completely removed during fractionation. These chains were likely also present in the images of larger assemblies, but would have become collected in the spherical cores or bilayer structures where there presence would not be noted. In the case of the f_{PS} = 0.9, the largest fraction of single chains would be hydrophobic and in aqueous solvent would try to find hydrophobic environments around the QD cores. As the unimicellar dots are much smaller, these chains add a significantly larger fraction of mass and electron density than they would for the larger assemblies.

3.3.9 Dynamic Light Scattering (DLS)

In order to understand the size of these assemblies aqueous dispersions, the effective hydrodynamic diameter, $d_{h,eff}$ of each assembly was determined by DLS (Table 3.5).

Table 3.5. DLS Measurements of $d_{h,eff}$ from Cumulant Analysis for each NP Assembly in Aqueous Solution

R_{NaCl}	c_o	f_{PS} = 0.5	f_{PS} = 0.7	f_{PS} = 0.8	f_{PS} = 0.9
0.0	0.25	149 ± 15	108 ± 1	100 ± 1	93 ± 1
	0.50	106 ± 6	114 ± 4	145 ± 20	97 ± 3
	0.75	112 ± 7	245 ± 20	210 ± 50	73 ± 2
1.5	0.25	1900 ± 400	360 ± 60	209 ± 10	460 ± 40
	0.50	380 ± 40	800 ± 200	150 ± 20	*
3.0	0.25	700 ± 200	250 ± 20	144 ± 4	*
	0.50	510 ± 90	345 ± 9	253 ± 4	*

All measurements were determined in nm. * denotes that macroscopic precipitation occurred in solution and no measurement could be taken. All measurements were taken at 90 °

There are several interesting features found in this data. The difference in size between unsalted assemblies and R_{NaCl} = 1.5 and 3.0 assemblies when f_{PS} = 0.5 and 0.7 is quite large, suggesting that the addition of salt to the aqueous solution leads to agglomeration of NPs in solution. As f_{PS} = 0.5 and 0.7 have the highest composition of PMAA in the polymer brush, the addition of salt would minimize more a larger number of charge interaction and allow the hydrophilic brushes to form agglomerates between particles. When salt is added to the f_{PS} = 0.9 assemblies, the morphologies have been shown to shift away from unimellar dots to vesicles and

compound vesicles, but this also leads to greater agglomeration in solution due to the increased colloidal instability. As only 10 % of the brush is the soluble block, the larger assemblies cannot remain dispersed in solution; thus macroscopic precipitation of these samples occurs

3.3.10 Imaging of PS/PMAA-(CdS) Assemblies by Laser Scanning Confocal Fluorescence Microscopy (LSFCM)

The fluorescent nature of the CdS QDs within self-assemblies of PS/PMAA-(CdS) allows LSFCM to be used to image selected aggregates. Figure 3.20 shows LSFCM images for each of f_{PS} = 0.5, 0.7, 0.8, 0.9 assemblies prepared at c_o = 0.50 wt % and R_{NaCl} = 0. As these particles were imaged in the solution phase, the degree of aggregation found by LCFMS was unexpected as the DLS data of this set of assemblies appeared to show particles minimal aggregation. Within the aggregates imaged, bright, circular particles can be found, demonstrating the fluorescent nature of the particles. The f_{PS} = 0.9 showed less aggregation than the others, allowing for single particles to be viewed clearly. It should be noted that when excited by the microscope beam, these assemblies were moving quite vigorously in solution, not remaining in one location for too long. As the microscope takes multiple images and creates an image based on the average of the dark and bright regions, it is possible the individual particles were moving too much during the imaging process. Larger particles, such as these aggregates, would be moving over a much longer timescale, allowing it to be much clearer in the final image. The f_{PS} = 0.9 was less active than the others, allowing for the single dots to be captured. As optical resolution by this method is limited below 200 nm, no internal structure cannot be discerned.

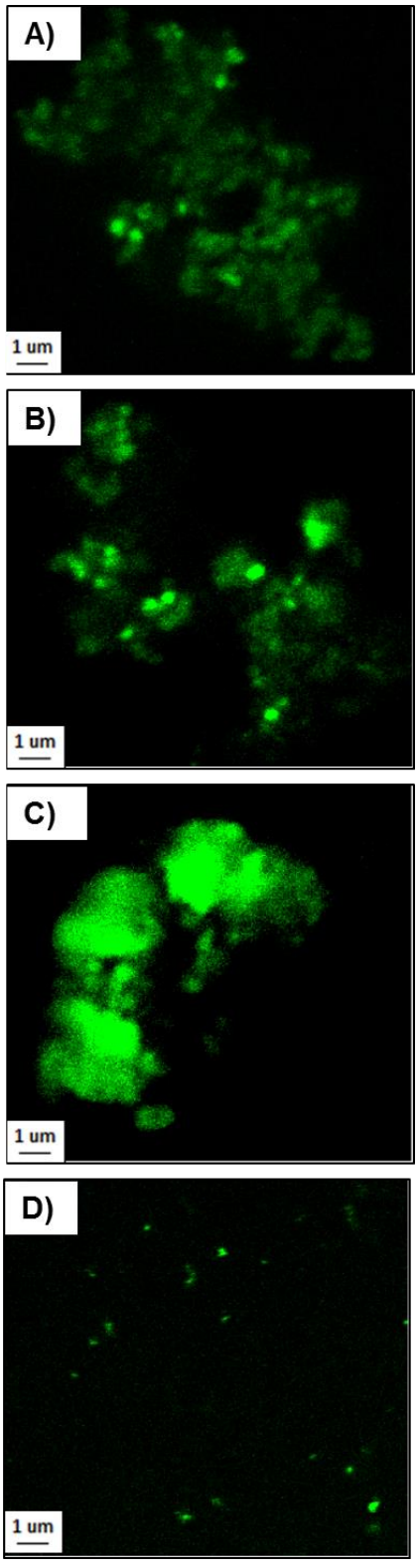

Figure 3.20 LSFCM images of f_{PS} = A) 0.5 B) 0.7 C) 0.8 and D) 0.9 at c_o = 0.50 and R_{NaCl} = 0.0. λ_{ex} = 488 nm, $\lambda_{em} \geq$ 515 nm.

3.4 Conclusion

This chapter has demonstrated the self-assembly PS/PMAA-(CdS) in THF/water to form a wide range of NP assemblies. We investigated the effect of the following variables: brush composition (the amount of hydrophilic and hydrophobic block in the polymer brush), initial nanoparticle concentration and initial salt content. As brush composition is increased to favour the hydrophobic PS, greater chain interactions limit internal PS chain extension, driving the assembly of lower curvature morphologies such as vesicles and multicompartment vesicles. Increases in c_o also lead to lower curvature structures, likely due to the increased aggregation number limiting chain extension and free volume within the NPs. The addition of salt to screen repulsive effects between PMAA chains helps to relax these reactions between hydrophobic brushes and allowing them to assume less entropically favoured configurations. This in turn allowed PS chains to reorient into bilayer structures or to even collapse around the QD cores, forming unimicellular dots. From this data, phase diagrams of self-assembled aggregates based on these three variables were developed, giving researchers a new tool to expand on this work in the future. The ability to select for specific assemblies allows scientists to apply them to modern problems. For example, the ability to select for vesicles and compound vesicles allows for the creation of hydrophobic pockets in the material that will could be used to carry pharmaceuticals. With knowledge of how polymer brush composition can tune morphological assemblies, this work can be expanded by selecting for more biocompatible polymers or selecting other inorganic NPS (such as Au or Fe_2O_3) to add magnetic or surface plasmon effects at the NP interface. The data presented in this chapter gives scientists a powerful new tool for predicting and selecting specific morphological assemblies for use in their work.

Chapter 4

Synthesis, Characterization and Amphiphilic Self-Assembly of Polystyrene/Poly(methacrylic acid) Mixed Brush-Functionalized Inorganic Nanoparticles of Variable Hydrophilic Chain Length

4.1 Introduction

The use of block copolymer templates for the creation of polymer brush functionalized nanoparticles (PBNPs) has given scientists one more methodology for creating useful polymer/inorganic nanoparticle (NP) hybrids. By creating amphiphilic micelles akin to the microphase separation of hydrophobic and hydrophilic segments of surfactant or phospholipids in aqueous solutions.[124-127], this technique has been used to help self-assembly inorganic NPs, including quantum dots (QDs), into larger aggregates with structural hierarchy using a polymer brush. This has led to a series of applications in fields as diverse as drug delivery[73,74,101,103], optics[105-108], bio-imaging[1,2,3,75] and sensor[6,8,104]. Following the inspiration of block copolymer amphiphiles, new techniques have been developed to create NP/polymer colloidal hybrids with amphiphilic character.[32,132,141-144]. In order to fine-tune their use in applications, it is necessary to find methods to adjust the morphology and control the internal organization of nanoparticle assemblies[16,24,109-113,145]. While approaches such as the use of "brick and mortar"[114-116] or layer-by-layer assembly[117-119] have proven useful in creating PBNPs, the block copolymer template approach to creating amphiphilic NPs allows for unique control of the polymer brush composition,[120-122,130,] as was seen in Chapter 2 of this work with the use of a mixture of diblock copolymers. These results show great promise, but also serve to demonstrate the limitations of the current toolbox. Chapter 3 of this work has shown how changes in the brush composition can affect the self-assembly of these PBNPs, indicating that more hydrophobic brush compositions lead to lower internal curvature structures such as compound vesicles. There are still many more variables to investigate.

In this chapter, the synthesis and characterization of amphiphilic CdS NPs that were surface functionalized with a hydrophobic and hydrophilic mixed polymer brush were created from a PS(361)-*b*-PAA(77)-*b*-PMMA(x) triblock copolymer in which x = 154 or 54 repeat units.

While in previous chapters of this work amphiphilic NPs were synthesized using a mixed diblock copolymer template in order to probe the effects of brush composition on self-assembly, the use of a triblock template allows for the creation of a PS/PMAA brush with equal number of PS and PMAA chains on the NPs in which the lengths of one or both of the chains can be varied by using different triblock copolymers. Our group has applied this technique before using a PS(296)-*b*-PAA(41)-*b*-PMMA(236) triblock as a template to form CdS NPs surrounded by a mixed brush of PS and PMMA chains that show structural environmental response to different solvent environments.[33] When the PMMA chains were then hydrolyzed to poly(methacrylic acid) (PMAA) chains, amphiphilic NPs were produced which self-assembled in aqueous solvent mixtures to form spheres, vesicles and unusual worm-like morphologies.[63] Due to this assortment of eccentric morphologies created by only a single block length, this current chapter hopes to further probe this triblock templated approach by probing the effect of the hydrophilic chain block. As chain length has been known to play a role in block copolymer self-assembly,[37] it is thought that this same variable would play a role in PBNP self-assembly. As brush composition effects have been studied in Chapter 2, the use of triblock copolymers allows for control of both the brush length and the brush composition by holding the PS constant and varying the PMAA.

An overview of the synthetic pathway is described in Figure 4.1 and is analogous to that presented for the diblock copolymer approach. These NPs were then self-assembled in aqueous solution to determine the effect that changing PMAA brush length would have on the assembled morphologies, while also holding the number of PS and PMAA chains constant. The effect of changing initial nanoparticle concentration (c_o) and salt addition (R_{NaCl}) on the self-assembly of these NPs will also be probed to determine how these parameters interact with the changing

PMAA brush length. The information determined in this chapter will add to the still-growing toolbox of amphiphilic polymer/NP composites.

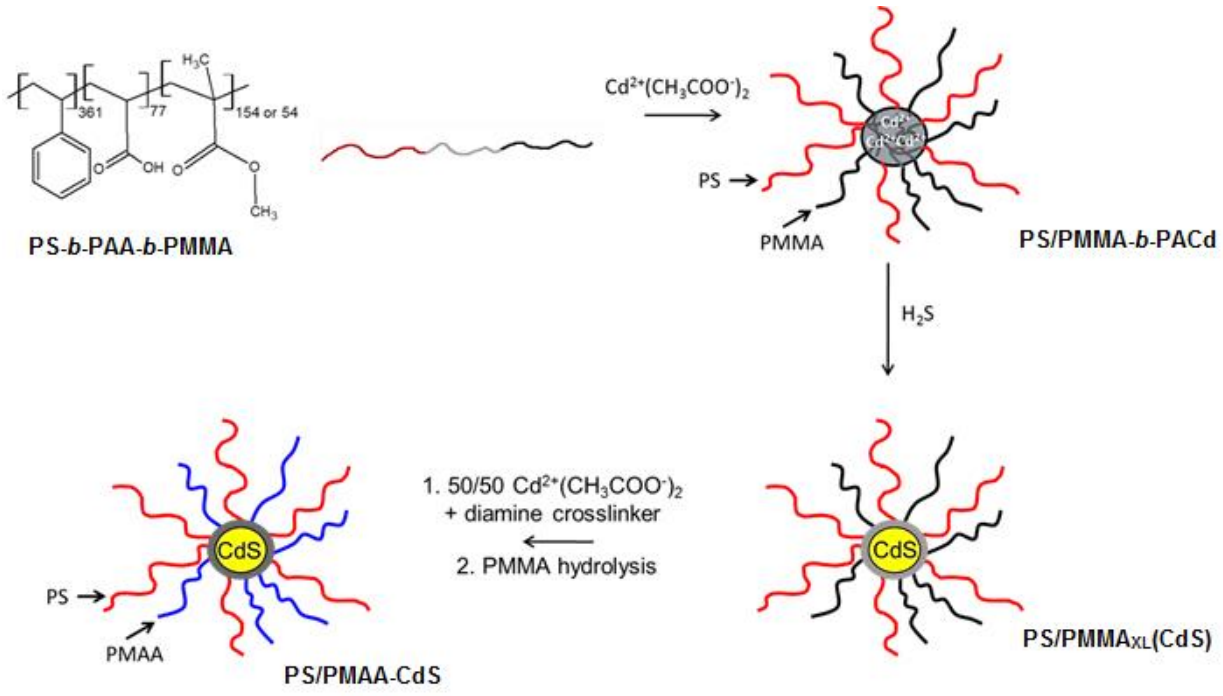

Figure 4.1 Synthetic pathway for the creation PS/PMAA-CdS NPs

4.2 Experimental

4.2.1 Preparation of Polystyrene-block-Poly(acrylic acid)-block-Poly(methyl methacrylate)(PS-b-PAA-b-PMMA) Triblock Copolymer

The PS-*b*-PtBA-*b*-PMMA starting materials used in this set of experiments were synthesized in our lab by Gavin Phinney using established method of sequential anionic polymerization (Appendix A). There are two samples: one triblock is PS(361)-*b*-PAA(77)-*b*-PMMA(54) and the other is PS(361)-*b*-PAA(77)-*b*-PMMA(154). The numbers in brackets

indicate the number-average degrees of polymerization for each block. Note that the PS and PAA block lengths of the two copolymers are identical, but the PMMA block length of one copolymer is short, designated PMMA-54, while the other is long, designated PMMA-154.

4.2.1.1. Hydrolysis of Polystyrene-*block*-Poly(*tert*-butyl acrylate)-*block*-Poly(methyl methacrylate (PS-*b*-PtBA-*b*-PMMA) to PS-*b*-PAA-*b*-PMMA

The central P*t*BA blocks of the PMMA-54 and PMMA-154 triblock copolymers were selectively hydrolyzed from the PS-*b*-PtBA-*b*-PMMA form to the PS-*b*-PAA-*b*-PMMA form following a method similar to that used for the diblock copolymers in section 2.2.1.1. The PS-*b*-PtBA-*b*-PMMA triblock copolymers were initially dried overnight at 70 ^{o}C under vacuum. It was then dissolved in toluene to make a 2% w/w solution. The clear, colourless solution was stirred for 15 minutes until all polymer was dissolved. The solution was then refluxed at 115 ^{o}C for 2 days with *para*-toluene sulfonic acid (5 mol % relative to the *tert*-butyl acrylate content). The dark brown, opaque solution was then concentrated to half of its initial concentration by evaporation and precipitated into cold isopropanol. The fluffy white powder was then removed by vacuum filtration and dried in a vacuum oven at 70 ^{o}C for two days.

4.2.2 Preparation of Amphiphilic CdS Quantum Dots with Polystyrene/Poly (methacrylic acid) (PS/PMAA) Mixed Brushes of Varying PMAA Block Lengths

4.2.2.1 Preparation of Polystyrene-*block*-Poly(Cadmium acrylate)-*block*-Poly(methyl methacrylate) (PS/PMMA-PACd) Reverse Micelles

The selectively hydrolyzed PAA forms of PMMA-54 and PMMA-154 were each dissolved in a 90/10 (v/v) benzene/methanol solution to make 2 % w/w solutions and stirred overnight to equilibrate. To each polymer solution 3 moles of $Cd(OAc)_2$ were added per mol of acrylic acid repeat unit in a continuous stream under constant stirring. The resulting solution was allowed to stir overnight, after which time they were freeze-dried to remove the solvent, producing a fluffy white powder. This sample was dried overnight in a vacuum oven at 70 ^{o}C. The resulting sample was then washed multiple times with methanol and the filtrate was tested with aqueous Na_2S solution. The sample was washed until three consecutive tests of the filtrate resulted in no yellow colour in the solution. Once completed, the NPs were dried again overnight at 70 $^{\circ}$C under active vacuum. Gel permeation chromatography (GPC) was used to determine the degree to which the polymer chains had micellized based on the comparative weight fractions of the resulting micelle and single chain peaks visible via the Refractive Index detector (RI). These samples are denoted PS/PMMA-PACd.

4.2.2.2 Fractionation of PS/PMMA-PACd Reverse Micelles

In order to remove unmicellized polymer chains, fractionation of the PS/PMMA-PACd NPs was required. The PS/PMMA-PACd samples were dissolved in THF (5 % w/w). The solution was then stirred at a constant rate while deionized water was added dropwise until the solution remained turbid for several minutes after the addition of the last drop. The solution was

left overnight, producing two layers. The top layer consisted of the lighter single chains while the bottom layer contains the heavier PS/PMMA-PACd NPs. The top layer was decanted. Deionized water was then added to the bottom layer to precipitate the samples, allowing them to be filtered. The filtrate was dried for overnight at 70 ^{o}C. The next day a portion was dissolved in THF and GPC analysis was performed to determine the amount of single chain that remained. This process was repeated until the GPC showed mostly the peak of the micelle population in the refractive index detector (with a correlating peak on the low-angle light scattering and right-angle light scattering detectors) and minimal amounts of the single chain population. Two to three fractionations were required per sample and fractionation ceased when less than 10% of the single chains remained by the weight fractions determined by the integration of these peaks. While this threshold of 10 % is a somewhat arbitrary value, it was selected as most polymers have about 10 % material that will not undergo micellization. Another reason relates to the technique itself. Some micelle material is removed each time a fractionation occurs and performing numerous repetitions can lead to a large loss of material. Therefore by aiming for 10 %, unnecessary fractionations are avoided that may limit the sample yield.

4.2.2.3 Preparation of CdS Quantum Dots in Reverse Micelle Cores

The newly fractionated PS/PMMA-PACd samples were now placed inside of a humidity chamber at 70 ^{o}C for one week. Upon completion these samples were placed under an atmosphere of "wet" H_2S. The H_2S was bubbled into the sample chamber containing the PS/PMMA-PACd NPs for 10 hours and was then followed by 1 h of nitrogen to purge the lines of H_2S. The now yellow NP sample was then placed inside a vacuum oven under ambient temperature and left overnight to remove any excess H_2S gas.

4.2.2.4 Core Cross-linking Reverse Micelles Containing CdS Quantum Dots

The cores of the NPs were now crosslinked in order to stabilize the NPs during the next step of the synthesis. The yellow NPs were first ground into a fine powder before being dispersed in THF to 2 wt%. Immediately upon dispersion, 0.5 equivalents of $Cd(OAc)_2$ in methanol (0.5 molar equivalents of $Cd(OAc)_2$ /1mol of acrylic acid repeat units) were added in one quick addition and the solution was allowed to stir overnight. The next day, a 1.0 wt % solution of *N*-ethyl-*N*'-(3-dimethylaminopropyl)-carbodiimide methiodide (EDC) activator in water (0.5 molar equivalents of EDC/1 mol acrylic acid repeat units) was added and allowed to stir for 2 hours. This was followed by the addition of a 1.0 wt % solution of 2,2'-(ethylenedioxy)bis(ethylamine) (EDDA) in water (0.25 molar equivalents/ 1 mol of acrylic acid repeat units) in one portion and was then left to stir overnight. The sample was concentrated further and precipitated into room temperature methanol. The resulting pale, yellow solid was then filtered and dried under vacuum for 2 days at 70 ^{o}C. The characterization of these NPs will be discussed in detail in the Results and Discussion section. These samples were designated PS/PMMA-*b*-PAA_{XL}(CdS), where x is the number of PMMA repeat units.

4.2.2.5 Hydrolysis of PMMA Brush Chains to PMAA

After the NP cores were crosslinked, the resulting PS/PMMA-*b*-PAA_{XL}(CdS) samples were dissolved to 10 wt % in 1,4-dioxane with KOH (2 molar equivalents/ 1 mol methyl methacrylate repeat units) and 18-crown-6 (0.2 molar equivalents/ 1 mol of methyl methacrylate repeat units). This solution was placed under argon in a sealed high-pressure Schlenk tube and the reaction was heated to 110 ^{o}C for 4 days. Once complete, the solution was concentrated further and precipitated into a cold 0.2 M acetic acid solution. This was then filtered by vacuum

and placed into a vacuum oven for 3 days at 70 ° C. The characterization of this reaction will be discussed further in the Results and Discussion section. This final sample was generally designated PS/PMAA-*b*-PAA_{XL}(CdS). Since these end products are the building blocks for subsequent self-assembly experiments, we also use the short-hand designation PS/PMAA(54)-CdS and PS/PMMA(154)-CdS when referring to these samples.

4.2.3 Self-Assembly of PS/$PMAA_{(x)}$-(CdS) Triblock NPs in Mixtures of THF and Water Under Various Conditions

4.2.3.1 Self-Assembly of PS/$PMAA_{(x)}$-(CdS) Triblock NPs in Mixtures of THF and Water (Immediate Quenching Method)

The QD/polymer aggregates that will be described throughout this chapter were created using the following method. The polymer solutions were formed by dispersing the PS/PMAA-(CdS) NPs in 2g of THF (HPLC grade). The THF solutions were set to stir at a constant rate while deionized water was added in a dropwise fashion at 10 µL/10 s. The point at which the solution became turbid was noted as the critical water concentration (cwc), or the point at which self-assembly began. Water was added at this same rate up to 75 wt % before being quenched in 10 mL of deionized water. The quenched solutions were dialyzed for 10 days against deionized water to kinetically freeze the aggregates in place.

4.2.3.2 Effect of Salt Addition on the Self-Assembly of PS/$PMAA_{(x)}$-(CdS) NPs

For this set of experiments, NaCl was added to solutions of either 0.25 or 0.50 wt % PS/PMAA-CdS in THF. The amount of NaCl added was related to the number of PMAA repeat units found in each NPs, with a ratio of R_{NaCl} = 1.5 and 3.0 chosen for each of the two NP

concentrations. The salt additions were performed before water addition began and the amount of water added from the salt solution was taken into account when determining the cwc of each experiment.

4.2.4 Gel Permeation Chromatography (GPC)

All GPC measurements were carried out on a Viscotek Model 302 liquid chromatography system. It was furnished with refractive index (RI), low-angle light scattering (LALS, $\theta = 7^{o}$) and right-angle light scattering (RALS, $\theta = 90^{o}$) detectors. The eluent for this system was THF run at a flow rate of 1mL/min and the column temperature was set at 35 ^{o}C. Polymer samples were dissolved in HPLC grade THF to concentrations of 1mol/L and filtered through poly(tetrafluoroethylene) (PTFE) filters with a nominal pore size of 0.45 μm nm before injection into the column. The data was collected on a Dell Dimension 2300 computer using GPC software from Viscotek. Three columns (purchased from Tosoh Biosciences LLC) were connected in series: one TSKgel G3000Hhr columns, one TSKgel GM-HHR-M and then a second TSKgel G3000Hhr. The packing material of these columns is styrene-divinyl benzene.

4.2.5 Nuclear Magnetic Resonance (NMR)

^{1}H NMR spectra of diblock copolymers and subsequent micellization products were recorded using a Bruker AC 300 MHz spectrometer. 2D ^{1}H nuclear Overhaueser effect spectroscopy (NOESY) experiments of the PS/PMMA-*b*-PAA_{XL}(CdS) products were performed on a Bruker Avance 500 MHz spectrometer at 27 ^{o}C. For the 2D NOESY spectra, 320 experiments of 2k data points were recorded. 24 scans were used for each increment using standard Bruker software. A mixing time of 500 ms was used for best results.

4.2.6 UV-Vis Absorption Measurements

Absorption spectra of PS/PMMA-*b*-PAA_{XL}(CdS) were recorded on a Perkin Elmer UV-Vis-NIR with a Three Detector Module. It consists of a photomultiplier tube (PMT) for the UV-Vis range, an indium gallium arsenide (InGaAs) detector and a lead sulfide (PbS) detector for the near infra-red (NIR) range. Samples were dissolved to 1 mg/mL in spectroscopic grade tetrahydrofuran, toluene, acetone and chloroform. A background of pure solvent was recorded for each individual solvent to subtract from the ensuing measurement.

4.2.7 Transmission Electron Microscopy

Microscopy was performed on a JEOL JEM-1400 TEM operating at a voltage of 80 kV with a Gatan Orius SC1000 camera. Crosslinked NP samples for transmission electron microscopy were prepared by dissolving the NPs in benzene at 1 wt %. 2 drops of this solution were applied to a copper grid (300 mesh) coated with a carbon film coating. The solution was allowed to settle on the grid for 15 seconds before excess solvent was dabbed off with a kimwipe. The grids were allowed to dry for 2 hours before images were taken. Once the PMMA was hydrolyzed to PMAA, these samples were prepared by dissolving the NPs in benzene at 1 wt %. Application and drying of these samples follows the previous procedure for the crosslinked samples. Self-assembly solutions were prepared for TEM by taking 2 drops of the aqueous solution and applying them to a 300 mesh copper grid coated with a carbon film coating. Application and drying of these samples follows the previous procedure for the crosslinked samples. Measurements were performed on the ImageJ software from Softonic. Three images were taken from three different randomly selected locations on each grid to find an average particle size.

4.2.8 dn/dc Determination

Measurements of d*n*/d*c* were carried out on a Brookhaven Instruments BI-DNDC Differential Refractometer. Stock solutions of PS/PMMA-(CdS) NPs were dispersed separately in THF, toluene and acetone at a concentration of ~5 mg/mL. A series of five solutions were created with a concentration range of 1-5 mg/mL with 1 mg/mL spacing between samples. All dilutions were performed by adding known quantities of appropriate filtered solvent. Measurements were performed in triplicate and carried out at 23 ^{o}C.

4.2.9 Dynamic Light Scattering (DLS)

DLS measurements were carried out on a Brookhaven Instruments photon correlator spectrometer equipped with a BI-200SM goniometer, a BI-900AT digital autocorrelator, and a Melles Griot He-Ne Laser (632.8 nm) with a maximum power output of 75 mW. In order to remove dust from sample vials, rigourous cleaning was applied.

The scintillation vials were first washed with 5 mL of 95 % ethanol filtered through two poly(tetrafluoroethylene) (PTFE) filters, connected in series with a 0.20 μm nominal pore size. The vials were then capped and vortexed for 30 seconds. The solvent was removed and the process was repeated 10 more times. Upon completion, the vials were covered with a piece of lens paper held on with an elastic band and placed upside down in an oven at 80 ^{o}C for 2 days to remove excess solvent.

Stock solutions of PS/PMMA$_{XL}$(CdS) NPs were dispersed separately in THF, toluene and acetone at concentrations of ~5 mg/mL. These solutions were filtered through two PTFE filters connected in tandem with a 0.45 μm nominal pore size. Any required dilutions were performed by adding known quantities of appropriate filtered solvent. DLS measurements to determine

concentration dependence were taken at 90°. For experiments probing angular dependence, the measured angles were 35°, 50°, 70°, 90° and 120°. For each experiment, 3 repeat measurements of the autocorrelation function were obtained. All measurements were performed at 23 °C.

4.2.10 Static Light Scattering (SLS)

SLS measurements were carried out on a Brookhaven Instruments photon correlator spectrometer equipped with a BI-200SM goniometer and a Melles Griot He-Ne Laser (632.8 nm) with a maximum power output of 75 mW. In order to remove dust from sample vials, rigourous cleaning was applied.

The scintillation vials were first washed with 5 mL of 95 % ethanol filtered through two poly(tetrafluoroethylene) (PTFE) filters, connected in series with a 0.20 μm nominal pore size. The vials were then capped and vortexed for 30 seconds. The solvent was removed and the process was repeated 10 more times. Upon completion, the vials were covered with a piece of lens paper held on with an elastic band and placed upside down in an oven at 80 °C for 2 days to remove excess solvent.

A stock solution of PS/PMMA$_{XL}$(CdS) NPs were dispersed in THF, toluene and acetone at a concentration of ~5 mg/mL. These solutions were filtered through two PTFE filters connected in tandem with a 0.45 μm nominal pore size. Three solutions were made from the same stock solution and diluted to ~ 1mg/mL. Measurements were performed at 12 angles from 30 °- 120 ° at five solution different concentrations created by adding filtered solvent gravimetrically. Concentration of the measured solutions remained between .05-1 mg/mL. All measurements were carried out at 23 °C.

4.2.11 Fourier Transform Infrared (FTIR) Spectroscopy

IR Spectroscopy measurements were carried out on a Thermo Nicolet IR 200 Spectrometer. Solutions of 1 mg NP per 1mL of carbon tetrachloride were prepared and allowed to stir overnight. The solutions were placed on a NaCl plate and allowed to dry to create a thin polymer film.

4.2.12. Powder X-Ray Diffraction (XRD)

About 5 mg of PS/PMAA-(CdS) NPs were placed onto a zero-background holder. Step-scan x-ray diffraction data was obtained on a Rigaku Miniflex diffractometer with variable divergence slit, 4.2 ° scattering slit and 0.3mm receiving slit. The results were scanned over a 2θ range 10-100° with Cr radiation (30 kv, 15 mA) (wavelength is 0.228 nm). The scanning step size was 2°/min.

4.3 Results and Discussion

4.3.1 Hydrolysis of Polystyrene-block-poly(tert-butyl acrylate)-block-poly(methyl methacrylate) (PS-b-PtBA-b-PMMA) to Polystyrene-block-poly(acrylic acid) (PS-b-PAA-b-PMMA)

PS-*b*-PtBA-*b*-PMMA triblock copolymers of different PMMA block lengths that had been synthesized by a Gavin Phinney (see Appendix A) were hydrolyzed into the acrylic acid form. Characterization for each of these polymers was performed by determining the signal ratio of the 5 PS aromatic protons (7.07 and 6.57 ppm) and the 2 PS methylene protons (1.42 ppm) by ^{1}H NMR (Figure 4.2). As the methylene peaks overlapped with the 9 PtBA tert-butyl ester protons, a 5/2 ratio by NMR integration suggests complete hydrolysis. The PMMA-154 triblock

copolymer shows a ratio of 5/2.2 and the PMMA-54 sample also has a ratio of 5/2.2. This suggests that a small fraction of PtBA may remain unhydrolyzed, but this variation also falls under the error inherent to NMR integration.

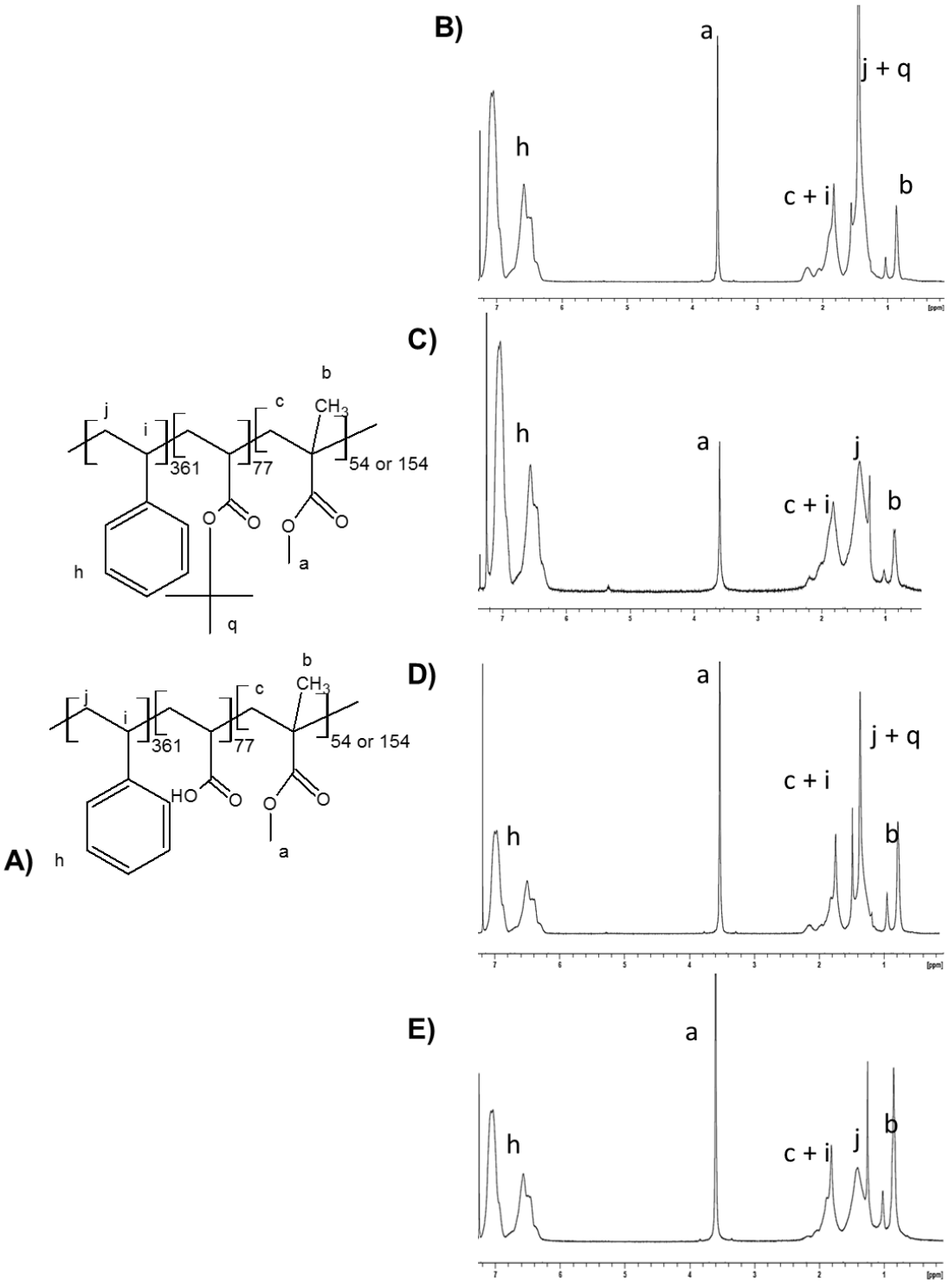

Figure 4.2. A) Schematic depicting the peak labels for the hydrolysis of PtBA to PAA and the NMR region of interest. ^{1}H NMR spectra of B) PMMA-54 (P*t*BA form) C) PMMA-54 (PAA form) D) PMMA-154 (P*t*BA form) and E) PMMA-154 (PAA form), showing the decrease in the q peak to show loss of P*t*BA tert-butoxy groups.

4.3.2 Micellization and Fractionation of Polystyrene-block-poly(cadmium)acrylate-block-poly(methyl methacrylate) Triblock Copolymers

The micellization process of each polymer was performed using $Cd(OAc)_2$ in a benzene/MeOH mixture. Upon addition of the $Cd(OAc)_2$, each polymer solution became cloudy as turbidity increased and displayed Tyndall scattering. Benzene was removed using a freeze-drying technique to create dry, white powders. GPC indicated that free polymer chains remained unmicellized in the sample and therefore fractionation was used to remove the free single chains. GPC was used to follow the fractionation, as can be seen in Figure 4.3.

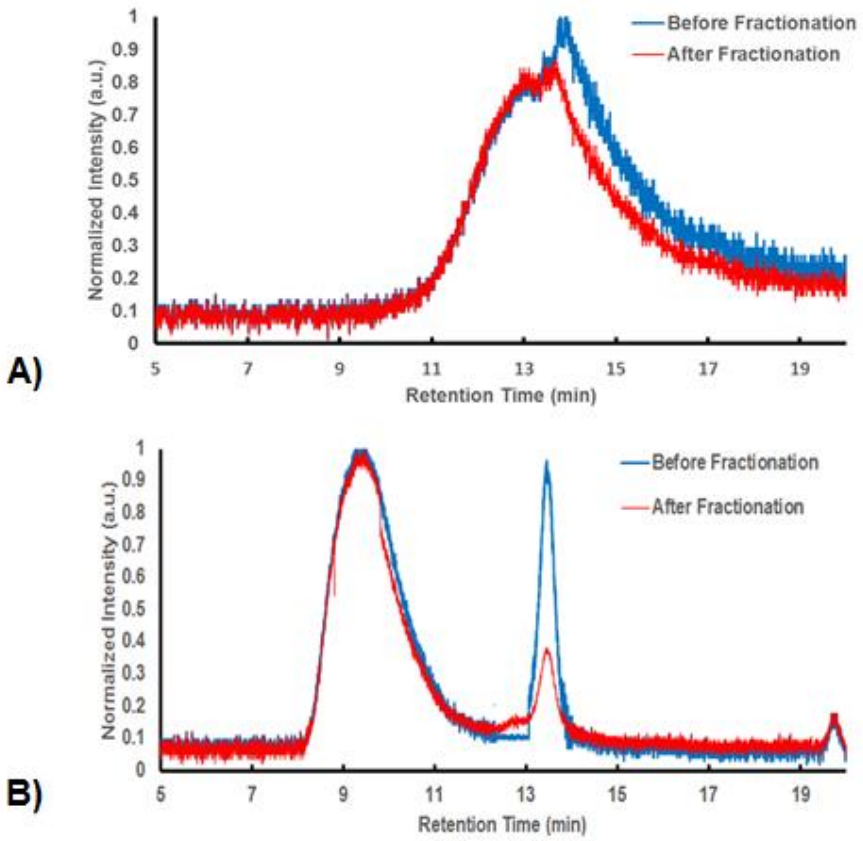

Figure 4.3. GPC spectra of PS/PMMA-PACd NPs for A) PMMA-54 and B) PMMA-154 samples, before and after fractionation.

The main peaks found at ~13 min PMMA-54 and ~9.5 min PMMA-154 represent the reverse micelles that were formed while the smaller, more narrow peaks around ~13.5 min represent the single chain fractions. The elution time of the two micelle peaks are different from each other, suggesting that the hydrodynamic size of these NPs are not the same. As large things come out first, the hydrodynamic profile of the PMMA-154 NPs appears larger than that of the PMMA-54. This may be due to the greater length of the PMMA-154 chains creating a more densely packed brush further from the core, while the chains of the PMMA-54 are shorter and take up less free volume further from the core. This allows for more flexibility of the of the PS chains in the mixed brush. Fractionation was performed once on each NP at which point single polymer chains represented less than 10 % of the total weight of the sample. The GPC spectra of the PMMA-154 NP sample shows a decrease of the single chain peak after fractionation, with only 10 % of the single chain fraction remaining for each sample as determined through the GPC's Omnisec software. Due to the overlap of the micelle and single chain peaks in the PMMA-54, Origin software was used to deconvolute these peaks (See Appendix B). The single chain peaks were also found to make up only 10 % of the total fraction weight.

In order to determine that the micelles were forming a mixed brush, dispersability tests in solvents of increasing dielectric constant were carried out in tetrahydrofuran, toluene, chloroform and acetone (Figure 4.4).

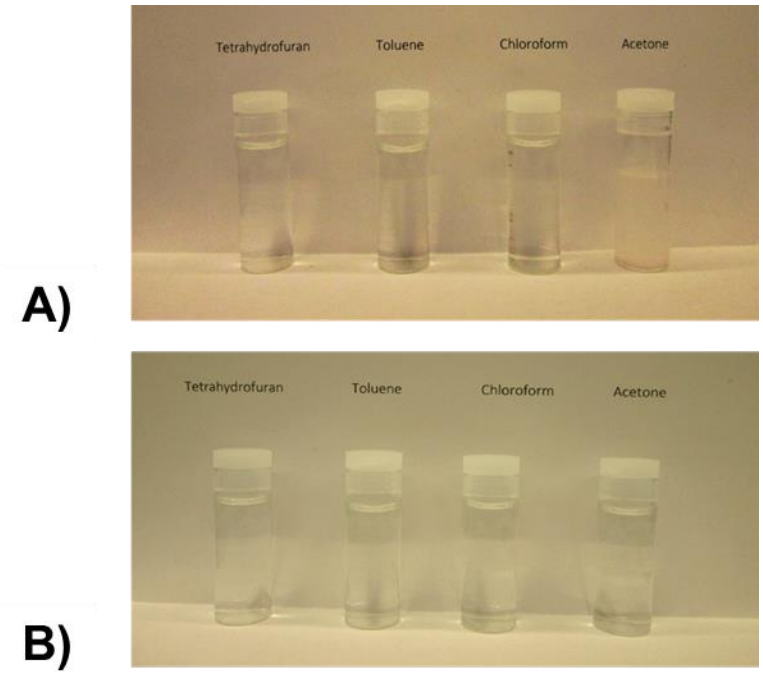

Figure 4.4. Images of A) PMMA-54) and B) PMMA-154 reverse micelles dispersed in tetrahydrofuran, toluene, chloroform and acetone.

As acetone is a good solvent for PMMA but not for PS, the presence of a mixed polymer brush should allow for the dispersion of each NP in these solvents. The PMMA-154 cadmium acrylate micelles disperse fully in all four solvents, indicating a mixed polymer brush on the NPs. The PMMA-54 reverse micelles disperse well in THF, toluene and chloroform and present as a cloudy dispersion for the acetone. The lack of precipitate indicates that dispersion in acetone has occurred. The turbidity of the solution likely arises from agglomeration of micelles in solution. As the PMMA-54 has a relatively short PMMA, they is less steric repulsion between particles than there is in the PMMA-154. This may allow the micelles to get close enough to form agglomerates. Based on the dispersion of both PS/PMMA-PACd samples in all 4 solvents results and the single micelle peak found in the GPC, it is believed that mixed brush NPs have been synthesized.

4.3.3 Characterization of Crosslinked PS/PMMA$_{XL}$(CdS) Mixed Brush Coated CdS QDs Before Hydrolysis of PMMA Chains

4.3.3.1 Gel Permeation Chromatography

The generation of CdS QDs in the core of the micelles leads to a destabilization of the core due to the reprotonation of the acrylic acid units by the addition of H_2S gas. The core is therefore cross-linked to prevent dissociation of the NP into individual polymer chains. GPC was used to compare the PS/PMMA-PACd with the newly crosslinked NPs (Figure 4.5). The NP peak of the PMMA-54 NPs spectrum shifts to lower retention times, suggesting a larger hydrodynamic radius. The PMMA-154 shifted to higher retention times and formed a much broader peak than the PS/PMMA-PACd form. It has been hypothesized that the cross-linking of the cores will make the cores undergo contraction, pulling the polymer brushes inwards and giving the particle a smaller average hydrodynamic size. While this may be true for the PMMA-154 case, the NPs appear to be getting bigger in the case of the PMMA-54 NPs. It is possible that during the precipitation of the CdS QDs that the polymer chains partially dissociated within the NP, gaining a degree of mobility and rearranging to create a slightly larger NP. As this NP has the shorter PMMA chain, fewer chain interactions may impede the movement of the polymer brushes as they reorient around the core.

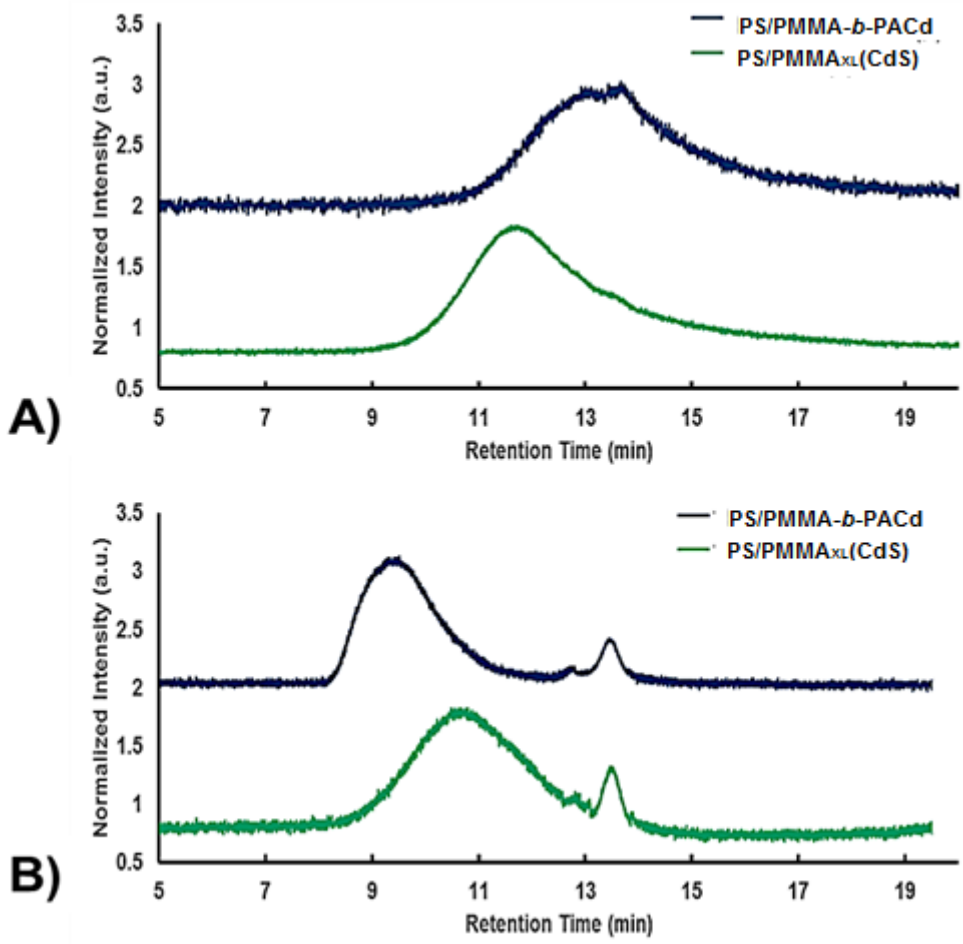

Figure 4.5. GPC (refractive index response detector) comparison of A) PMMA-54 and B) PMMA-154 before and after CdS core is crosslinked.

4.3.3.2 UV-Visible Spectroscopy and Transmission Electron Microscopy (TEM)

The optical properties of the CdS QDs were probed by UV-vis spectroscopy. The UV-vis spectra that are produced can give valuable insight about the QDs based on the quantum confinement effect. As these are semiconductor nanoparticles, the band gap energy between the conduction band and the valence band can be measured using UV-Vis by determining the excitation wavelength (λ_{ex}).[44] Figure 4.6 depicts UV-Vis absorbance spectra for both NPs after crosslinking in a series of solvents (THF, toluene and chloroform) of different dielectric constants. Each spectra represents the size distribution by way of the quantum confinement effect. Each exciton shoulder relates to emission from a single population distribution. In both Figure 4.6, A and B (PMMA-54 and PMMA-154 respectively), the normalized spectra for the different solvents are near identical curves, suggesting that each QD is stable within the core and does not change size depending on the solvent environment. One particular difference between the UV-Vis spectra in two curves is the presence of a single exciton shoulder for the PMMA-154 case and the presence of two shoulders for the PMMA-54 sample. It is possible that there are multiple quantum dot populations or a single QD population with multiple excition peaks. The well-defined exciton peak would suggest that electronic structure has multiple discrete energy states. The sizes of these populations can be determined using the absorbance threshold of the THF curves (see Figure 4.6 inset) and sizes were determined using Equation 4.1:

$$2R_{CdS} = \frac{1}{(0.1338 - 0.0002345 * \lambda_{thresh})} \qquad \text{(Equation 4.1)}$$

This formula was derived by Moffitt[146] by fitting data published previously by Henglein.[44] Size and absorbance data can be found in Table 4.1.

Table 4.1. UV-Vis Spectroscopy Data and TEM Core Diameter Measurements for PS/PMMA$_{XL}$(CdS) NPs

	λ_{thresh} (nm)	d_{CdS} (nm)	TEM QD Size (nm)
PMMA-54	495	5.6	7.4 ± 0.2
PMMA-154	487	5.1	5.6 ± 0.5

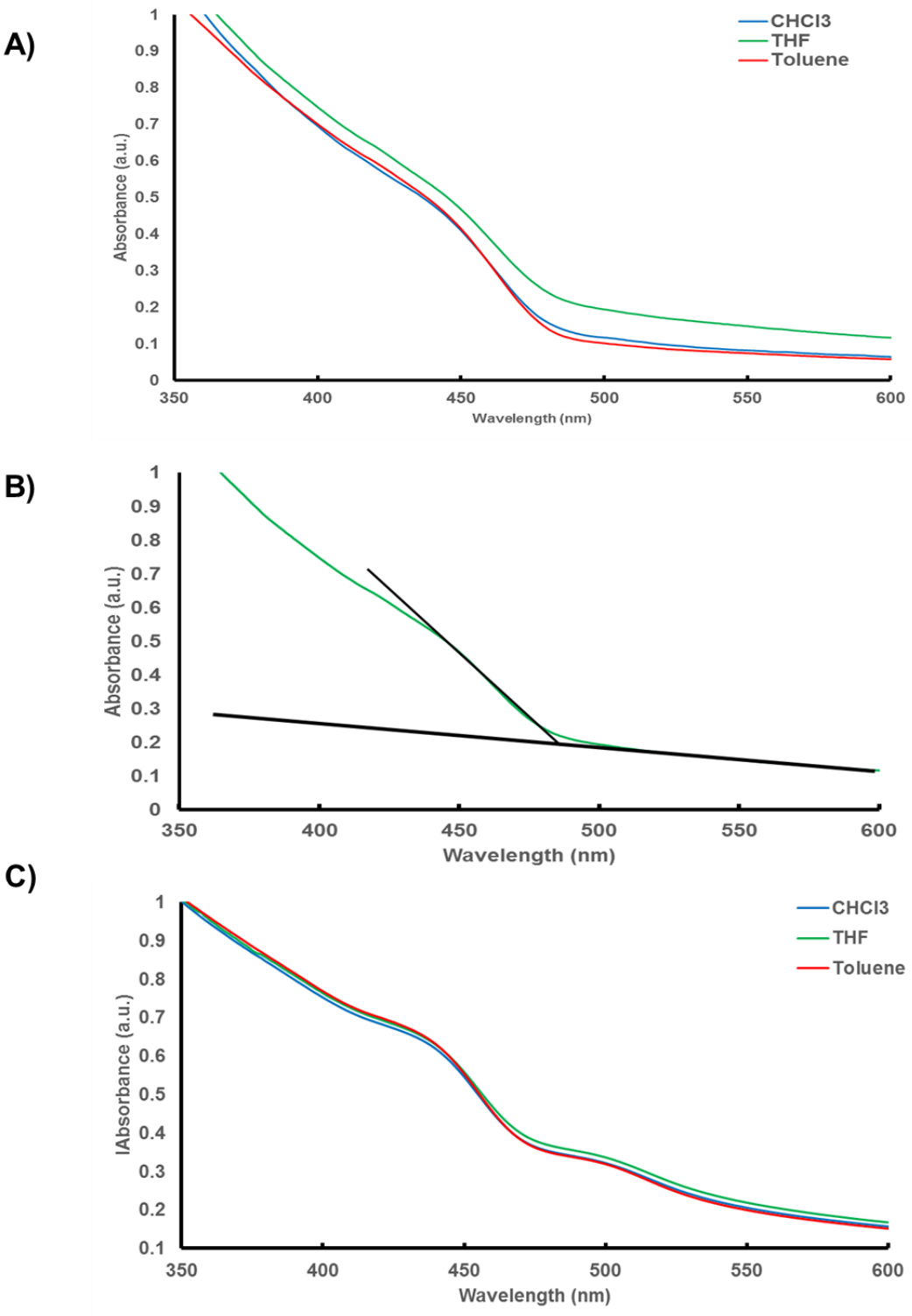

Figure 4.6. UV-Visible spectra of A) PMMA-154 and C) PMMA-54 NPs in THF, toluene and $CHCl_3$. B) shows how threshold energy was determined from the slope of the exciton shoulder of PMMA-154 in THF. The threshold determination for PMMA-54 can be found in Appendix C.

More detailed information about size and distribution was obtained by TEM. Figure 4.7 shows representative TEM images of each NP sample along with a size distribution histogram, while Table 4.1 shows the TEM sizes with standard deviation of measurements over three separate images. The QDs were well dispersed with limited clustering found for the PMMA-54 case. This dispersion suggests the each NP brush was capable of providing suitable solvent dispersion in the benzene casting solvent. Size histograms show a single QD population for each NP sample. These values compare quite nicely with the UV-Vis QD sizes. As the histogram shows a single population distribution for the PMMA-54 NPs, it is believed the second exciton peak is merely a secondary discrete energy state within the QDs.

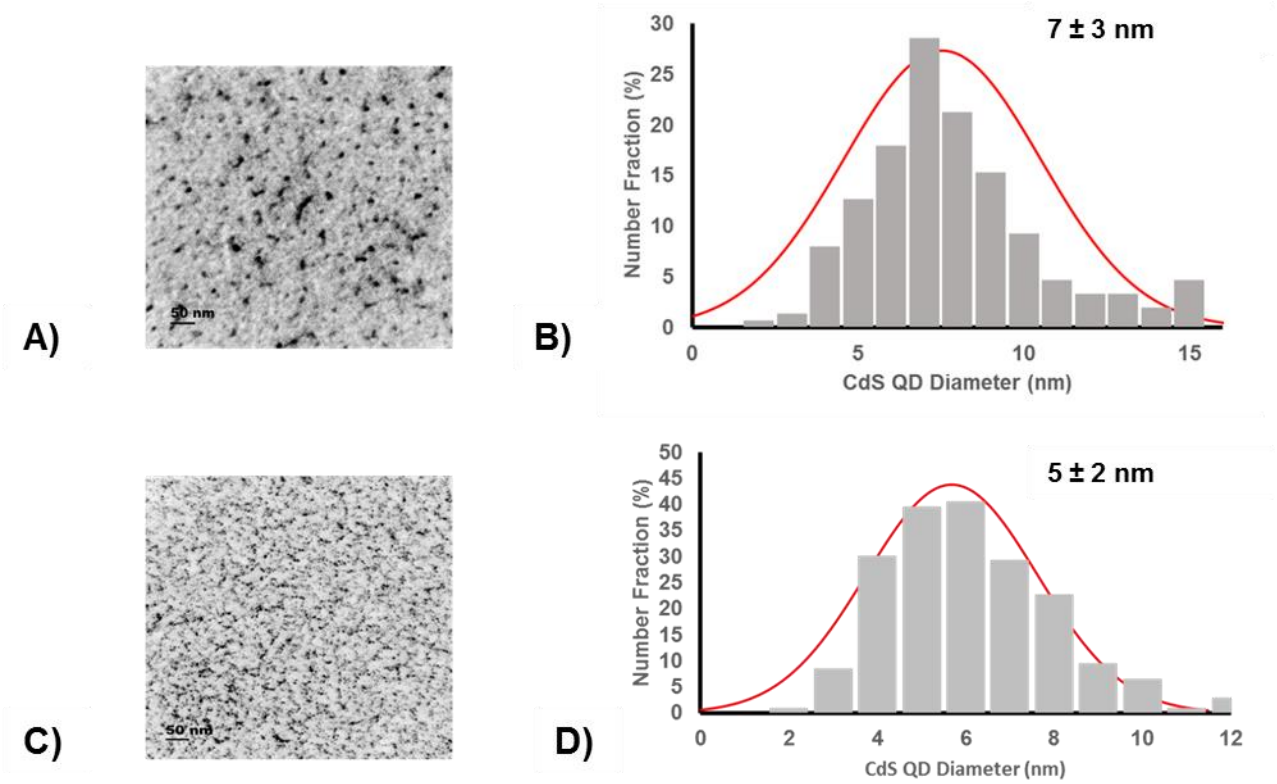

Figure 4.7. TEM image and associated CdS QD size distribution analysis of A,B) PMMA-54 and C,D) PMMA-154 cast from a 1 mg/mL benzene solution dispersed onto a carbon coated copper TEM grid. CdS QD size distribution determined from ~200 QD particles. Values show the uncertainty in the measurement of the individual grid.

4.3.3.3 NOESY NMR

Due to the mixed brush nature of these NPs, it is important to determine how the polymer brushes are distributed around the QD core. Figure 4.8 illustrates the three main distribution types that may arise: Janus, patchy and random.

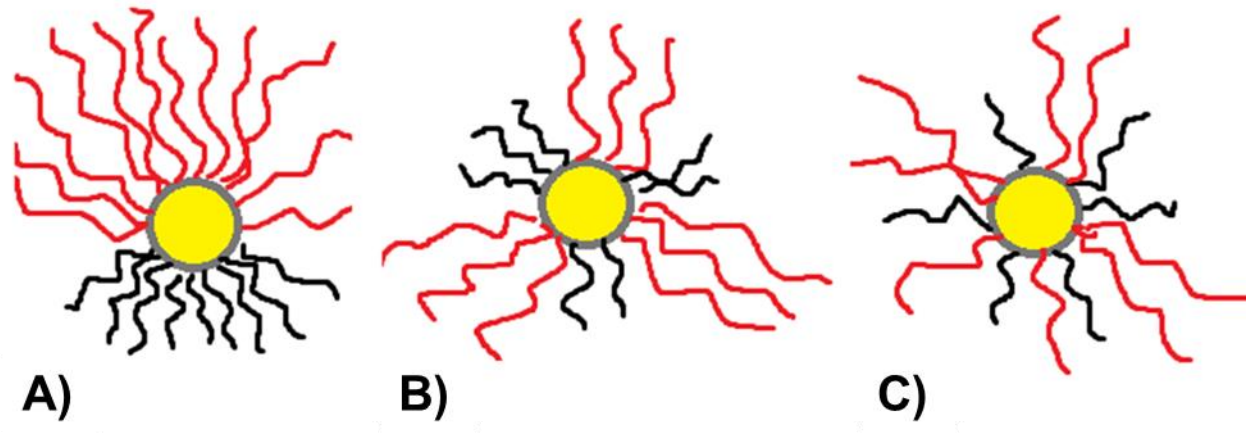

Figure 4.8. Schematic depicting a A) Janus distribution, B) patchy distribution and C) random distribution

A Janus distribution (A) is one that possesses an asymmetric brush structure in which the two polymer brushes segregate around the QD. A patchy distribution (B) possesses regions or "patches" of each polymer brush throughout the nanoparticle. A random distribution (C) refers to an instance in which the polymer chains are statistically distributed throughout the brush of the NP. One technique that has shown some promise in discerning between these different cases of brush distributions is 2D ^{1}H NOESY NMR. This technique looks at correlations between protons over short distances (~1 nm) through space, so examining the strength of NOE signal between PS and PMMA chains at the core can give information about the distribution of chains. A strong signal would indicate a random distribution, as the polymer brushes should be evenly distributed

throughout the brush. A weaker or non-existent signal likely indicates either a patchy or Janus distribution due to the segregation of the chains.

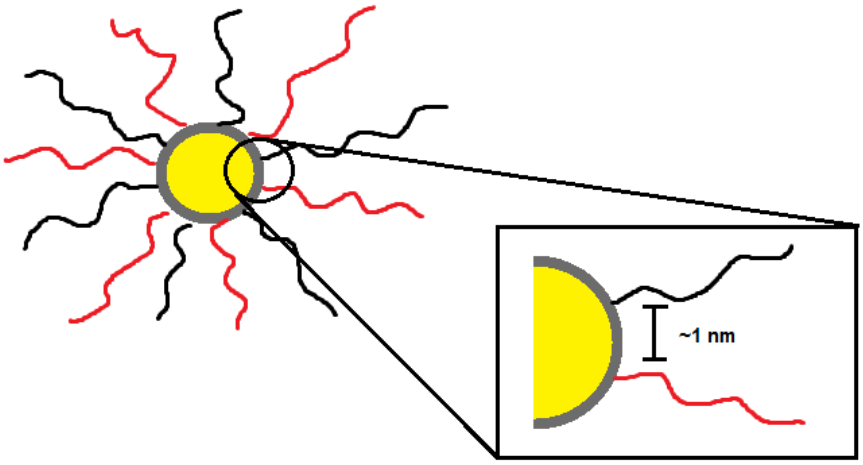

Figure 4.9. Schematic depicting the region of interest between polymer chains that will be probed by 2D ^{1}H NOESY NMR.

Previous work by Guo *et al.* determined the random distribution of the polymer brush when NPs were synthesized from a PS-*b*-PAA-*b*-PMMA triblock copolymer in which the PS and PMMA chains were of roughly equivalent length using 2D ^{1}H NOESY NMR.[33] The strength of the NOE signal between the PS styrene protons and the PMMA methoxy protons indicated a random distribution of polymer brushes around the CdS core.

This technique was also used to study the current polymers. Figure 4.10 shows the NOESY NMR spectra for each polymer as well as an unmicellized triblock copolymer for comparison. The blue circles indicate where a correlation between the PS styrene protons and the PMMA methoxy protons is expected to appear. In the case of each polymer, no signal was detected, suggesting the brush distribution in each NP was either a patchy or Janus distribution.

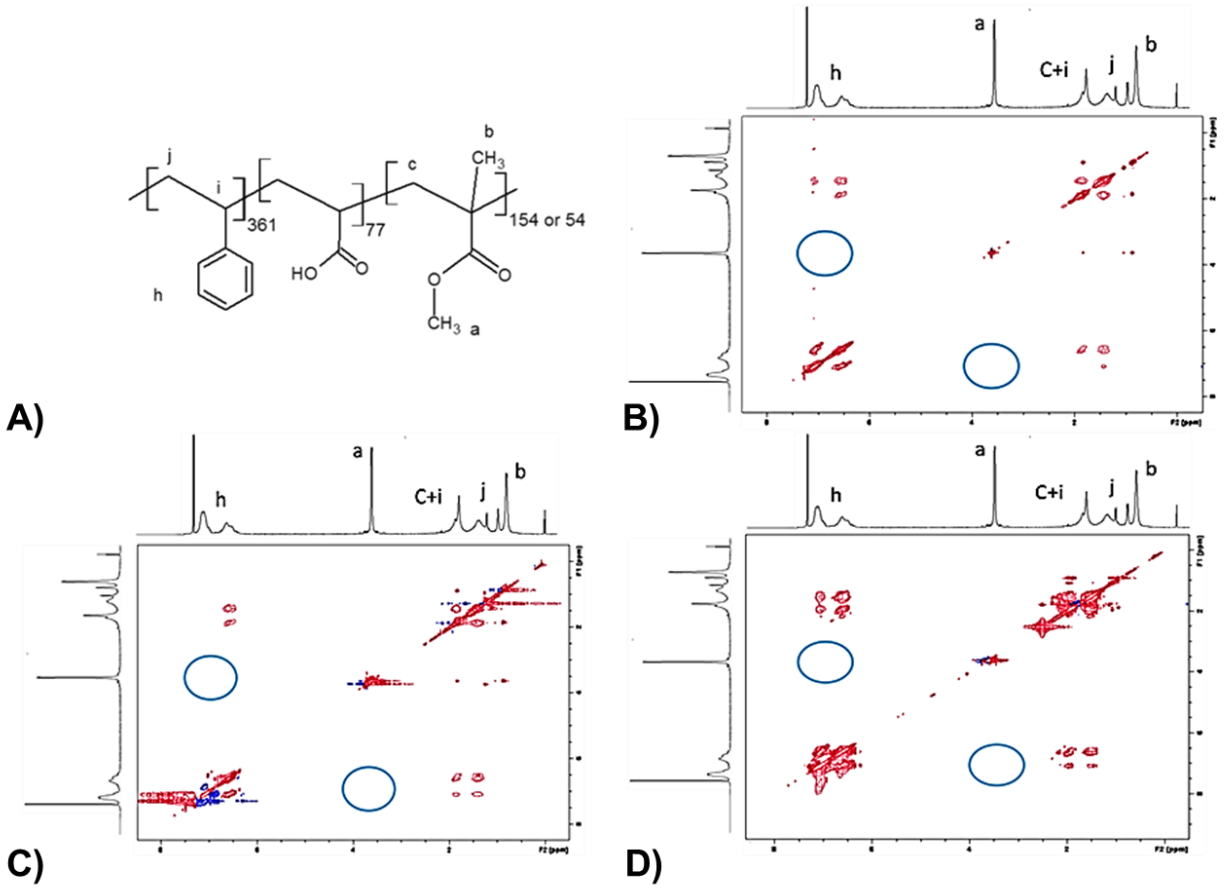

Figure 4.10. A) NMR Peak labelling for PS-*b*-PAA-*b*-PMMA triblock copolymer. 2D ^{1}H NMR NOESY spectra of B) PS-*b*-PAA-*b*-PMMA$_{(154)}$ triblock copolymer unmicellized, C) PMMA-54 NPs and D) PMMA-154 NPs. Reference in $CDCl_3$. Light blue circles in each spectra show the region where a cross-coupling signal is expected between the aromatic region of PS and the methacrylate region of PMMA. These signals were not present.

As noted above, a similar PS-*b*-PAA-*b*-PMMA polymer with roughly equivalent polymer lengths produced a random distribution,[33] while the current polymers had shorter PMMA chains indicating a patchy or Janus distribution. The shorter PMMA chain lengths likely allowed for greater mobility during cadmium acetate addition and micellization due to less steric crowding in the brush. This may have provided sufficient time for phase separation between PMMA and PS chains around the core before vitrification of the central PACd block.

4.3.3.4 Light Scattering

The use Zimm plot analysis by static light scattering (SLS) allowed for the determination of the weight-average molecular-weight, M_w, and the root-mean-square z-average radius of gyration, R_g, of each NP in THF. A representative Zimm plot for each NP sample in THF was presented in Figure 4.11. It should be noted that GPC has indicated a small amount of unmicellized polymer chain (<10%) still present such that measured values will have a minor contribution from these polymer chains. Each SLS measurement requires that the differential refractive index, d*n*/d*c*, for each PS/PMMA$_{XL}$(CdS) sample be determined as it is a component of *K* in the Zimm equation (see Chapter 1.7.2). The d*n*/d*c* values in THF were determined to be 0.16 ± 0.02 for PMMA-54 and 0.156 ± 0.002 for PMMA-154. Using this information together with the Zimm plot data, M_w values could be determined for each NP sample, M_w is directly related to the number of chains in the NPs, therefore the aggregation number, *Z*, can be calculated by dividing the M_w values by a weighted-average molecular weight of the two constituent unimers ($M_{n,PS\text{-}b\text{-}PAA\text{-}b\text{-}PMMA(54)}$ = 48553 g/mol and $M_{n,PMMA\text{-}b\text{-}PAA\text{-}b\text{-}PMMA(154)}$ = 58565 g/mol) plus one CdS unit per carboxylate group (77 × 144.47 g/mol = 11124 g/mol) and one additional Cd^{2+} ion for every two carboxylate groups (38.5 ×112.411 g/mol = 4312 g/mol), This

equation (Equation 4.2) is shown below with a sample calculation for PMMA-154. The results can be found in Table 4.3.

$$Z = \frac{M_w}{M_{PS-b-PAA-PMMA} + M_{CdS} + M_{Cd^{2+}}} \qquad \text{(Equation 4.2)}$$

$$= \frac{6.3e^6}{58565+11124+4312} = 85$$

The aggregation number for these particles is much lower than previously explored triblock and diblock mixed brush NPs. The Z = 85 of the PMMA-54 and the Z = 72 for the PMMA-154 are about half of Guo's PS/PMMA$_{XL}$(CdS) NPs at this stage in the synthesis (Z ~ 200)[33] and less than the analogous diblock copolymer NPs found in chapter 2 of this work (Z ~ 120). It is important to note that similarities between the two triblocks suggest despite the different lengths, they still create NPs of roughly the same number of polymer brushes, which allows for proper comparison during the self-assembly step to be described later.

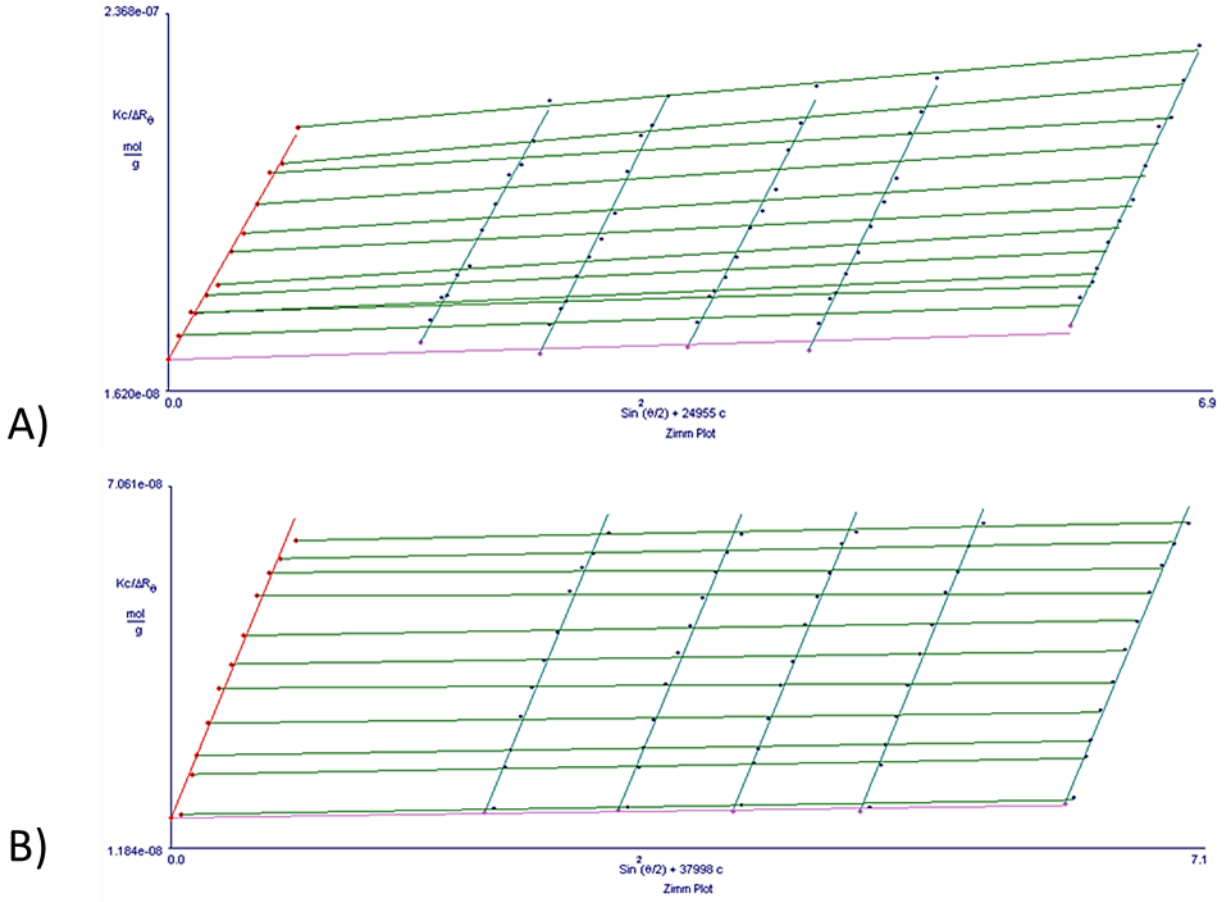

Figure 4.11. Representative Zimm plot for of light scattering data (SLS) for the A) PMMA-54 and B) PMMA-154 NPs in THF. The measured angles were from 30° to 145° in increments and the solution concentrations were from .1 mg/mL to .01 mg/mL

The chain density can be determined using the aggregation number and the surface area from the PAA the surface area of the PACd encapsulated QDs. The PS/PMMA polymer brush is grafted to a hybrid core consisting of a central QD and a surface layer of collapsed PACd chains; we estimate a total core diameter of $2r_c$ based on QDs size from TEM surrounded by Z chains with 77 PACd repeat units each in the melt state. This is determined by Equation 4.3 (a sample calculation is presented for PMMA-154) and QD sizes from UV-Vis (Table 4.1), and these are also reported in Table 4.2.

$$\frac{Z * 77 * (M_{PAA} + M_{Cd}/2)}{N_A} = mass\ of\ PACd\ layer$$

$\frac{85*77*(72+56)}{6.023e^{23}}$ = 1.39 x 10^{-18} g PACd

$$\frac{mass\ of\ PACd\ layer}{density\ of\ PACd\ layer} = volume\ of\ PACd\ layer \qquad \text{(Equation 4.3)}$$

$$\frac{1.39 \times 10^{-18} g}{2\frac{g}{cm^3}} = 6.95 \times 10^{-19} cm^3 = 695\ nm^3 = volume\ of\ PACd\ layer$$

$$V_{Cds} = \frac{4}{3}\pi r_{Cds}^3 = 69.4\ nm^3$$

$$= V_{Cds} + volume\ of\ PACd\ layer = 784.92\ nm^3$$

$$r_c = \sqrt[3]{\frac{3V_c}{4\pi}} = 5.68\ nm$$

As the cores appear to have a roughly spherical shape, their surface area was determined using Equation 4.4, with a sample equation performed for PMMA-154:

$$A = 4\pi r_c^2 \qquad \text{(Equation 4.4)}$$

$$A = 4\pi(5.68)^2 = 405\ nm^2$$

By using aggregation numbers from SLS (Table 4.2), the ratio of chains/nm^2 can be determined by Equation 4.5., which also shows a sample calculation for PMMA-154. The aggregation number is doubled as each triblock copolymer contributes a PS and a PMMA chain.

$$\rho_{chains} = \frac{2Z}{A} \qquad \rho_{chains} = \frac{170\ chains}{405 nm^2} = 0.42\ \frac{chains}{nm^2} \qquad \text{(Equation 4.5)}$$

The density of the chains in the PMMA-154 NPs are similar to those of the PMMA-54 NPs. This suggests the two brush of the two particles are quite similar, and only differ in the length of the PMMA brush.

Table 4.2. Summary of the PMMA-154 and PMMA-54 Results from Static and Dynamic Light Scattering in THF

x	***M*$_w$** **x *10^6 (g/mol)***	***Z***	**ρ$_{chains}$ (chains/nm^2)**	**r_g (nm)**	**r_h (nm)**	**r_g/r_h**	**t_b (nm)**	**Extension (%)**
54	4.6 ± 0.4	72 ± 7	0.35	108 ± 13	112 ± 3	0.99	104	115
154	6.3 ± 0.2	85 ± 4	0.40	111 ± 4	73 ± 3	1.48	65	72

Zimm plot data also gave radii of gyration, r_g, values for each NP sample (see Table 4.2). r_g's between the PMMA-54 and PMMA-154 are comparable within standard deviation. These

values are quite large if we compare with Guo's more compositionally symmetric triblock NPs (~30 nm). NOESY NMR data appears to indicate a Janus or patchy distribution of the polymer brush on the NPs. As PS and PMMA have a large difference in their d*n*/d*c* values (PS = 0.185, PMMA = 0.08 in THF), It is hypothesized that the polymers in the corona are phase separating into Janus or patchy particles, producing a scattering of the particle that is no longer spherical. The distribution of scattering centers goes form being isotropic (spherically symmetric) to anisotropic as the composition of the brush becomes highly asymmetric.

DLS was used to determine the hydrodynamic radii, r_h and are tabulated in Table 4.2. The r_h values for PMMA-54 are near identical with the r_g values, while the r_h for PMMA-154 is 40 nm less than the r_g. By using the r_g/r_h, we can once again determine shape information of the particles. As r_g is determined from the distribution of scattering centers and r_h is determined from solvent interactions, the full extension of the polymer brush creates more scattering centers far from the core, allowing r_g to be larger than r_h. A hard sphere would have an r_g/r_h of 0.77, while star-like micelles can hold values between 1.1-1.4.[66] The PMMA-154 sample appears to be on the high end of the micelle region, likely due to the longer PMMA chains creating more "open", star-like structures with large free volume on the periphery. The PMMA-54 sample is closer to 1, suggesting a more spherical shape. This likely arises due to the relatively short PMAA chains creating a more compact particle. The r_g will receive more contribution from the PMMA chains than the r_h as r_g is determined based on the information closer to the core.

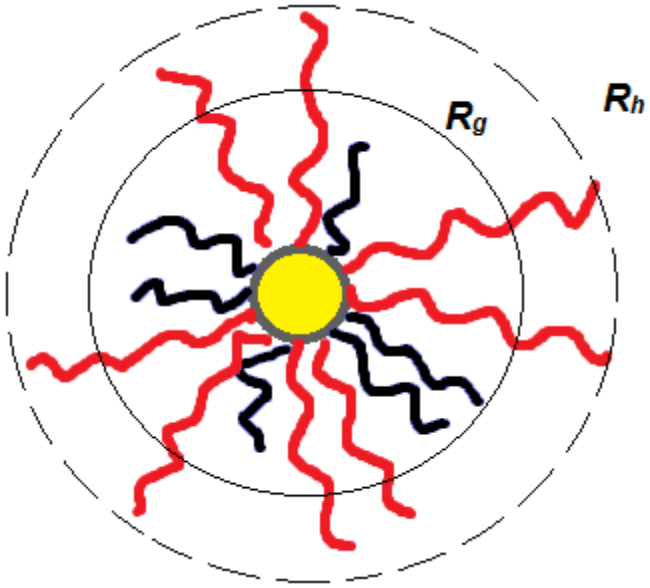

Figure 4.12 Schematic depicting r_h and r_g for the x = 54 NPs.

The r_h values displayed in Table 4.2. are based on the Cumulant analysis, which are average values from a fit of the distribution of exponentials to a Gaussian function. A CONTIN analysis can be performed to determine more information about the distribution of hydrodynamic particles in solution. For each sample, there was a single distribution of particles when experiments were performed at 90^o under low concentrations (Figure 4.12).

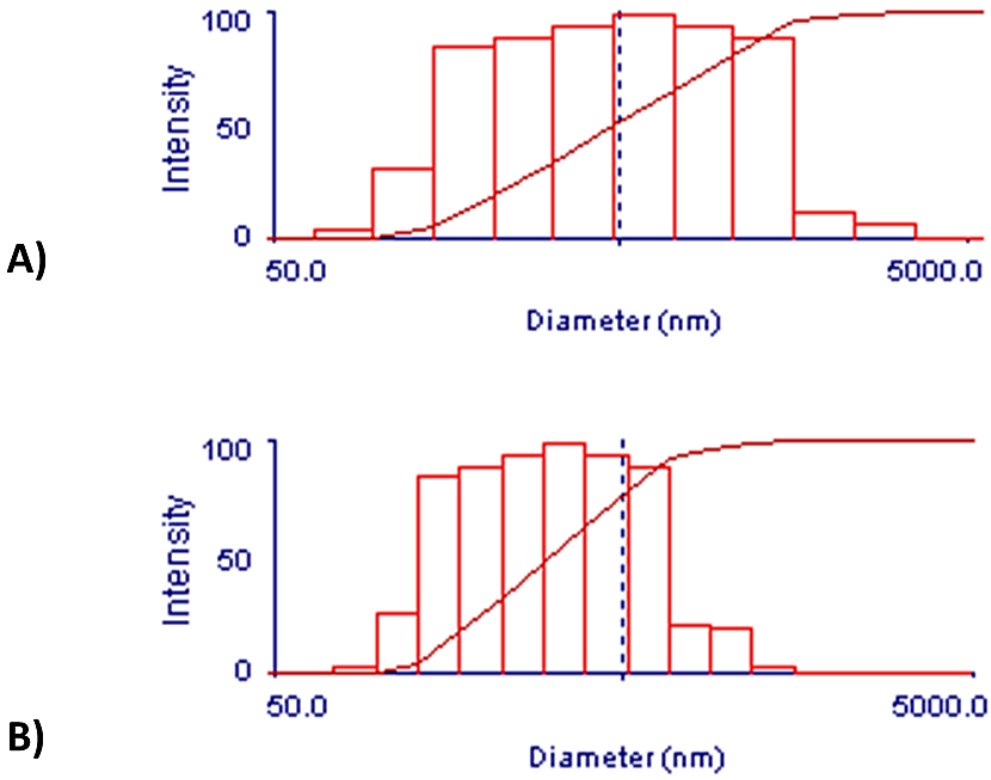

Figure 4.13. Hydrodynamic particle size distribution from CONTIN analysis of dynamic light scattering of A) PMMA-54 and B) PMMA-154 NPs in THF. These results were obtained at a 90 ^{o} scattering angle and concentration of ~0.1 mg/mL

R_h can also be used to determine the thickness of the polymer brush, t_b, in solution. This can be determined based on the difference of the r_h and the r_c (the radius of the TEM core size plus the thickness of the PAA layer) and is tabulated in Table 4.2. As THF is a good solvent for both PS and PMMA, the fact that the number of PS repeat units is much greater than the number of PMMA chains suggests that this brush thickness refers to the extension of the PS chains. The chain extension is calculated in equation 4.6 (with a sample calculation for PMMA-54).

Chain extension (%) = 100 x (t_b/[aN]) (Equation 4.6)

$$= 100 * (104/[0.25 * 361] = 115\ \%$$

Where a is the length of one repeat unit at full extension (a = 0.25 nm) and N is the number of PS repeat units in the polymer chain (N = 361). The PMMA-54 NP sample has an extension of ~120 %. This suggests that there is likely some aggregation in THF, as this value indicates the chains are extending beyond their possible limits. The 72 % chain extension experienced by the x = 154 is likely due to the ability of the PS chains to be solvated beyond the full extended length of the PMMA chains, having access to a region with far fewer chain interactions.

4.3.4 Hydrolysis of PMMA Brush Chains to PMAA: Converting PS/PMMA$_{XL}$(CdS) to PS/PMAA-(CdS)

4.3.4.1 Characterization of PS/PMAA-(CdS)

Upon completion of structural characterization at the PS/PMMA$_{XL}$(CdS), the hydrophobic PMMA chains were hydrolyzed to PMAA through the use of KOH and 18-crown-6 in refluxing dioxane for 4 days under and N_2 atmosphere. ^{1}H NMR spectra showing before and after hydrolysis can be found in Figure 4.14. The methoxy peak at 3.61 ppm is greatly reduced, leaving <5% of the PMMA unmicellized (mole % remaining by NMR integration). Attempts to separate this remaining component by fractionation and precipitation were unsuccessful.

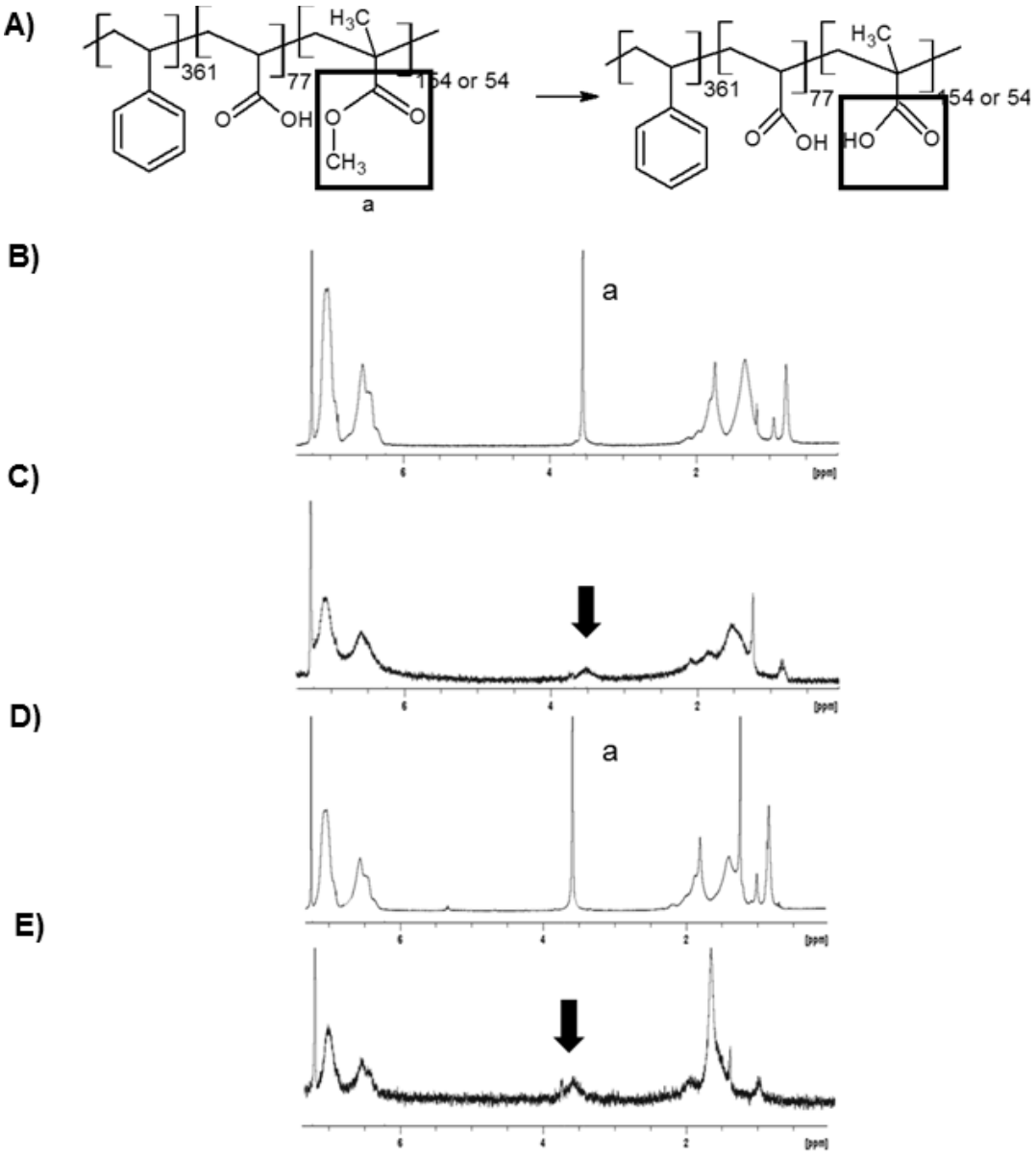

Figure 4.14. A) Schematic depicting the hydrolysis from PMMA to PMAA and the NMR region of interest. ^{1}H NMR spectra of B) PMMA-54 C) PMAA-54 D) PMMA-154 and E) PMAA-154, showing the loss of the methoxy group and the formation of the methacrylic acid unit

Due to the aggressive conditions of the hydrolysis reaction, GPC was used to determine the structural integrity of the NPs after hydrolysis (see Figure 4.15). For PMAA-54, the NP peak at ~11 min shifted to overlap with single chain peak, suggesting a decrease in hydrodynamic radii or a change in shape. Peak deconvolution (Appendix B) shows no increase in the single

chain population, indicating that the NPs remain intact after hydrolysis. The PMAA-154 NPs also show no change in the single chain population, indicating that the crosslinking was successful in holding the NP together during hydrolysis.

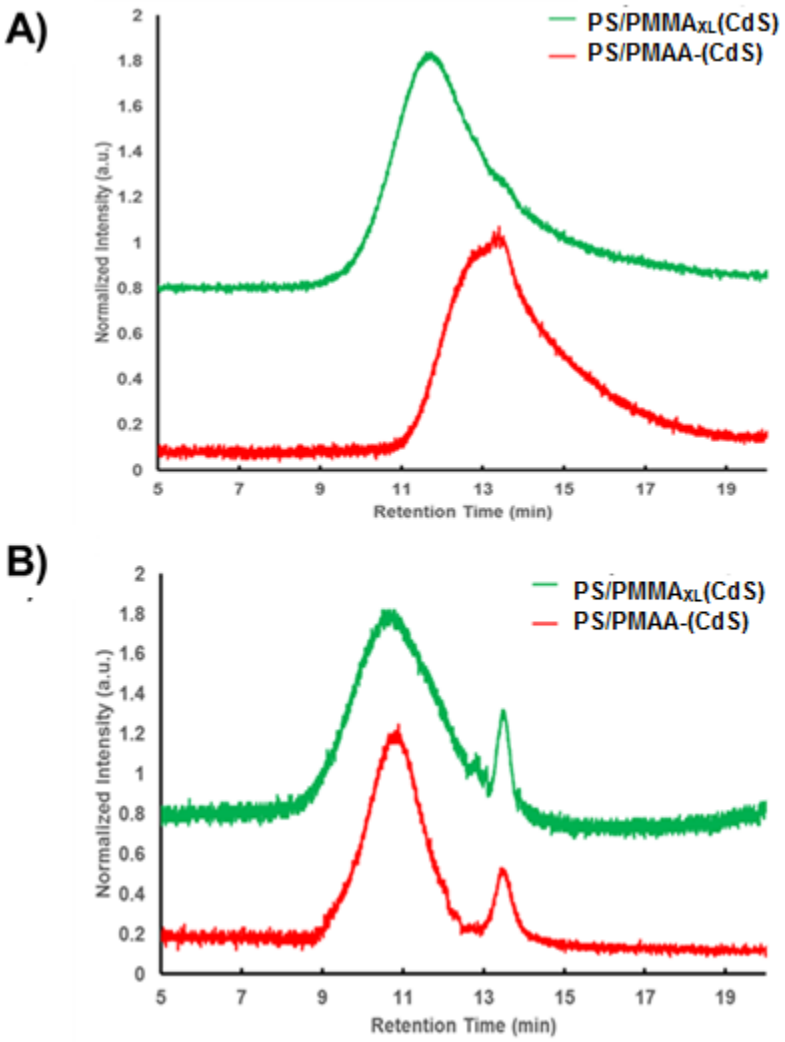

Figure 4.15. GPC (refractive index detector response) comparison of A) PMMA-54 and B) PMMA-154 before and after hydrolysis of PMMA brushes to PMAA. All GPC chromatograms were run using THF as the eluent solvent.

The hydrodynamic radii, r_h, in THF was measured after hydrolysis to compare with r_h in THF before hydrolysis. As table 4.3 shows, the hydrodynamic radii after hydrolysis appears to be ~2x greater than that before hydrolysis. As r_h is longer than the fully stretched length of the PS or PMAA chains, this suggests that some aggregation is occurring in solution. Since THF is the solvent used for self-assembly, it is important to note that limited assembly may be occurring before the addition of water in the self-assembly step.

Table 4.3. Hydrodynamic Radii, r_h, of each NP Sample in THF Before and After Hydrolysis as Determined by Dynamic Light Scattering

(x)	**r_h – PMMA (nm)**	**r_h – PMAA (nm)**
54	112 ± 3	196 ± 7
154	73 ± 3	142 ± 1

CONTIN analysis was also performed on these solutions, as can be found in Figure 4.16. The CONTIN analysis shows a single population distribution for each NP sample, suggesting that these r_h values were not arising from a mixed population of large and small particles.

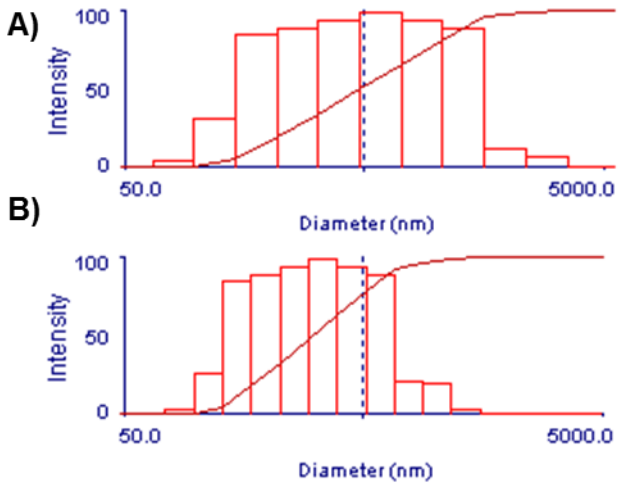

Figure 4.16. Hydrodynamic particle size distribution from CONTIN analysis of dynamic light scattering of A) PMAA-54 and B) PMAA-154NPs in THF. These results were obtained at a 90 ^{o} scattering angle and concentration of ~0.1 mg/mL.

4.3.4.2 Characterization of the CdS QDs by TEM and XRD

TEM images were taken of each NP sample to determine if QD core sizes remained the same after hydrolysis and to also visualize any aggregation that may be occurring. It is important to note that aggregation caused by drying does not necessarily indicate aggregation in the solution phase, but since disassembly is uncommon during the drying phase good dispersion on the grid likely indicates good dispersion in the solution phase. The TEM images (Figure 4.17) appear to show limited aggregation of QDs, which is in contrast with the DLS. It is important to note that DLS examines the sample in the solution phase, while TEM focuses on the dried sample. It should also be noted benzene was used as a casting solvent due to significant drying artifacts that appeared when cast in THF. For each case, individual QD sizes remain the same as

those measured before hydrolysis, suggesting the QDs were stable and did not undergo growth or dissolution throughout the reaction.

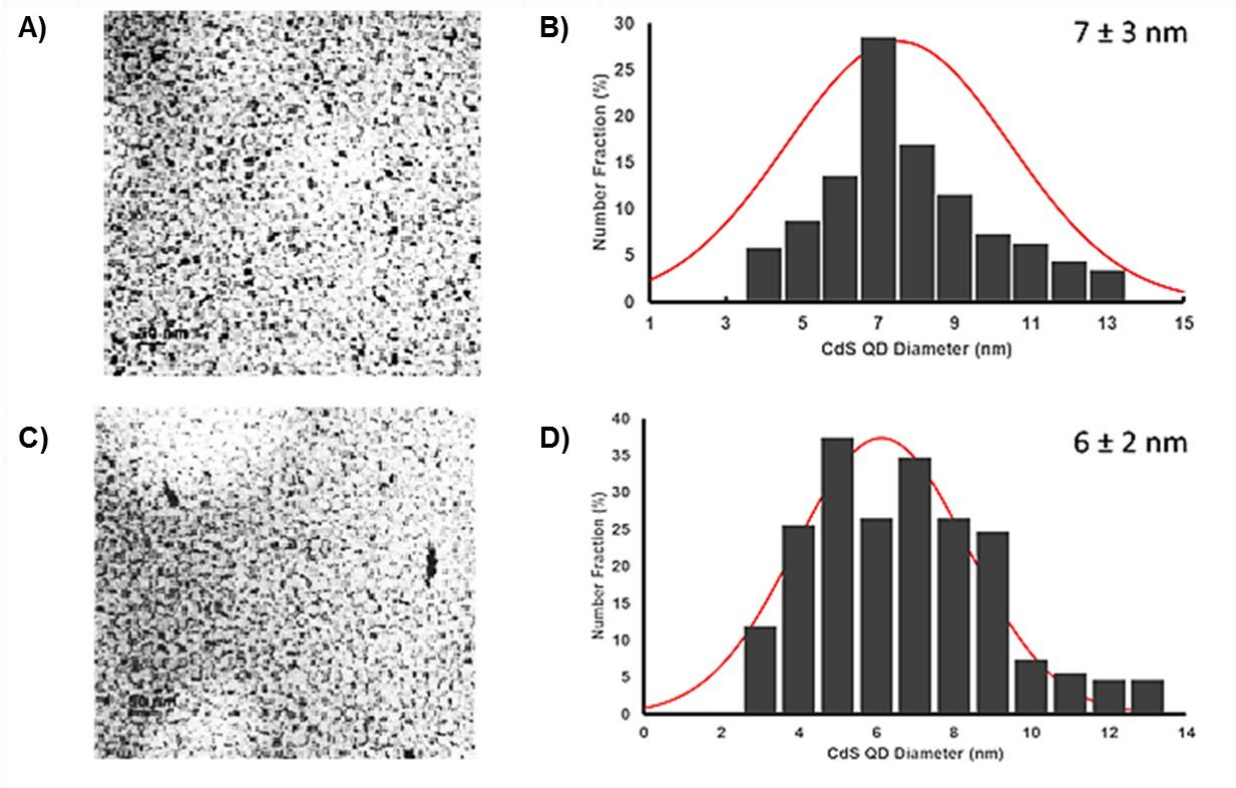

Figure 4.17. TEM imagery and CdS QD size distribution of A,B) PMAA-54 and C,D) PMAA-154 NPs cast from a 1 mg/mL benzene solution. The average size is displayed in the top left with the uncertainty in the measurement of the individual grids.

Table 4.4. TEM Measurements of the QD Core Sizes of PS/PMAA-(CdS)

	QD Size (nm)
PMMA-54	7.1 ± 0.3
PMMA-154	5.9 ± 0.4

X-ray diffraction experiments were also performed on each NP sample to show the lattice structure of the CdS core. Figure 4.18 shows the XRD patterns of PMAA-54 and PMAA-154. The red lines indicate these diffraction patterns match that of cubic CdS as found in the JCPDS database.[63] The one exception is the peak that is found at 2θ ~30 °. The *d* spacing of this peak (determined using Bragg's Law) is 0.56 nm. It was determined using light scattering that the chain density of each particle is ~1 chain/nm^2, corresponding to an interchain distance of ~1 nm. Therefore this scattering peak may arise from mean distance between PS and PMAA polymer chains at the surface of the CdS core, as proposed earlier in the work of Guo et al.[33] By looking at the brush composition dependence of the diffractograms for the first time, this work further supports the assignment of the 2θ ~30° peak to interchain scattering at the QD surface: we note that the intensity of the peak relative to the CdS reflections increases with the PS content, consistent with the fact that PS is a more electron dense polymer than PMMA and will therefore scatter x-rays more strongly.

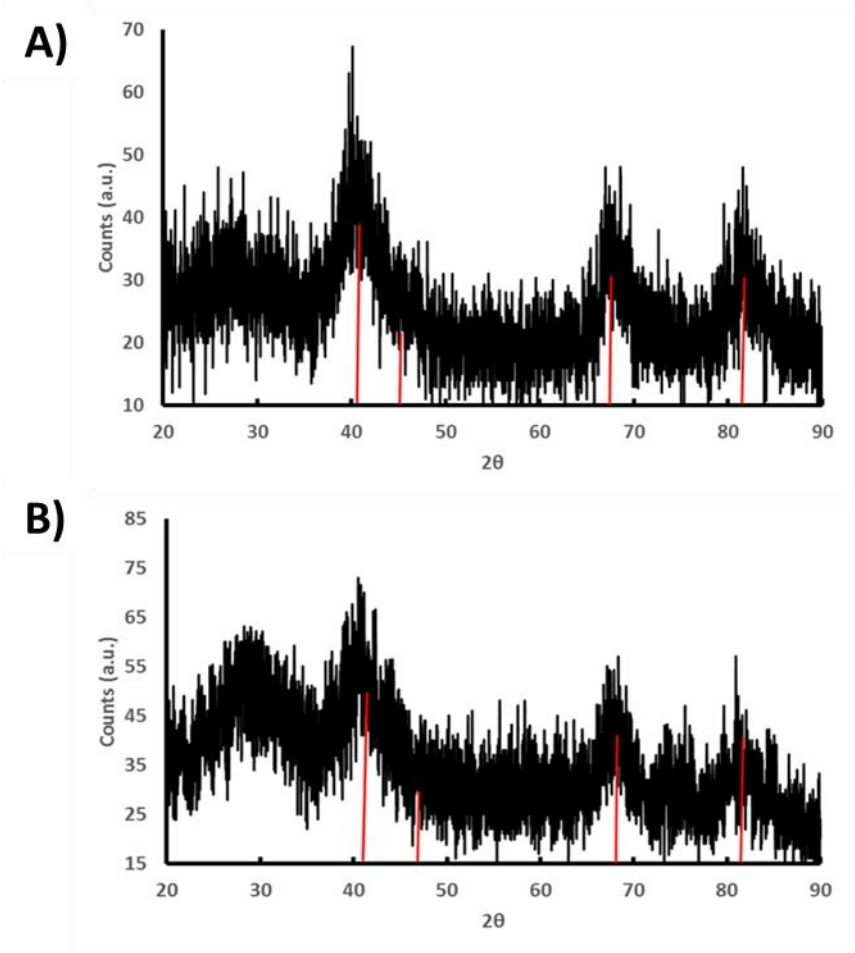

Figure 4.18. Powder x-ray diffractograms from A) PMAA-54 and B) PMAA-154 with red lines indicating the location of the four main peaks associated with cubic CdS

4.3.5 Overview of PS/PMAA-CdS Morphologies from the Self-Assembly of PS/PMA$_{XL}$(CdS) NPs in THF/H$_2$O Mixtures

When PS/PMAA-(CdS) NPs underwent self-assembly in THF/H_2O solutions, many different morphologies could be created based on the length of the PMAA chain (x), the initial polymer concentration (c_0) and the ratio of NaCl added in comparison to each PMAA repeat unit (R_{NaCl}). This section will give an overview of the different morphologies found and present representative TEM images of each. The present system showed spheres, vesicles, compound vesicles and large compound supermicelles, each of which have analogous structures when compared with block copolymer micelle systems.[43,130,134,135,147]

The morphologies presented in this work were identified using several key pieces of information. It is known that the preassembled structure of the NPs consist hydrophobic PS chains and hydrophilic PMAA chains tethered to a CdS QD in the core. This should lead to phase separation of the two chains around the CdS core, leaving the CdS to form the interface between each polymer region (Figure 4.19). As the self-assembly experiments are performed by transitioning from THF to H_2O, it is expected that the PMAA chains will form the outer surface or in the lumen of the superstructure and the PS chains will be found on internal surfaces.

Information derived from TEM images can also give clues to the self-assembled morphology in solution. TEM shows regions of high electron density as dark areas on an image, while lower electron density areas give lighter sections. As the CdS QD represents the highest electron density region of the NPs, they will present as the darkest region on the grid. PMAA will represent the lightest structure due to its minimal electron density, with PS chains a shade of grey in between the PMAA and CdS.

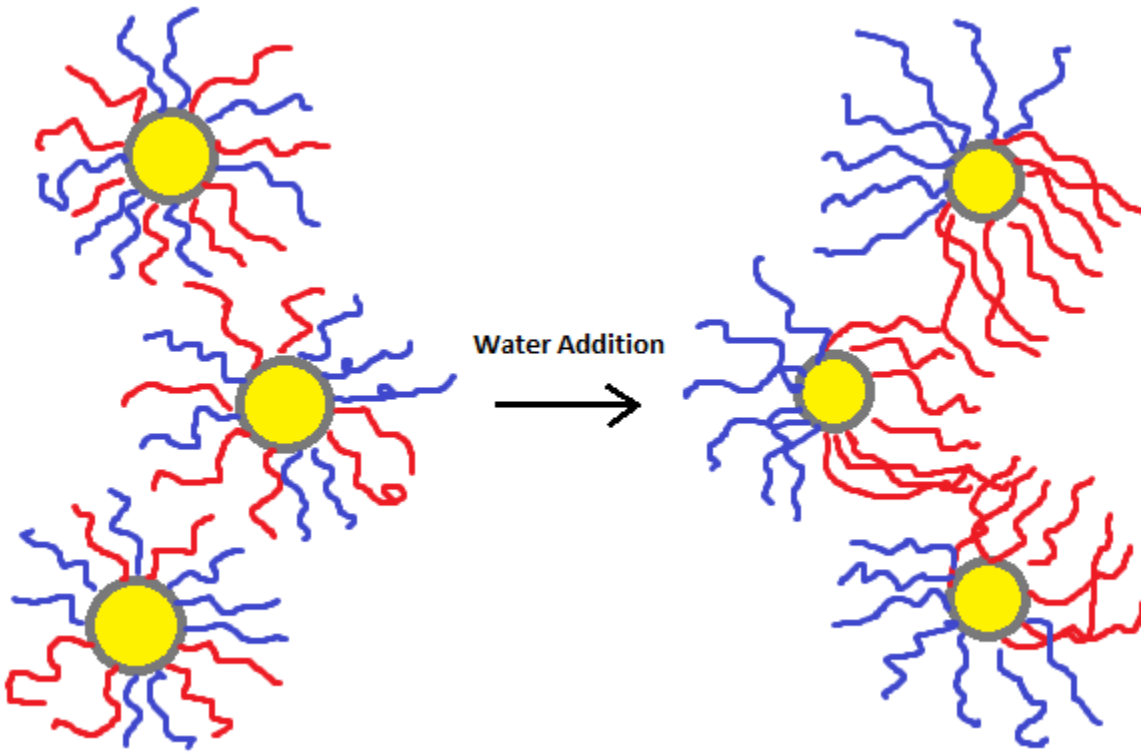

Figure 4.19. Schematic detailing the phase separation of PS and PMAA polymer chains when solution changes from THF to H_2O. The NPs form the interface between each region.

4.3.5.1 Spheres

Spheres are the morphology that have the highest internal curvature of those observed. Spheres consist of a spherical core filled with hydrophobic PS chains that are protected from the aqueous solvent environment by a coronal brush of PMAA. CdS QDs form an interface between the polymer chains due to the phase separation that occurs around them. Figure 4.20 A) shows a schematic diagram of a sphere formed from preassembled PS/PMAA-(CdS) NPs, while B) shows a representative TEM image of a sphere morphology.

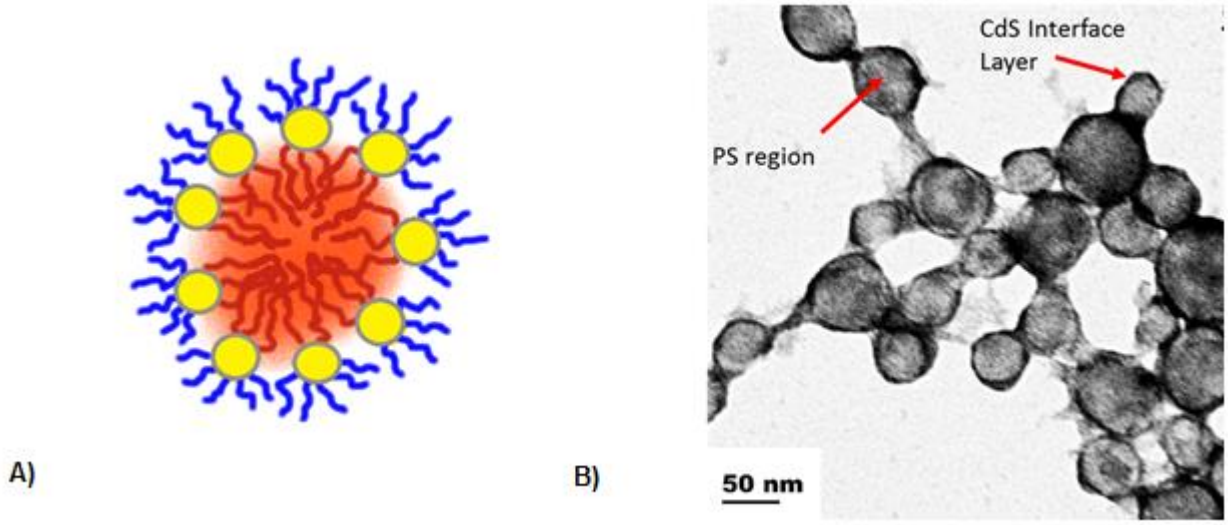

Figure 4.20. A) Schematic representing a spherical PS/PMAA-(CdS) assembly. B) Representative TEM image of spheres formed from the self-assembly of PMAA-154 with c_0 = 0.25 wt % and R_{NaCl} = 1.5

4.3.5.2 Vesicles

Another observed morphology was a vesicular NP assembly, analogous to vesicles seen when block copolymers are self-assembled. Vesicles are bilayer structures with inward pointing PS chains making up the vesicle wall. PMAA chains form both the external corona of the particle and the concave surface of the lumen found within the NP. These two layers are arranged with the CdS QDs forming the interface of both the lumen and the corona. A vesicle has less internal curvature than a sphere as the creation of the second layer allows for a minimization of chain interactions between PS chains, allowing the CdS NPs to pack closer together. Figure 4.21 A) shows a schematic diagram of a vesicle formed from preassembled PS/PMAA$_{(x)}$-(CdS) NPs, while B) shows a representative TEM image of a vesicle morphology.

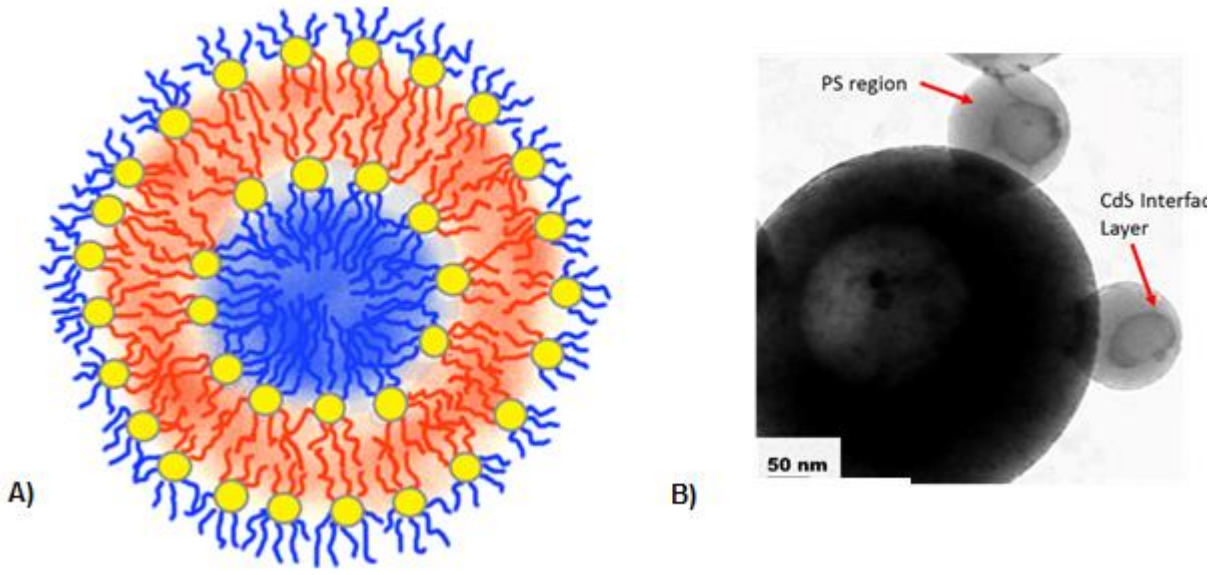

Figure 4.21. A) Schematic representing a PS/PMAA-CdS vesicle. B) Representative TEM image of vesicles formed from the self-assembly of PMAA-54 with c_0 = 0.25 wt % and R_{NaCl} = 0 (no salt added).

4.3.5.3 Compound Vesicles

A compound vesicle is similar to a vesicle morphology except that there are multiple lumen present within the NP. The multiple lumen create many convex surfaces where PS chains are located. This increases the free volume available to the PS chains and minimizes steric interactions between polymer chains compared to single lumen vesicles. This decrease in energy comes at a cost to the energy of the PMAA chains, which are now further distributed on the concave interfaces of the lumen. It has been suggested by Eisenberg[130] that compound vesicles are a kinetic structure as opposed to a thermodynamic structure. It is believed that they are formed from many vesicles that normally fuse together. But if the rate of collision between vesicles is faster than the rate of fusion, multiple lumen may be present. In this work, compound vesicles and vesicles are treated as separate assemblies as compound vesicles are found in solution after annealing, but further experimentation is needed to fully deem them separate assemblies. Figure 4.22 A) shows a schematic diagram of a compound vesicle formed from preassembled PS/PMAA-(CdS) NPs, while B) shows a representative TEM image of a compound vesicle.

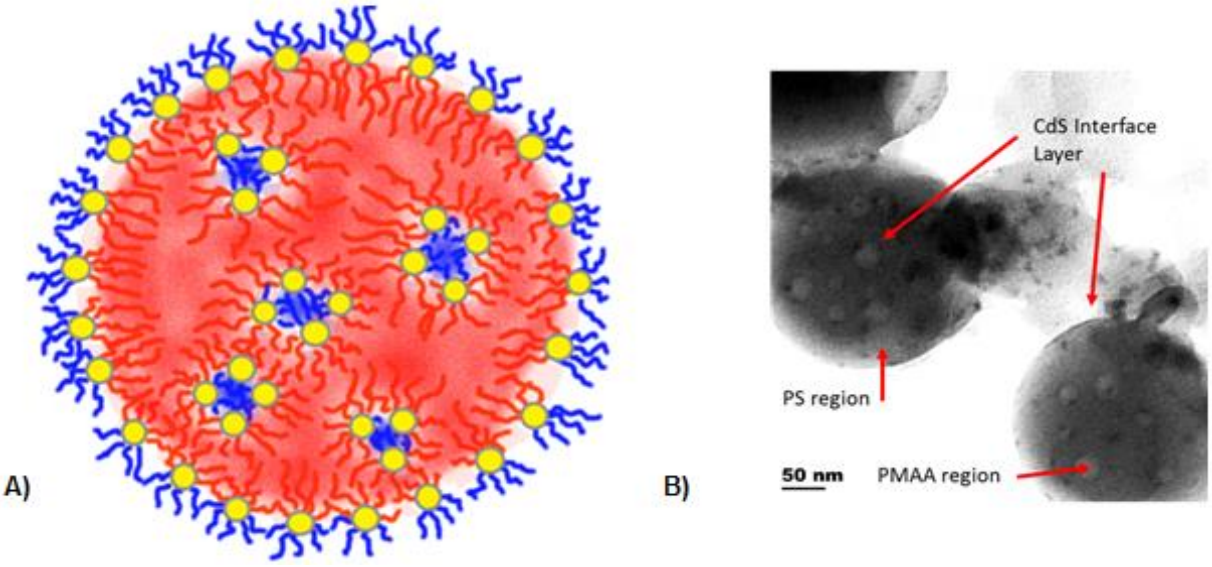

Figure 4.22. A) Schematic representing a PS/PMAA-CdS compound vesicle. B) Representative TEM image of compound vesicles formed from the self-assembly of PMAA-54 with c_0 = 0.25 wt % and R_{NaCl} = 0 (no salt added).

4.3.5.4 Large Compound Supermicelles (LCS)

The final morphology of note that was observed is that of the large compound supermicelle, which are analogous to the large compound micelles (LCMs) created from block copolymers as reported by Eisenberg *et al.*[134] These aggregates form roughly spherical shapes of individual NPs forming the periphery with PS chains pointing inwards and PMAA chains pointing outwards around the CdS interface. Other single NPs are found within the particle with PMAA chains collapsed around the QD core and PS chains forming a hydrophobic matrix. This morphology has the lowest convex surface area for PS chains, minimizing chain interactions and

steric crowding more than any other morphology that was discovered. A schematic and representative TEM image of a large compound supermicelle can be found in Figure 4.23.

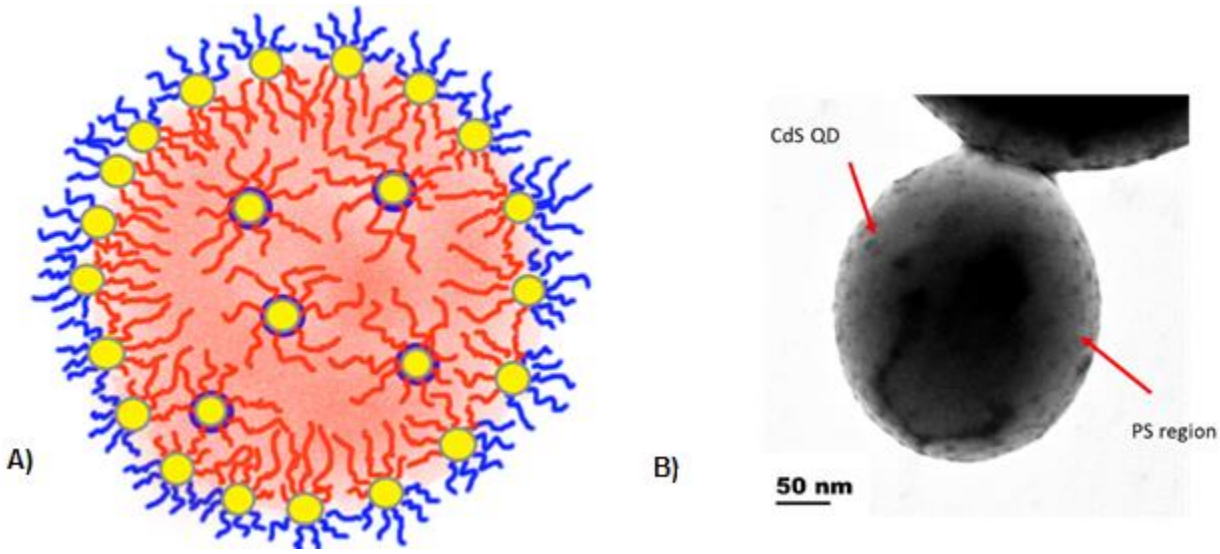

Figure 4.23. A) Schematic representing a PS/PMAA-(CdS) large compound supermicelle. B) Representative TEM image of compound vesicles formed from the self-assembly of PMAA-54 with c_0 = 0.50 wt % and R_{NaCl} = 3.0 (no salt added).

From these structures, it can be seen that the relaxation of steric interactions between PS chains through changes in the interfacial curvature can be a major driving force for morphological change in these systems. Therefore, the morphologies presented thus far can be ranked in order of decreasing PS steric interactions:

Spheres (*high concave curvature*) > Vesicles (*low concave curvature*) > Compound Vesicles (*intermediate convex curvature*) > Large Compound Supermicelles (*high convex curvature*)

4.3.6 Determination of the Critical Water Concentration (cwc)

During each self-assembly experiment, the critical water concentration (cwc) was determined visually when the clear solutions became turbid upon addition of water. These results can be found in Table 4.5. As each experiment was performed only once these are only roughly estimated values

Table 4.5 cwc Values Determined from the Addition of Water to a Solution of PS/PMAA-(CdS) in THF

R_{NaCl}	c_0 (wt %)	*PMAA-54*	*PMAA-154*
0.0	0.25	~12	~16
	0.50	~11	~14
	0.75	~7	~14
	1.00	~1	~13
1.5	0.25	~11	~14
	0.50	~7	~10
3.0	0.25	~11	~14
	0.50	~7	~12

The PMMA-54 NPs show lower cwc values in general than the PMMA-154 NPs. This is most likely due to the soluble block (PMAA) being shorter and less able to disperse the NPs in a poor solvent for the PS chains which makes up a large majority of the NP brush. The cwc also decreases for each sample as the c_o increases, as these particles will have a higher aggregation number of particles in which the soluble block makes up the smallest weight fraction of the

coronal brush. This is best noted in the case of PMMA-54 and c_o = 1.00, as this solution reaches its cwc almost instantaneously, most likely a result of short PMAA block lengths and very high aggregation numbers. The addition of salt to each solution appears to decrease the cwc, likely due to the salt screening out the PMAA charge interactions with the strong dipole found in water.

4.3.7 Effect of PMAA Brush Length on Amphiphilic Self-Assembly of NPs

The ability to create two different PS/PMAA-(CdS) NP samples with different lengths of the PMAA polymer chain allow the opportunity to probe the effect that the length of the hydrophilic block will have on self-assembly. As a triblock copolymer was used, the PMAA and PS chains are tethered together through the PAA/CdS core, meaning that there is an equal number of PS and PMAA chains in both PMMA-54 and PMMA-154 NPs. This suggests that any change in morphology under the same self-assembly conditions is the result of the different length of soluble chains in the two samples. Experiments were carried out at a series of c_o and R_{NaCl}, providing an opportunity to compare under many conditions. This chapter will focus on comparing the two different polymers at specific conditions and discussing the results. A complete list of all of the assemblies formed can be found in Table 4.6.

Table 4.6. Summary of Self-Assembly Morphologies for PS/PMAA-(CdS).

	R_{NaCl}	c_0 = 0.25	c_0 = 0.50	c_0 = 0.75	c_0 = 1.00
154	0.0	s	cv	cv	cv
	1.5	s	s		
	3.0	s	s		
54	0.0	s	cv	cv	
	1.5	l	cv		
	3.0	l	l		

When c_o = 0.25 wt %, both PMMA-154 and PMMA-54 self-assemble into spheres (Figure 4.24 A and B). The PMMA-154 NPs creates smaller spheres than the PMMA-54 NP sample, the TEM sizes of which can be found in Table 4.7. When the c_o is increased to 0.50 wt %, each block length creates compound vesicles (Figure 4.24 C and D). Compound vesicles are also created for the c_o = 0.75 case. The PMMA-154 remains relatively unchanged, while PMMA-54 NPs presents compound vesicles with many large lumen within the NP (figure 4.24 E and F). At the highest c_0 of 1.00 wt %, the PMMA-154 presents as compound vesicles (Figure 4.24 G), while the PMMA-54 undergoes macroscopic precipitation in solution.

Table 4.7 TEM Measurement of the Characteristic Dimensions for each PS/PMMA-CdS Assembly

	R_{NaCl}	c_0 = 0.25	c_0 = 0.50	c_0 = 0.75	c_0 = 1.00
PMAA-154	0.0	39 ± 2[s]	--	--	--
	1.5	47 ± 1[s]	64 ± 4 [s]		
	3.0	51 ± 6 [s]	48 ± 2 [s]		
PMAA-54	0.0	110 ± 20 [s]	--	--	--
	1.5	--	--		
	3.0	--	--		

Characteristic dimensions include: size (spheres), cylinder width (cylinders) and wall thickness (vesicles). Spheres are denoted by *. All other assemblies presented as compound vesicles or large compound supermicelles, of which there is no characteristic dimension

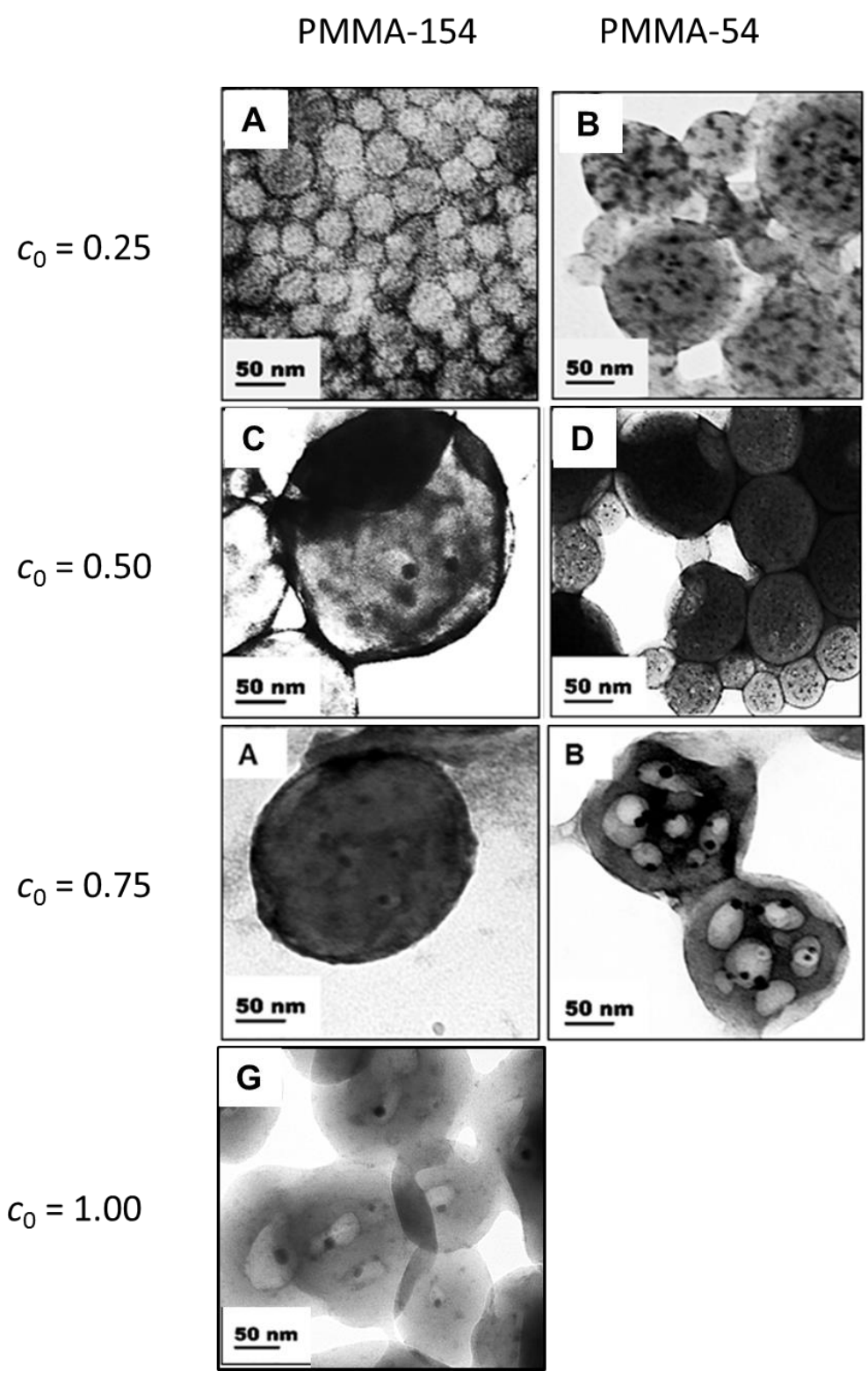

Figure 4.24. Representative TEM images comparing the morphologies produced during the self-assembly of each block length at multiple c_0.

In terms of the assemblies found for each c_0, the block length of the PMAA chain appears to have no major effect. The morphologies present for each case at PMMA-154 are the same found at PMMA-54, although there is some variation in the size of the particles and their individual lumen. This likely arises from the fact that although the chain lengths vary, the number of each PS and PMAA chain does not. As the PS composes the greatest fraction of each NP, PS chain interactions dominates the energetics of the system. The PMAA chains form on the corona and the lumen as a result of the minimization of PS chain interactions. While longer PMAA chains may increase the number of chain interactions in each lumen, the majority are found on the corona in the "crew-cut" region.[134] As this is the region where polymer chains are most densely packed (as demonstrated earlier in our use of 2D NOESY NMR to determine the chain distribution), this is where the greatest chain PMAA chain interactions will occur. Increasing the length of these chains will not change interactions at the CdS interface as the extra chain length will be extended into the solvent. (Figure 4.25). Therefore, changing the block length has a minimal effect on the self-assembly of these NPs.

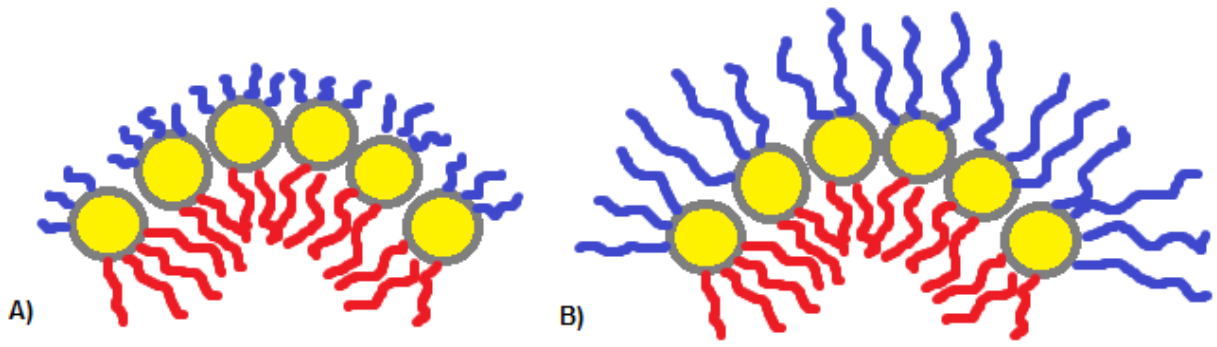

Figure 4.25. Schematic depicting the distribution of polymer chains in A) PMMA-54 and B) PMMA-154. Although the chain lengths increase, the number of PMMA chains remains the same on the corona.

While the block length may have limited effect on the morphology, it does have some effect on the size of the assembled spheres at low c_0. As the PMAA chains become further extended in the solvent, chain interactions will become more prevalent. The coronal chains on spheres will begin to feel repulsive effects from these chains, limiting the packing of QDs along the interface. The less dense the packing, the more the external curvature will increase to minimize PMAA chain interactions. Therefore, it makes sense that the PMMA-154 would produce smaller, higher curvature spheres.

4.3.8 Effect of Initial PS/PMAA(CdS) NP Concentration on Amphiphilic Self-Assembly of NPs

While the variation of the PMAA chain length was one variable of interest for the self-assembly of these NPs, another is the initial PS/PMAA(CdS) NP concentration (c_o) before self-assembly. It has been shown in the case of both block copolymer systems[43,123] and Guo's triblock NP samples[63] that the changes in c_o had an effect on the resultant morphologies and was therefore of interest in this work. Four c_o values were selected for this work: 0.25, 0.50, 0.75 and 1.00 wt %. For each PS/PMAA-(CdS) sample, morphological and structural changes were present as the c_o was increased, as can be seen in Figure 4.26.

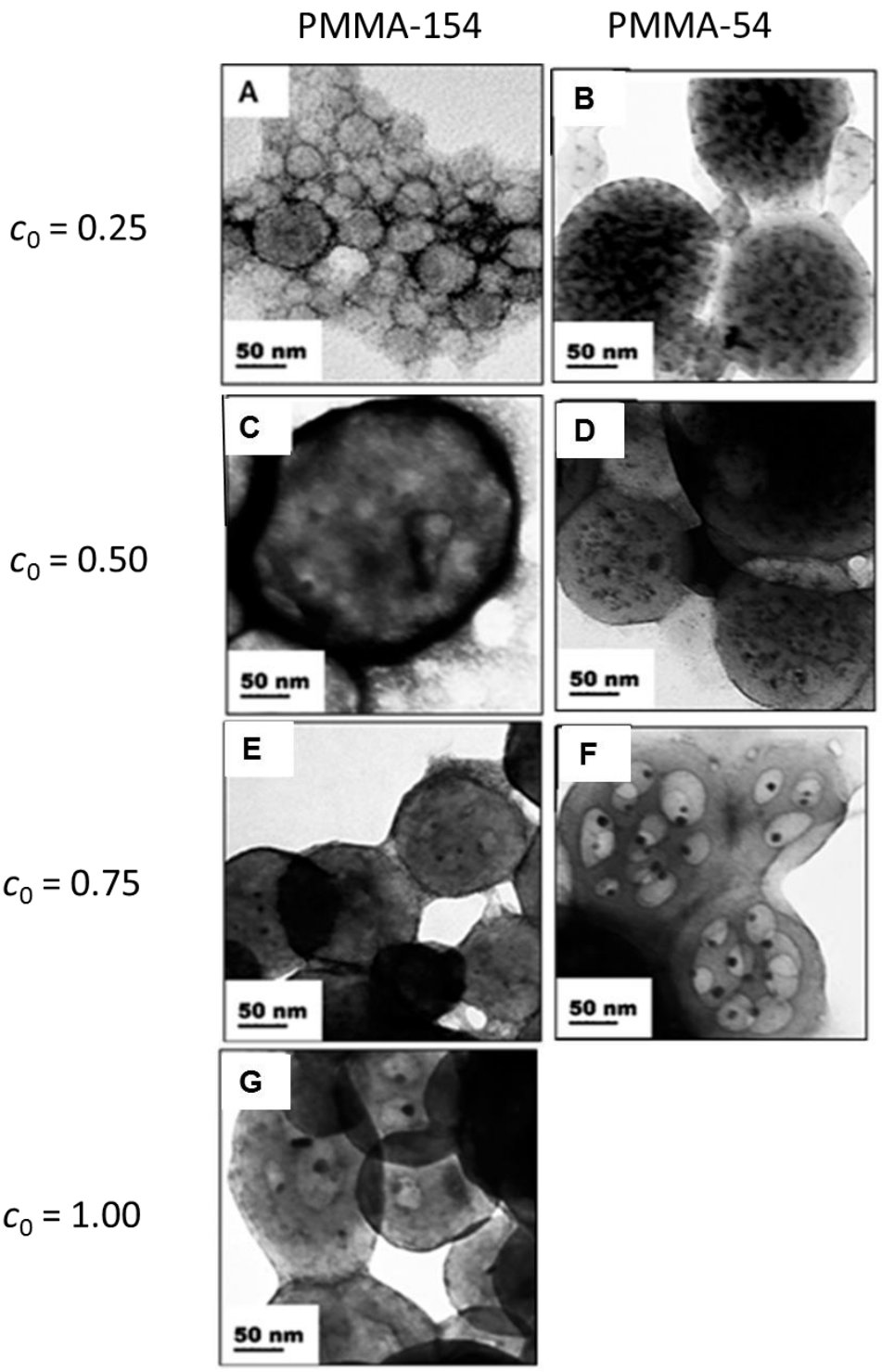

Figure 4.26. Representative TEM images comparing the morphologies produced during the self-assembly of each block length at multiple c_0.

At c_o = 0.25 wt %, the main morphology was spheres. As the c_o was increased, compound vesicles were found at c_o = 0.50, 0.75 and 1.00 wt %. This data suggests that increasing c_o has the effect of creating higher curvature structures from the PMMA-154 NPs at c_o = 0.50 than at 0.25, but that further increases induce no further change. The PMMA-54 NPs also show a similar trend, in which increasing the c_o from 0.25 to 0.50 wt % will induce compound vesicles compared to spheres, but further increases cause no morphological change. It should be noted that increasing c_o from 0.50 to 0.75 wt % appears to increase the size of the lumen, but it still remains a compound vesicle.

Eisenberg *et al.* has shown that increasing c_o leads to an increase in aggregation number in NPs as described by Equation 4.8.[43]

$$N_{agg} = 2\left(\frac{c_o}{cmc}\right)^{\frac{1}{2}} \qquad \text{(Equation 4.8)}$$

where N_{agg} is the aggregation number and *cmc* is the critical micelle concentration. Higher aggregation number leads to diminished chain extension of the PS on convex surfaces through increased chain interactions, as seen in Figure 4.27.

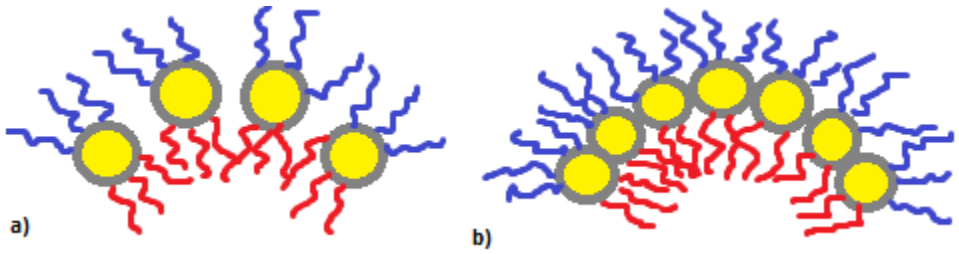

Figure 4.27. Schematic showing aggregation number and subsequent chain interactions at A) low c_o and B) high c_o. Higher aggregation numbers contribute more polymer brushes to each interface, decreasing chain extension through crowding effects.

In the case of Eisenberg's work, increased aggregation number correlated with the creation of lower curvature morphologies to accommodate the increased number of NPs. It is believed that increased c_o and, in turn, aggregation number leads to the self-assembly of lower curvature structures in these NP systems. The transition from spheres to compound vesicles in both PMMA-154 and PMMA-54 is a result of the increased aggregation number, leading to a change to lower curvature structures. Further transitions do not occur at higher c_o as the creation of the lumen pockets is enough to limit chain interactions between PS chains.

4.3.9 Effect of Salt Addition on the Amphiphilic Self-Assembly of NPs

As the PMAA chains are partially charged, there is an extra repulsive effect between chains due to charge repulsion. By adding NaCl, charge repulsion effects can be minimized and the free volume accessible to the polymer chains will be increased. NaCl was added before self-assembly began and was added in three different ratios of NaCl to PMAA repeat units: R_{NaCl} = 0.0, 1.5 and 3.0. In this section, each PS/PMAA-(CdS) NP sample will be shown self-assembled at a specific c_o, showing the morphologies found at each R_{NaCl}.

In the case of PMMA-154, very little morphological change can be found when c_o = 0.25 as spheres are predominant throughout (figure 4.28). When c_o = 0.50 wt %, the NPs change in morphology from low curvature compound vesicles to higher curvature spheres as the R_{NaCl} increases (Figure 4.29).

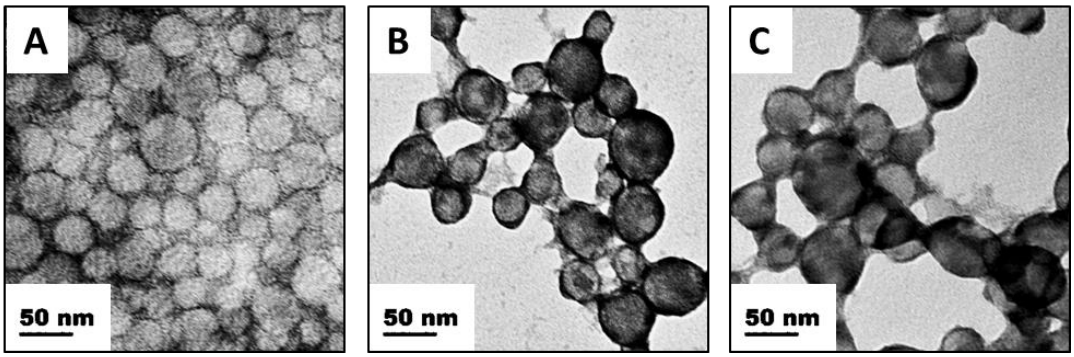

Figure 4.28 TEM images of PMMA-154 at c_o = 0.25 when R_{NaCl} = A) 0.0 B) 1.5 and C) 3.0.

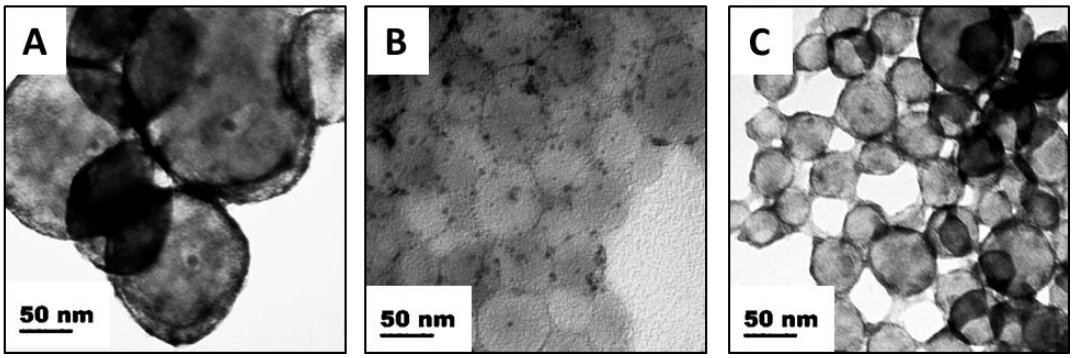

Figure 4.29 TEM images of PMMA-154 at c_o = 0.50 when R_{NaCl} = A) 0.0 B) 1.5 and C) 3.0.

In the case of the PMMA-54 NPs upon self-assembly at c_0 = 0.25, the morphologies decrease in curvature (spheres to large compound vesicles) as the R_{NaCl} increases (Figure 4.30). In the case of the c_0 = 0.50 wt % experiments, there is a progression of compound vesicle to LCS's (Figure 4.31).

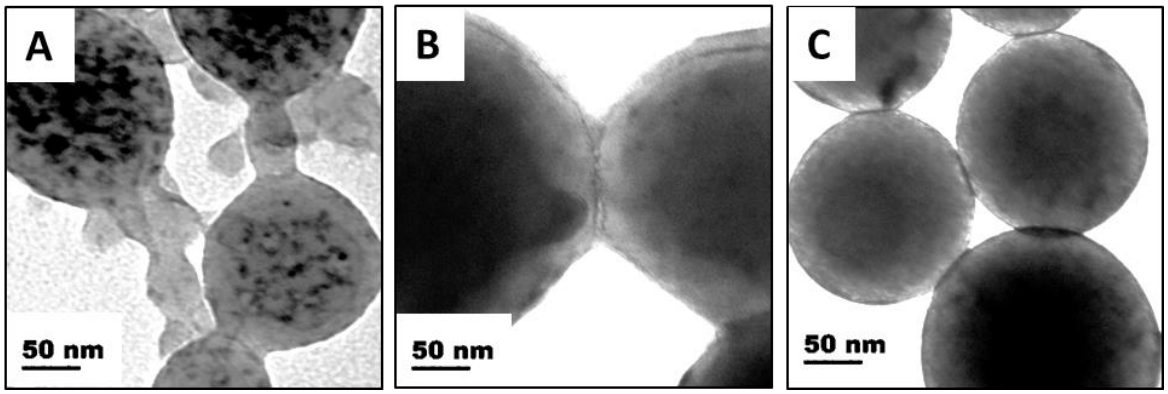

Figure 4.30. TEM images of PMMA-54 at c_o = 0.25 when R_{NaCl} = **A)** 0.0 **B)** 1.5 and **C)** 3.0

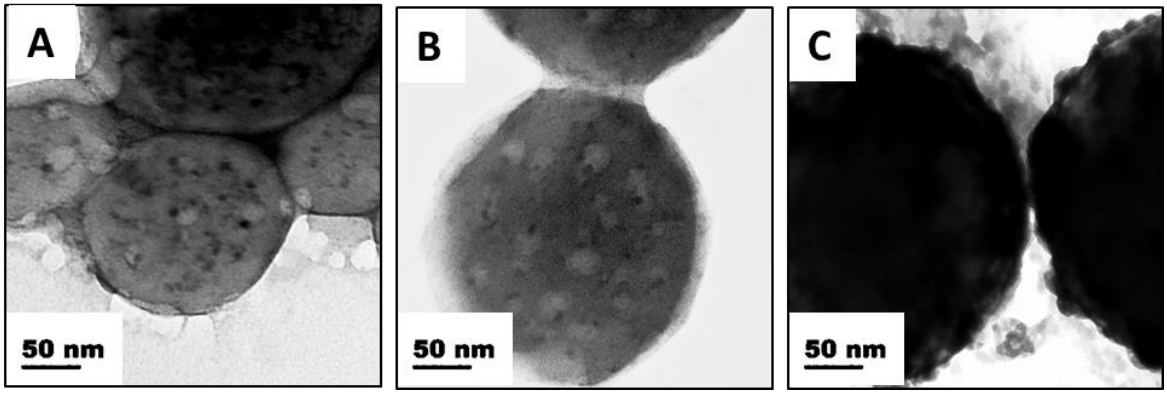

Figure 4.31. TEM images of PMMA-54at c_o = 0.25 when R_{NaCl} = **A)** 0.0 **B)** 1.5 and **C)** 3.0

For the case of the PMMA-154 NPs, there is an overall trend of high internal curvature (spheres) to lower internal curvature (compound vesicles and LCS's) as R_{NaCl} increases (See Figure 4.30 and 4.31). As the addition of salt screens out repulsive charge interactions between polymer chains, more free volume becomes accessible to the brushes. The PMAA chains can pack together tighter on the surface and in lumen pockets. As the energy associated with the PMAA chains is decreased, the longer PS chains will be capable of forming bilayer structures to minimize their chain interactions. At higher salt contents, the PMAA chains on internal NPs will collapse entirely around the CdS while PS chains aggregate to create a region of hydrophobicity within the macrostructure.

The results for the self-assembly of PMMA-54 with the addition of salt don't appear to follow the above trend (Figure 4.31). At c_o = 0.25 wt %, spheres present the dominant morphology at all salt contents. This is likely due to a low aggregation number at the interface allowing the charged PMAA brushes enough free volume for the relatively short chains to avoid interactions. When c_o = 0.50 wt % (Figure 4.31), the NPs form compound vesicles (a relatively low curvature structure) without salt, but as salt is added spheres (a higher curvature morphology) become dominant. This is the opposite of the trend above. As the addition of salt screens out repulsive effects between charged polymer brushes, the chains will be able to pack tighter together. As the PMAA polymer brushes are relatively short, there are still minimal chain interactions due to a lack of extension that is available to the PMMA-154 NPs. Therefore, the NPs prefer to form higher internal curvature structures due to their lower overall free energy.

4.3.10 Dynamic Light Scattering of NP Assemblies

Further information about the solution behaviour of these particles could be determined by determining the hydrodynamic radii (r_h) by dynamic light scattering (DLS). The PMMA-154 material appears to have undergone higher degrees of aggregation during the initial self-assembly experiments (R_{NaCl}), as noted from the large aggregation numbers and high polydispersity (Table 4.8). With the addition of salt (R_{NaCl}), the particles appear to undergo less aggregation and become much less polydisperse. This suggests that the aggregation results from the charged nature of the polymer brushes. As the PMAA chains have a partial charge, there are electrostatic interactions between these chains and the CdS surfaces of other NPs in solution.[63] This electrostatic interactions may be enough to cause aggregation, despite the PMAA charge

repulsion from surface chains. As salt is added, the PMAA charge is mitigated by the NaCl ions. The interactions between NPs are limited and aggregation is suppressed.

While values for the PMMA-154 sample were obtained in full, the PMMA-54 showed high levels of macroscopic precipitation upon self-assembly. Rigorous filtration of these samples was performed in an attempt to collect data, but the low dispersability afforded by the short PMAA blocks left little to no material in the solution phase. This aggregation likely also arises from the PMAA/CdS core electrostatic interaction. Since these PMAA chains are shorter, the particles can pack together tighter and the strength of the interaction will be stronger. This leads to aggregation and precipitation, even in the presence of salt.

Table 4.8. Summary of r_h Values Determined from Cumulant Analysis for the Self-Assembly of PS/PMAA-(CdS) NPs in Aqueous Solution by DLS

	R_{NaCl}	c_0 = 0.25 wt %	c_0 = 0.50 wt %	c_0 = 0.75 wt %	c_0 = 1.00 wt %
PMMA-154	0.0	460 ± 130	860 ±120	810 ±160	710 ± 60
	1.5	164 ± 2	158 ± 2		
	3.0	160 ± 2	164 ± 1		
PMMA-54	0.0	860 ± 80	--	--	580 ± 140
	1.5	--	--		
	3.0	--	--		

-- Many of the PMMA-54 samples underwent macroscopic precipitation and values could not be obtained. All values are in nm.

CONTIN analysis was also performed on each sample to determine the shape of the distribution of hydrodynamic sizes. Figure 4.32 shows a CONTIN plot for all of the above samples, showing that each of them presented as a single distribution.

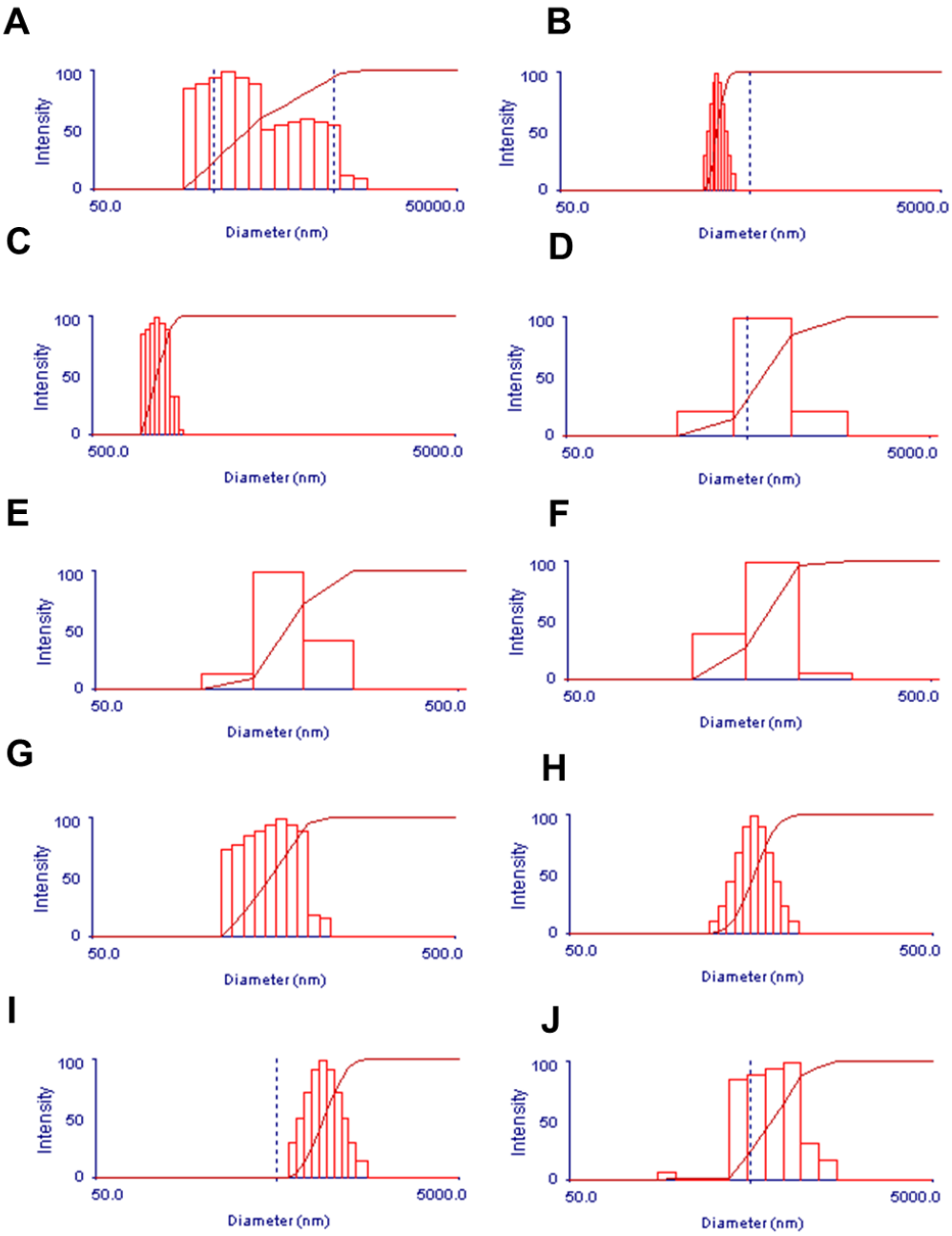

Figure 4.32. Hydrodynamic particle size distribution from CONTIN analysis of dynamic light scattering of PMMA-154 NPs under the following conditions: A) c_0 = 0.25 B) c_0 = 0.50 C) c_0 = 0.75 D) c_0 = 1.00 E) c_0 = 0.25, R_{NaCl} = 1.5 F) c_0 = 0.50, R_{NaCl} = 1.5 G) c_0 = 0.50, R_{NaCl} = 1.5 and H) c_0 = 0.50, R_{NaCl} = 3.0. Also contains CONTIN analysis of PMMA-54 NPs with I) c_0 = 0.25 and J) c_0 = 1.00. These results were obtained at a 90 º scattering angle and concentration of ~0.1 mg/mL.

4.3.11 Laser Scanning Confocal Fluorescence Microscopy

The ability of CdS QDs to fluoresce under specific excitation wavelengths allows for the probing of the surface region with LSCFM. Figure 4.33 shows an LSCFM image for A) PMMA-154 and B) PMMA-54 deposited on glass from an aqueous solution when c_0 = 0.50 wt % and R_{NaCl} = 0.0. Each image shows the fluorescence of the NPs that arises from the QDs situated on the surface of the NP. While the optical resolution of this technique is limited below 200 nm (rendering any internal structure undetectable), this technique shows that even in their self-assembled state, the PS/PMAA-(CdS) particles continue to fluoresce.

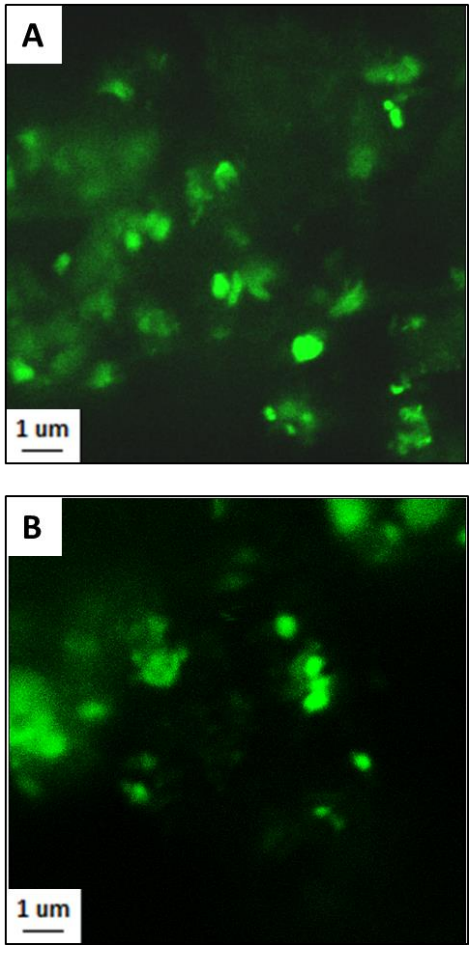

Figure 4.33. LSFCM images of A) PMMA-154 and B) PMMA-54 at c_0 = 0.50 and R_{NaCl} = 0.0. λ_{ex} = 488 nm, $\lambda_{em} \geq$ 515 nm.

4.4 Conclusion

This work has shown the synthesis, characterization and self-assembly of PS/PMAA-(CdS) NPs synthesized from PS-*b*-PAA-*b*-PMMA triblock copolymers that had variable PMMA lengths. Previous chapters have shown how changing the composition of the brush has a major effect on the assemblies created in THF/H_2O mixtures. By using a triblock copolymer template, the brush composition could be maintained at a 50/50 ratio of PS/PMAA, allowing the effects of brush lengths on self-assembly to be examined. Evidence suggests that the NPs formed a patchy or Janus mixed polymer brush around a core CdS QD with similar aggregation numbers and chains densities. The particles were stable in a series of solvents and showed good optical and fluorescent properties.

There are a few trends to be deduced from the self-assembly of PS/PMAA-(CdS). When comparing the given PS/PMAA-(CdS) NPs, the length of the PMAA polymer brush appears to have little control over the resultant morphology found in self-assembly when the brushes are in a 1:1 ratio. There is a noted difference in the size of the spheres produced by each block length at low c_0, as the PMMA-54 produces larger spheres than the PMMA-154. The size of the lumen of compound vesicles at c_0 = 0.50 and 0.75 also appears to increases as the PMAA block length decreases. It should be noted that previous work by Guo *et al.*[63] used a PS-*b*-PAA-*b*-PMAA triblock copolymer chain in which the PS and PMAA brushes were more equivalent in length to create a wide variety of structures not seen in this work, suggesting that more data is required before a true conclusion about the effect of block length can be drawn. It is hypothesized that the length of the PMAA chains are playing a role in the structures found when salt was added, as this may explain a counter intuitive increase in curvature for the PMMA-54 NP self-assembly. Changes in c_o and R_{NaCl} both appear to decrease the internal curvature of the self-assembled

macrostructures as a result of higher aggregation numbers in the interface and screening of electrostatic interactions.

Chapter 5

Conclusions and Future Work

5.1 Conclusions

In this thesis, we have shown the synthesis of amphiphilic polymer brush functionalized nanoparticles (PBNPs) using a block copolymer templated approach. This technique allowed for the control of brush composition and polymer chain length to determine their effects on the self-assembly of these nanoparticles.

Previous work in our group focused on the use of a triblock copolymer templated approach to making PBNPs. This current work expanded on the triblock approach by producing PBNPs with different hydrophilic block lengths than those reported by Guo. This approach yielded PBNPs with similar brush distributions, aggregation numbers and chain densities, despite the difference in PMAA block length, allowing for comparison of the effect block length has on self-assembly. We then used blends of diblock copolymers to produce mixed micelles with four different brush compositions that had minimal differences in aggregation number and chain density. Structural control within the brushes via chain length and composition lead to control of the interparticle interactions as the particles undergo amphiphilic self-assembly. The varied nature of the brush composition and the induced particle anisotropy are responsible for the great number of morphologies produced by the self-assembly process.

Each templated approach yielded control over the brush composition in separate ways. The triblock approach allowed for the alteration of the brush composition when the ratio of hydrophobic to hydrophilic chains remained even by changing a the length of the hydrophilic block, while the diblock approach allowed for the creation of a system in which both the brush composition and the ratio of hydrophobic to hydrophilic chains was dissimilar between samples. The addition of the innovative diblock copolymer templated approach to creating mixed brush

NPs gives scientists a new technique for creating type III PBNPs synthesized with a specific brush composition.

The results of the self-assembly experiments found within this work draws direct parallels with the trends and assemblies found in amphiphilic block copolymer micelle self-assembly. The introduction of inorganic NPs into the amphiphilic framework serves to add a new structural component at the interface of hydrophobic and hydrophilic regions. The parallels between the amphiphilic self-assembly of PBNPs and block copolymer micelles would suggest that regardless of the size and the diversity of particle or molecule involved, the nature of their self-assembly would remain the same. The phase diagrams presented would prove effective in predicting not only PS/PMAA-(CdS) systems, but a multitude of other systems driven by amphiphilicity.

Within this work, a host of variables were tested to determine their effect on the amphiphilic self-assembly of the synthesized NPs. Six different morphologies were assembled from the fine-tuning of these variables. With the knowledge gathered in this work, future researchers will have the ability to select specific morphologies for use in a wide range of applications. For example, if specific structures, such as vesicles, could be targeted, these assemblies could play a role as transportation vehicles for drug delivery. PBNPs also have the advantage of having an integrated inorganic nanoparticle; a component not shared by block copolymer micelles. When the tunability of the assemblies is combined with the properties of the materials, these materials can be chosen for even more specific roles. The fluorescent nature of these particles has been demonstrated and may be well suited to new applications in imaging. Their ability to disperse in aqueous solutions portends the possible use of these particles in blood and other aqueous media. By now having the capability to control the morphologies produced

and understanding the underlying patterns of amphiphilic self-assembly of PBNPs, we can now attempt to move these particles from the laboratory to everyday life.

5.2 Future Work

One of the most important experiment required for this data is to reproduce this data multiple times. As each self-assembly experiment was only performed once at each condition, repeated experiments are needed to prove that the perceived morphologies are indeed the correct ones. Further annealing experiments must also be performed to determine if compound vesicles are kinetic or thermodynamic structures.

The construction of the phase diagrams based on the generated assemblies creates a useful tool for predicting and targeting specific morphologies, but the phase diagrams that focus on the addition of salt are limited due to the lack of data above c_0 = 0.50 wt %. Further assembly experiments could be performed at these salt contents above c_0 = 0.50 wt % in order to complete the phase diagrams.

While the current work with the NPs constructed via the triblock copolymer template showed many well-known morphological varieties, the more exotic worm species viewed by Guo were not present under these conditions. A gap remains between the more symmetric brush construction of Guo's NPs and the asymmetric nature of the current work, suggesting samples of greater hydrophilic block length are needed to bridge the gap between the two works.

While Chapter 2 of this work focused on the effects of brush composition and Chapter 4 focused on the block length when the number of hydrophilic and hydrophobic chains are equivalent, neither study truly holds the brush composition steady. Future work could look into

PBNPs in which equal numbers of polymer chains are found on the CdS QD, but the length of the hydrophobic and hydrophilic brush will both be changed so that the overall composition of the brush remains constant to truly test the effect of block length on self-assembly.

The use of a PS/PMAA polymer brush limits the use of these NPs in the human body. With an understanding of how brush composition and chain length affect self-assembly, investigation can turn to more biocompatible polymers to allow for their use in medical applications. As vesicles are one morphology that has been assembled under a few sets of conditions, they could serve as transport materials in the bloodstream given the proper polymer.

The selection of different inorganic NPs instead of CdS would act to broaden the practicality of these PBNPs for many applications. The magnetic nature of Fe_2O_3 or the surface plasmon associated heating of Au nanoparticles present intriguing opportunities once placed inside an amphiphilic polymer brush. Essentially any inorganic nanoparticle could benefit from the solubility and selective self-assembly presented by these materials.

References

1. Gopalakrishnan, G., Danelon, C., Izewska, P., Prummer, M., Bolinger, P. Y., Geissbühler, I., Vogel, H. (2006). "Multifunctional lipid/quantum Dot Hybrid Nanocontainers for Controlled Targeting of Live Cells." *Angewandte Chemie - International Edition*, *45*(33), 5478–5483.

2. Babes L, Denizot B, Tanguy G, Le Jeune JJ, Jallet P. "Synthesis of Iron Oxide Nanoparticles used as MRI Contrast Agents: A Parametric Study." *Journal of Colloid and Interface Science* 1999; 212: 474–82.

3. Agarwal A, Huang SW, O'Donnell M, Day KC, Day M, Kotov N, et al. "Targeted Gold Nanorod Contrast Agent for Prostate Cancer Detection by Photoacoustic Imaging." *Journal of Applied Physics* 2007; 102, 064701/1-4

4. Ricciardi, A., Colombelli, A., Montagna, G., Manera, G., Milanese, M., Risi, A. De, & Rella, R. (2015). Sensors, *319*, 115–118.

5. Lee, J., Hernandez, P., Lee, J., Govorov, A. O. & Kotov, N. A. 2007. "Exciton-Plasmon Interactions in Molecular Spring Assemblies of Nanowires and Wavelength-Based Protein Detection." *Nature Mater*. 6, 291–295

6. Elghanian, R., Storhoff, J. J., Mucic, R. C., Letsinger, R. L. & Mirkin, C. A. 1997 "Selective Colorimetric Detection of Polynucleotides Based on the Distance-Dependent Optical Properties of Gold Nanoparticles." *Science* 277, 1078–1081.

7. Lee, J. S., Han, M. S. & Mirkin, C. A. 2007 "Colorimetric Detection of Mercuric Ion (Hg2+) in Aqueous Media using DNA-Functionalized Gold Nanoparticles. *Angew. Chem. Int. Ed.* 46, 4093–4096

8. Verma, R., & Gupta, B. D. 2015. "Detection of Heavy Metal Ions in Contaminated Water by Surface Plasmon Resonance Based Optical Fibre Sensor using Conducting Polymer and Chitosan." *Food Chemistry*, *166*, 568–575

9. Biswas, S., Liu, X., Jarrett, J. W., Brown, D., Pustovit, V., Urbas, A., Vaia, R. A. 2015. "Nonlinear Chiro-Optical Amplification by Plasmonic Nanolens Arrays Formed via Directed Assembly of Gold Nanoparticles." *Nano Letters*

10. Web, I. S. I., Press, H., York, N., & Nw, A. (2012). "Plasmonics : Merging Photonics," *189*(2006), 189–193.

11. Urbas, Augustine, Yoel Fink, and Edwin L. Thomas. 1999. "One-Dimensionally Periodic Dielectric Reflectors from Self-Assembled Block Copolymer-Homopolymer Blends." *Macromolecules* 32(14):4748–50.

12. Miyake, Garret M., Raymond A. Weitekamp, Victoria A. Piunova, and Robert H. Grubbs. 2012. "Synthesis of Isocyanate-Based Brush Block Copolymers and Their Rapid Self-Assembly to Infrared-Reflecting Photonic Crystals." *Journal of the American Chemical Society* 134(34):14249–54.

13. Zebli, B., Susha, A. S., Sukhorukov, G. B., Rogach, A. L. & Parak, W. J. 2005. "Magnetic Targeting and Cellular Uptake of Polymer Microcapsules Simultaneously Functionalized with Magnetic and Luminescent Nanocrystals." *Langmuir* 21, 4262–4265 (11).

14. Slowing, I. I., Vivero-Escoto, J. L., Wu, C.-W., & Lin, V. S.-Y. 2008. "Mesoporous Silica Nanoparticles as Controlled Release Drug Delivery and Gene Transfection Carriers." *Advanced Drug Delivery Reviews*, *60*(11), 1278–1288

15. Skirtach, A. G. *et al.* 2006. "Laser-Induced Release of Encapsulated Materials Inside Living Cells." *Angew. Chem. Int. Ed.* 45, 4612–4617.

16. Lin, Yang W., Wei Lung Tseng, and Huan Tsung Chang. 2006. "Using a Layer-by-Layer Assembly Technique to Fabricate Multicolored-Light- Emitting Films of CdSe/CdS and CdTe Quantum Dots." *Advanced Materials* 18(11):1381–86.

17. Labelle, André J. *et al.* 2015. "Colloidal Quantum Dot Solar Cells Exploiting Hierarchical Structuring." Nano Letters.

18. Bansal, Ashu K. *et al.* 2015. “In Situ Formation and Photo Patterning of Emissive Quantum Dots in Organic Small Molecules.” *Nanoscale* 11163–72.

19. Xu, Hao, Rui Hong, Tongxiang Lu, Oktay Uzun, and Vincent M. Rotello. 2006. “Recognition-Directed Orthogonal Self-Assembly of Polymers and Nanoparticles on Patterned Surfaces.” *Journal of the American Chemical Society* 128(10):3162–63.

20. Saner, ChaMarra K., Lu Lu, Donghui Zhang, and Jayne C. Garno. 2015. “Chemical Approaches for Nanoscale Patterning Based on Particle Lithography with Proteins and Organic Thin Films.” *Nanotechnology Reviews* 4(2):129–43.

21. Chen, Hongxu et al. 2015. “Ag Nanoparticle/polymer Composite Barcode Nanorods.” *Nano Research*.

22. Nicaise, Samuel M., Jayce J. Cheng, Amirreza Kiani, Silvija Gradečak, and Karl K. Berggren. 2015. “Control of Zinc Oxide Nanowire Array Properties with Electron-Beam Lithography Templating for Photovoltaic Applications.” *Nanotechnology* 26(7):075303.

23. Gschrey, M. *et al.* 2015. “Highly Indistinguishable Photons from Deterministic Quantum-Dot Microlenses Utilizing Three-Dimensional in Situ Electron-Beam Lithography.” *Nature Communications* 6(May):7662.

24. Tzeng, Shien Der, Kuan Jiuh Lin, Jung Chih Hu, Lih Juann Chen, and Shangjr Gwo. 2006. “Templated Self-Assembly of Colloidal Nanoparticles Controlled by Electrostatic Nanopatterning on a Si3N4/SiO2/Si Electret.” *Advanced Materials* 18(9):1147–51.

25. Mentzel, Tamar S. *et al.* 2012. “Nanopatterned Electrically Conductive Films of Semiconductor Nanocrystals.” 4404–8.

26. Mai, Y., & Eisenberg, A. (2012). “Selective Localization of Preformed Nanoparticles in Morphologically Controllable Block Copolymer Aggregates in Solution.” *Accounts of Chemical Research, 45*(10), 1657–1666.

27. Moffitt, M. G. (2013). “Self-Assembly of Polymer Brush-Functionalized Inorganic Nanoparticles: From Hairy Balls to Smart Molecular Mimics.” *Journal of Physical Chemistry Letters*, *4*(21), 3654–3666.

28. Seno, R., & Kobatake, S. (2015). “Synthesis and Characterization of Amphiphilic Silica Nanoparticles Covered by Block Copolymers Branching Photochromic Diarylethene Moieties on Side Chain.” *Dyes and Pigments*, *114*, 166–174.

29. Qiu, H., Hudson, Z. M., Winnik, M. A., & Manners, I. (2015). “Multidimensional Hierarchical Self-Assembly of Amphiphilic Cylindrical Block Comicelles,” *347*(6228), 1329–1332.

30. Pyun, J., Matyjaszewski, K., Kowalewski, T., Savin, D., Patterson, G., Kickelbick, G., & Huesing, N. (2001). “Synthesis of Well-Defined Block Copolymers Tethered to Polysilsesquioxane Nanoparticles and their Nanoscale Morphology on Surfaces [2].” *Journal of the American Chemical Society*, *123*(38), 9445–9446.

31. Gupta, S., Zhang, Q., Emrick, T., Balazs, A. C., & Russell, T. P. (2006). “Entropy-Driven Segregation of Nanoparticles to Cracks in Multilayered Composite Polymer Structures.” *Nature Materials*, *5*(3), 229–233.

32. Sill, K., & Emrick, T. (2004). “Nitroxide-Mediated Radical Polymerization from CdSe Nanoparticles.” *Chemistry of Materials*, *16*(7), 1240–1243

33. Guo, Y., & Moffitt, M. G. (2007). “Semiconductor Quantum Dots with Environmentally Responsive Mixed Polystyrene/poly(methyl methacrylate) Brush Layers.” *Macromolecules*, *40*(16), 5868–5878

34. Sperling, L.H. “Introduction to Physical Polymer Science”; John Wiley & Sons, Inc.: New York, 2006.

35. Cowie, J. M. G. “Polymer: Chemistry & Physics of Modern Materials,” *3rd ed.* New York, 2007.

36. Charles E., Carraher, J. “*Seymour/Carraher's Polymer Chemistry*,” *5th ed.*;; Marcel Dekker: New York, 2000.

37. Moffitt, M., Khougaz, K. and Eisenberg. A. 1996. “Micellization of Ionic Block Copolymers.” *Accounts of Chemical Research* 29(2):95–102.

38. Atkins, P.; and de Paula, J., *Physical Chemistry: Thermodynamics, Structure and Change 10th Ed.*, Oxford University Press, 2014.

39. Hadjichristidi, N.; Pispas, S.; Floudas, G. *Block Copolymers*; John Wiley & Sons, Inc: New Jersey, 2003.

40. Hamley, I. W. *The Physics of Block Copolymers*; Oxford University Press: 1998.

41. Tuzar, Z.; Kratochvil, P. *In Surface and Colloid Science; Matijevic, E., Ed.*; Plenum Press: New York, 1993; Vol. 15.

42. Webber, S. E.; Munk, P.; and Tuzar, Z. *Solvents and Self-Organization of Polymers* Kluwer Academic Publishers, 1996.

43. Zhang, L. F. and Eisenberg, A. (1998) “Formation of Crew-Cut Aggregates of Various Morphologies from Amphiphilic Block Copolymers in Solution.” *Polymers for Advanced Technologies* 9(May):677–99.

44. Henglein, Arnim. 1989. “Small-Particle Research: Physicochemical Properties of Extremely Small Colloidal Metal and Semiconductor Particles.” *Chemical Reviews* 89(8):1861–73.

45. Goldstein, A. N., Echer, C. M. and Alivisatos, A. P. (1992) “Melting in Semiconductor Nanocrystals.” *Science (New York, N.Y.)* 256(5062):1425–27.

46. Brus, Louis. 1986. “Electronic Wave Functions in Semiconductor Clusters: Experiment and Theory.” *The Journal of Physical Chemistry* 90(12):2555–60.

47. Corbierre, Muriel K., Neil S. Cameron, and R. Bruce Lennox. 2004. “Polymer-Stabilized Gold Nanoparticles with High Grafting Densities,” *Langmuir* 2004, 20, 2867−2873.

48. Corbierre, Muriel K., Neu S. Cameron, Mark Sutton, Khalid Laaziri, and R. Bruce Lennox. 2005. “Gold Nanoparticle/polymer Nanocomposites: Dispersion of Nanoparticles as a Function of Capping Agent Molecular Weight and Grafting Density.” *Langmuir* 21(13):6063–72.

49. Ohno, K., K. Koh, Y. Tsujii, and T. Fukuda. 2002. “Synthesis of Gold Nanoparticles Coated with Well-Defined, High-Density Polymer Brushes by Surface-Initiated Living Radical Polymerization.” *Macromolecules* 35:8989–93.

50. Matsuno, Ryosuke, Kazuya Yamamoto, Hideyuki Otsuka, and Atsushi Takahara. (2004) “Polystyrene- and Poly (3-Vinylpyridine) -Grafted Magnetite Nanoparticles Prepared through Surface-Initiated Nitroxide-Mediated Radical Polymerization.” *Synthesis* 37:2203–9.

51. Moessner, Stefan *et al.* (2000) “Solution Behavior of Poly(styrene)-b-poly(2-vinylpyridine) Micelles Containing Gold Nanoparticles.” *Macromolecules* 33:4791–98.

52. Spatz, Joachim P. *et al.* (2000). “Ordered Deposition of Inorganic Clusters from Micellar Block Copolymer Films.” *Langmuir* 16(2):407–15.

53. Spatz, Joachim P., Arno Roescher, and Martin Moeller. (1996) “Gold Nanoparticles in Micellar Poly(styrene)-B-Poly(ethylene Oxide) Films - Size and Interparticle Distance Control in Monoparticulate Films.” *American Chemical Society, Polymer Preprints, Division of Polymer Chemistry* 37(1):409.

54. Moffitt, M., L. McMahon, Pessel, V. and Eisenberg. A., (1995) “Size Control of Nanoparticles in Semiconductor-Polymer Composites. 2. Control via Sizes of Spherical Ionic Microdomains in Styrene-Based Diblock Ionomers.” *Chemistry of Materials* 7(6):1185–92.

55. Wang, C. W. and M. G. Moffitt. (2004) “Surface-Tunable Photoluminescence from Block Copolymer-Stabilized Cadmium Sulfide Quantum Dots.” *Langmuir* 20(26): 11784–96.

56. Kakefuda, Y., K. Narita, T. Komeda, S. Yoshimoto, and S. Hasegawa. 2008. “Synthesis and Conductance Measurement of Periodic Arrays of Gold Nanoparticles.” *Applied Physics Letters* 93(16):2–4.

57. Nie, Zhihong *et al.* (2007) “Self-Assembly of Metal-Polymer Analogues of Amphiphilic Triblock Copolymers.” *Nature Materials* 6(8):609–14.

58. Chen, Tao, Miaoxin Yang, Xinjiao Wang, Li Huey Tan, and Hongyu Chen. 2008. “Controlled Assembly of Eccentrically Encapsulated Gold Nanoparticles Controlled Assembly of Eccentrically Encapsulated Gold Nanoparticles.” *J. Am. Chem. Soc.* 130(August):11858–59.

59. Nikolic, Marija S. *et al.* (2009) “Micelle and Vesicle Formation of Amphiphilic Nanopartieles.” *Angewandte Chemie - International Edition* 48(15):2752–54.

60. Zubarev, Eugene R., Jun Xu, Arshad Sayyad, and Jacob D. Gibson. 2006. “Amphiphilicity-Driven Organization of Nanoparticles into Discrete Assemblies.” *Journal of the American Chemical Society* 128:15098–99.

61. He, Jie, Yijing Liu, Taarika Babu, Zengjiang Wei, and Zhihong Nie. (2012) “Self-Assembly of Inorganic Nanoparticle Vesicles and Tubules Driven by Tethered Linear Block Copolymers.” *Journal of the American Chemical Society* 134(28):11342–45.

62. Song, Jibin *et al.* (2011). “Plasmonic Vesicles of Amphiphilic Gold Nanocrystals: Self-Assembly and External-Stimuli-Triggered Destruction.” *Journal of the American Chemical Society* 133(28):10760–63.

63. Guo, Yunyong, Saman Harirchian-Saei, Celly M. S. Izumi, and Matthew G. Moffitt. 2011. “Block Copolymer Mimetic Self-Assembly of Inorganic Nanoparticles.” *ACS Nano* 5(4):3309–3318.

64. Malvern Omnisec Technical Notes 2011,Malvern Intrsutments Ltd, Worchestershire, UK, 2011

65. Tadd, Erica, Astra Zeno, Melissa Zubris, Nily Dan, and Rina Tannenbaum (2003) "Adsorption and Polymer Film Formation on Metal Nanoclusters." *Macromolecules* 36(17):6497–6502.

66. Moffitt, Matthew and Adi Eisenberg. 1997. "Scaling Relations and Size Control of Block Ionomer Microreactors Containing Different Metal Ions." *Macromolecules* 30(15):4363–73.

67. Foerster, S., M. Zisenis, E. Wenz, and M. Antonietti. (1996) "Micellization of Strongly Segregated Block Copolymers." *The Journal of Chemical Physics* 104(24):9956–70.

68. Agar, A. W.; Alderson, R. H.; Chescoe, D. *Priciples and Practice of Electron Microscope Operation*; American Elsevier Publishing Company, Inc: New York, 1974.

69. Fellers TJ, Davidson MW (2007). "Introduction to Confocal Microscopy". *Olympus Fluoview Resource Center*. National High Magnetic Field Laboratory.

70. http://emu.uct.ac.za/training/intro-to-electron-microscopy-for-biologists/confocal-laser-scanning-microscopy/ . Electron Microscopy Unit, University of Cape Town, updated 17 October 2012. Accessed 10 Feb 2016

71. Stefik, Morgan, Stefan Guldin, Silvia Vignolini, Ulrich Wiesner, and Ullrich Steiner. 2015. "Block Copolymer Self-Assembly for Nanophotonics." *Chem. Soc. Rev.*

72. Biswas, Sushmita *et al.* (2015) "Nonlinear Chiro-Optical Amplification by Plasmonic Nanolens Arrays Formed via Directed Assembly of Gold NPs." *Nano Letters*

73. Huang, Chun-Lin *et al*. (2015) "Application of Paramagnetic Graphene Quantum Dots as a Platform for Simultaneous Dual-Modality Bioimaging and Tumor-Targeted Drug Delivery." *J. Mater. Chem. B* 3(4):651–64.

74. Zhang, Yong, Nathan Kohler, and Miqin Zhang (2002) “Surface Modification of Superparamagnetic Magnetite NPs and Their Intracellular Uptake.” *Biomaterials* 23(7):1553–61.

75. Gupta AK, Berry C, Gupta M, Curtis A. (2003) “Receptor-Mediated Targeting of Magnetic NPs using Insulin as a Surface Ligand to Prevent Endocytosis.” IEEE Trans Nanobioscience. (4): 255-61.

76. Werne, Timothy Von and Timothy E. Patten. (1999) “Preparation of Structurally Well-Defined Polymer - NP Hybrids with Controlled / Living Radical Polymerizations.” *J. Am. Chem. Soc.* (33):7409–10.

77. Corbierre, Muriel K., Neu S. Cameron, Mark Sutton, Khalid Laaziri, and R. Bruce Lennox. 2005. “Gold NP/polymer Nanocomposites: Dispersion of NPs as a Function of Capping Agent Molecular Weight and Grafting Density.” *Langmuir* 21(13):6063–72.

78. Ohno, K., K. Koh, Y. Tsujii, and T. Fukuda. 2002. “Synthesis of Gold NPs Coated with Well-Defined, High-Density Polymer Brushes by Surface-Initiated Living Radical Polymerization.” *Macromolecules* 35:8989–93.

79. Mo, Stefan, Joachim P. Spatz, Martin Mo, Thomas Aberle, and Walther Burchard. 2000. “Solution Behavior of Poly(styrene)-.” 4791–98.

80. Spatz, J. P.; Roescher, A.; Moller, M. 1996. “Gold Nanoparticles in Micellar Poly(styrene)-b-Poly(ethylene oxide) Films - Size and Interparticle Distance Control in Monoparticulate Films.” *Adv. Mater.* 8, 337−340

81. Kumar, S.; Jouault, N.; Benicewicz, B.; Neely, T. 2013. “Nano- Composites with Polymer Grafted Nanoparticles.” *Macromolecules*, 46, 3199−3214.

82. Goel, V.; Pietrasik, J.; Dong, H.; Sharma, J.; Matyjaszewski, K.; Krishnamoorti, R. 2011. “Structure of Polymer Tethered Highly Grafted Nanoparticles.” *Macromolecules,* 44, 8129−8135.

83. Erhardt, Rainer et al. 2001. “Janus Micelles.” *Macromolecules.* (34):1069–75.

84. Hoppenbrouwers, Ernst, Zhao Li, and Guojun Liu. 2003. “Triblock Nanospheres with Amphiphilic Coronal Chains.” *Macromolecules* 36(3):876–81.

85. Hu, Jinming, Tao Wu, Guoying Zhang, and Shiyong Liu. 2012. “Efficient Synthesis of Single Gold Nanoparticle Hybrid Amphiphilic Triblock Copolymers and Their Controlled Self-Assembly.” *Journal of the American Chemical Society* 134(18):7624–27.

86. Li, Dejin, Xia Sheng, and Bin Zhao. 2005. “Environmentally Responsive ‘Hairy’ Nanoparticles: Mixed Homopolymer Brushes on Silica Nanoparticles Synthesized by Living Radical Polymerization Techniques.” *Journal of the American Chemical Society* 127(17):6248–56.

87. Julthongpiput, Duangrut, Yen Hsi Lin, Jing Teng, Eugene R. Zubarev, and Vladimir V. Tsukruk. 2003. “Y-Shaped Amphiphilic Brushes with Switchable Micellar Surface Structures.” *Journal of the American Chemical Society* 125(51):15912–21.

88. Zhao, Bin, Richard T. Haasch, and Scott MacLaren. 2004. “Self-Reorganization of Mixed Poly(methyl Methacrylate)/polystyrene Brushes on Planar Silica Substrates in Response to Combined Selective Solvent Treatments and Thermal Annealing.” *Polymer* 45(23):7979–88.

89. Stuart, Martien, A Cohen *et al*. 2010. “Emerging Applications of Stimuli-Responsive Polymer Materials.” *Naturematerials* 9(2):101–13.

90. Wang, Jiafang and Marcus Mueller. 2009. “Microphase Separation of Mixed Polymer Brushes: Dependence of the Morphology on Grafting Density, Composition, Chain-Length Asymmetry, Solvent Quality, and Selectivity.” *Journal of Physical Chemistry B* 113(33):11384–402.

91. Moffitt, Matthew and Adi Eisenberg. 1995. “Size Control of Nanoparticles in Semiconductor Polymer Composites. 1. Control via Multiplet Aggregation Numbers in Styrene-Based Random Ionomers.” *Chemistry of Materials* 7(6):1178–84.

92. Theisen, A.; Johann, C.; Deacon, M.P.; Harding, S.E. “Refractive Increment Data-Book for Polymer and Biomolecular Scientists”, Nottingham University Press, Nottingham UK, 2000. ISBN: 1-897676-29-8

93. Roh, Kyung-ho, David C. Martin, and Joerg Lahann. 2005. “Biphasic Janus Particles with Nanoscale Anisotropy.” *Nature Materials* 4(10):759–63.

94. Ziherl, P. & Kamien, R. D. 2001. “Maximizing Entropy by Minimizing Area: Towards a New Principle of Self-Organization.” *J. Phys. Chem. B* 105, 10147–10158

95. Kamien, R. D. 2002, “The Geometry of Soft Materials: A Primer.” *Rev. Mod. Phys.* 74, 953–971

96. Zhang, Z. 2015. “Interface-engineered Copolymers: Soft Patchy Particles of Block Copolymers.” *ACS Nano* 11(11):11333–41.

97. Zhu, Shuzhe, Zhan Wei Li, and Hanying Zhao. 2015. “Patchy Micelles Based on Coassembly of Block Copolymer Chains and Block Copolymer Brushes on Silica Particles.” *Langmuir* 31(14):4129–36.

98. Zhang, Z., M. A. Horsch, M. H. Lamm, and S. C. Glotzer. 2003. “Tethered Nano Building Blocks: Toward a Conceptual Framework for Nanoparticles Self-Assembly.” *Nano Lett.*3(10):1341–46.

99. Zhang, Zhenli and Sharon C. Glotzer. 2004. “Self-Assembly of Patchy Particles.” *Nano Letters* 4(8):1407–13.

100. Glotzer, Sharon C. 2004. “Some Assembly Required Space — The Final Frontier.” *Science* 306(Oct 15):419–20.

101. Anglin EJ. “Porous Silicon in Drug Delivery Devices and Materials.” *Advanced Drug Delivery Reviews* 2008; 60: 1266–77.

102. Slowing BII, Trewyn BG, Giri S, Lin VSY. “Mesoporous Silica Nanoparticles for Drug Delivery and Biosensing Applications.” *Advanced Functional Materials* 2007; 17: 1225–36.

103. Chertok B, Moffat BA, David AE, Yu F, Berqemann C, Ross BD, *et al.* “Iron Oxide Nanoparticles as a Drug Delivery Vehicle for MRI Monitored Magnetic Targeting of Brain Tumors.” *Biomaterials* 2008; 29: 487–96.

104. Frederix F, Friedt JM, Choi KH, Laureyn W, Campitelli A, Mondelaers D, *et al.* “Biosensing based on Light Absorption of Nanoscaled Gold and Silver Particles.” *Analytical Chemistry* 2003; 75: 6894–900.

105. Kundu TK, Kark N, Barik P, Saha S. “Optical Properties of ZnO Nanoparticles Prepared by Chemical Method using Poly (vinyl alcohol) (PVA) as Capping Agent.” *International Journal of Soft Computing and Engineering* 2011; 1: 19–24.

106. Dakhlaoui A, Jendoubi M, Smiri LS, Kanaev A, Jouini N. “Synthesis, Characterization and Optical Properties of ZnO Nanoparticles with Controlled Size and Morphology.” *Journal of Crystal Growth* 2009; 311: 3989–96.

107. Singh AK. “Synthesis, Characterization, Electrical and Sensing Properties of ZnO Nanoparticles.” *Advanced Powder Technology* 2010; 21: 609–13.

108. Ortega MA, Rodriguez L, Castillo J, Piscitelli V, Fernandez A, Echevarria L. “Thermo-Optical Properties of Gold Nanoparticles in Colloidal Systems.” *Journal of Optics A: Pure and Applied Optics* 2008; 10, 104024/1-4.

109. Nie, Zhihong, Alla Petukhova, and Eugenia Kumacheva. 2010. “Properties and Emerging Applications of Self-Assembled Structures Made from Inorganic Nanoparticles.” *Nature nanotechnology* 5(1):15–25.

110. Rycenga, M., McLellan, J. M. & Xia, Y. 2008. “Controlling the Assembly of Silver Nanocubes through Selective Functionalization of their Faces.” *Adv. Mater.* (20): 2416–2420.

111. Sharma, J. et al. 2009 “Control of Self-Assembly of DNA Tubules through Integration of Gold Nanoparticles.” *Science* (323): 112–116.

112. Tang, Z. Y., Zhang, Z. L., Wang, Y., Glotzer, S. C. & Kotov, N. A. 2006 “Self-Assembly of CdTe Nanocrystals into Free-Floating Sheets.” *Science* (314): 274–278

113. Park, S. Y. et al. “DNA-Programmable Nanoparticle Crystallization.” (2008) *Nature* (451): 553–556

114. Naka, Kensuke, Hideaki Itoh, Yoshihiro Tampo, and Yoshiki Chujo. 2003. “Effect of Gold Nanoparticles as a Support for the Oligomerization of L-Cysteine in an Aqueous Solution.” *Langmuir* 19(9):5546–49.

115. Shenhar, By Roy, Eunhee Jeoung, Sudhanshu Srivastava, Tyler B. Norsten, and Vincent M. Rotello. 2005. “Crosslinked Nanoparticle Stripes and Hexagonal Networks Obtained via Selective Patterning of Block Copolymer Thin Films.” *Advanced Material* 1: 2206–10.

116. Srivastava, S., B. L. Frankamp, and V. M. Rotello. 2005. “AuNP135-Controlled Plasmon Resonance of Gold Nanoparticles Self- Assembled with PAMAM Dendrimers.” *Chemistry of Materials* 17(3):487–90.

117. Caruso, Frank. 2001. “Nanoengineering of Particle Surfaces.” *Advanced Materials* 13(1):11–22.

118. Gaponik, Nikolai, Andreas Kornowski, and Andrey L. Rogach. 2001. “Core±Shell Structures Formed by the Solvent-Controlled Precipitation of Luminescent CdTe Nanocrystals on Latex Spheres.” *Advanced Materials* (22):1684–87.

119. Wang, Dayang, Andrey L. Rogach, and Frank Caruso. 2002. “Semiconductor Quantum Dot-Labeled Microsphere Bioconjugates Prepared by Stepwise Self-Assembly.” *Nano Letters* 2(8):857–61.

120. Kang, Youngjong, Kris J. Erickson, and T. Andrew Taton. 2005. “Plasmonic Nanoparticle Chains via a Morphological, Sphere-to-String Transition.” *Journal of the American Chemical Society* 127(40):13800–801.

121. Kang, Youngjong and T. Andrew Taton. 2005. “Core/shell Gold Nanoparticles by Self-Assembly and Crosslinking of Micellar, Block-Copolymer Shells.” *Angewandte Chemie - International Edition* 44(3):409–12.

122. Zhang, Mingfu, Markus Drechsler, and Axel H. E. Müller. 2004. “Template-Controlled Synthesis of Wire-Like Cadmium Sulfide Nanoparticle Assemblies within Core-Shell Cylindrical Polymer Brushes.” *Chemistry of Materials* 16(3):537–43.

123. Moffitt, Matthew, H. Vali, and Adi Eisenberg. 1998. “Spherical Assemblies of Semiconductor Nanoparticles in Water-Soluble Block Copolymer Aggregates.” *Chemistry of Materials* 10(14):1021–28.

124. Discher, B. M. *et al.* 1999. “Polymersomes: Tough Vesicles Made from Diblock Copolymers.” *Science* 284(May):1143–46.

125. Bates, F. S. 1991. “Polymer-Polymer Phase Behaviour.” 251(4996):898–905.

126. Zhang, L., K. Yu, and A. Eisenberg. 1996. “Ion-Induced Morphological Changes in ``Crew-Cut'' Aggregates of Amphiphilic Block Copolymers.” *Science* 272(5269):1777–79.

127. van Hest, J. C., D. a Delnoye, M. W. Baars, M. H. van Genderen, and E. W. Meijer. 1995. “Polystyrene-Dendrimer Amphiphilic Block Copolymers with a Generation-Dependent Aggregation.” *Science (New York, N.Y.)* 268(5217):1592–95.

128. Neil S., Cameron, M. K. Corbierre and Adi. Eisenberg. 1999. “Asymmetric Amphiphilic Block Copolymers in Solution: A Morphological Wonderland.” 77(1):1311–26.

129. Discher, Dennis E. and Fariyal Ahmed. 2006. “Polymersomes.” *Annual Review of Biomedical Engineering* 8(1):323–41.

130. Zhang, Lifeng and Adi Eisenberg. 1996. “Morphogenic Effect of Added Ions on Crew-Cut Aggregates of Polystyrene-B-Poly(acrylic Acid) Block Copolymers in Solutions.” *Macromolecules* 29 (27): 8805–15

131. Mao, Zhengwei, Haolan Xu, and Dayang Wang. 2010. “Molecular Mimetic Self-Assembly of Colloidal Particles.” *Advanced Functional Materials* 20(7):1053–74.

132. Ohno, K.; Morinaga, T.; Takeno, S.; Tsujii, Y.; Fukuda, T. 2006. “Suspensions of Silica Particles Grafted with Concentrated Polymer Brush: A New Family of Colloidal Crystals.” *Macromolecules*, 39, 1245−1249

133. Zubarev, Eugene R., Jun Xu, Arshad Sayyad, and Jacob D. Gibson. 2006. “Amphiphilic Gold Nanoparticles with V-Shaped Arms.” *Journal of the American Chemical Society* 128(15):4958–59.

134. Zhang, L. and A Eisenberg. 1995. “Multiple Morphologies of ‘Crew-Cut’ Aggregates of Polystyrene-B-Poly(acrylic Acid) Block Copolymers.” *Science (New York, N.Y.)* 268(5218):1728–31.

135. Blanazs, Adam, Steven P. Armes, and Anthony J. Ryan. 2009. “Self-Assembled Block Copolymer Aggregates: From Micelles to Vesicles and Their Biological Applications.” *Macromolecular Rapid Communications* 30(4-5):267–77.

136. Semsarilar, Mona, Elizabeth R. Jones, Adam Blanazs, and Steven P. Armes. 2012. “Efficient Synthesis of Sterically-Stabilized Nano-Objects via RAFT Dispersion Polymerization of Benzyl Methacrylate in Alcoholic Media.” *Advanced Materials* 24(25):3378–82.

137. Xu, Jihua *et al.* 2013. “Self-Assembled Morphologies of ABA Triblock Copolymer Brushes in Selective Solvents Self-Assembled Morphologies of ABA Triblock Copolymer Brushes.” 114905.

138. Simocko, Chester K., Amalie L. Frischknecht, and Dale L. Huber. 2016. “Phase Behavior of Ternary Polymer Brushes.” *ACS Macro Letters* 149–53.

139. Shen, Hongwei and Adi Eisenberg. 1999. “Morphological Phase Diagram for a Ternary System of Block Copolymer PS310-B-PAA52/Dioxane/H2O.” *The Journal of Physical Chemistry B* 103 (44): 9473–87.

140. Discher, Dennis E. and Adi Eisenberg. 2002. “Polymer Vesicles.” *Science (New York, N.Y.)* 297 (5583): 967–73.

141. Cummins, C. C.; Schrock, R. R.; Cohen, R. E. 1992. “Synthesis of Zinc Sulfide and Cadmium Sulfide within ROMP Block Copolymer Microdomains.” *Chem. Mater.* (4): 27−30

142. Jia, H.; Titmuss, S. 2009. “Polymer-Functionalized Nanoparticles: From Stealth Viruses to Biocompatible Quantum Dots.” *Nano Med.* 4(20): 951−966.

143. Min, K.; Gao, H.; Yoon, J. A.; Wu, W.; Kowalewski, T. 2009, “One-Pot Synthesis of Hairy Nanoparticles by Emulsion ATRP.” *Macromolecules* (42): 1597−1603.

144. Kim, B. J.; Fredrickson, G. H.; Hawker, C. J.; Kramer, E. J. “Nanoparticle Surfactants as a Route to Bicontinuous Block Copolymer Morphologies.” Langmuir 2007, 23, 7804−7809

145. Park, S., Lim, J. H., Chung, S. W. & Mirkin, C. A. 2004 “Self-Assembly of Mesoscopic Metal-Polymer Amphiphiles.” *Science* (303):348–351.

146. Moffitt, Matthew and Adi Eisenberg. 1995. “Size Control of Nanoparticles in Semiconductor-Polymer Composites. 1. Control via Multiplet Aggregation Numbers in Styrene-Based Random Ionomers.” *Chemistry of Materials* 7(6):1178–84.

147. Lin, Yung-Chih and Shiao-Wei Kuo. 2012. “Hierarchical Self-Assembly Structures of POSS-Containing Polypeptide Block Copolymers Synthesized Using a Combination of ATRP, ROP and Click Chemistry.” *Polymer Chemistry* 3(4):882.

148. He, Jie *et al*. 2013. “Self-Assembly of Amphiphilic Plasmonic Micelle-like Nanoparticles in Selective Solvents.” *Journal of the American Chemical Society* 135(21):7974–84.

149. Wang, C. W. and M. G. Moffitt. 2005. “Use of Block Copolymer-Stabilized Cadmium Sulfide Quantum Dots as Novel Tracers for Laser Scanning Confocal Fluorescence Imaging of Blend Morphology in Polystyrene/poly(methyl Methacrylate) Films.” *Langmuir* 21(6):2465–73.

150. Alivostatos, A. P. 1996. “Semiconductor Clusters, Nanocrystals, and Quantum Dots.” 271(5251):933–37.

151. Omar, Ali M., Elementary Solid State Physics, (Pearson Education, 1999), pp68- 75;213-215.

152. Murray, Christopher B., DJ Norris, and Moungi G. Bawendi. 1993. “Synthesis and Characterization of Nearly Monodisperse CdE (E= S, Se, Te) Semiconductor Nanocrystallites.” *Journal of the American Chemical Society* 115(4):8706–15.

153. Grätzel, Michael. 2005. “Solar Energy Conversion by Dye-Sensitized Photovoltaic Cells.” *Inorganic Chemistry* 44(20):6841–51.

154. https://www.thermofisher.com/ca/en/home/brands/molecular-probes/key-molecular-probes-products/qdot/qdot-citations.html, retrieved April 25, 2016.

155. http://www.nanoshel.com/product/quantum-dot-biolabeling/, retrieved April 25, 2016.

156. Hanaki, Ken Ichi et al. 2003. “Semiconductor Quantum Dot/albumin Complex Is a Long-Life and Highly Photostable Endosome Marker.” *Biochemical and Biophysical Research Communications* 302(3):496–501.

157. Lin, Cheng-An J. et al. 2007. “Bioanalytics and Biolabeling with Semiconductor Nanoparticles (Quantum Dots).” *Journal of Materials Chemistry* 17(14):1343–46.

158. Su, Xiao-Li and Yanbin Li. 2004. “Quantum Dot Biolabeling Coupled with Immunomagnetic Separation for Detection of Escherichia Coli O157:H7.” *Analytical chemistry* 76(16):4806–10.

159. Walker, John M. 2009. *Micro and Nano Technologies in Bioanalysis*.

160. Kloeffel, Christoph and Daniel Loss. 2013. “Prospects for Spin-Based Quantum Computing in Quantum Dots.” *Annual Review of Condensed Matter Physics* 4(1):51–81.

161. Loss D, DiVincenzo DP. 1998. Phys. Rev. A 57:120–26

162. Imamoglu A, Awschalom DD, Burkard G, DiVincenzo DP, Loss D, et al. 1999. Phys. Rev. Lett. 83:4204–7

163. Frecker, Talitha, Danielle Bailey, Xochitl Arzeta-Ferrer, James McBride, and Sandra J. Rosenthal. 2016. “Review—Quantum Dots and Their Application in Lighting, Displays, and Biology.” *ECS Journal of Solid State Science and Technology* 5(1):R3019–31.

164. Li, Xiaoming et al. 2016. “CsPbX $_3$ Quantum Dots for Lighting and Displays: Room-Temperature Synthesis, Photoluminescence Superiorities, Underlying Origins and White Light-Emitting Diodes.” *Advanced Functional Materials*

165. Song, Jizhong et al. 2015. “Quantum Dot Light-Emitting Diodes Based on Inorganic Perovskite Cesium Lead Halides (CsPbX3).” *Advanced Materials* 27(44):7162–67.

Appendix

Appendix A

Synthesis of Polystyrene-b-poly(tert-butyl acrylate)-b-poly-(methyl methacrylate) (PS-b-PtBA-b-PMMA) Triblock Copolymer.

The triblock copolymer that was used as a precursor material in the Chapter 4 was synthesized using anionic polymerization techniques by previous co-worker Gavin Phinney as described elsewhere in the literature.[1,2,3] All monomers were stirred over calcium hydride for 24 h, distilled under vacuum, and stored under nitrogen at 20 °C. Immediately prior to the polymerization reaction, styrene, tert-butyl acrylate, and methyl methacrylate monomers (Aldrich) were further purified by the addition of fluorenyllithium to styrene, and triethylaluminum to tert- butyl acrylate and methyl methacrylate, followed by vacuum distillation into flame-dried cylinders. The tetrahydrofuran (THF) reaction solvent was freshly distilled following reflux over sodium/ benzophenone. Solvents, monomers, and initiator were transferred using rigorous Schlenk-line techniques under ultrahigh-purity (UHP) nitrogen atmosphere and vacuum. Several drops of R-methylstyrene (Aldrich) were added to the reaction flask containing LiCl (10 mol of LiCl:1 mol of sec- butyllithium) dissolved in THF. The sec-butyllithium initiator (1.3 M in hexanes, Aldrich) was then added dropwise until a dark red color persisted, followed by the addition of the desired quantity of initiator. The reaction flask was cooled to -78 °C using a dry ice/ acetone bath, followed by the sequential addition of styrene, *tert*-butyl acrylate, and methyl methacrylate monomers, allowing 30 min for the polymerization of each block. Aliquots of the reaction mixture were withdrawn following polymerization of each of the first two blocks (PS and P*t*BA) for analysis by gel permeation chromatography (GPC). Finally, the polymerization reaction was terminated by the addition of degassed methanol.

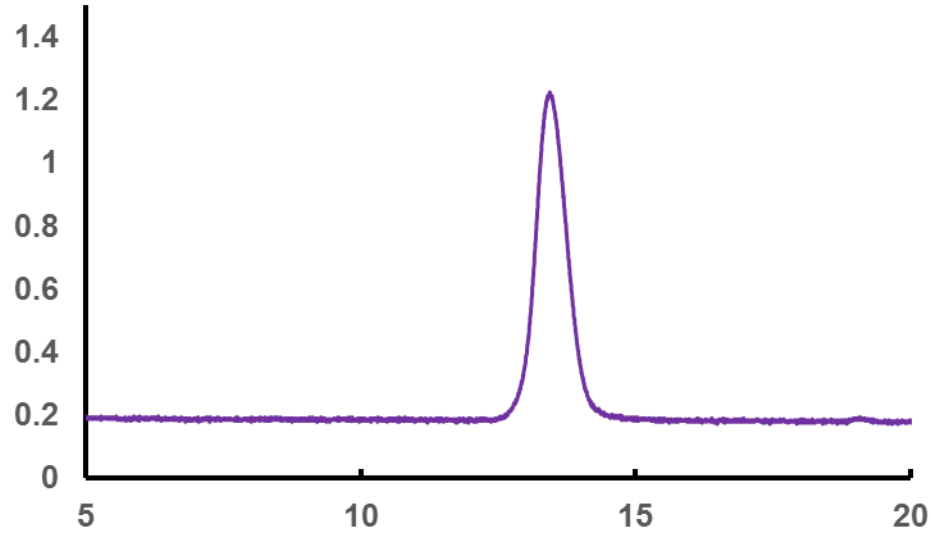

Figure A1. GPC spectrum (refractive index detector) of PS-*b*-PtBA-*b*-PMMA for PMMA-54

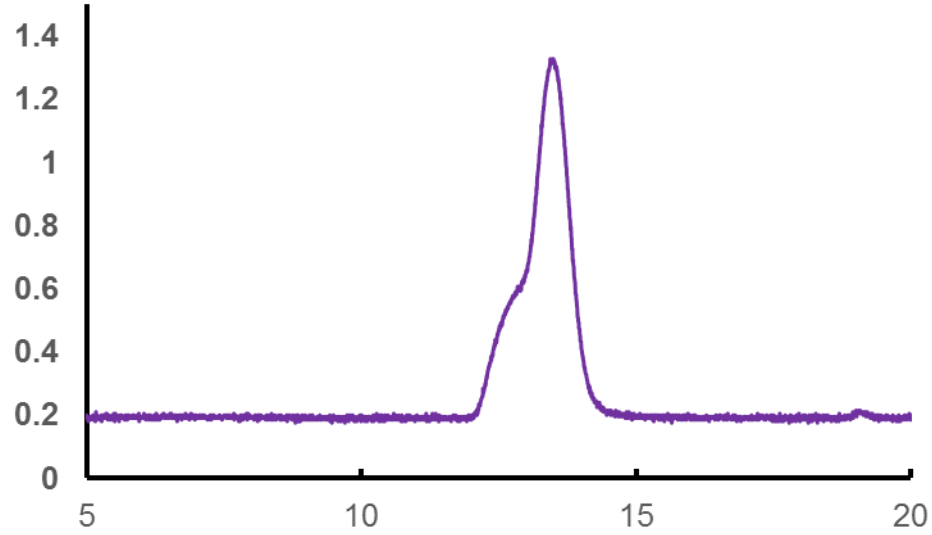

Figure A2. GPC spectrum (refractive index detector) of PS-*b*-PtBA-*b*-PMMA for PMMA-154

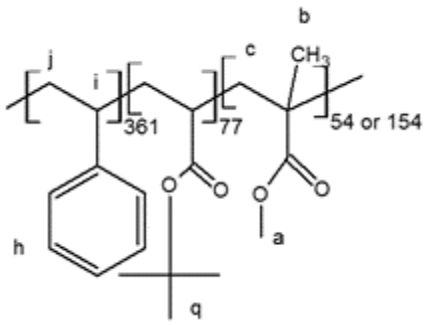

Figure A3. Schematic depicting the peak labels of PS-*b*-PtBA-*b*-PMMA

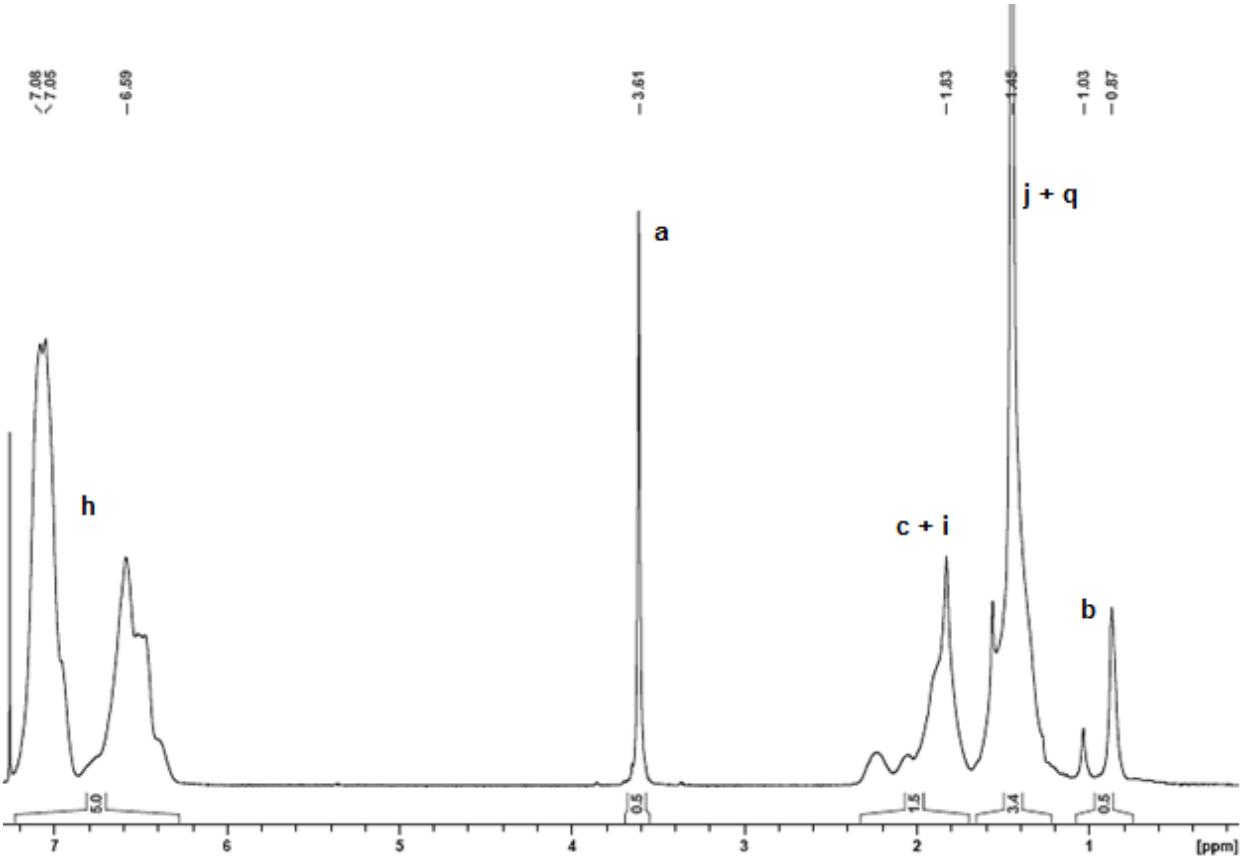

Figure A4. ^{1}H NMR spectra of PS-*b*-PtBA-*b*-PMMA when PMMA-54.

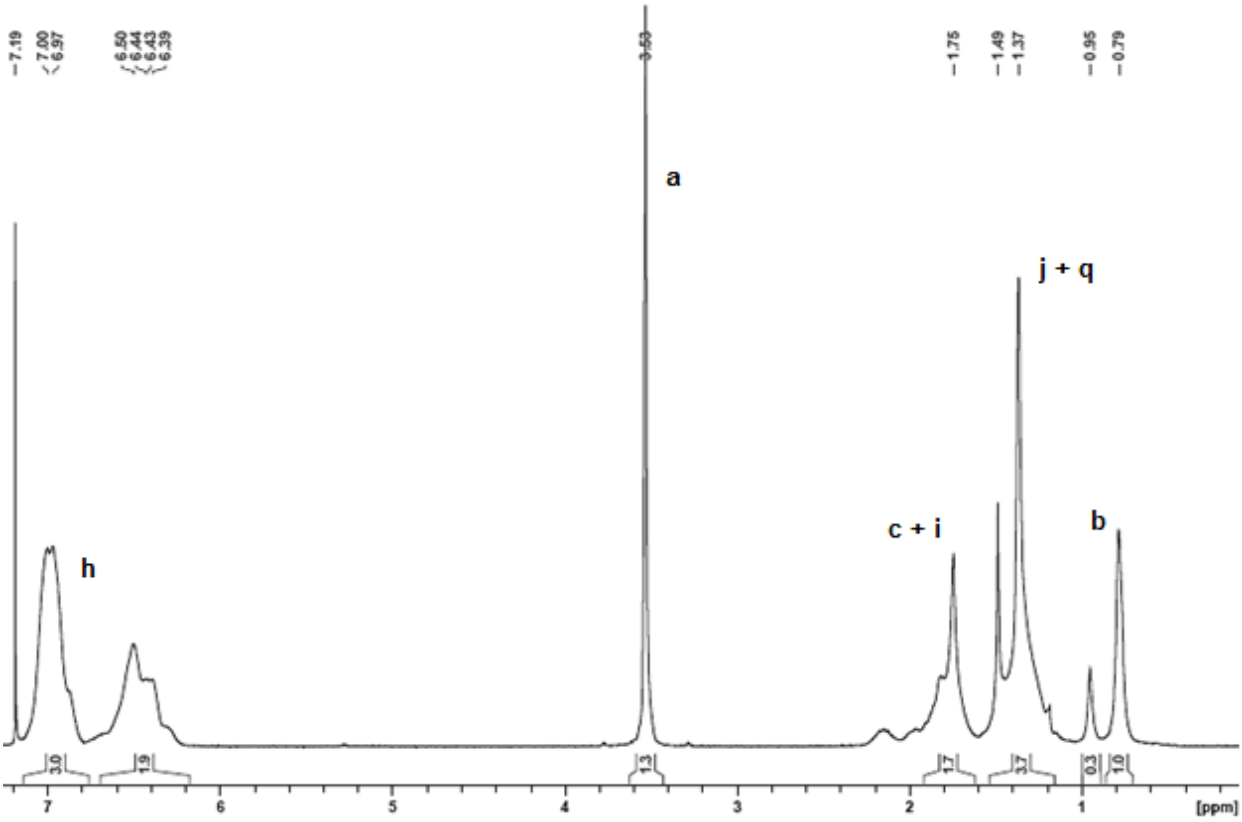

Figure A5. ^{1}H NMR spectra of PS-*b*-PtBA-*b*-PMMA when PMMA-154.

Table A1. Molecular Weight Information as Determined by GPC and ^{1}H NMR[3]

x	M_w (g/mol)	M_w/M_n	N_{PS}	N_{PtBA}	N_{PMMA}
54	52351	1.015	361	77	54
154	62874	1.023	361	77	154

Appendix B. Peak Deconvolution of GPC Spectra

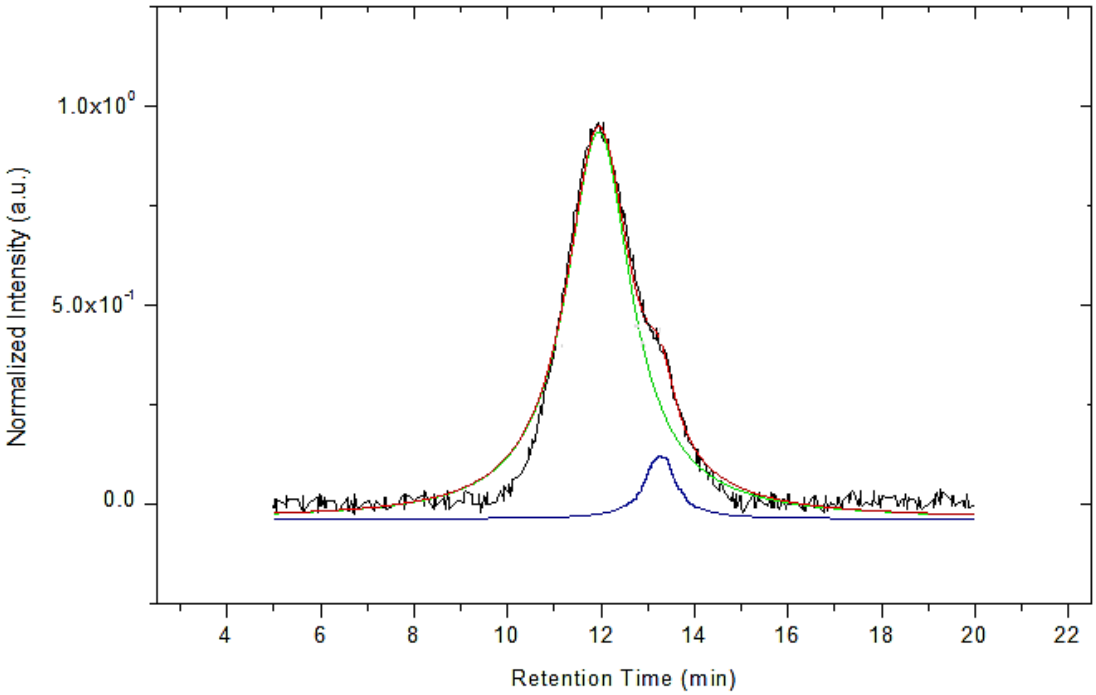

Fitting Results

Peak #	Peak Type	Area Intg	FWHM	Max Height	Center Grvty	Area IntgP
1	Lorentz	2.6055	1.7042	0.97331	11.94738	91.4301
2	Lorentz	0.19869	0.77973	0.16222	13.26449	22.89994

Figure B1. Peak deconvolution of the GPC spectrum refractive index detector) produced by f_{PS} = 0.8 PS/PMAA-(CdS) NPs. The original spectrum is in black, the NP peak deconvolution is in green and the single chain deconvolution is in blue and the sum of the two deconvolution peaks are in red.

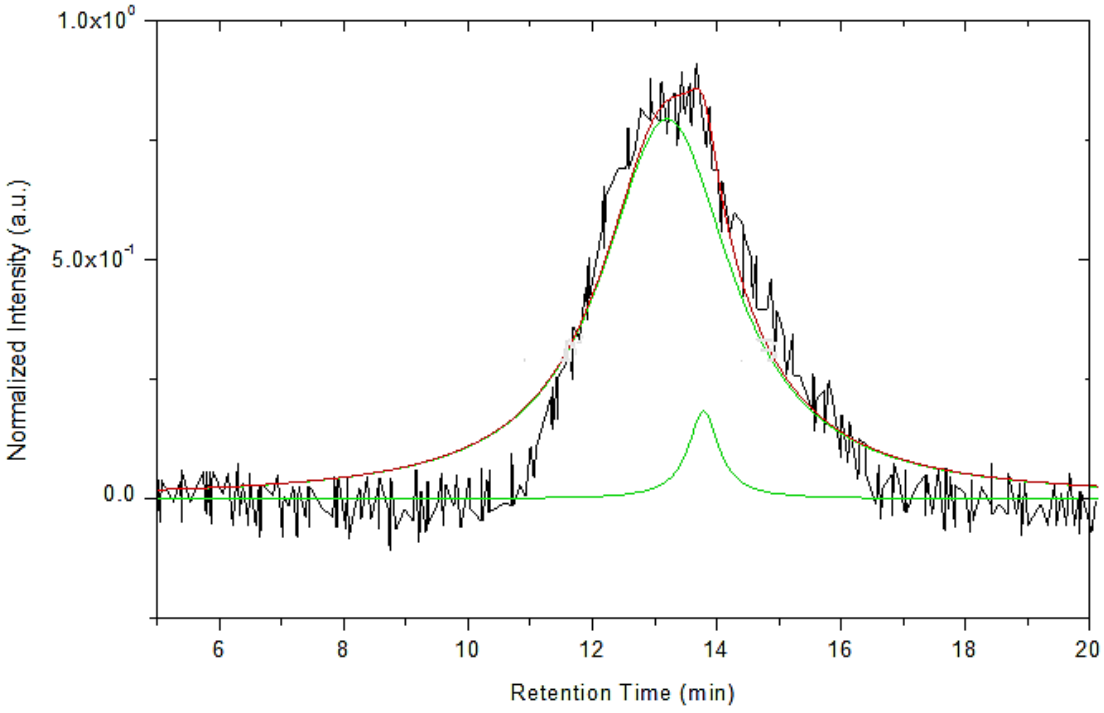

Fitting Results

Peak #	Peak Type	Area Intg	FWHM	Max Height	Center Grvty	Area IntgP
1	Lorentz	3.18558	2.55	0.79529	13.19997	94.42947
2	Lorentz	0.17308	0.6	0.18364	13.78639	5.57053

Figure B2. Peak deconvolution of the GPC spectrum refractive index detector) produced by PMMA-54 PS/PMMA-*b*-PACd NPs. The original spectrum is in black, the NP peak deconvolution and the single chain peaks are in green and the sum of the two deconvolution peaks is in red.

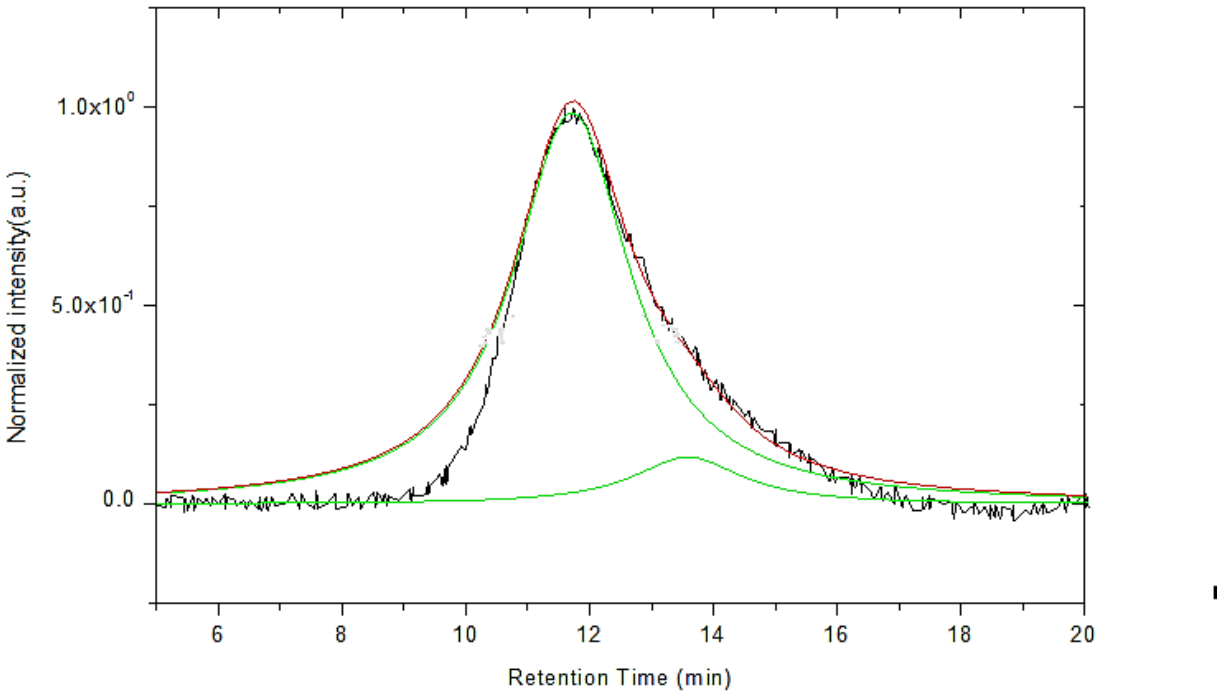

Fitting Results

Peak #	Peak Type	Area Intg	FWHM	Max Height	Center Grvty	Area IntgP
1	Lorentz	3.564	2.3	0.98648	11.71421	89.85012
2	Lorentz	0.4	2.15	0.11844	13.57998	10.14988

Figure B3. Peak deconvolution of the GPC spectrum refractive index detector) produced by PMMA-54 PS/PMMA$_{XL}$(CdS) NPs. The original spectrum is in black, the NP peak deconvolution and the single chain peaks are in green and the sum of the two deconvolution peaks is in red.

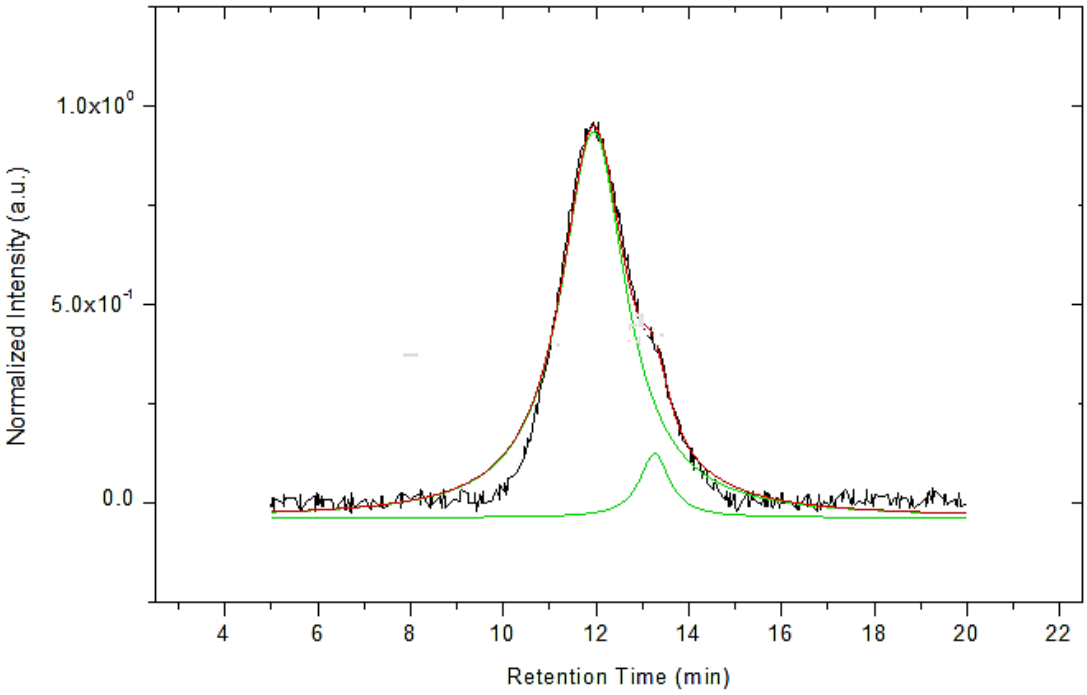

Fitting Results

Peak #	Peak Type	Area Intg	FWHM	Max Height	Center Grvty	Area IntgP
1	Lorentz	2.6055	1.7042	0.97331	11.94738	91.4301
2	Lorentz	0.19869	0.77973	0.16222	13.26449	22.89994

Figure B4. Peak deconvolution of the GPC spectrum refractive index detector) produced by PMMA-54 PS/PMAA-(CdS) NPs. The original spectrum is in black, the NP peak deconvolution and the single chain peaks are in green and the sum of the two deconvolution peaks is in red.

Appendix C. UV-Visible Spectroscopy Threshold Determination

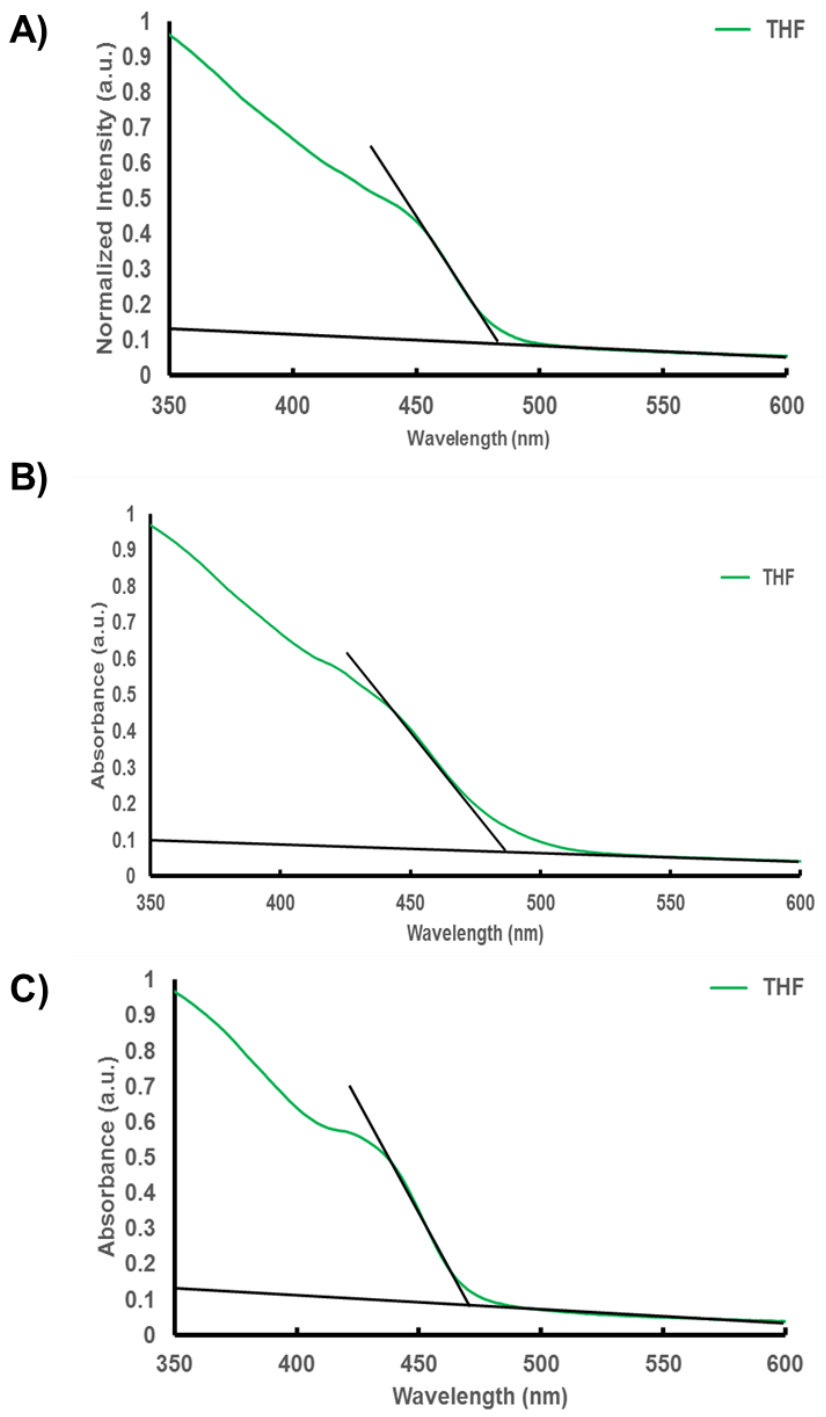

Figure C1. UV-Visible spectra of f_{PS} = A) 0.7 B) 0.8 and C) 0.9 PS/PMMA$_{XL}$(CdS) NPs in THF showing the threshold determination from the extrapolation of the steepest part of the curve and the extrapolation of the baseline.

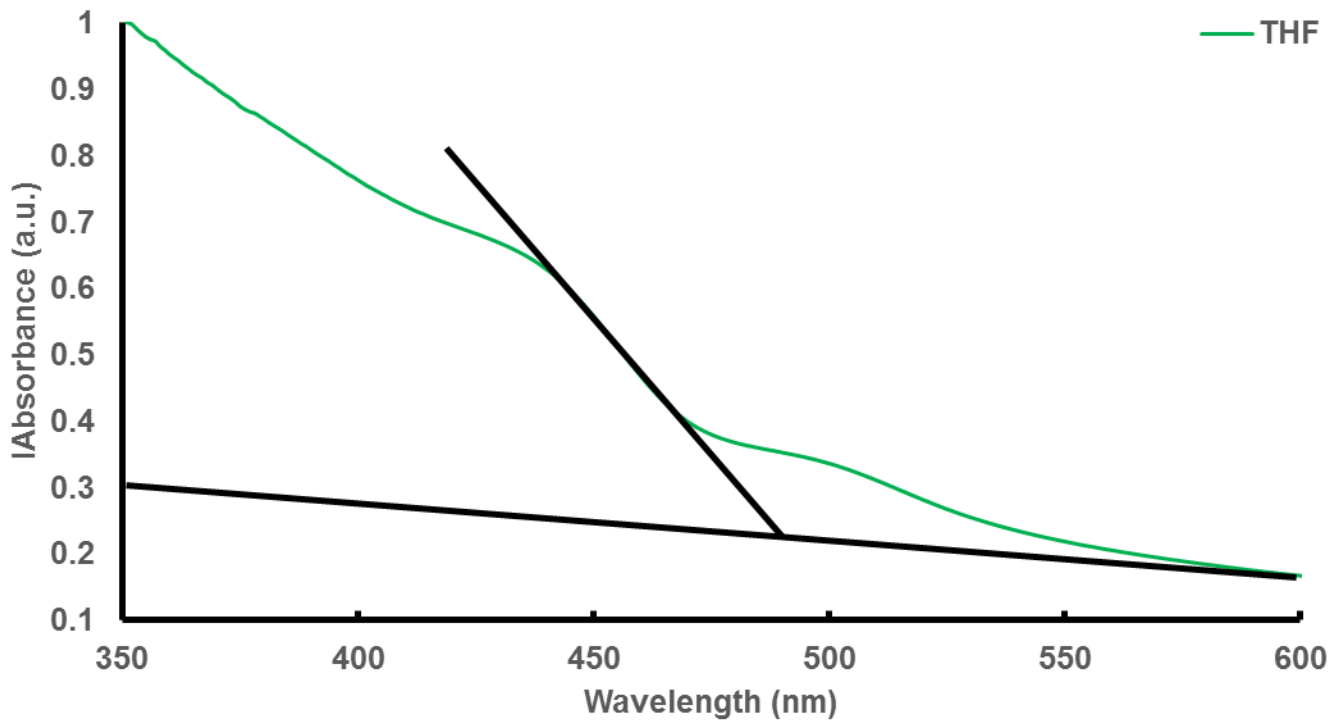

Figure C2. UV-Visible spectra of PMMA-54 PS/PMMA$_{XL}$(CdS) NPs in THF showing the threshold determination from the extrapolation of the steepest part of the curve and the extrapolation of the baseline.

Appendix D TEM Images of Self-Assembly

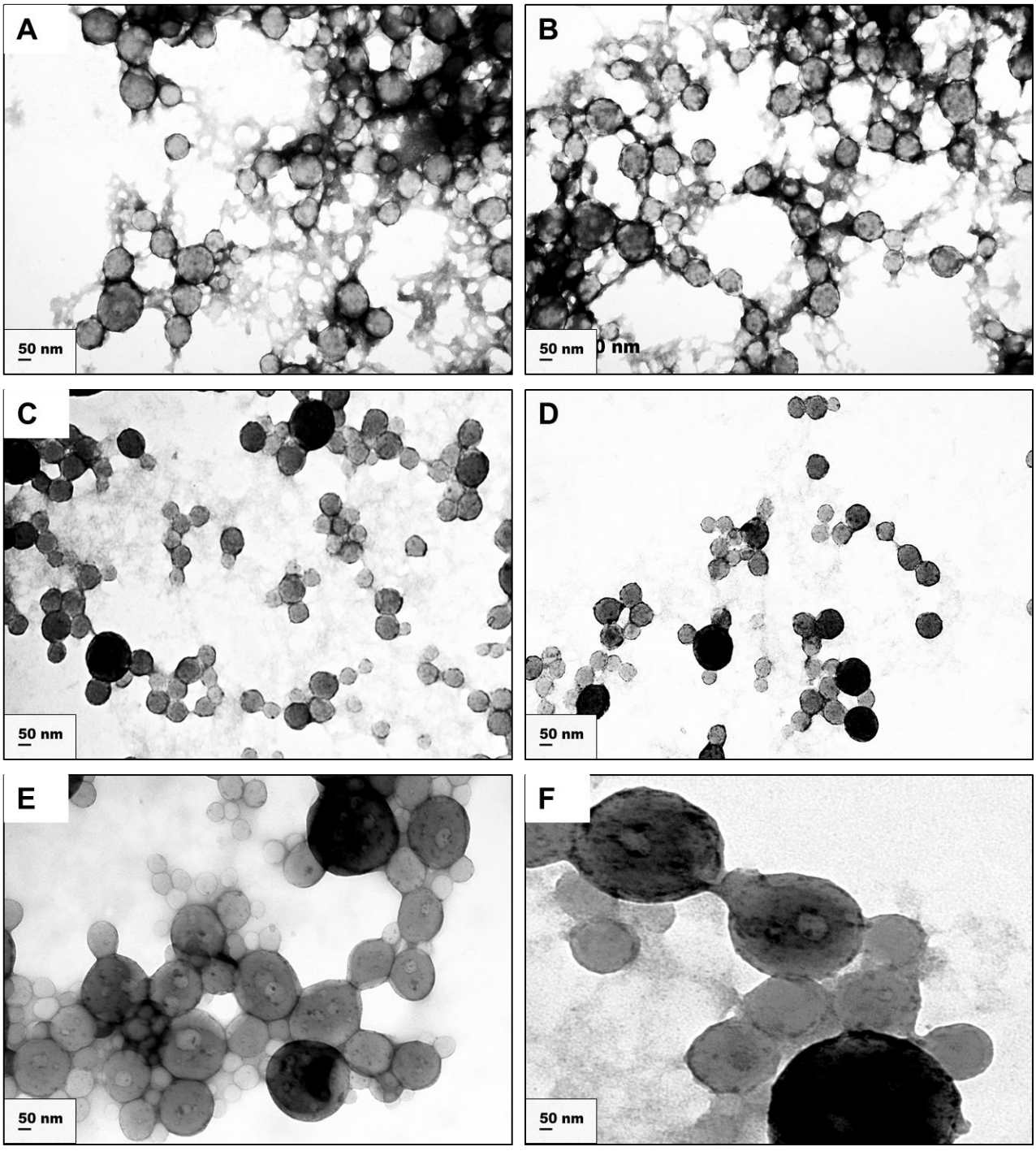

Figure D1. TEM images of f_{PS} = 0.5 when R_{NaCl} = 0.0 and c_0 = A,B) 0.25 wt % C,D) 0.50 wt % and E,F) 0.75 wt %

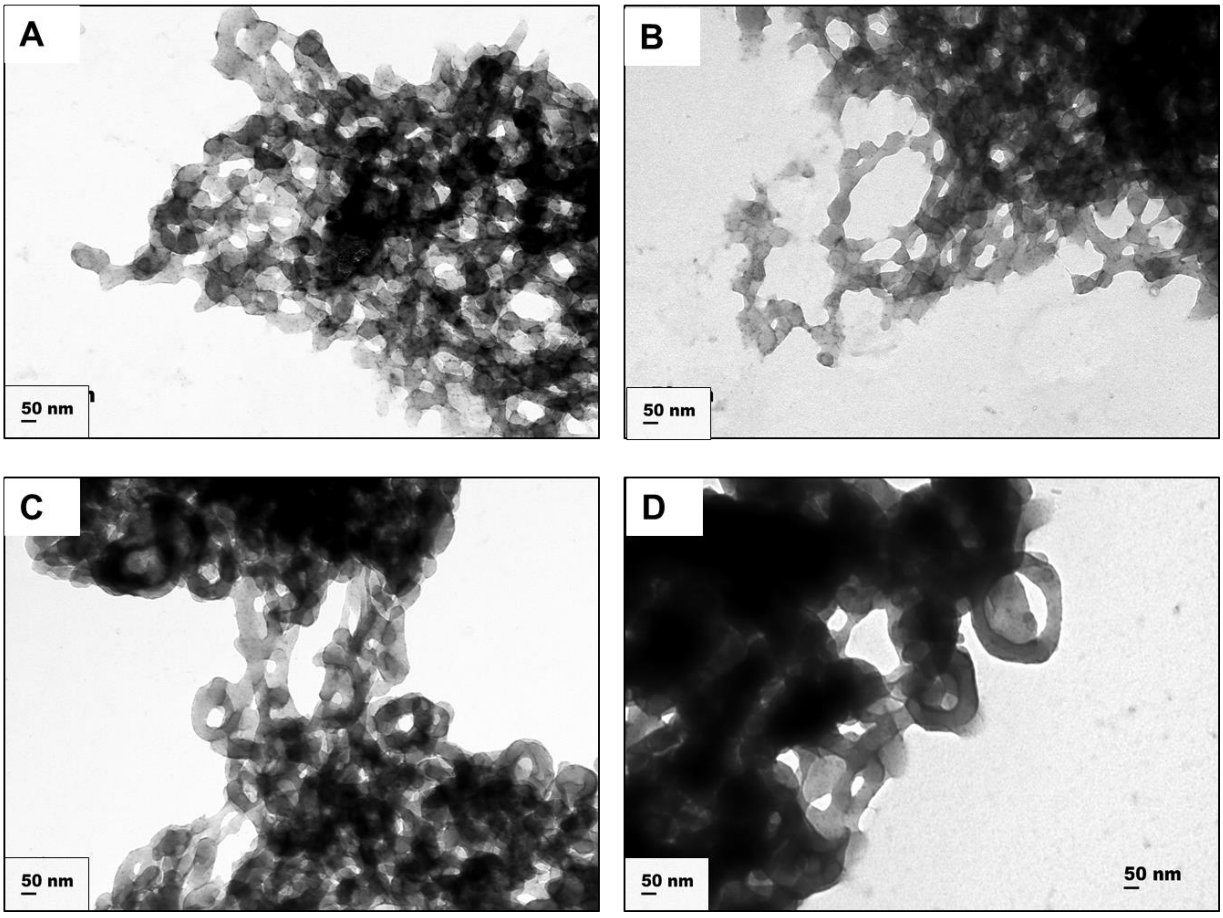

Figure D2. TEM images of f_{PS} = 0.5 when R_{NaCl} = 1.5 and c_0 = A,B) 0.25 wt % and C,D) 0.50 wt %

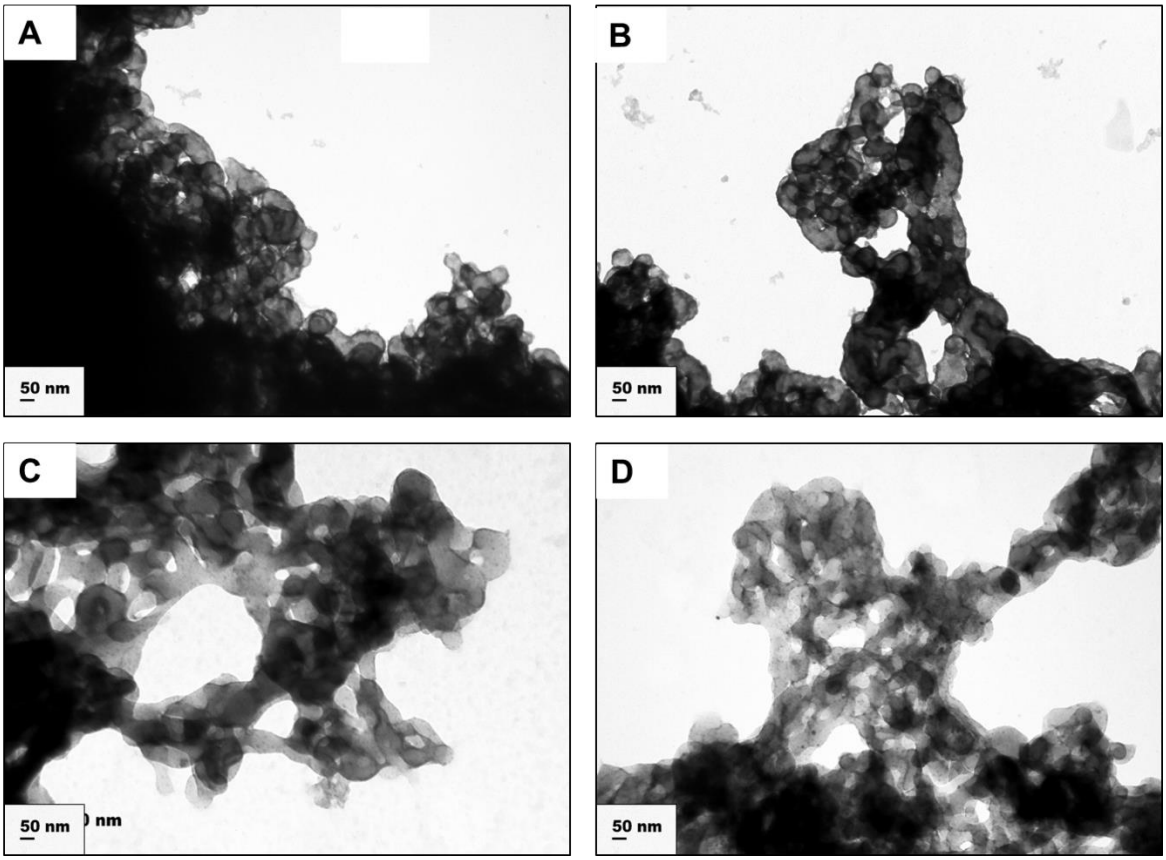

Figure D3. TEM images of f_{PS} = 0.5 when R_{NaCl} = 3.0 and c_0 = A,B) 0.25 wt % and C,D) 0.50 wt %

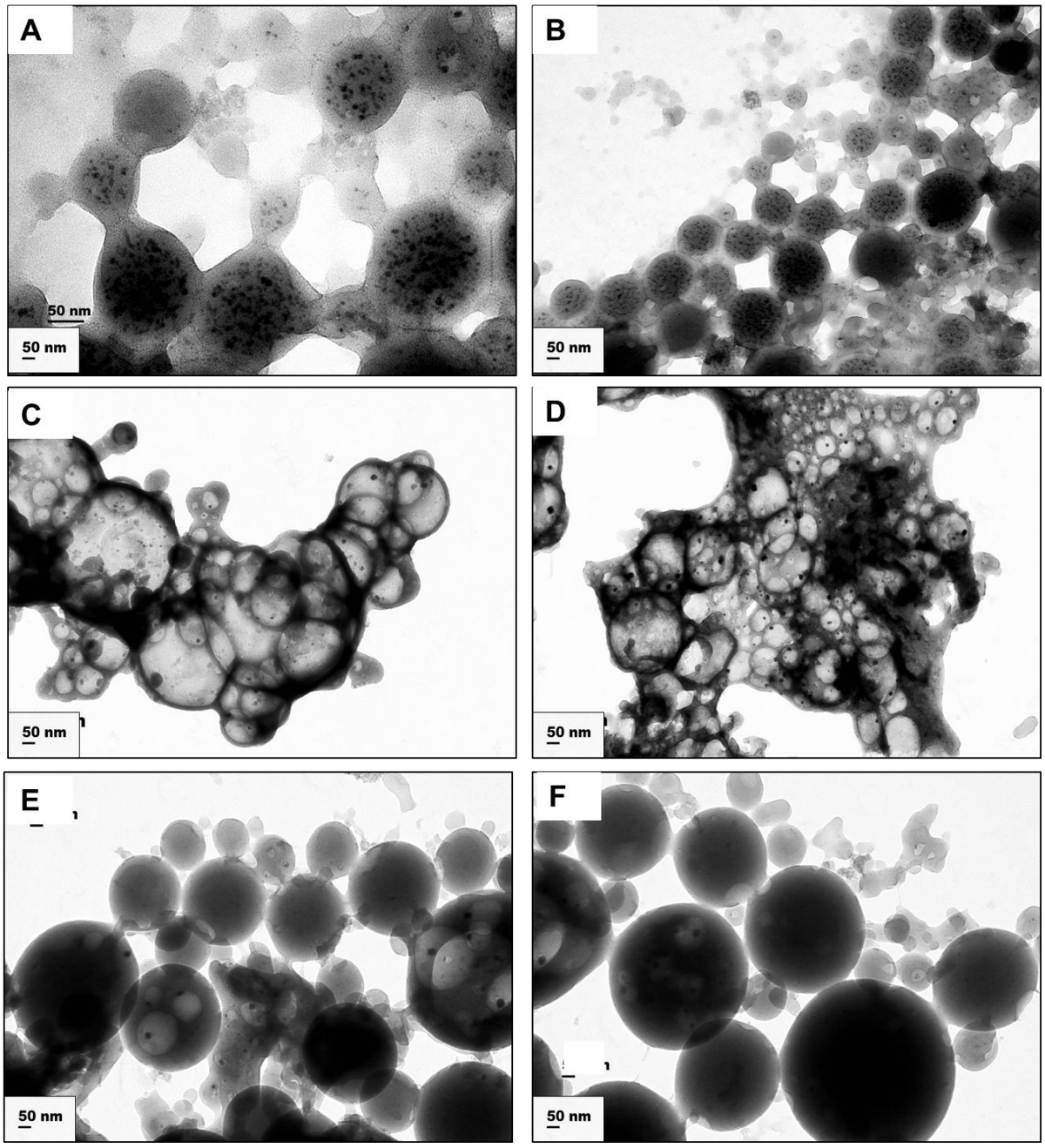

Figure D4. TEM images of f_{PS} = 0.7 when R_{NaCl} = 0.0 and c_0 = A,B) 0.25 wt % C,D) 0.50 wt % E,F) 0.75 wt %

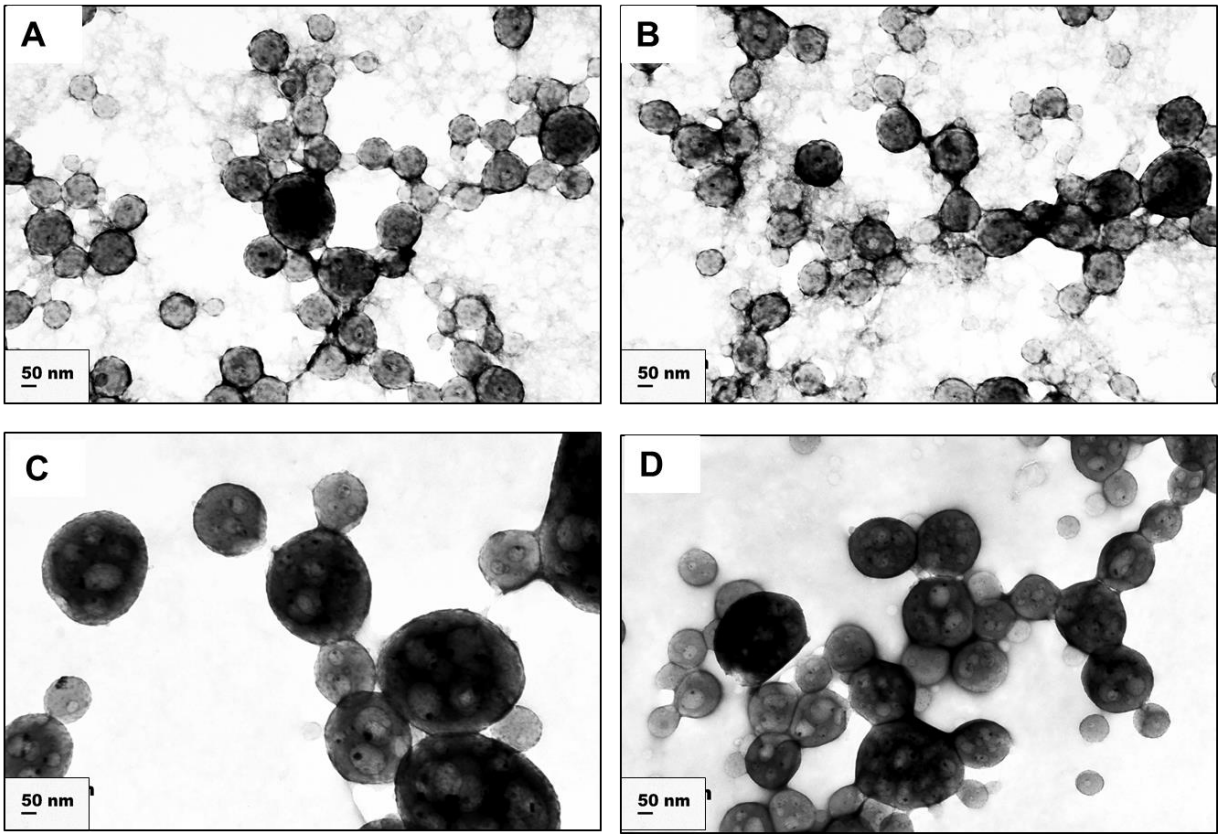

Figure D5. TEM images of f_{PS} = 0.7 when R_{NaCl} = 1.5 and c_0 = A,B) 0.25 wt % and C,D) 0.50 wt %

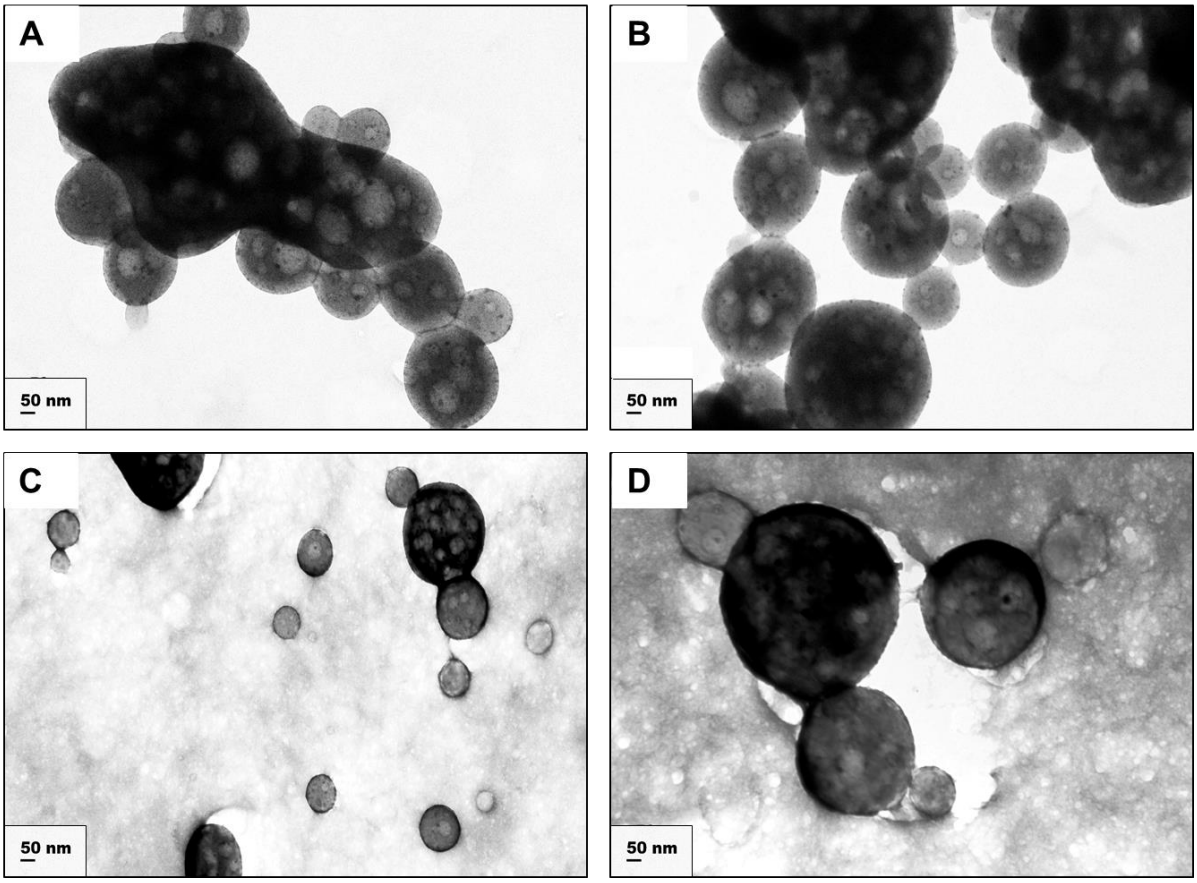

Figure D6. TEM images of f_{PS} = 0.7 when R_{NaCl} = 3.0 and c_0 = A,B) 0.25 wt % and C,D) 0.50 wt %

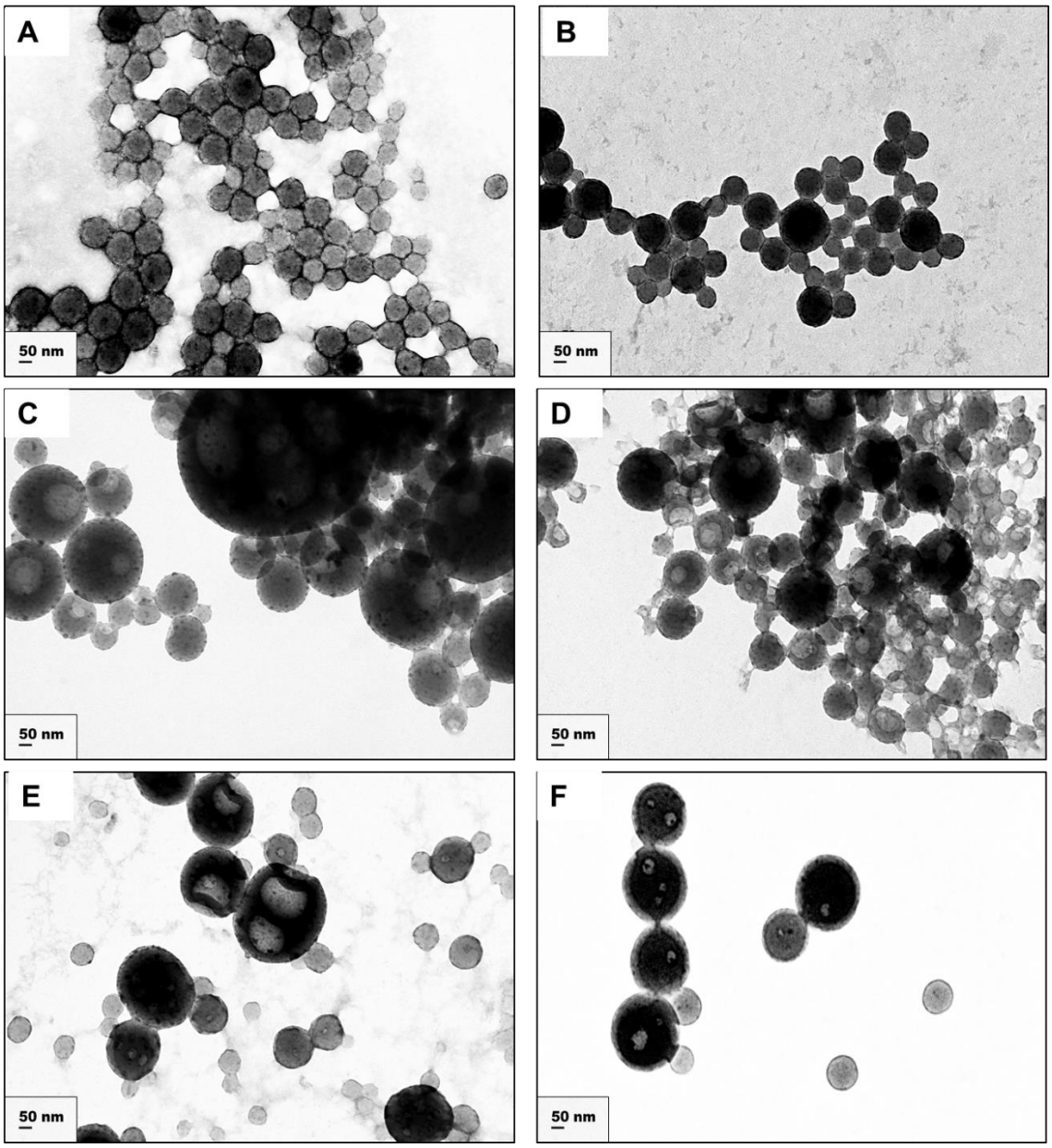

Figure D7. TEM images of f_{PS} = 0.8 when R_{NaCl} = 0.0 and c_0 = A,B) 0.25 wt % C,D) 0.50 wt % and E,F) 0.75 wt %

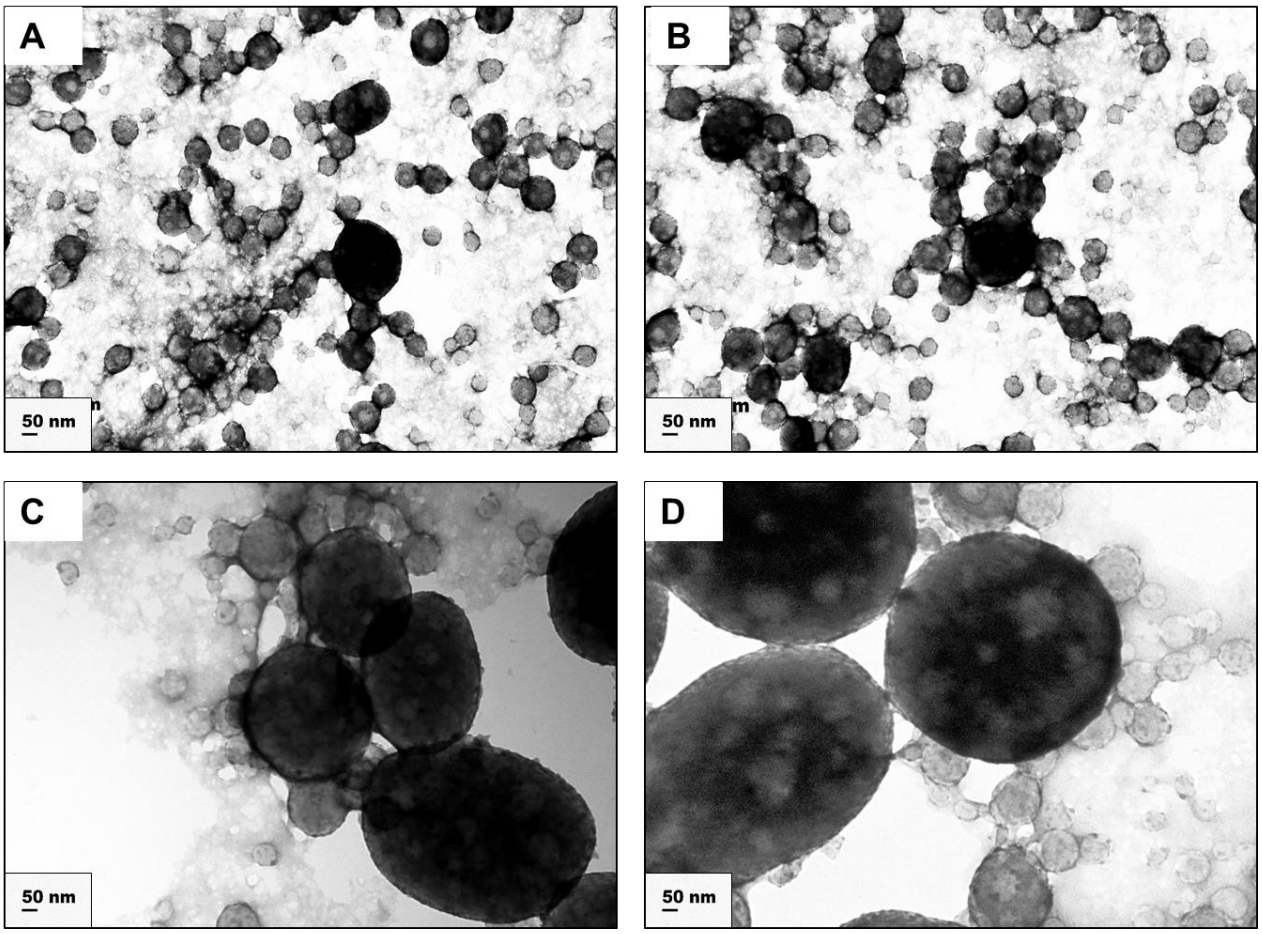

Figure D8. TEM images of f_{PS} = 0.8 when R_{NaCl} = 1.5 and c_0 = A,B) 0.25 wt % and C,D) 0.50 wt %

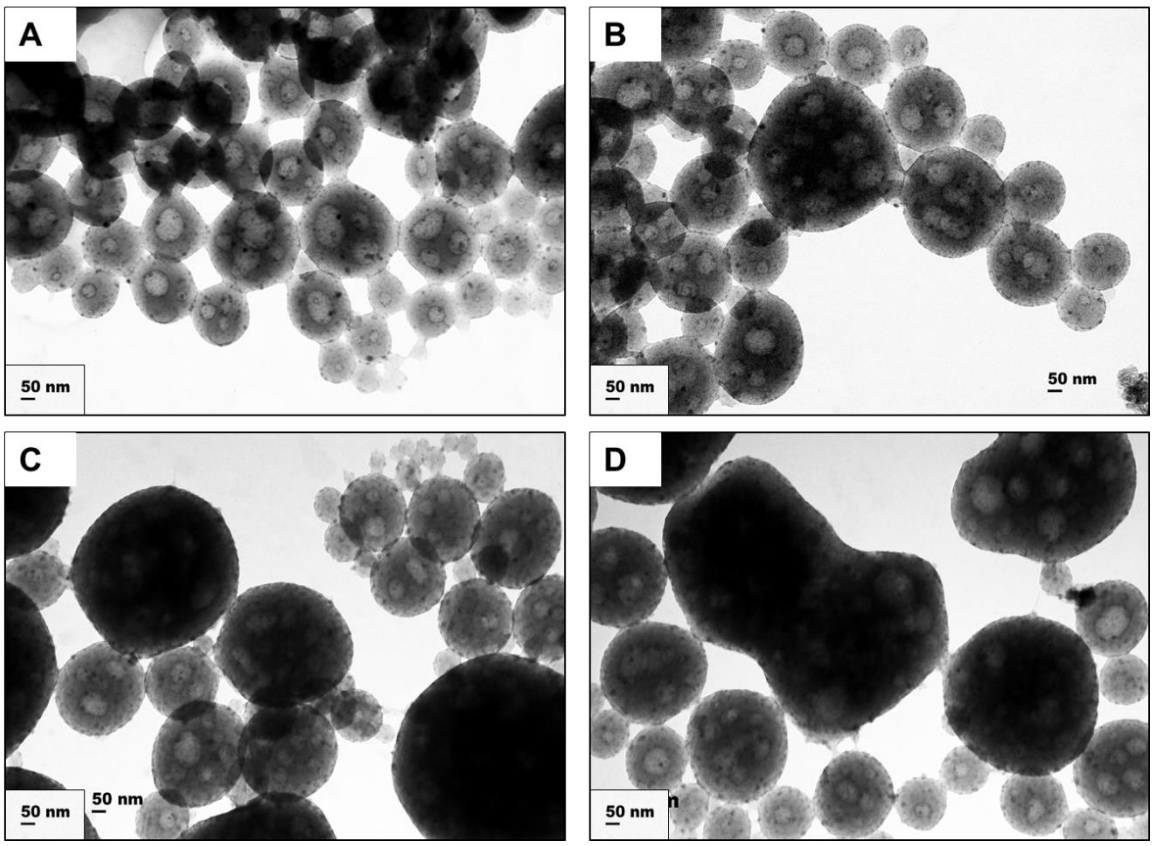

Figure D9. TEM images of f_{PS} = 0.8 when R_{NaCl} = 3.0 and c_0 = A,B) 0.25 wt % and C,D) 0.50 wt %

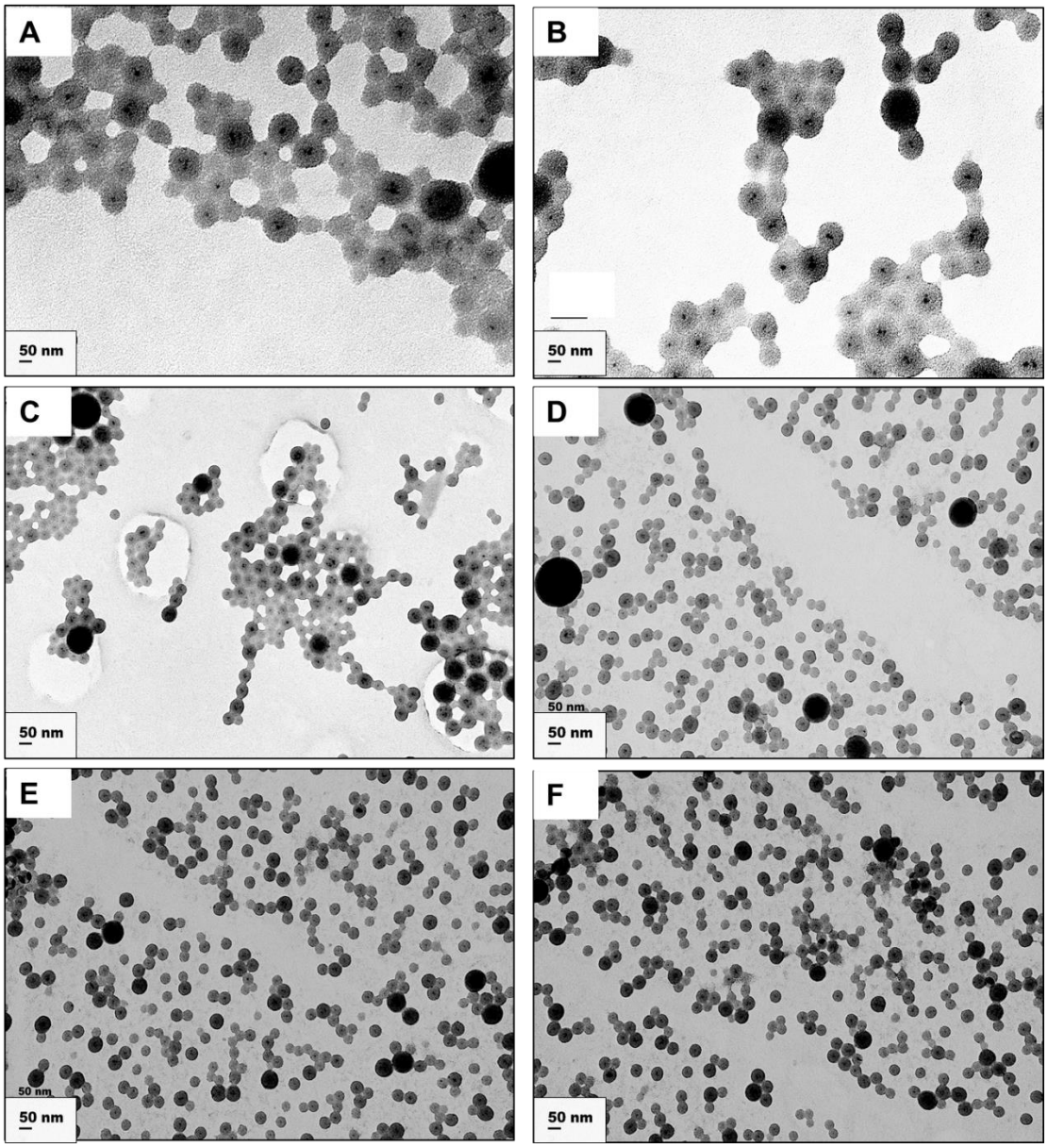

Figure D10. TEM images of f_{PS} = 0.9 when R_{NaCl} = 0.0 and c_0 = A,B) 0.25 wt % C,D) 0.50 wt % and E,F) 0.75 wt %

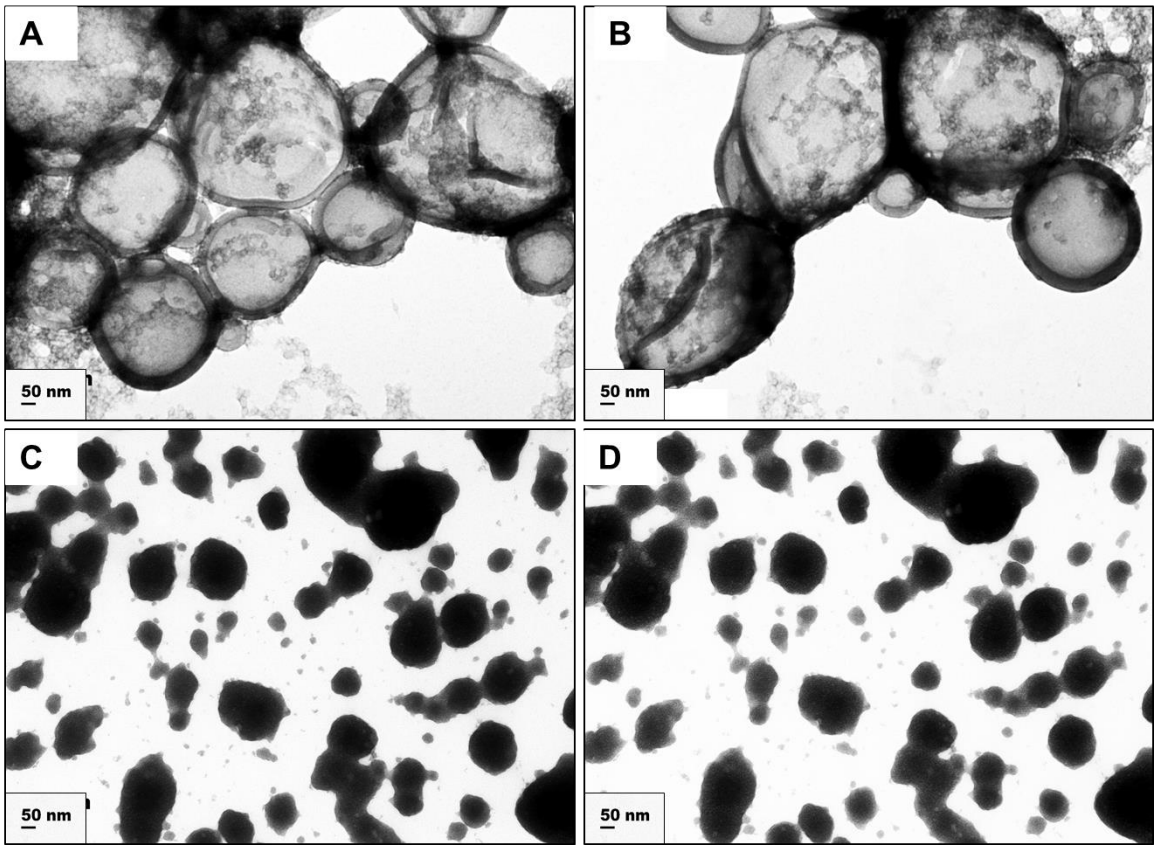

Figure D11. TEM images of f_{PS} = 0.9 when R_{NaCl} = 1.5 and c_0 = A,B) 0.25 wt % and C,D) 0.50 wt %

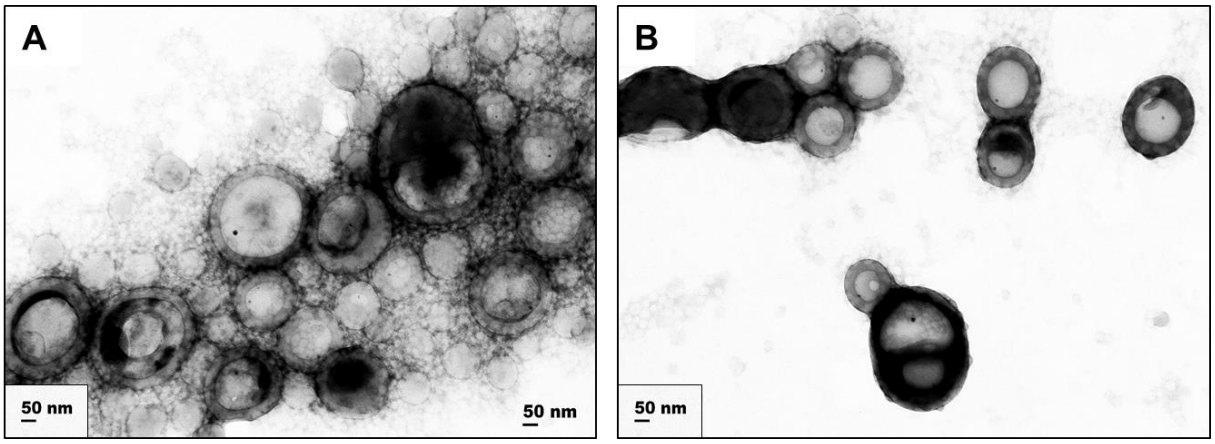

Figure D12. TEM images of f_{PS} = 0.9 when R_{NaCl} = 3.0 and c_0 = A,B) 0.25 wt %

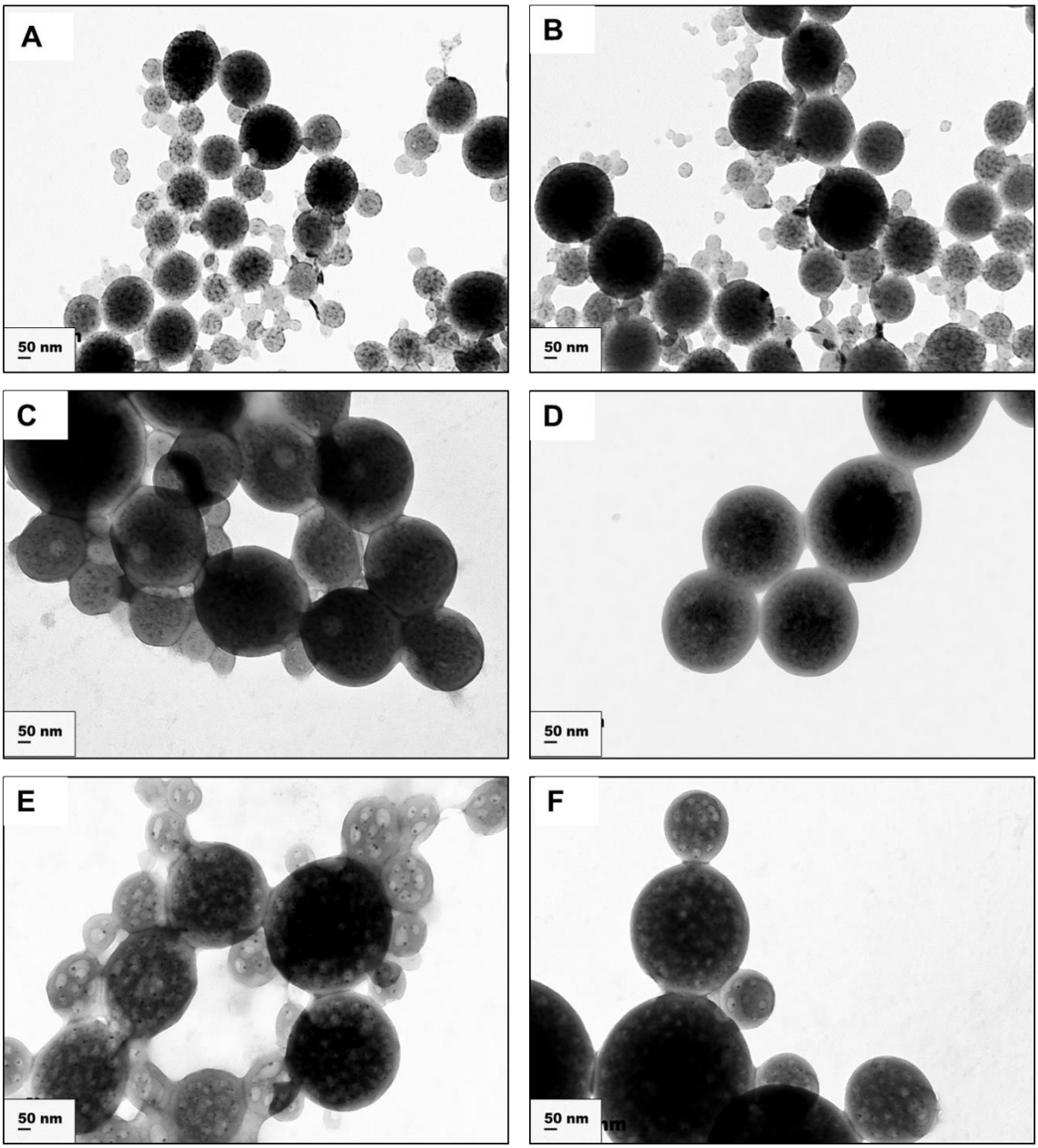

Figure D13. TEM images of PMAA-54 when R_{NaCl} = 0.0 and c_0 = A,B) 0.25 wt % C,D) 0.50 wt % and E,F) 0.75 wt %

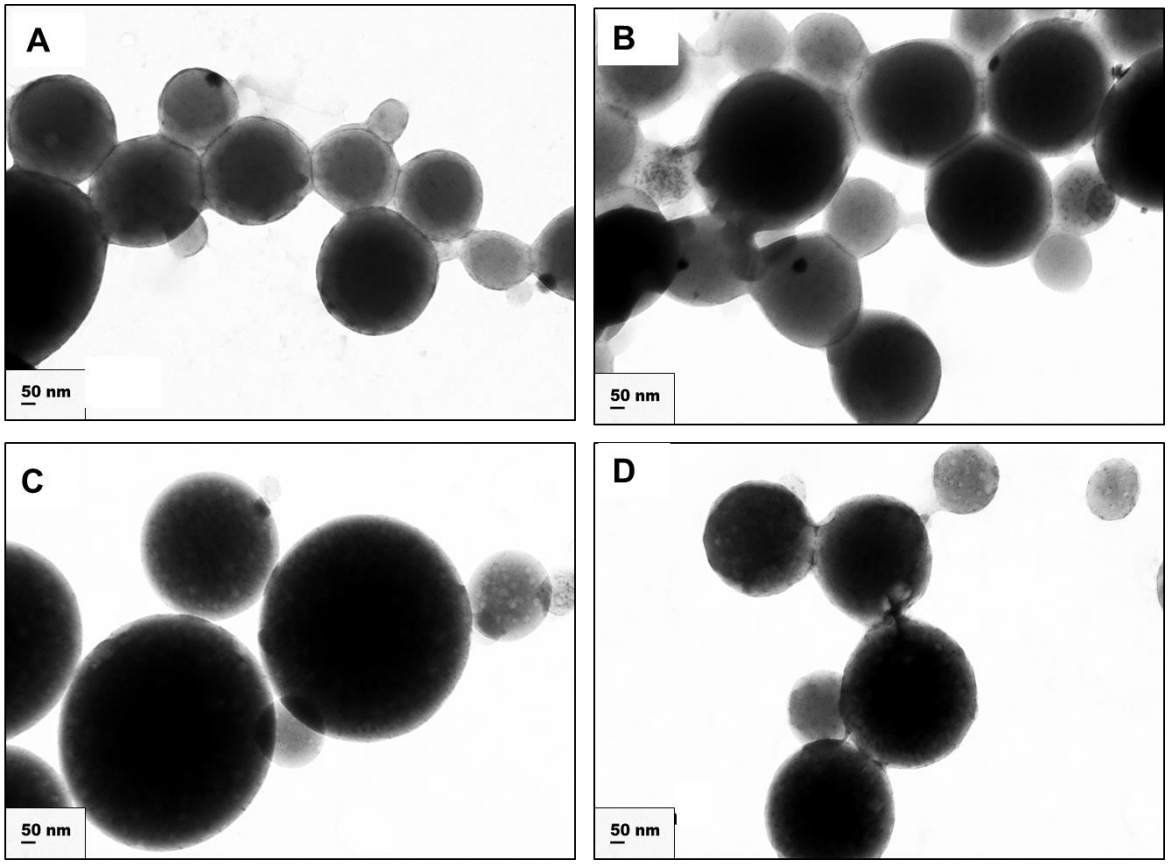

Figure D14. TEM images of PMAA-54 when R_{NaCl} = 1.5 and c_0 = A,B) 0.25 wt % and C,D) 0.50 wt %

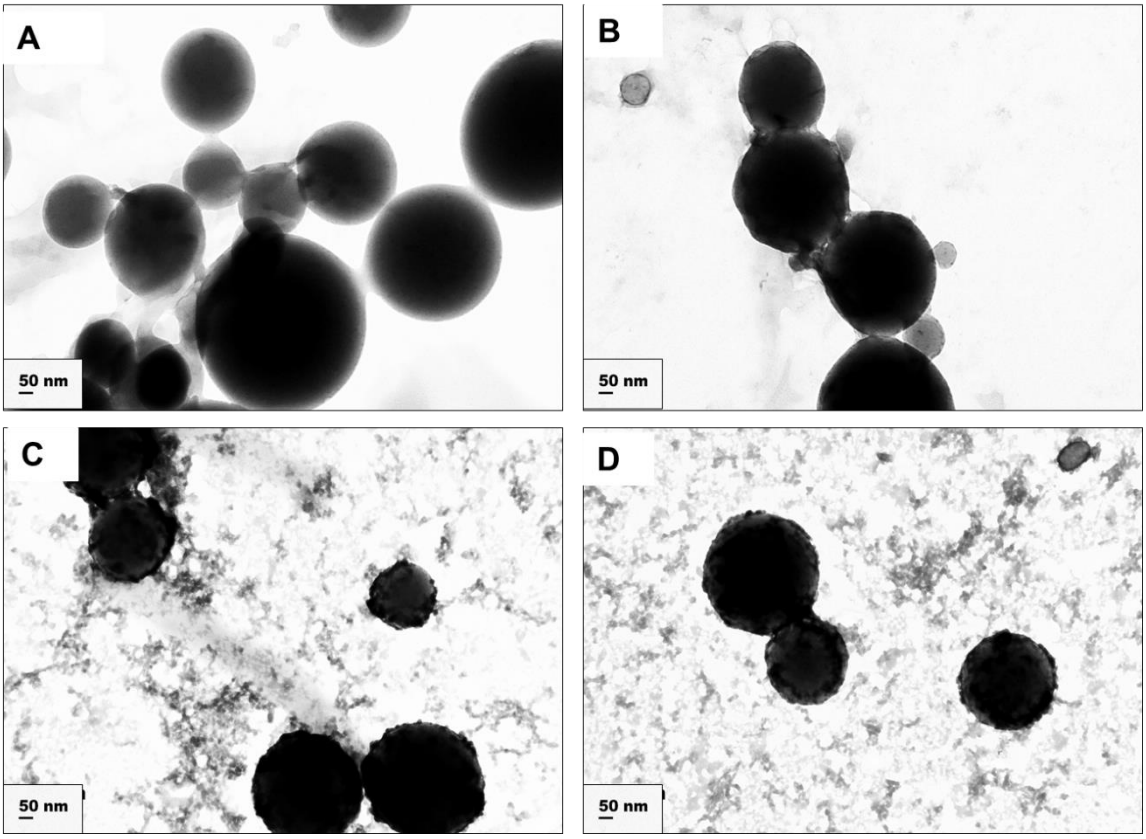

Figure D15. TEM images of PMAA-54 when R_{NaCl} = 3.0 and c_0 = A,B) 0.25 wt % and C,D) 0.50 wt %

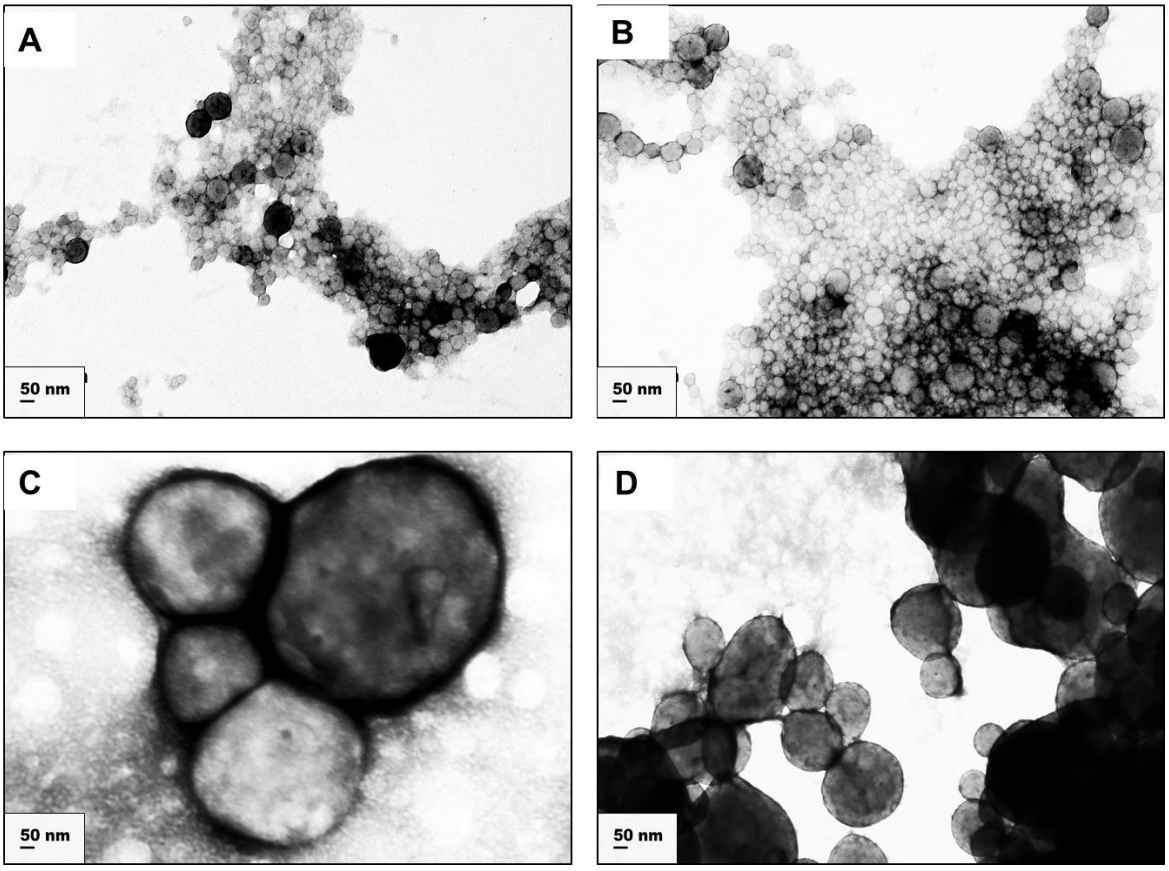
A
50 nm
B
50 nm
C
50 nm
D
50 nm

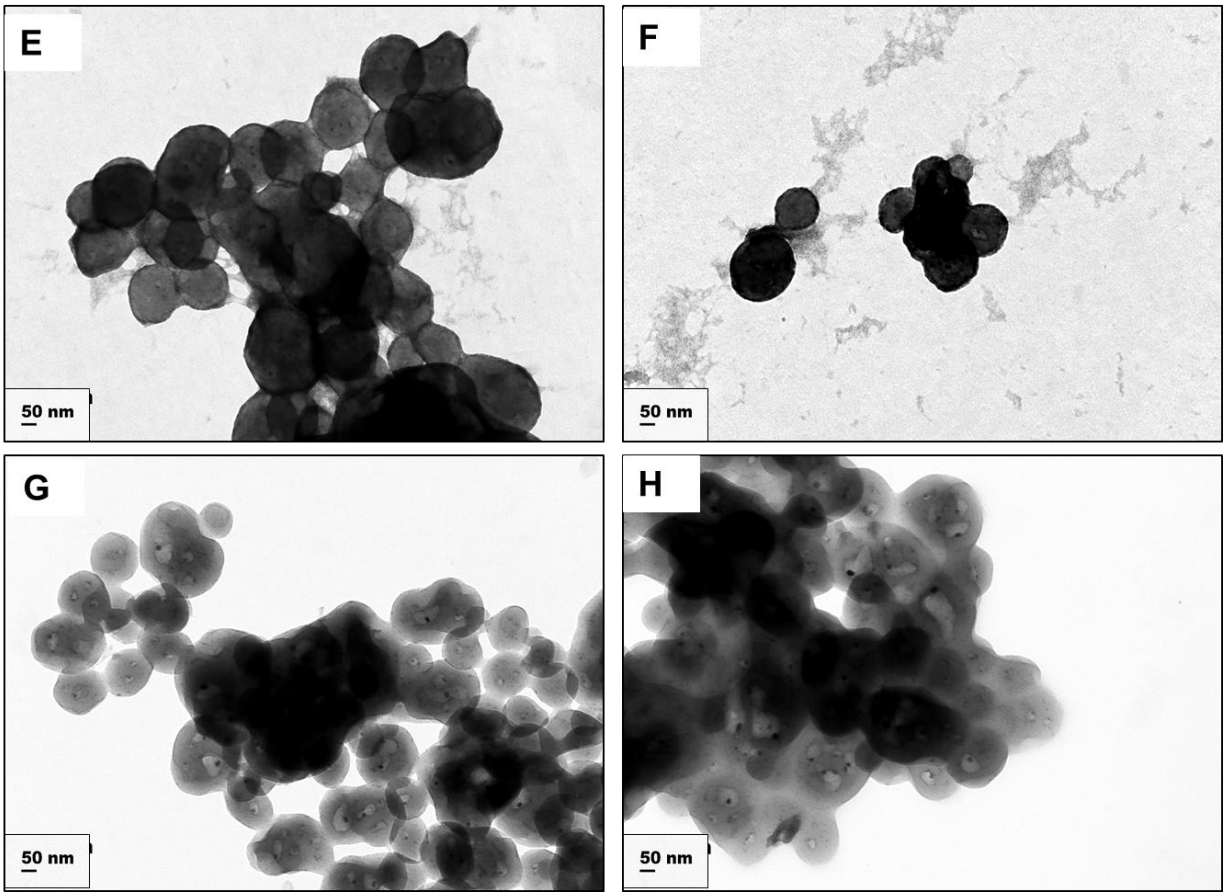

Figure D16. TEM images of PMAA-154 when R_{NaCl} = 0.0 and c_0 = A,B) 0.25 wt % C,D) 0.50 wt % E,F) 0.75 wt % and G,H) 1.00 wt %

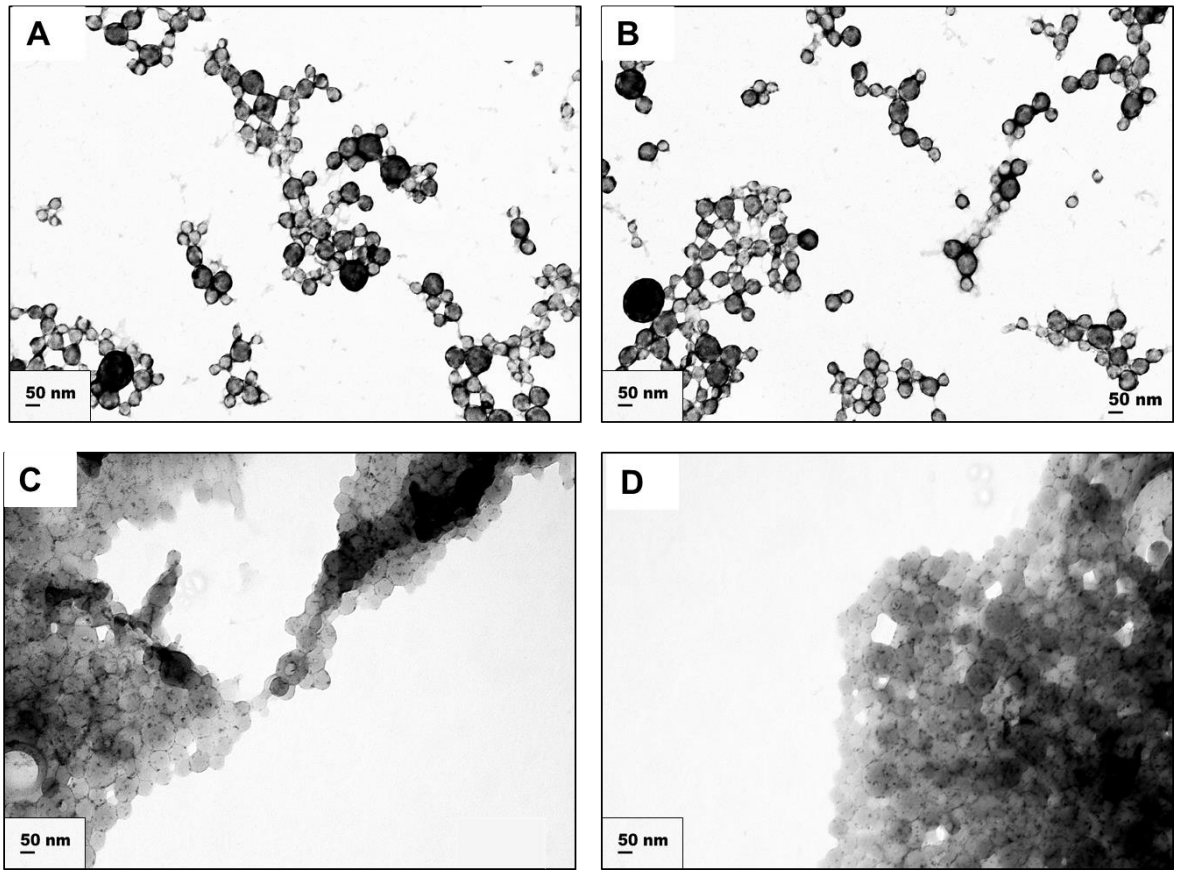

Figure D17. TEM images of PMAA-154 when R_{NaCl} = 1.5 and c_0 = A,B) 0.25 wt % and C,D) 0.50 wt %

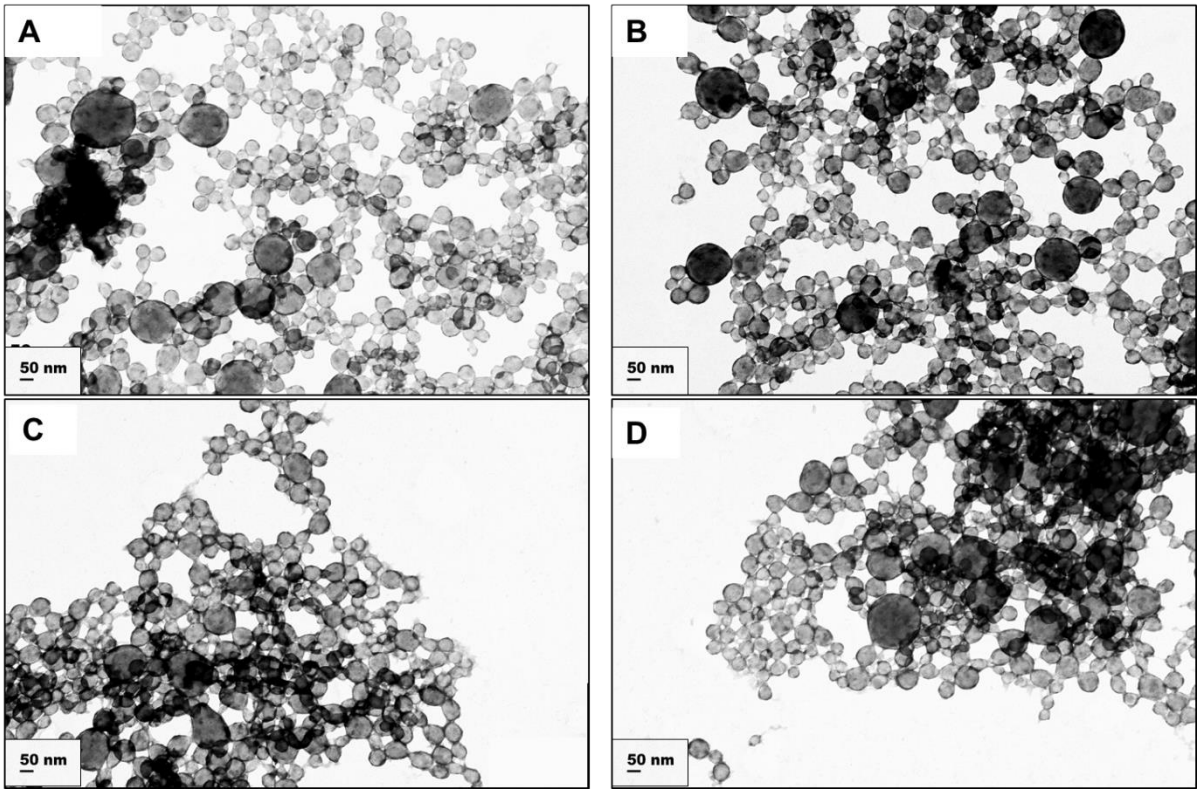

Figure D18. TEM images of PMAA-154 when R_{NaCl} = 3.0 and c_0 = A,B) 0.25 wt % and C,D) 0.50 wt %

1. Hautekeer, J.-P.; Varshney, S. K.; Fayt, R.; Jacobs, C.; Jerome, R.; Teyssie, P. Macromolecules 1990, 23, 3893.

2. Zhong, X. F.; Varshney, S. K.; Eisenberg, A. Macromolecules 1992, 25, 7160.

3. Guo, Yunyong and Matthew G. Moffitt. 2007. "Semiconductor Quantum Dots with Environmentally Responsive Mixed Polystyrene/poly(methyl Methacrylate) Brush Layers." *Macromolecules* 40(16):5868–78.